UNIVERSITY OF Southampton

Faculty of Engineering and the Environment

A Mixed Particle-Mode function Method for Nonlinear Marine Fluid-Structure Interaction Problems with Free Surface

by **Zhe Sun**

Thesis for the degree of

Doctor of Philosophy

Supervisors: Dr. K. Djidjeli , Prof. J.T. Xing

September 2016

UNIVERSITY OF SOUTHAMPTON

ABSTRACT

FACULTY OF ENGINEERING AND THE ENVIRONMENT

Doctor of Philosophy

A MIXED PARTICLE-MODE FUNCTION METHOD FOR NONLINEAR MARINE FLUID-STRUCTURE INTERACTION PROBLEMS WITH FREE SURFACE

by Zhe Sun

In this study, a computational model which couples particle method for fluid part and modal superposition for structure part is developed to investigate the Fluid Structure Interaction problems with free surface.

As a Lagrangian mesh-free method, the MPS (Moving Particle Semi-implicit) method is very suitable for simulating violent flows such as breaking waves on free surface. However, despite its wide range of applicability, the original MPS algorithm suffers from some inherent difficulties in obtaining an accurate fluid pressure in both spatial and time domain. Different modifications to improve the method have been proposed in the literature. In this study, the following modifications are proposed to improve the accuracy of pressure calculations and the stability of the method: i) A density error compensation source term in the pressure Poisson equation with no artificial term in the formulation, ii) New solid and free surface boundary handling methods, iii) Particle position shifting and collision handling, and iv) A new version of "cell-link" neighbour particle searching strategy, which reduces about 6.5/9 (72%) of the searching area compared with traditional "cell-link" algorithm. For problems where violent free surface deformation only occur in a constrained area, the efficiency of MPS is further improved by weakly coupling with BEM (Boundary Element Method).

For the structure that undergoes very large rigid motions and relatively small elastic deformation, an efficient computational model that couples the rigid-body and flexible modes in the same set of formulation. Unlike the traditional modal analysis, this model takes into account the mutual effect between rigid-body motion and flexible deformation. It is more efficient compared with FE (Finite Element) method, regardless of the size of the structure. For $2D$ cases,

if only the first three modes are chosen to represent the flexible deformation of the structure, it only results in a 6×6 equation system to be solved.

For the fluid structure interaction coupling, the Gauss-Seidel iteration with Aitken relaxation scheme is used.

The effectiveness of the proposed modifications for MPS method is validated by a $2D$ Dam-break flow. Furthermore, various typical impact flow problems in marine engineering are simulated to test the applicability of the modified MPS method. It includes $2D/3D$ Dam-break with different boundary conditions (such as obstacle in the middle of the tank, spring supported rigid wall and flexible cantilever beam), liquid sloshing, wedge-shape and ship-section-shape dropping problems. The weak coupling scheme between MPS and BEM are also tested by the $2D$ breaking solitary wave impacting a flexible wall problem. The coupling of fluid and structure solver is also tested by various problems including $2D$ flexible wedge dropping and $2D/3D$ floating beam/ship slamming problems. The numerical results obtained are found to be in good agreement with the available numerical or experimental results. With the proposed modifications, the stability and accuracy of the pressure field are improved in spatial and time domains. The proposed structure model also proves to be effective.

Contents

List of Figures

List of Tables

Declaration of Authorship

I, Zhe Sun, declare that the thesis entitled *A Mixed Particle-Mode function Method for Nonlinear Marine Fluid-Structure Interaction Problems with Free Surface* and the work presented in the thesis are both my own, and have been generated by me as the result of my own original research. I confirm that:

- this work was done wholly or mainly while in candidature for a research degree at this University;
- where any part of this thesis has previously been submitted for a degree or any other qualification at this University or any other institution, this has been clearly stated;
- where I have consulted the published work of others, this is always clearly attributed;
- where I have quoted from the work of others, the source is always given. With the exception of such quotations, this thesis is entirely my own work;
- I have acknowledged all main sources of help;
- where the thesis is based on work done by myself jointly with others, I have made clear exactly what was done by others and what I have contributed myself;
- parts of this work have been published as: [145], [144] ,[146] and [148]

Signed:.....

Date:.....

List of publications

1. Zhe, Sun, Kamal Djidjeli, J. T. Xing, F. Cheng, A. Javed, *Some modifications of MPS method for incompressible free surface flow*, 11th World Congress on Computational Mechanics (WCCM XI) Barcelona, Spain, July 2014.

2. Zhe Sun, K. Djidjeli, J.T. Xing, F. Cheng, *Modified MPS method for the 2D Fluid Structure Interaction problems with free surface*, Computers and Fluids **122**, (2015).

3. Zhe Sun, K. Djidjeli, J.T. Xing, F. Cheng, *Coupling MPS and Modal Superposition Method for Flexible Wedge Dropping Simulation*, 25th International Offshore and Polar Engineering Conference (ISOPE), Kona, Hawaii, US, 21-26 June 2015.

4. Zhe Sun, K. Djidjeli, J.T. Xing, F. Cheng, *Coupled MPS-modal superposition method for 2D nonlinear fluid structure interaction problems with free surface*, Journal of Fluids and Structures **61**, (2016).

Acknowledgements

Firstly, I would like to thank my supervisors Dr K. Djidjeli and Prof. J.T. Xing, who give me the opportunity and guidance of my PhD study. Dr K. Djijdeli is always able to give me patient illustration and helpful discussion on various issues of this research at different stages. I really appreciate his encouragement and help during my PhD study. Prof. Xing has a comprehensive understanding and profound insight of the flied of Fluid Structure Interaction dynamics. I have been benefited immensely during those discussions with him on various topics.

Secondly I am also very grateful to all the persons who have help me in my research group, especially Ali Javed who kindly provided many help during my first year of the research.

This research was co-sponsored by Lloyd's Rigister Group (LR), University of Southampton and China Scholarship Council (CSC). I would like to express my sincere gratitude to them for supporting this PhD study.

Finally, to my dearest parents, I would like to thank their continuous support and unconditional love. Their encouragement and support are without doubt one of the most important reasons that make me get through all the difficulties of this PhD study.

感谢父母一直以来的理解与支持。

Nomenclature

$X-Y$ system	the global coordinates system
$x_R - y_R$ system	the local system attached with rigid-body part of the whole structure
$s - w$ system	the local system attached with flexible part of the whole structure
α	the coefficient defined in Eq. (2.39)
α_u	the geometry coefficient of Eq. (B.2)
β, β_{3d}	the control parameter for free surface particle identification in Eq. (2.24) and Eq. (2.44), respectively
γ	the control parameter used in Eq. (2.28)
$\Gamma_{fs}, \Gamma_{wm}, \Gamma_{fw}$	the boundary of BEM domain
$\mathbf{\Gamma}_{fsi}^k$	fluid structure interface position at k^{th} time step
ϵ	the control parameter used in Eq. (2.46)
η	the deflection function along the beam
θ_R, θ_f	the rotation angle of rigid-body and flexible parts of the structure in the proposed model
θ_b	the rotation angle of the rigid wall with spring hinged joint in Section 5.1.1.2
κ	parameter used in beam mode function defined by Eq. (3.15)
λ	the parameter used in Laplace operator (Eq. (2.19)) of MPS
Λ	vector of the nature frequencies of structure
ν_d	diffusion coefficient used in Eq. (2.15)
ν	kinematic viscosity coefficient
ρ_0	fluid density

ρ_l	the line density of beam
σ_d^2	variance of the diffusion process
σ	parameter used in beam mode function defined by Eq. (3.17)
$\mathbf{\Phi} = [\phi_1, \phi_2, \phi_3, \cdots]$	mode functions of structure
φ	velocity potential
$\mathbf{\Psi}_0, \mathbf{\Psi}_1$	parameters defined in the Eq. (3.51) and 3.52 to simplify the proposed structure model
$\boldsymbol{\tau}$	tangent vector of the solid or free surface boundary
ω	natural frequency
$\boldsymbol{\xi}$	the coordinates of beam central line represented in $s - w$ system
C	speed of sound
C_d	the scaling coefficient of beam mode functions
d	number of space dimensions
$\mathbf{D}$	the vector of generalized position variables for the proposed structure model defined by Eq. (3.53)
E	Young's Module
$\mathbf{g}$	vector pointing to direction of gravity
i, j	index number of a particle or different parts of structure
I_d^k, I_s^k	the integration of distributed dipole and source over k^{th} element in BEM
$\mathbf{I}_N$	the $N \times N$ identity matrix
I_R, I_f, I_b	rotational inertia of the corresponding structure
J	the 2^{nd} order moment of cross section
k	the index number of different time step
K_b	the stiffness of the spring in Section 5.1.1.2
l, L, L_b	the length of the corresponding structure
M, M_f, M_R, M_b	the mass of corresponding part of structure
n	particle density defined by Eq. (2.8)
$\mathbf{n}$	normal vector of the solid or free surface boundary

N_u	particle number in an unit volume
N, N_p	neighbour particle numbers of a particular particle in its support domain or the number of modes that has taken into account
p	pressure
$\mathbf{Q}$	the vector of generalized forces variables for the proposed structure model defined by Eq. (3.54)
$\mathbf{q} = [q_1(t), q_2(t), q_3(t), \cdots]^T$	generalized coordinates corresponding to beam mode functions
$\mathbf{r}_i$	position vector of particle i
r_{ij}	value of the distance between particle i and j
r_0	initial distance between particles
r_e	the radius of the local support domain
$\mathbf{R}_f, \mathbf{R}_R$	the rotation matrix defined by Eq. (3.34)
$t, \Delta t$	time or time interval
$\mathbf{T}$	viscous stress tensor
T, T_R, T_f	kinetic energy of the structure
T_b	the torque applied on the beam structure in Section 5.1.1.2
u_f	an arbitrary scalar function
$\mathbf{u}_f$	an arbitrary vector function
$\mathbf{u}$	fluid velocity
$\mathbf{u}_b$	solid boundary velocity
$\mathbf{U}$	a constant matrix define by Eq. (3.37)
V, V_R, V_f	potential energy of the structure
$\mathbf{V}, \mathbf{V}_p$	velocity of the boundary in BEM
$w(r_{ij})$	the weight function
$\mathbf{X}_{cR} = [X_{cR}, Y_{cR}]$	the coordinates of the mass centre of the rigid-body part of structure in global $X - Y$ system
$\mathbf{X}_{cf} = [X_{cf}, Y_{cf}]$	the coordinates of the mass centre of the flexible part of structure in global $X - Y$ system
$\mathbf{x}_{of} = [x_{of}, y_{of}]$	the coordinates of flexible part mass centre of whole structure in $x_R - y_R$ system

$\mathbf{x}_R = [x_R, y_R]$	the coordinates of the rigid-body part mass centre of whole structure in $x_R - y_R$ system

Chapter 1

Introduction

1.1 Background and Motivation

The violent free surface flow and structure interactions are very common for ship and other offshore structures. Some typical phenomena include slamming between ships and waves, sloshing of the liquid inside the tanks for LNG ships, the Green Water loading when run-up water impacting the upper structure on the deck, etc. Generally, the experimental approach is still regarded as the most reliable way to test the performance of the marine structures. However experimental study comes with some limitations as well, for example the high financial and time cost, scale problem due to the restriction of physical size, etc. The rapid development of the computer science makes the large scale numerical simulation realistic. This provides the alternative to overcome the shortcomings of experimental study aforementioned. To simulate and understand these phenomena, and consequently provide some guidance for the design of the marine structures to guarantee their performance and safety under various sea conditions are a vital part of the marine engineering research. Despite recent advances in numerical methods and computer technology, the numerical simulation of nonlinear Fluid-Structure Interaction (FSI) problems still remain as a challenge [156].

Generally, instead of solving a simultaneous set of equation system for both fluid and structure domain, for most of the engineering problems, two different solvers will be used to solve each of them separately with a coupling mechanism to exchange information (A brief review of the FSI coupling strategy will be given in Section 1.2).

For the fluid part, various types of solvers have been used for different situations such as potential flow model, mesh-based Navier-Stokes (NS) solver and the emerging particle methods. The potential flow model is an efficient and stable approach for many wave-structure interaction problems. However, it can not handle the situations where breaking waves are involved. The general CFD (Computational Fluid Dynamics) solvers that are based on Navier-Stokes equation are capable of dealing with these violent free surface deformations. Based on the way of domain geometry discretization, the NS type solvers could be further classified as mesh-based and mesh-less methods (including particle method). The large free surface deformation can cause mesh distortion or other problems in the mesh-based approaches such as Volume of Fluid (VOF) [47], Level Set(LS) method [115] and Constrained Interpolation Profile (CIP) [51]. On the other hand, the particle method, which is a mesh-less and Lagrangian approach, is very straightforward and suitable for the aforementioned violent free surface and structure interaction problems. The SPH (Smoothed Particle Hydrodynamics) [35, 97] and MPS (Moving Particle Semi-implicit) [73] are both representatives of the so-called particle method. Although the rapid development of this method, the application to wave and flexible structure interaction especially the $3D$ case still needs more research and development.

For the structure part, the Finite Element (FE) method is generally applicable to both small flexible deformation [139, 167] and large nonlinear deformation [173]. However it doesn't mean that it is the most suitable one for all problems. Actually for a floating structure like a ship hull, the typical feature of motion is a large rigid-body motion plus a relatively small deformation. This feature makes the modal superposition technique suitable and accurate enough to describe the flexible deformation, which has already been used in the traditional Hydroelasticity calculation [155]. More specifically, in the Hydroelasticity theory, the fluid force is calculated using potential flow model based on the mean rigid-body wave-structure interface without considering the structure displacement, which means the highly nonlinear violent fluid motion and the effect due to the large structure displacement could not be taken into account. The rigid-body and flexible motions computation are based on these resultant forces separately without considering the mutual effect between them. Therefore, an efficient modal analysis model which first considers the coupling between rigid-body and flexible modes, and then allows the fluid solver to consider the structure displacement effect in an iterative manner, would certainly improve the capacity of the modal analysis for marine engineering problems.

Motivated by the above considerations, this thesis aims at developing an improved particle method for fluid and model superposition technique for structure for accurate simulation of complex free-surface fluid flow and floating flexible structure interaction problems. In the following section of this Chapter, a review of the fluid structure interaction strategy will be given, then the various ways of simulating nonlinear free surface flow and flexible structure dynamics will be examined. Finally the research objective, thesis structure and major findings are presented.

1.2 Fluid Structure Interaction dynamics

The Fluid Structure Interaction (FSI) dynamics, as defined in Xing et al. [167, 170], is "an interdisciplinary subject to study the dynamic behaviour of a system consisting of both solids (structures) and fluids simultaneously", in which neither the fluid nor solid variables could be eliminated when solving the other domain. FSI problems in engineering involves inter-disciplinary studies relating to fluid, flexible structure and their physical coupling mechanisms. Their interaction gives rise to a rich variety of physical phenomena in many fields of engineering, for example, sloshing in LNG tankers, offshore structures, free surface channel flows, ship-wave interaction, etc. For most practical fluid-structure interaction problems, it is difficult to find analytical solutions and reliance on numerical methods become the only way forward. However, despite the recent advances in numerical methods and computer technology, the numerical simulation of fluid-structure interaction problems still remain a challenge, and in particular for problems characterized by large displacements of the fluid-structure interface or by a rapidly moving fluid free-surface (which are still highly intractable).

As mentioned before, based on the solving strategy, the FSI problems can be classified into two categories, i.e. monolithic and partitioned approaches.

In a monolithic method, the governing equations of both fluid and solid domain are normally formulated in the same mathematical framework (or using a uniform constitutive relationship for both domains) and then discretized into a single algebraic system. The boundary conditions (e.g. velocity continuity condition on the interface) will be substituted into this algebraic system [59]. The resultant linear system will be solved by a single solver [32] (instead of

one for each part). This approach is suitable for the problems where no clear interface exist such as flow in porous medium [167].

Since this kind of approach is an inherent implicit method, it tends to give a more stable solution and will allow a relatively large time increment. This approach is especially suitable for the cases when two subdomains have similar densities (e.g. the mass ratio is close to one) [122]. However, in this situation, another problem called "added mass" effect [54] will become important, which can result in instability or poor convergence. This phenomena is more serious in biomechanics [54] in which the muscles and arteries are more similar with the blood (the interacting fluid) in material property than the situations in the field of marine or aerodynamic engineering. The light-weight structures can suffer this problem as well [122].

Actually, the mass ratio is also the reason why monolithic approach has difficulty in handling fluid interacting with stiffer structures [42], such as water-ship interaction. Considering that different subsystems have different scaling of variables in such situations, which will result in poorly conditioned coupling matrix (e.g. including zero entries on the diagonal [43]), it is difficult to solve this linear system without any pre-processing [32, 46]. One of the key parts of the existing monolithic methods is consequently to develop effective pre-conditioners [45, 46] for the resultant algebraic system after discretization. Another issue arises in monolithic method is that since the time increment is equal in each subsystems, the efficiency may not be as good as that in partitioned methods in which one subsystem can be solved with larger time intervals if necessary [43].

The main advantage of partitioned method, compared with its monolithic counterpart, is the high code modularity and flexibility which permits to adopt various, and more importantly—suitable solvers for each sub-domain [174]. The resultant subsystems are smaller and better conditioned [122], which will be easier to solve. The state-of-the-art achievements for the fluid and solid computations could be adopted, and the code maintenance is easier, e.g. keeping the other solver generally unchanged when updating one solver. The drawback is the convergence and stability problem [45, 174], especially for the weakly coupling in which the interface compatibility condition may not be satisfied accurately at each time step. But the introduction of iteration within each time step can, to a large extent, overcome this problem, although sometimes the convergence rate is slow.

Based on the above discussion, the partitioned methods are supposed to be more suitable, at least in marine engineering, for FSI simulation, although monolithic approach could be effective for other special applications (e.g. bio-engineering [54]).

For the partitioned approach (sometimes also referred to as iterative approach), two criteria could be used to classify the various methods: 1) the type of the boundary condition adopted for fluid and structure solver on the interface; 2) whether an iterative procedure is employed within one time step. Regarding boundary conditions, the most commonly used ones for fluid and structure solver are essential and natural conditions respectively, which means the position, velocity and acceleration of the interface (from the structure solver) are used to solve the fluid force, and then the pressure from fluid are applied on the interface to solve the structure response. There are also some other types of boundary conditions such as natural boundary for fluid and essential for structure or using natural boundary condition for both fluid and structure solvers [174].

For the ways of integrating the two computational domain together, there are several options. If a linear problem is considered, where the motion of the interface is relatively small or even negligible, either no coupling (which strictly speaking is rather a separate fluid or solid mechanics problem instead of a FSI problem) or weak coupling is accurate enough such as in the field of Hydroelasticity [10]. But, although the weak (i.e. no iteration) interaction between fluid and structure solvers have been applied in some situations [9, 116], for most of the cases, in order to reach a certain level of convergence accuracy, some kinds of iteration between the two solvers are required. As a consequence, the problem of making the iteration convergent and efficient arises. The result of each iteration is the new position of interface, therefore using some forms of preconditioning on this interface before applying it as an input into the next iteration would be necessary to improve the convergence property. Various approaches such as Gauss-Seidel method with relaxation [76, 139], Newton Krylov method [70] or the so-called IQN-ILS [28] ,etc, are used. Among all these techniques, the Gauss-Seidel iteration with Aitken relaxation method, as described in Ref [76], "shows very good convergence properties at surprisingly low cost". Therefore, this technique is adopted in this study as well.

1.3 Nonlinear free surface flow simulation

1.3.1 Potential flow vs. Navier Stokes model

The invisid and irrotational assumption of free surface flow have been extensively used in the field of marine hydrodynamics. The resulting potential flow model is governed by Laplace equation. The numerical solution strategy of this equation could be categorized by various criteria such as the geometric discretization; the Green's function used on the free surface; and the way of handling the time dimension.

More specially, the computational domain could be directly discretized by volume mesh and then solved by various numerical scheme such as FE (Finite Element) [100, 163] or HPC (Harmonic Polynomial Cell) [129]. On the other hand, by using the Green theorem, the Laplace equation could be transformed into a boundary integral equation, which is then solved by BEM (Boundary Element Method) [147]. Clearly the later approach reduces the problem by one dimension and consequently improves the efficiency, which is also why the BEM is more popular in the field of hydrodynamics.

Two types of Green function could be used in BEM to solve the free surface flow problem. One is the so-called free surface Green function which means it satisfies both the Laplace equation and the free surface boundary condition. The discretization only requires to be conducted on the solid boundaries. This approach demands high computational effort and becomes very complicated for nonlinear cases [31]. An alternative option is the simple Green function (or Rankine source) which is only the general solution of Laplace equation. Hence in order to satisfy the free surface boundary condition, a series of this source function has to be distributed along the whole boundary of the problem including both the free surface and solid boundaries. A detailed review of these two approaches could be found in Ref [31].

For the way of handling the time dimension, if the problem under investigation is a periodic flow with single frequency, the time dimension could then be separated and the resultant equation is purely about space variable which depends on the boundary configuration. This is then called frequency domain problem [24, 84]. However for many nonlinear situations where the dynamics of the system is not necessary periodic, the free surface and solid boundaries have to be updated to new position at every time step and then solved. This situation

is called time-domain problem. The MEL(Mixed Euler-Lagrange) algorithm [31, 39, 41, 94] is one of the most popular one used to solve a time domain problem.

Although the potential flow model has been successfully applied for many hydrodynamic problem as mentioned above, one inherent flaw of this model is that it can not handle the situation where wave breaking or re-entry is involved. It means the violent free surface deformation, which is quite common in slamming or sloshing problems, can't be simulated by potential flow model. Also the viscosity effect is ignored in the potential flow, although it does not play a significant role in wave dynamics. On the other hand, as a general approach for almost any fluid dynamic problem, the CFD (Computational Fluid Dynamics) method that is based on Navier-Stokes equations provides the possibility of solving this kind of problem. The review of the traditional mesh-based and the emerging mesh-less CFD methods are given in the next section.

1.3.2 Meshless vs. Mesh-based CFD methods

1.3.2.1 Current mesh-based CFD methods

For the traditional mesh-based CFD approaches, the grids could be generated to conform (body-fitted mesh) or not (fixed Cartesian mesh) to the moving fluid-structure interfaces. The associated numerical schemes such as Finite Volume (FV) [30, 157], Finite Difference (FD) [50–52, 177] and Finite Element (FE) [153, 162, 165, 166] are then applied to these grid configurations to solve the Navier-Stokes equations. In order to simulate the constantly moving free surface, a simple idea is that the grid could be generated to fit (conform) this dynamic shape [140]. But, this approach cannot deal with breaking waves. The main stream strategy of handling free surface, including the post-breaking phase, is to use a scalar function ϕ to identify the phase of fluid, air or solid [177]. A corresponding convective equation with the form of $\partial\phi/\partial t + \mathbf{u} \cdot \phi = 0$ is constructed to calculate the transportation of a particular phase (e.g. fluid phase). In this category, some of the most popular approaches [157, 177] used in mesh-based CFD include MAC [104] (Marker and Cell), VOF [47] (Volume of Fluid), LS [115] (Level Set), CIP [50, 51, 177](Constrained Interpolation Profile) etc.

This type of free surface capturing approaches could be very complicated, especially for large deformation like wave breaking and water splashing. Moreover, the main difficulty for the above mentioned free surface capturing method, i.e. VOF etc., is that the numerical diffusion occurred in the calculation of convective term will corrupt the accuracy, i.e. the sharp free surface may become thicker during simulation [128, 177], especially when the deformation of free surface is very large. Although it is reported that the adoption of a "transformation function" [177], which will enhance the critical value of the marker function corresponding to free surface, will avoid the diffusion to a large extent.

For fluid structure interaction problems, the fluid motion is usually described in an Eulerian frame, where the motion of the mesh (if there it is a dynamic mesh) is not necessary to be the same of the fluid at that position; while a material coordinate system, i.e. Lagrangian description, is assigned to each discrete solid node and follow its motion. For linear problems [168], The effect of the fluid structure interface changing due to the displacement of the solid could be neglected, so that the initial static equilibrium configuration of the fluid-solid interaction system could be maintained for developing the numerical scheme. However, for nonlinear problems that involves large interface deformation, the configuration of the interface has to be constantly updated during the numerical simulation. The difference between Lagrangian and Eulerian descriptions means there has to be a special scheme to handle the changing of interface. For the grid generation of fluid part in this situation, one strategy is creating mesh to conform to the geometric shape of the solid boundaries, and the mesh would then need to be re-generated at each time step. The Arbitrary Lagrange Eulerian approach (ALE) [59, 96, 169], which allows the mesh moving in an arbitrary velocity and the corresponding convective terms in governing equations need to be adapted according to the moving mesh velocity, is the most popular solving strategy for this situation.

However, for this conforming type mesh [130] (body-fitted grid), the topological connectivity between nodes, i.e. elements in FE or control volume in FV etc. may experience severe distortion (e.g. negative volume) during violent boundary changing, which will terminate the simulation. But these highly non-linear scenarios such as large motion of surface ships and the consequent ship-water interface deformation are sometimes inevitable for marine engineering simulation. Additionally, because this kind of mesh is fitted with the boundaries at each time step, it will need to keep re-generating mesh during the simulation. This will increase the CPU burden and also the corresponding numerical errors

when mapping values from old to updated mesh. Even for ALE, where mesh could move independently from material motion, simulation will also deteriorate due to the increased anisotropy or uneven distribution of grid points [95] when large deformation occurs, and consequently severe error or termination of calculation would be observed. Moreover, a high order and smooth local interpolation is not convenient for arbitrary geometry in mesh based methods.

For the fixed Cartesian grid (immersed boundary method [105] and CIP-based approach by Hu et al [50, 51]), the above mentioned free surface capturing methods, i.e. VOF, CIP or LS etc. are also employed, so it also unavoidably suffers from the numerical diffusion problem as in body-fitted type mesh. In addition, local refinement of the grid would be required for some kind of situations such as high Reynolds number flow [105], and this manipulation increases the complexity of the algorithm which to some extent counteract the advantage of the fixed Cartesian grid generation, i.e. simplicity.

Based on the above discussion, for fluid-structure interaction problems involving disintegration of fluids and large deformation of free surfaces (e.g., breaking waves, fragmentation of the fluid, fluid-solid separation), mesh-based methods have limitations.

1.3.2.2 Meshless methods and their advantages

As mentioned above, since the connectivity of mesh between nodes may constrain the large geometrical deformation of the computational field, a natural alternative strategy is to discretize the continuum field with a set of independent particles without the topological constraints (i.e. mesh). The physical values on a particular particle are then represented by some kind of data interpolation or fitting (e.g. kernel or MLS approximation) among the values on adjacent particles. The differential equations (i.e. strong form) or integration equations (i.e. weak form) are then discretized by the function values on discrete particles into a linear algebraic system. After solving this algebraic system, the fluid or solid field could be updated for the next time step under an Eulerian or Lagrangian frame (the hybrid Eulerian and Lagrangian approaches i.e. the ALE in meshless method, has also been introduced [14]). This is the basic idea of a typical meshless method.

Since the SPH method [35, 97], which is regarded as a pioneer method in the category of meshless method, is first developed to deal with astrophysical

problems in open space (certainly, now it is not limited to this field [36]), many variations have been introduced into the computational mechanics.

From computational point of view, the meshless methods can be categorized based on two different criteria [86, 130, 175]: the methods of function approximation, i.e. different interpolating methods; and the form of governing equations, i.e. strong form and weak form.

a) Field approximation method

Currently, the well-known function approximation strategies in meshless methods include Kernel integration (e.g. SPH and MPS) and Reproducing Kernel function method (RKPM); Moving Least Square method (MLS); Radical Basis Function method (RBF), etc.

In the two landmark papers by Monaghan [35] and Lucy [97], one of the currently most popular meshless method—Smoothed Particle Hydrodynamics (SPH) was developed, in which the kernel approximation was introduced. It utilizes the integration of a kernel function over a compact support domain to approximate a particular function. This kind of approximation method has the advantage of a high computational efficiency and easy to implement. But it also suffers inaccuracies, especially when the particles are irregularly distributed. This is maybe because, in the discrete form, the unity condition of kernel sometimes cannot be satisfied for random particle distribution or in the area which is close to and truncated by the boundaries. In order to tackle this kind of problem, the Reproducing Kernel Particle Method (RKPM) [92, 130] has been developed. In RKPM, for every particle, the original kernel is multiplied by a correction function such as a polynomial basis with a series of unknown coefficients. Then, the modified kernel is substituted into the discrete form of moment condition, by which the corresponding unknown coefficients in the correction function can be solved. The same process should be conducted to every particle to get the modified kernel function for each of them.

MPS (Moving Particle Semi-implicit) method [61, 73] adopts the kernel integration method to approximate the field value as well. The main distinguished feature lies on the approximation of gradient and Laplacian operators. In MPS method, the derivative of kernel function will not be used to calculate these operators, instead, the gradient or Laplacian between each particle pair of center particle $\mathbf{r}_i$ and its neighbouring particle $\mathbf{r}_j$ will be first calculated, and then the

gradient or Laplacian of this centre particle $\mathbf{r}_i$ is obtained by the kernel integration of these "local" ingredients [61]. The details will be discussed in Chapter 2.

Moving Least Square (MLS) approximation exists as a traditional data fitting technique for quite a long time [78, 130]. The first meshless method which introduce this MLS method as a function approximation technique is Diffuse Element Method (DEM) [108, 130][35, 49], and followed by Element-Free Galerkin Method (EFGM) [7, 130] which applies MLS with a Galerkin weak form for crack growth simulation. MLS method also conducts the function approximating within a compact support domain Ω. The difference is MLS defines the approximation by the summation of a series of linear independent polynomials [7, 130]. The coefficients of these basis functions are optimized in the weighted least square sense using the discrete function values on the particles within the support domain [130]. The first and second derivatives can be obtained by taking the derivation of the shape functions. The word "moving" in the name of MLS means that this least square fitting is in the local sense.

The Radial Basis Functions (RBF) method, just like MLS, also originates from the scattered data fitting [151]. The basic idea is that different particles interact with each other through a radial basis function which is defined as the function of distance between different particles. There are basically two kinds of RBF, namely "global" and "local" ones. The global RBF is regarded to generate a large, dense, ill-conditioned linear system [151, 164] for large number of particles, and this hinders the application of RBF. Consequently, the "local" RBF is developed, in which the unknown function is approximated based on the particles within a compact support domain. RBF-FD (RBF-based Finite Difference) [158] and RBF-DQ (RBF-based Differential Quadrature) [135] are all under this category. Generally, these MLS and RBF approaches are more time-consuming than the kernel integration i.e. SPH and MPS.

b) Strong form and weak form

The strong form of governing equation means the differential form, in which the equations are established on an arbitrary point of a continuum according to some physical laws. So in the meshless methods, the governing equations are also established and then discretized on each particle. This is origin of the name "collocation" method

The SPH method [35, 97] and its variation MPS method [73], the FPM (Finite Point Method) [111, 112] are all the examples of the application of strong form governing equations. Different function approximation methods can be adopted in solving the strong form equation such as kernel integration (e.g. SPH, MPS), Moving Least Square (e.g. FPM), hp-cloud [89] etc.

The so-called weak form of governing equations can be derived from the Weighted Residual Method [90, 175]. The integration form of governing equation is again could be discretised by different field approximation techniques as aforementioned. A typical example with this situation is the Element-Free Galerkin Method (EFGM) [7, 108]. EFGM, adopts MLS approach to represent the function. This method is mainly applied in structural analysis such as the propagation of a crack.

If the weight functions are not generated from the same basis functions of trial functions, which means they are either from different basis functions or have different support size (definition domain), and the resultant method is Petrov-Galerkin method.

Meshless Local Petrov-Galerkin (MLPG) method [4, 88] is under the category of meshless Petrov-Galerkin methods. In MLPG, the most distinguishing feature, compared with global weak form, is that the weak form equation (the integration) is performed over a set of local sub-domains which could have arbitrary shapes and may overlap each other. Normally, each sub-domain is centred by a particle, so the number of equations is equal to the number of unknown variables (particles), which is more straightforward and clear than EFGM in the construction of the final linear system [4].

A distinguishing example of employing MLPG method in water wave and FSI simulation is the *MLPG_R* (MLPG based on Rankine source solution) method [98, 99, 139, 176]. In *MLPG_R*, the Petrov-Galerkin method is applied to the pressure Poisson equation which is derived from the projection procedure of the original Navier-Stokes equation. The weight (test) function is selected to be a Green's function, and decayed to be zero on the edge of the sub-domain. Considering that the Green's function satisfies the Laplace equation except the domain centre $\mathbf{r}_I$, and after some mathematical operation, the local weak form can be deduced into a form where no differential operator exists. The most distinguished feature of the formula is that the Laplacian operation of pressure and the divergence operation of the velocity in the original Poisson equation are reduced into the pressure and velocity themselves respectively.

Finally, it is worth mentioning that the meshless method is only a different spatial discretization strategy compared with conventional mesh-based method. It does not imply that the fluid will be solved under Lagrangian or Eulerian frames. That is to say, when updating the field status from the current time step to next one, these discrete "points" could either be treated as material particles (i.e. possess mass, density etc.) which will move to next position according to its velocity or just interpolation points as the nodes in mesh-based method which is fixed [151] or moving [14] in an ALE scheme. Generally, the Lagrangian meshless method is referred as "particle" method and meshless or mesh-free method could also be regarded as Eulerian meshless method in a narrowed sense.

The main advantages of meshless methods in Lagrangian or Eulerian frames (in comparison with the traditional mesh-based methods) could be summarized as follows [91, 130]:

i) It is easier and more straightforward to deal with large deformation, since there is no topological connectivity between discrete particles. For the Lagrangian meshless methods, the tracing largely deformable boundaries such as free surface are more effective.

ii) Adding and eliminating particles during calculation will not affect the adjacent particles because there is no restraint between particles. This means that flexible adaptive refinement is easier.

iii) As different interpolation strategies could be used among particles, to include a priori knowledge about the local behaviour is possible as well as a high order interpolation could also be considered.

iv) For the Lagrangian meshless method, i.e. particle method (e.g. SPH, MPS), it is easy to simulate the waver breaking and fragmentation without sophisticated free surface tracking schemes in mesh-based methods.

v) The convection term of the Navier-Stokes equations vanishes in the Lagrangian frame, so the particle method will not suffer the diffusion problem. In addition, fundamental conservation laws, such as conservation of mass, are satisfied accurately.

It should be mentioned that there are also some intrinsic drawbacks of many meshless or particle methods such as the difficulty of imposing boundary conditions, the instability issue when using fully Lagrangian frame, computational

burden for large scale particle numbers. However, the recent research including this study have proposed many techniques to tackle these issues.

1.3.2.3 The Lagrangian Meshless method–Particle method

The Particle method is a combination of meshless spatial domain discretization and Lagrangian type description of advancing the computational points in time domain. The typical features of the violent free surface flow around floating bodies (i.e., large deformation of the free surface and the large displacement of floating body) imply that the Lagrangian frame is more convenient and straightforward for the description of wave breaking, fragmentation, re-entry etc. Moreover, meshless spatial discretization will overcome the distortion of mesh due to large boundary motions and make the free surface tracking easier. Additionally, the Lagrangian approach also avoids the calculation of convection term which will appear in the Eulerian form of the Navier-Stokes equations. As a consequent, the N-S equations could be solved more directly without numerical diffusion, instability or topological problems [157].

SPH and MPS are all widely used particle methods. As one of the oldest meshless method, SPH was first introduced to compute the astrophysical problems. Later, researchers found out that it is also suitable for the simulation of continuum mechanical problems, i.e. solid and fluid dynamics. In 1994, Monaghan [106] applied SPH to free surface flow simulation. In this paper and many subsequent ones [18, 19, 25, 33], the fluid is considered to be "weakly" compressible. That means pressure is calculated through the Equation of State (EOS), in which the pressure evolution is related with density variation. The kind of SPH which employs this explicit pressure-velocity decoupling approach is referred as Weakly Compressible SPH (WCSPH). The EOS in this WCSPH requires calibration of sound speed for different cases. And this limitation also restricts the use of large time step. Another way to impose the incompressibility condition is introduced by Koshizuka [73] in the so called Moving Particle Semi-implicit (MPS) method. In MPS the two-step projection approach is adopted, in which the pressure is calculated by a Pressure Poisson Equation (PPE) in the corrector (second) step of the algorithm. This technique makes it possible to choose a larger time step (certainly still controlled by stability condition such as CFL condition). The PPE was also adopted to integrate with SPH methodology by Rudman [23] and Shao [128]. This new version of SPH is called Incompressible SPH (ISPH). MPS and ISPH were all successfully used to calculate many violent

free surface problems such as Dam-break [61, 128], Sloshing [82], Green water [134] and Slamming [2, 127] etc. Additionally, MPS adopts a simpler differential operator (gradient and Laplacian) based on the weighted function averaging process which avoids the gradient and Laplacian operation of kernel function in SPH.

In this research, MPS method is employed as a basis to further improve the violent free surface calculations, especially for suppressing the pressure fluctuation and numerical instability (which are the major shortcomings in MPS method). A more detailed review of state-of-the-art MPS is given in the Chapter 2.

1.3.2.4 Brief review of particle methods for FSI problems

Most of the current applications of particle methods in marine engineering lie in the local violent flow such as Green water, slamming or sloshing etc.

One of the most popular application of particle methods is the simulation of sloshing phenomena. A comprehensive review could be found in [156]. Some typical examples include: Delorm et al. [29] who used SPH method to investigate 2D shallow water sloshing and compared the numerical solution with experimental results; Lee et al. [83] adopted MPS method to calculate violent free surface and floating body motion as well as impact pressure.

For Green water and slamming phenomena, there are also some studies based on particle methods. For example, Shibata et al. [133] applied the MPS method to investigate the pressure on the deck when ships are towed in head waves; Le Touze et al. [81] applied the SPH method to predict the flow phenomena of two flooding scenarios; Veen and Gourlay [161] also used the SPH method to simulate slamming with the emphasis of $2D$ wedge forms on a hydrostatic tank with free surface.

The application of particle methods to full-ship interacting with waves is very limited. However, there are also some work such as that in Patel et al. [120], who used a coupled SPH and FE method to calculate the ship-wave interaction including green water.

For the FSI calculations, the particle methods are normally coupled with FE method (for the structural part), but fully particle approach (where the particle method is used for both fluid and structure dynamics calculation) exists as well. In this kind of problem, the data transfer across the interface is the essential

issue. Some typical approaches are reviewed here. Though they may not be originally introduced for marine engineering, it is obvious that they are applicable to this field.

SPH-FE [34]:A straightforward idea is to calculate the average pressure near the solid boundary and exert this force to the FE nodes to update the positions and velocities of structure. Consequently, the fluid domain can be updated by the new structure position. It should be mentioned that the traditional ghost particles boundary condition is also employed to prevent penetration of the fluid particle into the structure domain.

SPH-FE [27]:A more sophisticated method introducing a potential between fluid particles and FE nodes near the interface. The potential is defined based on the kernel function with some control parameters, and also has a compact influence domain. The interaction between fluid and solid is realised by adding a source term, i.e. the interacting force, into the governing equations of both fluid and solid domain in the area adjacent to the interface. The force is obtained by calculating the gradient of the potential. The FE nodes are regarded as particles when calculating the potential gradient.

MPS-FE [85]: In MPS method, the fluid pressure is calculated by a Poisson equation, and the non-penetration boundary condition (or non-slip condition for viscous flow) is guaranteed by involving the innermost layer of solid particles in the pressure calculation, by which to give a repulsive force to the fluid particles. There are also several layers of "dummy" particles covering the first layer solid particles to help the "particle density" calculation of the first layer solid particles. So considering that the pressure is automatically calculated on the first layer solid particles, this pressure can directly applied to the structure response calculation.

SPH-SPH [154]: One simple way for viscous fluid is to conduct the kernel summation regardless of the particle nature (i.e. fluid or solid particle) and this can automatically satisfy the velocity and normal stress continuity conditions. However, for inviscid fluid, this kind of approach can not satisfy the non-slip condition on the interface. Another technique is employed to realise the non-penetration and normal stress continuity conditions. The location of interface is captured based on the edge of solid domain i.e. the solid particles closest to fluid. For the momentum equation, the kernel summation of a boundary particle (fluid or solid) is only conducted within its own physical domain, and the force exerted by other domain is added explicitly. The force is first calculated

from the pressure gradient of fluid field adjacent to the solid domain, and then the action-reaction principle is applied to get the force exerted by solid to fluid (i.e. same magnitude but opposite direction). The calculation of this force is conducted by taking the surface integration into account when deriving the pressure gradient operator in SPH

SPH-SPH [103]: Covering the boundaries of contacting bodies with small spheres, which are called "Pinballs" and conducting the interactions, and generating penalty forces when these pinballs belong to different bodies contact with each other is the basic idea of "pinball" method. Different methods can be employed in the penalty forces generating [8, 103].

1.3.3 Hybrid fluid solvers

Both of the Navier-Stokes and the potential flow models have their strength and weakness [138]. As mentioned above, the potential flow model can not handle the case where wave-breaking is involved. But it is usually more efficient and stable for large scale and long time simulation. The Navier-Stokes model (or often referred as CFD approaches) on the other hand is a general and robust solver that can simulate the violent and complicated free surface deformation cases. The disadvantage of the CFD approaches includes the heavy computational cost and energy loss for long time simulation.

It is a logical choice to combine these two solvers for the problems in which the violent wave-breaking only occurs in small constrained area and the flow motion in majority of the fluid domain is relatively gentle. In a hybrid model, the whole computational domain is divided into sub-domains where different solvers are applied appropriately. Based on the way of information exchanging between these two solvers, the hybrid model could be classified as strong and weak couplings. A detailed review of the hybrid solver can be found in [38, 138]. A brief outline of the representative works about both the strong and weak couplings is given below.

In the strong coupling, the two solvers are mutually dependent on each other, i.e. the boundary values of each solver have to be calculated based on information from the other one. Both the mesh-based and meshless CFD methods have been incorporated with potential solvers for free surface flow problems. Colicchio et al [20] combined a fixed-grid FD (Finite Difference) method (using VOF to capture the free surface) with BEM method to calculate various free surface

flow problems. There is an overlap area between two sub-domains where the information is exchanged and consequently provide the necessary boundary condition to drive each solver. Grilli [38] implemented the coupling in a different way in which the Navier-Stokes domain is fully submerged inside the potential flow domain and the later solver covers the whole computational domain. The dynamic pressure is included as a source term in the Navier-Stokes equation. For the coupling with meshless method, Sueyoshi et al. [141] used the MPS method to model the upper domain which includes free surface and BEM to simulate the area which is close to the bottom of tank. The information is exchanged on the interface where MPS particle moves in Lagrangian way and BEM boundary is fixed in space. Sriram et al. [138] combined the FE based potential flow model with another particle method *MLPG_R*. The communication between the two solvers are conducted via a moving overlapping area. The velocity of the *MLPG_R* particle in this area is determined by linearly interpolating velocity from both solvers. The strong coupling strategy normally tends to be more accurate since some kind of convergence criteria is required during the exchanging of information. But for the same reason, several iterations will also have to be conducted, and consequently make the simulation more computationally expensive.

The weak coupling strategy means one of the solvers covers the whole computational domain and provide the boundary condition for the other one during the whole simulation process without the need of any feedback from it. Normally it is the potential flow model, which acts as the "base" solver to initialize and drive the Navier-Stokes solver in the sub-domain where the violent free surface deformation occurs. The notable examples that involve the mesh-based CFD methods include the weak coupling between FVM (Finite Volume Method) and BEM for breaking of solitary wave on slop [77]. The weak coupling between meshless method Lattice Boltzmann method and BEM were conducted for solving the same problem as well [55]. The particle method SPH has also been used to calculate the post-breaking waves incorporated with Boussinesq method [60].

Finally, a summary of the methods used for free surface flow simulation is given in Table 1.1.

Table 1.1: Summary of the methods for free surface flow simulation

	Mesh-based	Meshless
Potential flow	Efficient for linear problem, but can not handle violent free surface deformation such as wave breaking	\
Navier-Stokes	• Capable of simulating various flow situations, typically FV, FD or FE with VOF or LS for free surface capturing. • Lagrangian or ALE type meshes are capable to handle small or medium boundary deformation, but will suffer from mesh distortion or frequent remeshing for large deformation problems. • Eulerian mesh (fixed in space) also need complex free surface capturing algorithm with numerical diffusion problem.	• Meshless methods (Eulerian or Lagrangian) are easier to handle large deformation without mesh distortion problems. • Particle methods (Lagrangian type meshless methods) e.g. MPS, SPH, are very suitable for violent free surface deformation problems. Drawbacks are high computational cost, stability issue etc.
Hybrid	Suitable for improving the efficiency of problems where violent free surface deformation only occurs locally.	Similar to the mesh-based cases, however not much research has been done yet.

1.4 Computation of flexible structure dynamics

For FSI problems with flexible structures, Finite Element (FE) method has been extensively used to calculate the structure dynamics, in combination with MPS [85, 144] method or other traditional mesh-based methods [87, 167] for the calculation of fluid motions. For the cases where large structure displacement is involved, the non-linearity of the structure dynamics comes from two sources: the geometric large deformation and non-linear stress-strain relationship. The geometric effect could be handled by the so-called Total Lagrangian or Updated Lagrangian FE formulation [6]. And the use of non-linear constitutive relation could take the special material property into account [6]. As an example, the co-rotational FE method [49], which follows the idea of Updated Lagrangian

formulation, is used to solve the beam dynamics under large overall motion but small deformation.

For a typical ship structure, the overall motion could be described as a large rigid-body motion (such as a combination of large forward motion, pitch, heave motions) plus a relatively small flexible bending deformation. This feature makes the modal superposition theorem adequate and quite suitable for representing this flexible deformation part. Moreover, it is also more efficient than its FE counterpart in terms of computational cost. In practice, considering the geometrically slimness of a ship structure, the beam model is normally adopted to describe its dynamics response to external excitations. Even for a non-beam like structure, for example a floating oil drilling platform, as long as the flexible motion part is relatively small, the modal superposition theorem is also applicable. What is worth mentioning here is that the mode function for a general shape structure is normally obtained from FE method rather than from analytical solution of beam theory, however this only requires one time prior-calculation instead of solving FE model at each time step during the FSI computation.

Actually, this modal superposition technique has been successfully used to calculate interaction problems between water and large floating flexible structures [57, 58, 109]. In these simulations, the fluid domain is computed by potential flow with linearized boundary conditions, and as such it could not handle the highly deformable free surface situations. For the structure part, either no rigid-body modes [57] or only some of them such as heave and pitch [58, 109] are included in the computation, since the rigid-body motion part is very small and the elastic deformation is the main concern for these particular problems. In [143], the rigid-body motion and modal superposition are also coupled in the problem of elastic cylindrical shell entering water. This coupling is only in terms of force computation, which means that the force for rigid-body motion takes into account the effect of flexible deformation. However, it is not a "genuinely" coupling because the rigid-body force (i.e. total force and torque applied on the structure) will also affect the flexible kinetic parameters (i.e. generalized coordinates of each mode), as shown in Section 3.2.

Similarly, in ship Hydroelasticity [11, 15, 155], this idea has also been extensively applied to compute the structure dynamics in regular and irregular waves (irregular wave calculation is also based on the regular case using spectral method). However, this computation is usually based on the small wave

amplitude assumption (linear wave), and consequently the fluid domain is calculated using potential flow theory, subject to the boundary conditions at the mean free surface and structure positions [155]. This means that both the rigid-body and flexible motion parts can only be relatively small in this method. Moreover, in the governing equations [155], there are no terms representing the mutual effect between rigid-body motion and flexible deformation, although the rigid and flexible variables are solved simultaneously. This way of handling FSI computations may be accurate enough for small motions, but in the case of violent water structure interaction, in which the rigid-body motion part is very large, the effect from structure flexibility to rigid-body motion should be considered and vice versa (which can be seen from the new structure governing equations in Section 3.2).

1.5 Research Objective

The aim of the research is to develop an efficient computational model that is capable to simulating highly nonlinear fluid structure interaction problems with violent free surface deformation (including breaking waves, fluid fragmentation and separation).

For the fluid part, the MPS method was investigated to improve the pressure stability and accuracy. For the structure part, the model that couples the rigid-body and flexible modes, which includes their coupling effects, was developed.

1.6 Thesis structure

The structure of this thesis is organized as follows:

Following this introduction where the general background of this study is illustrated, the methodology of the original MPS method, the proposed modifications and also the weak coupling between BEM (Boundary Element Method) and MPS are presented in Chapter 2. In Chapter 3, brief review of the flexibility computation and the detailed derivation of the coupled rigid-body and modal superposition model is illustrated. Also, the details of the Gauss-Seidel coupling procedure of the Fluid Structure Interaction computation is given in the end of this Chapter.

In Chapter 4 to 6, numerical results using the developed models are analyzed and compared with the available experimental and numerical results in the literature. Specifically in Chapter 4, the performance of the proposed modifications to MPS is validated by the well-known Dam-break problem. In Chapter 5, a variety of different impact problems, which includes Dam-break with various boundary conditions, sloshing, slamming are simulated to further show the capability of the proposed models. Then, the weak coupling between MPS and BEM is investigated and used to simulate the breaking wave impacting on flexible wall. The hydroelasticity simulation results including flexible wedge dropping and 2D/3D floating structure slamming are presented in Chapter 6.

Finally, conclusion as well as suggestions for future works are given in Chapter 7.

1.7 Major findings

The major findings of this study could be summarized as follows:

1) The modification of the original MPS method

Despite its wide range of applicability, the original MPS algorithm suffers from some inherent difficulties in obtaining an accurate fluid pressure in both spatial and time domain. Different modifications to improve the method have been proposed in the literature [63, 66, 82, 159]. In this study, the following modifications are proposed to improve the accuracy of pressure calculations and the stability of the method:

i) A mixed source term in the pressure Poisson equation with no artificial term in the formulation.

The combination of velocity divergence and a particle density error compensation is proposed to control the uneven particle distribution and consequently improve the pressure calculation and stability.

ii) New solid and free surface boundary handling methods.

The Neumann type boundary condition is applied for the solid boundary particles instead of applying the pressure Poisson equation directly on them. The accuracy of the intermediate velocity of the solid boundary particle is also improved by considering the pressure. For free surface boundary, different

schemes for $2D$ and $3D$ cases respectively are proposed to identify the free surface particles more accurately.

iii) Particle position shifting and collision handling.

A simple particle shifting scheme is proposed to improve the regularity of the particle distribution. And to avoid the collision of particles such as between free surface particles, a scheme to manipulate the relative velocity is adopted.

iv) A new version of "cell-link" neighbour particle searching strategy.

By using a smaller cell size and avoiding repetitively checking of a pair of particle, the searching area can be reduced by about 6.5/9 (72%) compared with traditional "cell-linked" algorithm.

v) Weakly coupling between MPS and BEM

As an attempt to improve the computational efficiency, the weakly coupling between MPS and the potential solver BEM is investigated and applied to the problem of breaking solitary wave impacting on a flexible structure. The result shows that for this kind of problems where the rapid fluid motion occurs in a constrained area, the coupling with the efficient BEM method in the far field is an effective way of reducing the computational effort.

2) Coupled rigid-body motion and modal superposition model

A structural dynamic computation model, which is designed for the structure that undergoes very large rigid motions and relatively small elastic deformation, is derived in this study. Unlike the traditional modal superposition analysis, this model considers the mutual effect between rigid-body motion and flexible deformation. And the coupled overall rigid-flexible motion is calculated simultaneously by a set of small scale equation system. This model is more efficient compared with FEM, regardless of the size of the structure. For 2D cases, if the first three modes are chosen to represent the flexible deformation of the structure, it only results in a 6×6 matrix equation to be solved.

Chapter 2

MPS and modifications

2.1 Original MPS methodology

In this section, the original MPS method [73] is briefly described, including the governing equations, particle interaction model and time stepping procedure to enforce the incompressibility.

The problems investigated here are all marine related short duration impact problems with high Reynolds numbers and rapid changing physical processes, which means that the viscosity effect is quite small. As such, the Lagrangian form of incompressible and inviscid Navier-Stokes equations (which is Euler equations) are employed here as the governing equations of the flow.

$$\begin{aligned} &\frac{D\mathbf{u}}{Dt} = \frac{\mathbf{u}^{(k+1)} - \mathbf{u}^{(k)}}{\Delta t} = \mathbf{g} - \frac{\nabla p}{\rho_0} \\ &\nabla \cdot \mathbf{u} = 0 \end{aligned} \tag{2.1}$$

where $\mathbf{u}$, p and ρ_0 are the fluid velocity, pressure and density, respectively. The superscripts k and $k+1$ refer to the k^{th} and $(k+1)^{th}$ time steps, respectively. This superscript notation will also be used in the subsequent sections. $\mathbf{g}$ is the vector pointing to the gravity direction, i.e. $\mathbf{g} = [0, -g]$, where g is the value of gravity acceleration. In Eq. (2.1), the time derivative $\frac{D\mathbf{u}}{Dt}$ is discretized by a first order Lagrangian finite difference.

In order to verify the fact that the viscous effect is negligible for the high Reynolds number problems investigated in this study, the viscous incompressible Navier-Stokes equations Eq. (2.2) are also used to simulate a $2D$ dam-break

problem in Chapter 4, and the results compared to those from Euler equations. The numerical implementation process below is based on Eq. (2.1), though the same process could be applied to Eq. (2.2).

$$\begin{aligned} &\frac{D\mathbf{u}}{Dt} = \frac{\mathbf{u}^{(k+1)} - \mathbf{u}^{(k)}}{\Delta t} = \mathbf{g} - \frac{\nabla p}{\rho_0} + \nu \nabla^2 \mathbf{u} \\ &\nabla \cdot \mathbf{u} = 0 \end{aligned} \tag{2.2}$$

The parameter ν in Eq. (2.2) is the kinematic viscosity coefficient. The value corresponding to water in the room temperature is used in this study, i.e. $1.0037 \times 10^{-6} Pa \cdot s$.

The numerical implementation of the original MPS method is first described in the following sections. Next, its drawbacks/shortcomings are discussed. Then, the sate-of-the-art of MPS method is briefly reviewed. Finally, several modifications are proposed to improve the performance of the MPS method.

2.1.1 Enforcing incompressibility—Projection method

As a typical approach for the incompressible fluid computation, the two-step projection method, which is introduced by Chorin [16], is adopted here to decouple the velocity and pressure calculation:

The first step is to calculate the intermediate velocity without considering pressure, and then move the particles to the intermediate location according to this velocity:

$$\begin{aligned} \mathbf{u}^{(*)} &= \mathbf{u}^{(k)} + \Delta t \mathbf{g} \\ \mathbf{r}^{(*)} &= \mathbf{r}^{(k)} + \Delta t \mathbf{u}^{(*)} \end{aligned} \tag{2.3}$$

where $\mathbf{r}$ represents the location vector of particles. The superscript $*$ indicates the value of intermediate status of a particular time step. A pressure Poisson equation is then derived as follows to solve the pressure field:

$$\nabla^2 p^{(k+1)} = \rho_0 \frac{n_0 - n^{(*)}}{n_0 \Delta t^2} \tag{2.4}$$

Here, the term n_0 and $n^{(*)}$ are called "particle density", with n_0 the desired value corresponding to uniform particle distribution, and $n^{(*)}$ the actual value

at the intermediate status. They are proportional to the physical density and the definition is provided in Section 2.1.2

After obtaining the pressure, the velocity and location are then updated as:

$$\begin{aligned} \mathbf{u}^{(k+1)} &= \mathbf{u}^{(*)} - \Delta t \frac{\nabla p^{(k+1)}}{\rho_0} \\ \mathbf{r}^{(k+1)} &= \mathbf{r}^{(k)} + \Delta t \mathbf{u}^{(k+1)} \end{aligned} \tag{2.5}$$

2.1.2 Particle interaction model

The function approximation method in MPS is weighted average approach. Normally, the weight function (or "kernel" as quite often referred in literature) is chosen as the following form (although other forms have also been successfully applied):

$$w(r_{ij}) = \begin{cases} \frac{r_e}{r_{ij}} - 1, & 0 < r_{ij} \leq r_e \\ 0, & r_{ij} > r_e \end{cases} \tag{2.6}$$

where $r_{ij} = |\mathbf{r}_i - \mathbf{r}_j|$ is the distance betwen particle i and j, and r_e is radius of the local support domain. The distinguished feature of this function [61] is that the value is infinity at $r_{ij} = 0$, and this is regarded to be helpful to avoid the particle clustering. It is also infinitely differentiable except at $r_{ij} = 0$. It is easy to check that this kernel does not satisfy the “unity” property (i.e. the integration of the kernel over the support domain is not one), which is one of the basic properties of kernel interpolation in SPH methodology. Hence, it is more reasonable to call it “weight function” [136] instead of kernel.

The interpolation of a field function $u_f(\mathbf{r}_i)$ is as follow:

$$u_f(\mathbf{r}_i) = \sum_{j \neq i}^{N} \frac{u_f(\mathbf{r}_j) w(r_{ij})}{n_i} \tag{2.7}$$

where N is the particles number in the support domain. The length of the support domain r_e is usually different for Laplacian and gradient operators. As suggested by [73], they are chosen to be 4 and 2.1 times of the initial particle distance r_0, respectively. The notation of n_i is defined as:

$$n_i = \sum_{j \neq i}^{N} w(r_{ij}) \tag{2.8}$$

It is also called a "particle density" in MPS, and it is related to the physical density. More specifically, if n_i is divided by the integration of weight function over the support domain (except the small centre part occupied by particle i), the particle number in a unit volume—N_{u_i} will be obtained:

$$N_{u_i} = \frac{n_i}{\int_{\Omega_i} w(r) d\Omega} \tag{2.9}$$

The denominator of the above equation could be regarded as n_i multiplied with the volume that occupied by a single particle . As a consequence, the right hand side of Eq. (2.9) is actually the reciprocal of this "particle volume", which the particle number in a unit volume. Furthermore, assuming the mass of each particle is m, then the physical density could be represented as:

$$\rho_i = m N_{u_i} = \frac{m n_i}{\int_{\Omega_i} w(r) d\Omega} \tag{2.10}$$

The continuity condition in Eq. (2.1) will be satisfied if the particle number is constant everywhere in the domain. The notation of n_0 is used to represent this constant, and defined as the value calculated by Eq. (2.8) based on the initial regular particle distribution.

In MPS method, the derivative of weight function will not be used to calculate these operators like in SPH. Instead, the first and second order spatial derivatives between particle pair of centre particle $\mathbf{r}_i$ and its neighbouring particle $\mathbf{r}_j$ will be first calculated, and then the gradient or Laplacian of this centre particle $\mathbf{r}_i$ is obtained by the weighted averaging process [61]. The element of gradient of a scalar variable u_f between particle $\mathbf{r}_j$ and centre $\mathbf{r}_i$ is:

$$\frac{u_f(\mathbf{r}_j) - u_f(\mathbf{r}_i)}{r_{ij}^2}(\mathbf{r}_j - \mathbf{r}_i) \tag{2.11}$$

The gradient at $\mathbf{r}_i$ is represented by the weighted averaging of these "local elements", i.e. by employing Eq. (2.7) and replacing n_i with n_0:

$$\nabla u_f(\mathbf{r}_i) = \frac{d}{n_0} \sum_{j \neq i}^{N} \frac{u_f(\mathbf{r}_j) - u_f(\mathbf{r}_i)}{r_{ij}^2}(\mathbf{r}_j - \mathbf{r}_i) w(r_{ij}) \tag{2.12}$$

where d is the number of space dimension. Similarly, the divergence of a vector is:

$$\nabla \cdot \mathbf{u}_f(\mathbf{r}_i) = \frac{d}{n_0} \sum_{j \neq i}^{N} \frac{(\mathbf{u}_f(\mathbf{r}_j) - \mathbf{u}_f(\mathbf{r}_i)) \cdot (\mathbf{r}_j - \mathbf{r}_i)}{r_{ij}^2} w(r_{ij}) \tag{2.13}$$

where $\mathbf{u}_f$ represents a vector. According to the suggestion in [73], if the particle distribution is or could roughly be regarded as symmetric, then $\sum_{(j \neq i)}^{N} \frac{\mathbf{r}_j - \mathbf{r}_i}{\mathbf{r}_{ij}^2} w(r_{ij})$ very close to zero, which means $u_f(\mathbf{r}_i)$ in Eq. (2.12) or (2.13) would not affect the final result. As a consequence, in the pressure gradient calculation, if the value $u_f(\mathbf{r}_i)$ is replaced by the minimum value among all the particles within the current support domain, the gradient computation will be the same order of accuracy. That means the pressure gradient is calculated as:

$$\nabla p(\mathbf{r}_i) = \frac{d}{n_0} \sum_{j \neq i}^{N} \frac{p(\mathbf{r}_j) - \tilde{p}(\mathbf{r}_i)}{r_{ij}^2} (\mathbf{r}_j - \mathbf{r}_i) w(r_{ij}) \tag{2.14}$$

where $\tilde{p}(\mathbf{r}_i)$ is the minimum pressure among all the particles within the current support domain. This change could make sure that the interaction force (i.e. the opposite pressure gradient term in Eq. (2.1)) experienced by centre particle $\mathbf{r}_i$ from neighboring particle $\mathbf{r}_j$, is always repulsive, which is helpful to maintain the regularity of particle distribution.

For the discretization of Laplacian, the following time-dependent diffusion problem of u_f is used for derivation [73, 149, 160]:

$$\frac{\partial u_f}{\partial t} = \nu_d \nabla^2 u_f \tag{2.15}$$

where ν_d is the diffusion coefficient. The quantity of u_f will be redistributed constantly by Eq. (2.15). The basic concept used in the following derivation is that the variance (i.e. σ_d^2) increase of this redistribution during time interval Δt should be equivalent to the analytical result, which is

$$\sigma_d^2 = 2d\nu_d \Delta t \tag{2.16}$$

Considering this requirement, in MPS model the quantity transferred from particle i to j during Δt is assumed to be [73]:

$$\Delta_{i \to j} u_f = \frac{2d\nu_d \Delta t}{n_0 \lambda} u_f(\mathbf{r_i}) w(r_{ij}) \tag{2.17}$$

where λ is a parameter that will be determined by the aforementioned variance

equivalence principle later. As a consequence, the discretized time derivative at position $\mathbf{r}_i$ in Eq. (2.15) could be represented as:

$$\frac{u_f(\mathbf{r}_i)^{(k+1)} - u_f(\mathbf{r}_i)^{(k)}}{\Delta t} = \frac{2d\nu_d\Delta t}{n_0\lambda}\sum_{j\neq i}^{N}(u_f(\mathbf{r}_j)^{(k)} - u_f(\mathbf{r}_i)^{(k)})w(r_{ij}) \tag{2.18}$$

If we compare Eq. (2.18) with Eq. (2.15), the discretization of Laplacian operator is:

$$\nabla^2 u_f(\mathbf{r}_i) = \frac{2d}{n_0\lambda}\sum_{j\neq i}^{N}[u_f(\mathbf{r}_j) - u_f(\mathbf{r}_i)]w(r_{ij}) \tag{2.19}$$

The final step is to determine the parameter λ. As mentioned above, it is calculated based on the variance increase equivalence principle. In order to simplify the variance calculation at $t = (k+1)\Delta t$, the initial value at $t = k\Delta t$ is chosen to be:

$$u_f(\mathbf{r}_j)^{(k)} = \begin{cases} 0, & j \neq i \\ 1, & j = i \end{cases} \tag{2.20}$$

The value of u_f of all the neighboring particles at $t = (k+1)\Delta t$ could be obtained as:

$$\begin{aligned} u_f(\mathbf{r}_j)^{(k+1)} &= u_f(\mathbf{r}_j)^{(k)} + \frac{2d\nu_d\Delta t}{n_0\lambda}\sum_{m\neq j}^{N}(u_f(\mathbf{r}_m)^{(k)} - u_f(\mathbf{r}_j)^{(k)})w(r_{ij}) \\ &= \begin{cases} \frac{2d\nu_d\Delta t}{n_0\lambda}w(r_{ij}), & j \neq i \\ 1 - \frac{2d\nu_d\Delta t}{n_0\lambda}\sum_{m\neq i}^{N}(u_f(\mathbf{r}_m)^{(k)} - u_f(\mathbf{r}_i)^{(k)})w(r_{ij}), & j = i \end{cases} \end{aligned} \tag{2.21}$$

The variance increase after the time interval of Δt is calculated as:

$$\sigma_d^2 = \sum_{m\neq i}^{N} u_f(\mathbf{r}_m)^{(k+1)} r_{mj}^2 = \frac{2d\nu_d\Delta t}{n_0\lambda}\sum_{m\neq i}^{N} w(r_{mi})r_{mi}^2 \tag{2.22}$$

By comparing Eq. (2.16) and (2.22), the parameter λ is obtained as:

$$\lambda = \frac{1}{n_0}\sum_{j\neq i}^{N} w(r_{ij})r_{ij}^2 \tag{2.23}$$

2.1.3 Boundary conditions

a) Free surface boundary

In the pressure Poisson Equation, for the linear system to have a unique solution, the pressure value of free surface particles should be imposed to be zero ($p = p_0 = 0$) explicitly as boundary condition. Thus, the particles which are located at free surface at each time step must be recognized. It is worth mentioning that, unlike in mesh-based methods in which the positions of free surface should be "calculated", in MPS, we need just to "find" which particles lie exactly on the free surface.

As within the neighbor domain of a free surface particle, there would be no fluid particles in the area which is outside the fluid domain, particle density $n^{(*)}$ of these free surface particles will drop dramatically. This difference of the particle density value between free surface and inner fluid particles makes the identification of the free surface particle possible. As a consequent, the particles which satisfy the following condition are identified as free surface particle:

$$n^{(*)} < \beta n_0 \tag{2.24}$$

where β is a parameter slightly smaller than 1 (e.g. 0.97).

b) Solid boundary

The solid particles which lie in the support domain of the adjacent fluid particles are also included in the pressure Poisson equation calculation. As a consequence, its pressure will push away the fluid particles which are too close to the solid, and thus avoiding the penetrating of fluid particles into solid boundary. To compensate the deficiency of neighbour particles for the solid and "near-solid" fluid particles when calculating $n^{(*)}$, two additional layers of dummy particles are placed just outside the inner solid particle layer. These particles are only involved in the particle density calculation in standard MPS method. The Laplacian and gradient discretization do not take these dummy particles into account.

2.1.4 Shortcomings of the original MPS method

1) Non-physical pressure fluctuation in both temporal and spatial domain

This pressure fluctuation is the biggest problem which hinders its application to practical engineering purpose. Figure 4.5(a) (2D dam-break problem) illustrates a typical pressure history monitor at a point which is being impacted. Although

its main trend coincides with the experimental result, this large amplitude fluctuation implies that it cannot calculate the Fluid Structure Interaction properly.

2) False identification of free surface particle

In the original MPS method, there are many falsely identified particles inside the main fluid body. And considering that the pressures of free surface particles are enforced to be zero, this inaccurate free surface identification will produce wrong pressure distribution result.

3) Improper proximity of free surface particles

Because there is no pressure gradient that exists between the free surface particles, when they get close enough, they will be identified as inner fluid particles as a result of the increase of particle density (see Eq. (2.24)). However, this improper proximity of two fluid particles will cause singularity problem when solving the pressure Poisson Equation. As a consequence, they will be pushed away from each other by the extremely high singular pressure between them. This issue will affect the stability of the computation or even terminate the simulation under some circumstances.

2.2 State-of-the-art of MPS method

MPS method has been successfully applied to simulate various engineering problems such as incompressible free surface flow [37, 63, 73], nuclear reactor safety [74] and even blood flow simulation. Here, a brief review of the developments is given below:

1) Linear momentum conservation

In the original MPS, the pressure gradient forces between a pair of particles do not satisfy the Newton's third law (i.e. the action must be equal to reaction) which means the momentum will not be exactly conserved during the simulation. So, there are some modifications [63, 82, 152] to revise the gradient operation to meet the linear momentum conservation. One typical example [63] is:

$$\nabla p(\mathbf{r}_i) = \frac{d}{n_0} \sum_{j \neq i}^{N} \frac{p(\mathbf{r}_j) + p(\mathbf{r}_i) - (\tilde{p}(\mathbf{r}_i) + \tilde{p}(\mathbf{r}_j))}{r_{ij}^2} (\mathbf{r}_j - \mathbf{r}_i) w(r_{ij}) \tag{2.25}$$

where $\tilde{p}(\mathbf{r}_i)$ and $\tilde{p}(\mathbf{r}_j)$ has the same meaning as in original model, i.e. the minimum pressure among all the particles within the support domain for particle i and j respectively. However, as mentioned in [114], the numerical error arising from the non-exact conservation momentum might be less important than that caused by an imprecise pressure gradient formulation.

2) Poisson equation

Considering that the pressure fluctuation is quite large in MPS, intensive researches have been conducted to modify the pressure Poisson equation. It includes two types: modification to the source term (i.e. R.H.S.); and introducing high order Laplacian operator.

i. Source term modification

This category includes different strategies. First is to replace the $\frac{n_0-n^{(*)}}{n_0}$ with other forms. One typical example is using material derivative as source term on R.H.S. [61, 63]. And if the weight function is selected as Eq. (2.6), the source term for 2D case will be given by:

$$\frac{Dn^{(*)}}{Dt} = \sum_{j\neq i}^{N} \frac{Dw(r_{ij})}{Dt} = -\sum_{j\neq i}^{N} \frac{r_e}{r_{ij}^3}(x_{ij}u_{ij}^{(*)} + y_{ij}v_{ij}^{(*)}) \tag{2.26}$$

Another approach is to add a compressible term into the source term [63], and the Poisson equation will be changed to the following form:

$$\nabla^2 p^{(k+1)}(\mathbf{r}_i) = \frac{1}{\Delta t^2 C^2}(p^{(k+1)}(\mathbf{r}_i) - p^{(k)}(\mathbf{r}_i)) + \frac{\rho_0}{\Delta t}\nabla \cdot \mathbf{u}^{(*)}(\mathbf{r}_i) \tag{2.27}$$

where C is the speed of sound. This compressible term has a stabilizing effect on the calculation of pressure.

Moreover, a combination of divergence of the intermediate velocity field and particle density variation [82, 152] is also introduced into the source term in order to stabilizing the pressure fluctuation, that is,

$$\nabla^2 p^{(k+1)}(\mathbf{r}_i) = \gamma\rho_0 \frac{n_0 - n^{(*)}}{\Delta t^2 n_0} + (1-\gamma)\frac{\rho_0}{\Delta t}\nabla \cdot \mathbf{u}^{(*)}(\mathbf{r}_i) \tag{2.28}$$

where γ is an artificial coefficient, and normally takes a small value (e.g. $0.01 < \gamma < 0.05$ [82]).

This approach actually attempts to include a certain amount of the accumulated density error arising from the numerical computation. Khayyer and Gotoh [65] also proposed another scheme based on this idea, namely:

$$\frac{\Delta t}{\rho_0}\nabla p^{(k+1)}(\mathbf{r}_i) = \frac{1}{n_0}\frac{Dn^{(*)}}{Dt} + \frac{1}{n_0}\frac{Dn^{(k)}}{Dt}\left|\frac{n^{(k)}-n_0}{n_0}\right| + \frac{\Delta t}{n_0}\frac{Dn^{(k)}}{Dt}\left|\frac{n^{(k)}-n_0}{\Delta t n_0}\right| \quad (2.29)$$

where $\frac{Dn^{(*)}}{Dt}$ is given by Eq. (2.26), which has an analogous effect as the divergence of velocity.

Finally, there is also another proposal which returns to explicit pressure-velocity de-coupling [124] scheme like in Weakly Compressible SPH, i.e., using Equation of State to relate the pressure and density instead of solving Poisson equation.

The aforementioned source term modification is an efficient way of improving the MPS method; similar technique has also been developed in this study as illustrated in the next part.

ii. High order Laplacian

A high order Laplacian operator is introduced in [64]. If Eq. (2.6) is selected as the kernel function, the form in 2D is as follows:

$$\nabla^2 u_f(\mathbf{r}_i) = \frac{1}{n_0}\sum_{j\neq i}^{N}\frac{3(u_f(\mathbf{r}_j)-u_f(\mathbf{r}_i))r_e}{r_{ij}^3} \quad (2.30)$$

However, as admitted by the authors of Ref [64], this kind of modification do not improve the performance very much.

3) Viscosity

i. Strain-based viscosity model

In the Navier-Stokes equations, the viscous term $\nu\nabla^2\mathbf{u}$ is normally calculated by the original Laplacian model as Eq. (2.19). In [61, 62], this is modified to the following form:

$$\nu\nabla^2\mathbf{u} = \frac{1}{\rho}\nabla\cdot\mathbf{T} = \frac{1}{\rho n_0}\sum_{j\neq i}^{N}\mathbf{T}_{ij}\cdot w_{ij} \quad (2.31)$$

where $\mathbf{T}$ is the viscous stress tensor, which could be related to the strain rate. For more details, one can refer to the work in Ref [62].

ii. SPS (Sub-Particle-Scale) for high Reynolds number flow

In the traditional mesh-based CFD, the LES (Large-Eddy Simulation) model is frequently employed to simulate the turbulence flow. In LES, the SGS (Sub-Grid-Scale) model is used to take the sub grid scale turbulence ingredients into account. This idea is also introduced in MPS, and the corresponding model is called SPS (Sub-Particle-Scale) turbulence model. More information is given in [37].

4) Two-phase flow

The two phase flow model has also been simulated by MPS, for example, wave generation due to the inflow of sediment and the gas-liquid two phase flow. The implementation procedure is provided in [37, 125].

5) Improving the interpolation accuracy

i. Different kernel functions

Although the original kernel function, i.e. Eq. (2.6) is predominately used in the MPS method, other forms of kernel are also tested to compare with the original one [3, 124, 131]. Ref [131] proposed a new form of "kernel function" that satisfy the unit condition (which means its integration over whole domain is one), but no performance comparison with the original form i.e. Eq. (2.6) is given. Six different kernel functions are investigated in Ref [3], and a piecewise polynomial function is found to be more stable than others. In Ref [124], a third-order polynomial spiky function is found to be "slightly" more accurate than the commonly used one (i.e. Eq. (2.6)) for the water bubble problem. It is worth to mention that none of the above researches have reported the pressure calculation accuracy could be affected by choosing different kernel functions.

ii. High order gradient model

Khayyer and Gotoh [65] introduced a corrective matrix in the pressure gradient formulation. This term is reported to be effective in improving the accuracy of computation.

iii. MLS-like function approximation

In [71, 150], the 2nd order Taylor series is employed to approximate the function within the local support domain, and then the unknown coefficients of the Taylor series are obtained by MLS procedure, i.e. local least square

fitting. Because the coefficients of the Taylor series are also the first and second order derivatives of the unknown function, the gradient and Laplacian are consequently obtained after this MLS fitting procedure. But as mentioned in [150], this kind of least square approach has to be incorporated with other measures to guarantee the stability of simulation due to the Lagrangian way of particle advancing in time domain.

6) Free surface identification

i. Using particle number rather than particle number density

As mentioned in Section 2.1.4, the traditional free surface identification scheme trends to falsely recognize some inner fluid particles as free surface particles. One modification [82, 152] of this is using the particle number within its neighbour rather than particle number density $n^{(*)}$.

ii. "Arc" type

Another approach [71] is proposed based on checking the "arc" which would be fully covered by its neighbour particles for the inner particles. More detailed information is given in Section 2.3.2.4.

7) Dynamic Stabilization

In [159], a dynamic stabilization term is introduced in the correction step. This term produces a repulsive force to avoid the inter-particle penetration and thus stabilizes the simulation.

2.3 New modifications to MPS

2.3.1 Density error compensation in source term of Poisson equation

Basically, there are two forms of source term in the Poisson equation [171], namely the Density Invariant (DI) type and Divergence-Free velocity (DF) type. The one used in standard MPS (Eq. (2.4)) is the DI type. A heuristic explanation is given below to show the difference between DI and DF types. The momentum equation is reformulated and then split into two successive equations as:

$$\mathbf{u}^{(*)} = \mathbf{u}^{(k)} + \Delta t \mathbf{g} \tag{2.32}$$

$$\mathbf{u}^{(k+1)} - \mathbf{u}^{(*)} = -\Delta t \frac{\nabla p^{(k+1)}}{\rho_0} \tag{2.33}$$

Similarly, the Lagrangian form of the continuity equation is also reformulated as:

$$\frac{\rho^{(*)} - \rho^{(k)}}{\Delta t} = -\rho_0 \nabla \cdot \mathbf{u}^{(*)} \tag{2.34}$$

$$\frac{\rho^{(k+1)} - \rho^{(*)}}{\Delta t} = -\rho_0 \nabla \cdot (\mathbf{u}^{(k+1)} - \mathbf{u}^{(*)}) \tag{2.35}$$

Different types of Poisson equations could be obtained using different combinations of Eq. (2.32) to (2.35).

The DI type Poisson equation could be obtained by first taking the divergence of Eq. (2.33) and then substituting the resultant equation into Eq. (2.35). The incompressibility condition is realized by enforcing $\rho^{(k+1)}$ to be the initial density ρ_0. The final result is Eq. (2.4) (replacing the physical density with particle density).

On the other hand, if we take the divergence operation of Eq. (2.33) and apply the incompressibility condition by enforcing the divergence of $k+1$ time step $\nabla \cdot \mathbf{u}^{(k+1)}$ to be zero, the DF type Poisson equation is obtained as:

$$\nabla^2 p^{(k+1)} = \rho_0 \frac{\nabla \cdot \mathbf{u}^{(*)}}{\Delta t} \tag{2.36}$$

The relation between DI type (Eq. (2.4)) and DF type (Eq. (2.36)) could be obtained by substituting Eq. (2.34) into Eq. (2.36) (also replacing the physical density with particle density), which leads to:

$$\nabla^2 p^{(k+1)} = \rho_0 \frac{\nabla \cdot \mathbf{u}^{(*)}}{\Delta t} = \rho_0 \frac{n^{(k)} - n^{(*)}}{n_0 \Delta t^2} \tag{2.37}$$

The comparison between Eq. (2.4) and Eq. (2.37) shows that the DI form is the DF form plus the accumulated density error $(n_0 - n^{(k)})$ from the last time step. Due to the inevitable error introduced by any numerical scheme, the accumulated density error will always exist. As a consequence, the DF approach is reported to suffer from the particle clustering and void, which will result in density error accumulation and bad pressure distribution [123, 128]. On the other hand, the DI type source will lead to large density variation (probably caused by the full inclusion of accumulated density error), and consequently large pressure fluctuations in both spatial and temporal domain [53], which reduce the stability of the pressure computation.

To tackle this problem, Hu et al. [16] proposed to use the DI and DF conditions in succession in ISPH. However this approach means to solve the Poisson equation two times, which is more time-consuming than both DI and DF methods. Xu *etal*. [172] have shown that the calculation time is 4 to 5 times larger than any of DF or DI scheme. Another strategy is to combine DF and DI in the source term [66, 72, 82] as:

$$\nabla^2 p^{(k+1)} = \rho_0 \frac{\nabla \cdot \mathbf{u}^{(*)}}{\Delta t} + \alpha \rho_0 \frac{n_0 - n^{(k)}}{n_0 \Delta t^2} \tag{2.38}$$

where α is a coefficient which is normally far smaller than 1. Unlike DI scheme, this strategy attempts to take a certain amount (not all of them like in DI) of accumulated density error into account. In most of these similar modifications that have been proposed, the coefficient α needs to be calibrated based on different cases. One exception is shown in Ref [66], where the authors coupled the absolute density variation accumulated and the rate of density variation at the last time step to formulate a density error compensation term. Similarly, a new density error compensation term is proposed with no artificial coefficient (which requires no calibration for different cases).

The coefficient α in Poisson equation (Eq. (2.38)) is chosen in the following way:

$$\alpha = \begin{cases} |\frac{n_0 - n^{(k)}}{n_0}| + \Delta t |\nabla \cdot \mathbf{u}^{(k)}|, & (n_0 - n^{(k)}) \nabla \cdot \mathbf{u}^{(k)} \geq 0 \\ |\frac{n_0 - n^{(k)}}{n_0}|, & (n_0 - n^{(k)}) \nabla \cdot \mathbf{u}^{(k)} < 0 \end{cases} \tag{2.39}$$

This form of α could be interpreted as the percentage of the absolute density variation, which is then multiplied by the density changing rate in the DI term (i.e. $\frac{n_0 - n^{(k)}}{n_0 \Delta t}$).

The condition $(n_0 - n^{(k)}) \nabla \cdot \mathbf{u}_n \geq 0$ means that the fluid is compressed, i.e. $(n_0 - n^{(k)}) \leq 0$ (or expanded, i.e. $(n_0 - n^{(k)}) \geq 0$) in the last time step ($t = k\Delta t$), and will be further compressed according to the motion trend of particles, that is, $\nabla \cdot \mathbf{u}^{(k)} \leq 0$ (or expanded, i.e. $\nabla \cdot \mathbf{u}^{(k)} \geq 0$). Under this situation, an additional term ($\Delta t |\nabla \cdot \mathbf{u}^{(k)}|$) is added into the coefficient to help to control further the compression (or expansion).

2.3.2 Boundary condition

2.3.2.1 Pressure Neumann condition on solid boundaries

In most of the cases, the solid boundary in particle method will normally be handled by ghost (dummy) particle [128, 171] method , repulsive force method [142] or the combination of these two [126]. These traditional techniques require careful handling of the ghost (dummy) particle arrangement or repulsive force parameter selection according to various cases. In this study, as proposed in another particle method, MLPG_R [99] (Meshless Local Petrov Galerkin method with Rankine source solution), instead of applying Poisson equation (Eq. (2.38)) as in the standard MPS, the following Neumann condition (Eq. (2.40)) is applied on the inner most layer of solid boundary. The gradient of Pressure is calculated between the current boundary particle and the nearest fluid particle (or the linear interpolation between nearest fluid particles), which will avoid the deficiency of particles within its support domain.

$$\mathbf{n} \cdot \nabla p^{(k+1)} = \rho_0 (\mathbf{n} \cdot \mathbf{g} - \mathbf{n} \cdot \dot{\mathbf{u}}_b^{(k+1)}) \tag{2.40}$$

where $\dot{\mathbf{u}}_b$ is the acceleration of the boundary, and $\mathbf{n}$ is the normal vector of the boundary. For the FSI case in which the motion of the boundary is determined by the pressure of the surrounding fluid, the acceleration of next time step $\dot{\mathbf{u}}_b^{(k+1)}$ would be unknown when solving the pressure Poisson equation. As an approximation, the value from the last time step $\dot{\mathbf{u}}_b^{(k)}$ (or the last iteration when iterative process is involved in the fluid structure interaction) is adopted instead.

2.3.2.2 Laplacian operator compensation near solid boundary

For the fluid particles which are close to the solid boundary, the Laplacian operator needs to be modified to be consistent with the Neumann condition on solid boundary and compensate for the insufficiency of neighbour particles. More specially, as shown in Figure 2.1, if the virtual particle, which is along the local normal direction and towards the outside of solid boundary with a distance of r_0, is within the support domain of the fluid particle, this virtual particle will also be included in the calculation of Laplacian operator. The pressure value is derived according to Eq. (2.40), i.e.

$$p_v = p_s + \rho_0 (\mathbf{n} \cdot \mathbf{g} - \mathbf{n} \cdot \dot{\mathbf{u}}_b) r_0 \tag{2.41}$$

where, p_v is the pressure of virtual particle, and p_s is the pressure of the corresponding solid particle.

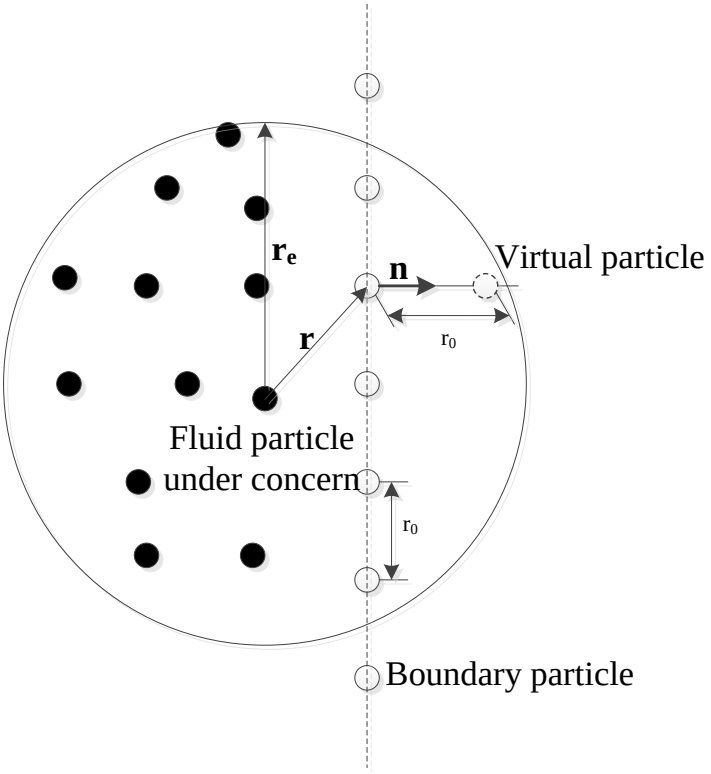

Figure 2.1: Demonstration of virtual particle for compensating the Laplace operator near solid boundary

This virtual particle will only affect the Laplacian coefficients of corresponding fluid particle.

2.3.2.3 Intermediate velocity of boundary particles

The choice of intermediate velocity $\mathbf{u}^{(*)}$ on solid boundary will affect the accuracy of pressure which is computed from the Poisson equation (Eq. (2.38)), since the divergence of intermediate velocity is the source term of this equation [12]. According to the idea of Ref [12], for the case of viscous flow, the non-slip condition should be applied. This means the choice of $\mathbf{u}^{(*)}$ should guarantee that, at $k+1$ time step, the fluid velocity on boundary ($i.e.\mathbf{u}^{(k+1)}|_{\partial\Omega}$) is equal to the solid body velocity on the fluid-solid interface ($\mathbf{u}_b^{(k+1)}$). Thus,

if $\mathbf{u}^{(k+1)}$ is replaced by boundary velocity $\mathbf{u}_b^{(k+1)}$ in Eq. (2.32), and using $\nabla p^{(k)}$ to approximate $\nabla p^{(k+1)}$ (since it is not known at this stage), the intermediate velocity of boundary particles is:

$$\mathbf{u}_b^{(*)}|_{\partial\Omega} = \mathbf{u}^{(k+1)}|_{\partial\Omega} = \mathbf{u}_b^{(k+1)} + \Delta t \frac{\nabla p^{(k)}}{\rho_0} \tag{2.42}$$

Furthermore, the above equation could be split into two components after projecting to the tangent (i.e.,$\boldsymbol{\tau}$) and normal (i.e.,$\mathbf{n}$) directions, respectively. And Eq. (2.40) could be used to calculate the normal component of the pressure gradient. The tangent part is calculated by simple finite difference approach between its neighbour solid particles. Finally, the intermediate velocity of the boundary particles is chosen as:

$$\begin{aligned}
\frac{\partial \mathbf{u}_b^{(*)}}{\partial n} &= \mathbf{n}\cdot\mathbf{u}^{(k+1)}|_{\partial\Omega} + \frac{\Delta t}{\rho_0}\frac{\partial p^{(k)}}{\partial n} = \mathbf{n}\cdot\mathbf{u}_b^{(k+1)} + \Delta t(\mathbf{n}\cdot\mathbf{g} - \mathbf{n}\cdot\dot{\mathbf{u}}_b^{(k+1)}) \\
\frac{\partial \mathbf{u}_b^{(*)}}{\partial \tau} &= \boldsymbol{\tau}\cdot\mathbf{u}^{(k+1)}|_{\partial\Omega} + \frac{\Delta t}{\rho_0}\frac{\partial p^{(k)}}{\partial \tau} = \boldsymbol{\tau}\cdot\mathbf{u}_b^{(k+1)} + \frac{\Delta t}{\rho_0}\frac{\partial p^{(k)}}{\partial \tau}
\end{aligned} \tag{2.43}$$

In this study, since the viscosity is not taken into account, the free-slip boundary condition should be applied. The only difference that should be made is the tangential part of the fluid velocity on boundary (i.e., $\boldsymbol{\tau}\cdot\mathbf{u}^{(k+1)}|_{\partial\Omega}$) is different to $\boldsymbol{\tau}\cdot\mathbf{u}_b^{(k+1)}$. So in this case the term $\boldsymbol{\tau}\cdot\mathbf{u}_b^{(k+1)}$ is then replaced by the velocity projection of the nearest fluid particle on the direction of $\boldsymbol{\tau}$. Also, as mentioned in Section 2.3.2.1, the solid boundary velocity and acceleration of $(k+1)^{th}$ time step is approximated by the value in last time step or last iteration, for the FSI interface boundaries.

As pointed out in [12], using the above intermediate velocity boundary condition, the accuracy for both the velocity and the pressure are second-order.

2.3.2.4 Free surface particle identification

a) 2D case

A simplified version of the method used by Koh *et al* [71] is adopted. As shown in Figure 2.2, a circle (with radius of $1.05r_0$) is assigned to each particle with itself to be the center. If the "circle" is completely covered by its neighbours, then it is recognized as an inner fluid particle, otherwise it is a free surface particle. To realise this checking process, the circle is discretised by 360 points which

locate evenly along the circle. If all these points are covered by the circles from its neighbour particles, the centre particle is then regarded as an inner particle. For example, in Figure 2.2, particle A is recognised as free surface, because the yellow points on its "circle" are not covered by its neighbors. In contrast, particle B is identified as inner fluid particle.

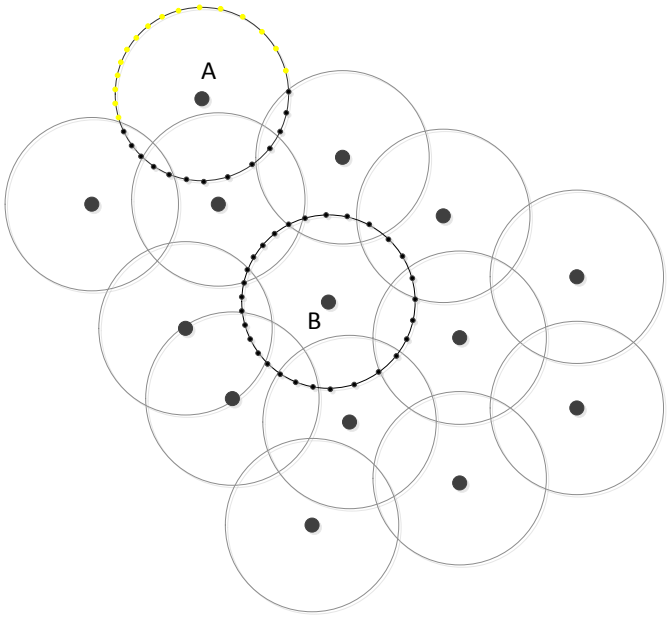

Figure 2.2: Demonstration of free surface particle identification for 2D case

Because the use of Neumann boundary could avoid the discretization of Laplacian operator and the calculation of particle density for the boundary particles as explained in Section 2.3.2.1, the two layers of dummy particles in the standard MPS are not required. However, in order to cover the outside of the solid boundary to prevent them to be falsely recognized as free surface particles, one additional layer of virtual particles are still have to be placed. The generation of this layer of particles does not have to fit any pattern sophisticatedly. It is simply along the inner solid particles to make sure that the inner layer of solid particles will not be exposed to void area towards the outside of fluid domain and falsely be identified as free surface particle. It is worth to mention that this additional layer of particle is not the same as the virtual particle in Section 2.3.2.2, whereas the virtual particle does not has to be generated in the geometry like this additional layer of particle.

This pure geometric free surface identification approach could avoid the situation as mentioned in Section 2.1.4 that when two particles are close enough, they will be identified as inner fluid particles as the result of particle density increasing, though they are actually free surface particles. According to this proposed approach, no matter how close two particles are, they will not be identified as inner fluid as long as they are not surrounded by enough neighbour particles. Certainly, instability issue will be caused if two particles are getting too close even if they are correctly identified as free surface. This problem will be handled by the collision handling approach, which will illustrated in Section 2.3.3.

b) $3D$ case

The multi-level searching strategy is widely used for free surface identification because it normally will be more efficient especially for $3D$ case [101, 150]. Similarly, in this study a two-step scheme is proposed for the $3D$ case: a preliminary filtering by neighbor particle number and then a geometric scheme that employs the same principle of the $2D$ case. The details are given below:

i) Preliminary filtering by neighbour particle number

The neighbour particle number N_p is checked for each particle by the following equation:

$$N_p < \beta_{3d} N_{p0} \tag{2.44}$$

where N_{p0} is the neighbour particle number of a typical inner fluid particle under the uniform particle distribution, which means $N_{p0} = 32$; β_{3d} is a tuning parameter and the value is taken as 0.96 in this study.

The reason of using the neighbour particle number instead of particle density is the same as explained in part (3) of Section 2.1.4, i.e. for the case when some particles are very close to each other, the particle density could be very high although they may still on the free surface. But the neighbour particle number approach will not suffer from this problem.

ii) Refine the searching by geometric property

For the particles whose neighbour particle number is less than the threshold, the following geometrical scheme will be applied for refining the searching. More specially, a vector $\mathbf{n}_z$, which points towards the most sparse particle distribution of the concerned particle's neighbour, is determined by a weighted averaged approach. Then, on the sphere which is centered by the concerned particle,

a circular patch around n_z will be discretised by evenly distributed points, as shown in Figure 2.3. If these points are all covered by the same spheres of its neighbor particles, this particle is recognised as inner fluid particle; otherwise it is regarded as a free surface particle. The radius r and angle θ are selected as $r = 1.05 \times r_0$ and $\theta = \pi/4$;

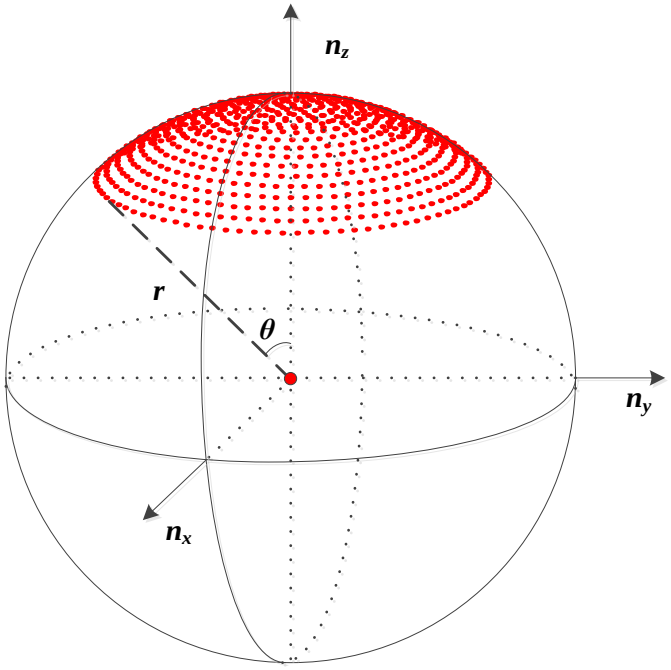

Figure 2.3: Demonstration of free surface particle identification for 3D case

2.3.3 Particle shifting and collision handling

The disorder of particle distribution is one of the main sources of pressure fluctuation suffered by particle method. Many researchers have developed some techniques to handle this problem [13, 82, 119, 123, 159, 171]. Among these improvements, rearranging the particle positions after each time step is considered to be a very effective approach. It could stabilise the pressure calculation in both spatial and temporal domain [119, 159]. For example, in Ref [159], a dynamic force is introduced during the evolution of the particle movement. The force is the summation of all the contributions from the neighbour particles. For each force component between the pair of the concerned particle and a neighbour particle, the principle of calculating this force is to guarantee that

they will be separated and verged on each other by a distance, which is around r_0, for the next particle configuration. However for an arbitrary particle distribution, it is obvious that each force component will affect each other, and consequently makes the final particle configuration not exactly evenly distributed. But the overall distribution is much more improved and consequently makes the computation more stable and accurate. Following similar idea, in this study, a simple particle shifting method, which also intends to avoid the improper short distance between each pair of particles, is proposed to improve the stability of computation. The difference is that in this scheme the position is manipulated directly instead of by applying an artificial force.

After each time step, the positions of particles are slightly shifted to regularize their distribution. This technique could also be regarded as a re-meshing procedure. Moreover, since the Poisson equation is derived based on the incompressibility condition (i.e. the second equation in Eq. (2.1)), the resultant pressure would roughly keep the distance between neighboring particles to be around the same value (i.e. the initial particle distance r_0). As a consequence, the space left for this further shifting would be very small. Therefore not mapping the value onto the new positions will not corrupt the result.

The amount of shifting is chosen as:

$$\delta \mathbf{r}_i = \sum_{j \neq i, |r_{ij}| \leq \bar{r}_0} \frac{\bar{r}_0 - |r_{ij}|}{2} \cdot \frac{\mathbf{r}_i - \mathbf{r}_j}{|r_{ij}|} \tag{2.45}$$

where $\bar{r}_0$ normally is set to be 99% of the initial particle distance.

For the free surface particles which are far away from the main fluid body, their motions will barely be affected by pressure. Under some circumstances, they may get extremely close. This unusual and "suddenly-formed" very short distance between fluid particles will cause singularity problem when solving pressure Poisson Equations. This situation will not be completely eliminated by the aforementioned particle shifting. For example, the current distance between two particles are not very small (which will not activate the particle shifting scheme), but they have large relative velocities which mean they will get very close after prediction step Eq. (2.3). As a consequence, similar to the one proposed in [71], a simple collision handling technique is applied here. The basic idea of this approach is that the relative velocities between particles are set to be zero when they are expected to be closer than the threshold before the prediction step. Accordingly, before the calculation of each time step, we

apply the following velocity manipulation for each fluid particle:

$$\delta \mathbf{u}_i = \sum_{j \neq i, (r_{ij} - \mathbf{u}_{\tau_{ij}} \Delta t) \leq r_{min}} -\epsilon(r_{ij}) \mathbf{u}_{\tau_{ij}} \tag{2.46}$$

where $\mathbf{u}_{\tau_{ij}}$ is the tangential relative velocity between particle i and j, and r_{min} is the threshold to activate the scheme. It is selected as roughly 30% of the initial particle distance in this study. Parameter ϵ depends on the property of particle j. If particle j is a fluid particle, ϵ is equal to 0.5, otherwise, if it is a solid boundary particle, ϵ is equal to 1.0. This kind of setting is chosen to make sure that the solid particles velocity involved will not be affected while the relative velocity between its neighbor fluid particles will still be set to be zero.

2.3.4 Neighbour particle searching strategy

The discretizing of gradient /divergence and Laplacian operators on the position of each particle requires the information of its neighbour particles. Because of the Lagrangian nature of particle method, all the particles are constantly moving during the computation, and thus the neighbour particle lists need to be updated after every advance of the particle distribution. This neighbour particle searching could be very time-consuming if the primitive "all-pair" searching strategy is used. In terms of computational efficiency, the state-of-the-art neighbour particle searching acceleration strategy could basically be classified into three types: (1). Verlet list method, whose algorithm complexity is $O(N^2)$ [80]; (2). Cell-linked method and the Verlet list enhanced by cell-linked approach. The "cell-link" and also the Verlet list enhanced by "cell-link" methods have a linear complexity [17] i.e. $O(N)$. This is proved by the results in Section 4.1 as well. (3). The so-called "tree algorithm", which uses hierarchically tree-structure to partition the computational domain into a sequence of squares (in $2D$, for $3D$, it becomes cubes) until each square contains only one particle or nothing [137]. It generally has a complexity with the order of $O(Nlog(N))$ [137]. Furthermore, this kind of algorithm is designed to handle the situation where the particles are highly unevenly distributed, which is not the case of this study. As a consequence, only the second type of methods i.e. the linear type is first reviewed in the following context. And then a new strategy based on the cell-linked method is proposed.

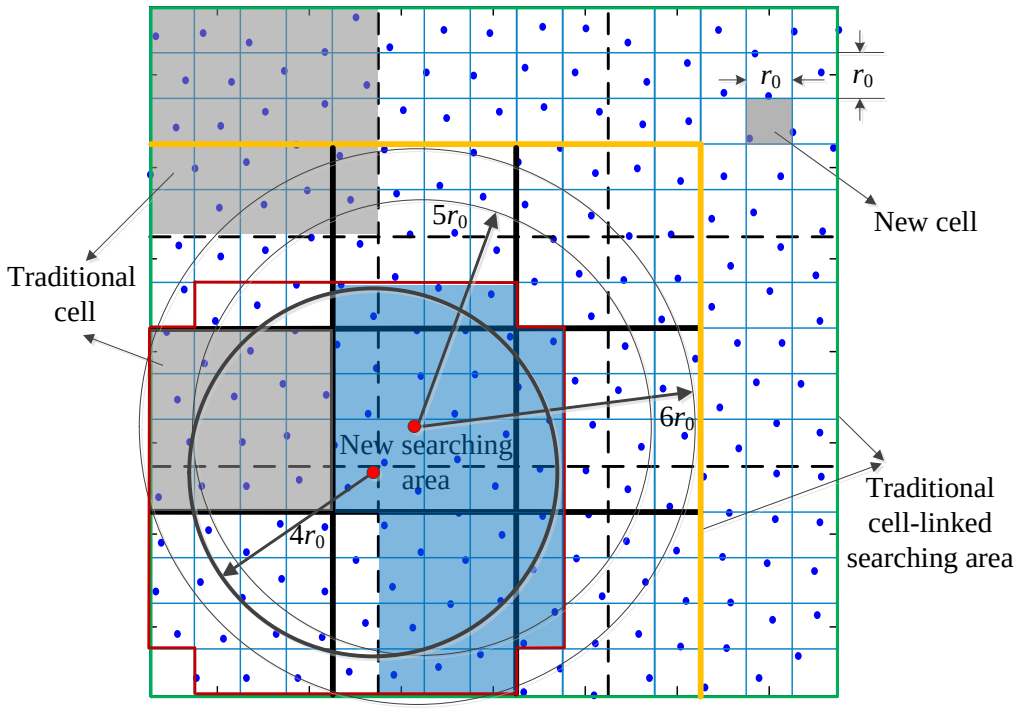

Figure 2.4: Demonstration of the neighbour particle searching strategy

In cell-linked method, all particles are distributed into a set of regular square cells which cover the entire computation domain. The length of the cell side is at least the cut-off distance of supporting domain for Laplacian operator, i.e. four times of the initial particle distance ($4r_0$). As a consequence, the neighbour searching for a particular particle could be conducted just within the surrounding cells (nine cells in $2D$, i.e., the rectangular area constrained by the yellow and green lines in Figure 2.4).

Alternatively, the Verlet list algorithm establishes a neighbour candidates list for each particle. This list contains all the particles with a larger distance from the concerned particle than the exact cut-off length of the Laplacian supporting domain (e.g., $5r_0$ or $6r_0$). Because the radius is chosen to be larger than $4r_0$, the neighbour particles will not exceed the scope of this list for the next several particle distributions, consequently this list could be used as the base pool of refined searching for several time steps without the need of updating.

The generation of the Verlet list could be accelerated by cell-linked method with the radius as the cell length instead of using "all-pair" searching. The tricky problem of Verlet list method is the choice of its radius. If it is too large, the candidates in the list might be more than those covered by the nine adjacent cells

with exact $4r_0$cell length (in $2D$ case), which means it would be meaningless to generate Verlet list since it is more time-consuming than using the cell-linked approach directly. Actually, the circle with the radius of $6r_0$ already makes the area covered by Verlet list circle (shown in Figure 2.4) almost the same as the nine cells with $4r_0$ cell length (rectangular area limited by the yellow and green line in Figure 2.4). The radius of $5r_0$ will make the Verlet list circle smaller than the nine cells with exact $4r_0$cell length. However, if we add the time used on establishing Verlet list with $5r_0$ length cells (the green line covered area in Figure 2.4) which contains more particles than the $4r_0$ length cells (rectangular area limited by the yellow and green line in Figure 2.4), the total time consumed would be similar or even larger. These facts about these two approaches will be further illustrated in Section 4.1.

There is only one issue remaining, which is in "cell-link" approach, after each changing of the particle distribution, all the particles need to be "re-registered" to the cells again. While this is not required in Verlet list approach at every time when the particle configuration changes (as aforementioned, the Verlet list is valid for several time steps depending on the size of the list). This seems to be an advantage for Verlet list, however, as will be shown in Section 4.1, the time spent on particle registering is almost negligible compared to the time spent on other processes. As a consequence, the cell-linked method is overall better than Verlet list method or the combination of these two methods. In this study, in order to further reduce the computation burden, this cell-linked principle is further explored by making the cell smaller than the traditional one, i.e. to be the initial particle distance (r_0), as shown in Figure 2.4. This change means the searching could be performed just within the red line covered area instead of the area contained by yellow and green lines in Figure 2.4. This reduces about $4/9$ of the searching area compared with the traditional cell (with $4r_0$ cell length). It is worth mentioning that the time spent on cell establishing is basically the same for the smaller and traditional cell, because in both of these situations each of the particles is only required to be checked once for registering them to a particular cell (no matter larger or smaller cells). This means the cell establishing time is only proportional to the total particle number regardless of the cell length.

Another strategy was developed to avoid repetitive checking of particle pair by Crespo [21] for the traditional cell-linked approach. The core idea is that if particle j is in the neighbour list of particle i, particle i is obviously also in the neighbour list of particle j. Hence, the repeating of pair interaction could be avoided if the neighbour list is updated simultaneously for both of the

particles in the pair when one of them is currently regarded as a centre particle. And then this centre particle will be excluded during the following neighbour list generation process for the rest of particles. This means if the checking is conducted cell by cell (i.e. after the establishment of neighbour list is finished for all the particles in one cell, and then moving to the next cell), only the particles in the cells with higher indexes in the related neighbour cells are needed to be checked (as the particles in the lower-index-cells have already been checked previously). This idea is also applicable to the new cell model aforementioned. If the cells are indexed vertically from bottom to top, the generation of neighbour list could be conducted just in the area covered by blue color in Figure 2.4. This means that the computation burden is further reduced by half.

To summarise, the new proposed neighbour searching strategy is essentially a further improvement of the traditional cell-linked approach. It consists of two parts, i.e. smaller (i.e. r_0) and more economical cell length and the non-repeating particle pair checking. Generally speaking, this new strategy is applicable for the improvement of traditional cell-linked model with any cell length (e.g. $4r_0$, $5r_0$ or $6r_0$), and the searching area required by this new strategy is always about 2.5/9 of the corresponding traditional "cell-link" model (the comparison of the blue color with the yellow and green line covered area is an example for the case of $4r_0$ length criteria).

Finally, it is worth to discuss the computational complexity of the methods mentioned in this section. For the incompressible flow studied in this study, the particles are roughly evenly distributed (although not regular, that is the reason of introducing the particle shifting in Section 2.3.3), hence the number of particles that is required to be checked for neighboring particle searching of a particular particle would be proportional to the area of the searching.

As discussed above, the searching area of each particle is always the same for a particular method (e.g. the blue area for the proposed strategy and the yellow line covered area for the traditional cell-linked method in Figure 2.4). Moreover, the cell establishing time is only proportional to the total particle number regardless of the cell length. Based on these discussions, the number of particles that needs to be searched is a constant for each particle for any method mentioned in this section (although this constant is different for different method), so the overall searching time is proportional to the overall number of particles, which means the complexity is linear, i.e. $O(N)$.

Chapter 3

Structure Dynamics and FSI coupling scheme

3.1 Mode theory for beam structure

The beam structure approximation is commonly encountered in the marine engineering such as ship hull. The elastic deformation of a beam could be well described by modal superposition. This approach could significantly reduce the degrees of freedom for the structure dynamics analysis. A brief review of this theory for beam structure is given in this section [10, 56].

3.1.1 Euler-Bernoulli equation

For a non-uniform beam shown in Figure 3.1, the deflection along y direction is defined as $y(x,t)$. The stiffness of cross-sections along x axis is defined as $E(x)J(x)$. The beam deflection is governed by the following Euler-Bernoulli equation:

$$\frac{\partial^2}{\partial x^2}(E(x)J(x)\frac{\partial^2 y(x,t)}{\partial x^2}) + \rho_l(x)\frac{\partial^2 y(x,t)}{\partial t^2} = z_{load}(x) \tag{3.1}$$

where $\rho_l(x)$ is the line density of beam (i.e. mass per unit length), $z_{load}(x)$ is the load applied on the beam along x axis. If this external load $z_{load}(x)$ is set to be zero, the problem becomes the following free vibration equation:

$$\frac{\partial^2}{\partial x^2}(E(x)J(x)\frac{\partial^2 y(x,t)}{\partial x^2}) + \rho_l(x)\frac{\partial^2 y(x,t)}{\partial t^2} = 0 \tag{3.2}$$

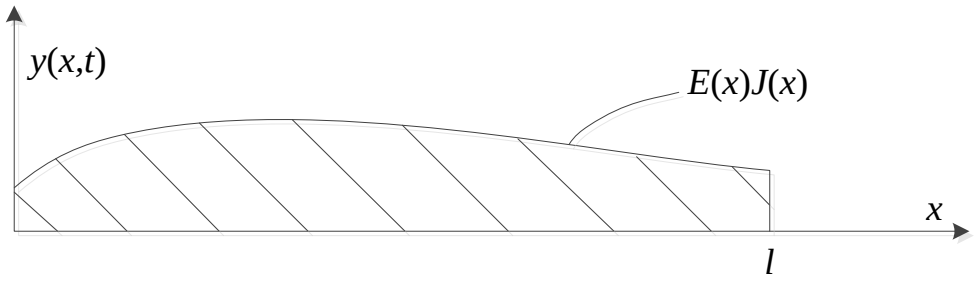

Figure 3.1: Sketch of a non-uniform beam

In order to solve Eq. (3.2), the trial solution is defined in Eq. (3.3).

$$y(x,t) = \phi(x)sin(\omega t) \tag{3.3}$$

After substituting Eq. (3.3) into Eq. (3.2), the following equation then is obtained:

$$\frac{\partial^2}{\partial x^2}(E(x)J(x)\frac{\partial^2\phi(x)}{\partial x^2}) - \rho_l(x)\omega^2\phi(x) = 0 \tag{3.4}$$

The problem represented by Eq. (3.4) is known as an eigenvalue problem. With boundary conditions being specified on both ends of the beam, a series of discrete value of the natural frequencies ω_i $(i = 1, 2, 3, ...)$ together with a series of corresponding spatial functions $\phi_i(x)$ $(i = 1, 2, 3, ...)$ could be obtained by solving this equation. These series of functions $\phi_i(x)$ are defined as the "mode functions" for the beam.

3.1.2 Orthogonality of natural modes

The most important property for the mode function $\phi_i(x)$ is the orthogonality, which will be briefly illustrated as follows: If we substitute the mode function $\phi_i(x)$ corresponding to ω_i into Eq. (3.4), then multiply both side of Eq. (3.4) by a different mode function $\phi_j(x)$ (corresponds to natural frequency ω_j), and finally

apply the integration along the beam (i.e. x axis), we have:

$$\begin{aligned}\omega_i^2 \int_0^l \rho_l(x)\phi_i(x)\phi_j(x)dx &= \int_0^l \frac{\partial^2}{\partial x^2}(E(x)J(x)\frac{\partial^2\phi_i(x)}{\partial x^2})\phi_j(x)dx \\ &= [\frac{\partial}{\partial x}(E(x)J(x)\frac{\partial^2\phi_i(x)}{\partial x^2})\phi_j(x)]|_0^l - [E(x)J(x)\frac{\partial^2\phi_i(x)}{\partial x^2}\frac{\partial\phi_j(x)}{\partial x}]|_0^l \\ &+ \int_0^l E(x)J(x)\frac{\partial^2\phi_i(x)}{\partial x^2}\frac{\partial^2\phi_j(x)}{\partial x^2}dx\end{aligned} \tag{3.5}$$

The two integrated terms will vanish due to various boundary conditions (e.g. cantilever, free, simply supported), which means:

$$\omega_i^2 \int_0^l \rho_l(x)\phi_i(x)\phi_j(x)dx = \int_0^l E(x)J(x)\frac{\partial^2\phi_i(x)}{\partial x^2}\frac{\partial^2\phi_j(x)}{\partial x^2}dx \tag{3.6}$$

The result in Eq. (3.6) will remain valid if the subscripts i and j are swept, i.e.

$$\omega_j^2 \int_0^l \rho_l(x)\phi_i(x)\phi_j(x)dx = \int_0^l E(x)J(x)\frac{\partial^2\phi_i(x)}{\partial x^2}\frac{\partial^2\phi_j(x)}{\partial x^2}dx \tag{3.7}$$

Comparing Eq. (3.6) and (3.7) lead to the following relation:

$$\int_0^l \rho_l(x)\phi_i(x)\phi_j(x)dx = \int_0^l E(x)J(x)\frac{\partial^2\phi_i(x)}{\partial x^2}\frac{\partial^2\phi_j(x)}{\partial x^2}dx = 0 \tag{3.8}$$

These orthogonality relations means that the modes corresponding to different natural frequencies satisfy the following equations:

$$\int_0^l \rho_l(x)\phi_i(x)\phi_j(x)dx = a_{ij}\delta_{ij} \tag{3.9}$$

$$\int_0^l E(x)J(x)\frac{\partial^2\phi_i(x)}{\partial x^2}\frac{\partial^2\phi_j(x)}{\partial x^2}dx = \omega_i^2 a_{ij}\delta_{ij} \tag{3.10}$$

where δ_{ij} is the Kronecker delta function, and a_{ij} is simply a constant determined by the scale of the mode functions.

3.1.3 Modal superposition method

Due to the orthogonality relations between different modes, any elastic deformation of the beam could be represented by the function space expanded by all

the mode functions, that is:

$$y(x,t) = \sum_{i=0}^{\infty} q_i(t)\phi_i(x) \tag{3.11}$$

where $q_i(t)$ is the i^{th} generalized time-dependent coordinate corresponding to $\phi_i(x)$. If Eq. (3.11) is substituted into Eq. (3.1), the following equation could be obtained:

$$\sum_{i=0}^{\infty} \rho_l \ddot{q}_i(t)\phi_i(x) + \sum_{i=0}^{\infty} q_i(t)\frac{\partial^2}{\partial x^2}[E(x)J(x)\frac{\partial^2 \phi_i}{\partial x^2}] = z_{load}(x,t) \tag{3.12}$$

If we multiply a mode function corresponding to a different natural frequency i.e. $\phi_j(x)$ to both sides of Eq. (3.12), and then integrate with respect to x along the beam, the orthogonal relations represented by Eq. (3.9) and (3.10) lead to the following set of equations:

$$a_{jj}\ddot{q}_j + a_{jj}\omega_j^2 q_j = \int_0^l z_{load}(x,t)\phi_j(x)dx, \quad (s = 0,1,2,...) \tag{3.13}$$

Although Eq. (3.13) will not be used directly to solve the beam motion in the model developed in Section 3.2, the core idea of modal superposition in the above process will be adopted in the derivation of the proposed numerical model.

3.1.4 Obtaining the mode functions

There are different approaches to obtain the mode functions depending on different situations such as modal testing experiment, analytical approach and numerical methods. In this section, the analytical approach for uniform beam and a numerical approach for non-uniform beam are briefly illustrated.

a) Analytical approach for uniform beam

For an uniform beam, the problem could be solved analytically. Based on the orthogonality property mentioned in Section 3.1.2, the mode function $\phi(x)$ is assumed to be of the following form:

$$\phi(x) = b_1 \sin \kappa x + b_2 \cos \kappa x + b_3 \sinh \kappa x + b_4 \cosh \kappa x \tag{3.14}$$

where the parameter κ is defined as:

$$\kappa = \sqrt[4]{\frac{\rho_l \omega^2}{EJ}} \tag{3.15}$$

The stiffness EJ is a constant since the beam is uniform. As mentioned in Section 3.1.1, the four parameters b_1, b_2, b_3, b_4 could be solved by substituting Eq. (3.14) into Eq. (3.4) and using the corresponding boundary conditions. The cases of free-free beam and cantilever beam are listed below for the later use in Section 3.2

For free-free beam, the boundary conditions are: the 2^{nd} (moment) and 3^{rd} (shear force) derivatives of the beam deflection $\phi(x,t)$, and they are zero at both ends. The resulting i^{th} mode function is:

$$\phi_i(x) = C_d[\cosh \kappa_i x + \cos \kappa_i x - \sigma_i(\sin \kappa_i x + \sinh \kappa_i x)], i = 1, 2, 3, \cdots \tag{3.16}$$

where

$$\sigma_i = \frac{\sin \kappa_i l + \sinh \kappa_i l}{\cosh \kappa_i l - \cos \kappa_i l} \tag{3.17}$$

The parameter κ_i is determined by the following equations:

$$\cos \kappa_i l \cdot \cosh \kappa_i l - 1 = 0, i = 1, 2, 3, \cdots \tag{3.18}$$

In Eq. (3.16), the parameter C_d is a factor to adjust the scale of the function. After obtaining the parameter κ_i by solving Eq. (3.18), the natural frequency ω_i for this mode could then be calculated by Eq. (3.15). The parameter $\kappa_i l$ corresponding to the first three flexible natural frequency (the rigid-body case $\kappa_0 l = 0$ is not included) are given by:

$$\begin{aligned} \kappa_1 l &= 4.730041 \\ \kappa_2 l &= 7.853205 \\ \kappa_3 l &= 10.995608 \end{aligned} \tag{3.19}$$

For cantilever beam, the boundary conditions are: zero deflection and rotation (1^{st} order derivative of $\phi(x)$) at the fixed end; zero moment and shear force at the free end. The mode functions are:

$$\phi_i(x) = C_d[\cosh \kappa_i x - \cos \kappa_i x - \sigma_i(\sinh \kappa_i x - \sin \kappa_i x)], i = 1, 2, 3, \cdots \tag{3.20}$$

where

$$\sigma_i = \frac{\sin \kappa_i l - \sinh \kappa_i l}{\cos \kappa_i l - \cosh \kappa_i l} \tag{3.21}$$

And the parameter κ_i in this case is determined by:

$$\cos \kappa_i l \cdot \cosh \kappa_i l + 1 = 0, i = 1, 2, 3, \cdots \tag{3.22}$$

The parameter C_d in Eq. (3.20) has the same meaning as the one in Eq. (3.16). For this case, the parameter $\kappa_i l$ corresponding to the first three natural frequency are:

$$\begin{aligned} \kappa_1 l &= 1.875104 \\ \kappa_2 l &= 4.694091 \\ \kappa_3 l &= 7.854757 \end{aligned} \tag{3.23}$$

b) Numerical method for non-uniform beam

The FE method is obviously able to calculate the mode function by directly discretizing Eq. (3.4) with the corresponding boundary conditions as aforementioned. There are also some approximate numerical approaches that are more efficient such as Rayleigh-Ritz and Myklestad's methods. In Rayleigh-Ritz method, the deflection is expressed by the expansion of a series of base functions. These known base functions satisfy the required boundary conditions. The coefficients of the base function in the expansion is determined by minimizing the frequency ω with respect to each of the coefficients. The key part of this method is to use proper base functions. However it requires experience and understanding of the system dynamics, which is not always easy to do.

On the other hand, the Myklestad's method is purely based on the configuration of the beam without the requirement of using empirical functions. In this method, the beam is first discretized as a set of lumped mass that are connected with massless flexible beams. By using the dynamical equilibrium of the beam element, the deflection, rotation angle, moment and shear force at each cross section of the discrete beam could be determined by a recurrence manner from one end to the other of the beam. More specially, the boundary values at the starting end are chosen to be compatible with the requirement for the case in concern. The values at the other end are adjusted by tuning the value of the natural frequency ω. Finally the deflection value at each discrete position on the beam, which is mode function for this frequency, could be obtained by the ω

values. In this study, this Myklestad's method will be used for the non-uniform beam case and the details of the implementation are given in Appendix C.

3.2 The proposed model

As discussed before, for a floating structure like a ship hull, the typical feature of motion is a large rigid body motion plus a relatively small deformation. This feature makes the modal superposition method suitable and accurate enough to describe the flexible deformation. In this section, the $2D$ Coupled Rigid-body and Flexible mode (CRF) model are developed in details in this section. First, the dynamics of the general equations for a rigid body with flexible beams attached to it is first derived. Based on this general assumption, the governing equations for three special cases are derived, i.e. pure rigid body, floating flexible beam (a reasonable approximation of ship structure) and wedge with flexible bottoms.

3.2.1 Kinetic description

In Figure 3.2, one rigid body with two flexible beam-like structures attached to it are investigated here. The proposed formulation is, however, generally applicable for the cases with more beams. The beam-like structures are either firmly connected with the rigid-body if only one end is attached, or at least simply supported at both ends if they are all connected to the rigid-body. This kind of configuration could enforce that the beam-like structure will not freely rotate with respect to the rigid-body, which is a reasonable assumption for most of the physical situations in marine engineering. This means the relative position between these local systems (as will be defined below) will not change during the movement.

3.2.1.1 Coordinate systems

Two types of coordinate systems are used in this study, which include a global $X-Y$ system and body-attached (local) $x_R - y_R$ and $s_i - w_i$ systems ($i = A, B$, represents the index of Beams A and B, respectively).

The global $X-Y$ system is fixed in the space, whereas the body-attached (local) coordinate systems follow the translational and rotational motions of the

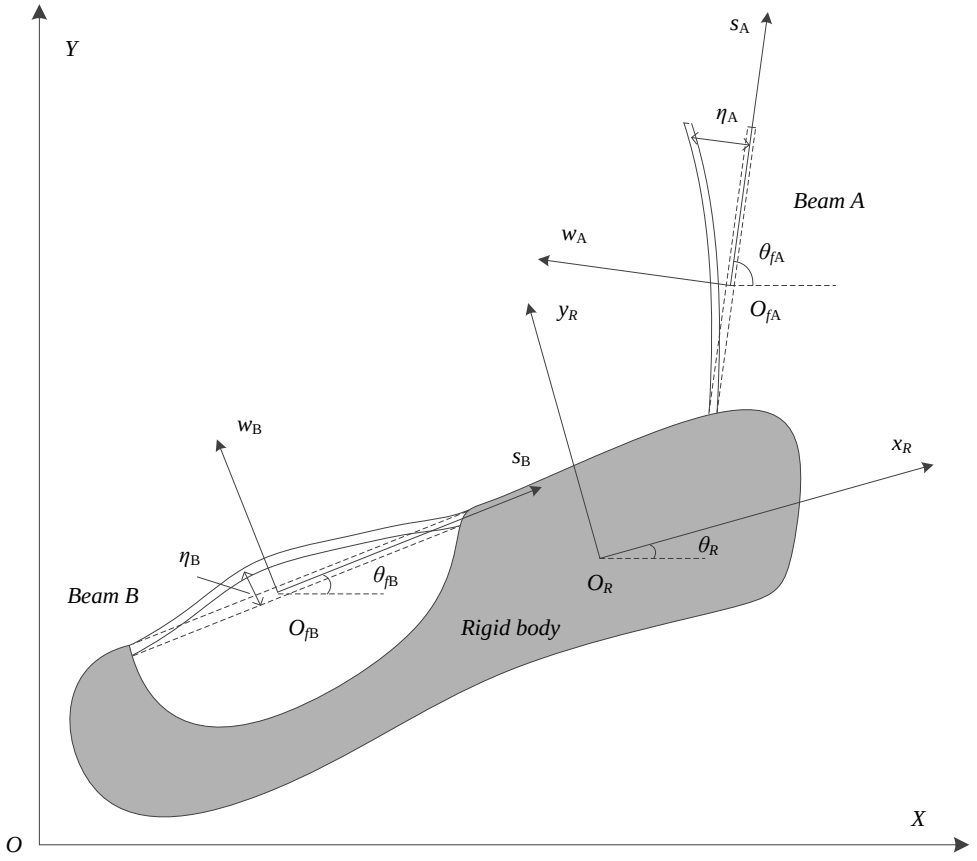

Figure 3.2: Sketch of general rigid body with flexible beams system

corresponding components, but do not deform with the body if it is attached to the beam-like structure. The origins of these local coordinate systems are always chosen to be the mass center of corresponding undeformed substructures.

3.2.1.2 Definition of the motion variables

The motion of the rigid-body part could be described by position of its mass centre $\mathbf{X}_{cR} = [X_{cR}(t), Y_{cR}(t)]^T$, which is the coordinate of the $x_R - y_R$ system origin (i.e., O_R) represented in global system, and the angle $\theta_R(t)$ from $O - X$ axis (anti-clockwise) to $O_R - x_R$ axis. For the flexible beam-like part, except for the mass centre (O_{fA} and O_{fB}), positions $\mathbf{X}_{cfi} = [X_{cfi}(t), Y_{cfi}(t)]^T$ and rotational

angles θ_{fi} (t); additional variables $\eta_i(s_i, t)$, which describe the deflection of beam i with respect to the corresponding beam central lines, are used.

To describe the relation between rigid and flexible parts, the variables $\mathbf{x}_{ofi} = [x_{ofi}, y_{ofi}]^T$ are defined as the vectors from O_R to O_{fi}, respectively. Compared with the aforementioned position vectors, e.g. $\mathbf{X}_{cfi}$, this $\mathbf{x}_{ofi}$ is represented in the $x_R - y_R$ system instead of the global $X - Y$ system. As the relative positions between different local systems are unchanged during the motion, these vectors would be constants. Moreover, the angular differences between different systems are constants as well, i.e.

$$\begin{aligned} &\theta_R(t) - \theta_{fi}(t) \equiv const. \\ &\mathbf{x}_{ofi} \equiv const. \end{aligned} \tag{3.24}$$

Thus, their time derivatives of the angular variables are the same, i.e.

$$\dot{\theta}_R = \dot{\theta}_{fi} \tag{3.25}$$

$$\ddot{\theta}_R = \ddot{\theta}_{fi} \tag{3.26}$$

Similarly, $\mathbf{x}_R = [x_R, y_R]^T$ is defined as the vector from the mass centre of the rigid body O_R to each point on the rigid body. And it is also represented in the local $x_R - y_R$ system. Hence, for each point, the corresponding representation of the vector would remain unchanged.

3.2.1.3 Kinetics of each point on structure

With the above definitions, the global coordinates of each point on rigid-body part, i.e. $\mathbf{X}_R = [X_R(t), Y_R(t)]^T$ could be represented as:

$$\mathbf{X}_R = \mathbf{X}_{cR} + \mathbf{R}_R \mathbf{x}_R \tag{3.27}$$

where $\mathbf{R}_R$ is the rotation matrix which relates the local $x_R - y_R$ system to the global $X - Y$ system. Its definition is given in Eq. (3.34). For the flexible beam-like structure, its motion could be described by the coordinates of the points on the central line $\mathbf{X}_{fi} = [X_{fi}(t), Y_{fi}(t)]^T$ as:

$$\mathbf{X}_{fi} = \mathbf{X}_{cfi} + \mathbf{R}_{fi} \boldsymbol{\xi}_i^T \tag{3.28}$$

where $\boldsymbol{\xi}_i$ is the coordinate of the points on i^{th} beam's central line in the local $s_i - w_i$ system:

$$\boldsymbol{\xi}_i = [s_i, \eta_i] \tag{3.29}$$

where $\eta_i(s,t)$ is the deflection function along the beam. According to the beam assumption, the deformation only occurs in the direction perpendicular to the beam central line, which means that s_i would not change for each point during the movement, i.e.

$$\dot{\boldsymbol{\xi}}_i = [0, \dot{\eta}_i]^T \tag{3.30}$$

$$\ddot{\boldsymbol{\xi}}_i = [0, \ddot{\eta}_i]^T \tag{3.31}$$

$\mathbf{X}_{cfi}$ could be related to $\mathbf{X}_{cR}$ as:

$$\mathbf{X}_{cfi} = \mathbf{X}_{cR} + \mathbf{R}_R \mathbf{x}_{ofi} \tag{3.32}$$

By submitting Eq. (3.32) into Eq. (3.28), $\mathbf{X}_{fi}$ could be expressed as:

$$\mathbf{X}_{fi} = \mathbf{X}_{cR} + \mathbf{R}_R \mathbf{x}_{ofi} + \mathbf{R}_{fi} \boldsymbol{\xi}_i \tag{3.33}$$

Here, $\mathbf{R}_{fi}$ is similar to $\mathbf{R}_R$, and is also the rotation matrix which converts the coordinate in local $s_i - w_i$ system to the global $X - Y$ system. The definitions of $\mathbf{R}_R$ and $\mathbf{R}_{fi}$ are of the form:

$$\mathbf{R}_j = \begin{bmatrix} \cos\theta_j & -\sin\theta_j \\ \sin\theta_j & \cos\theta_j \end{bmatrix} \tag{3.34}$$

where j indicates different local systems, i.e. R for rigid body; fA for beam A; fB for beam B. Their first and second order time derivatives, which will be used in the later derivation, are given as

$$\dot{\mathbf{R}}_j = \mathbf{R}_j \mathbf{U} \dot{\theta}_j \tag{3.35}$$

$$\ddot{\mathbf{R}}_j = \dot{\mathbf{R}}_j \mathbf{U} \dot{\theta}_j + \mathbf{R}_j \mathbf{U} \ddot{\theta}_j = -\mathbf{R}_j \dot{\theta}_j^2 + \mathbf{R}_j \mathbf{U} \ddot{\theta}_j \tag{3.36}$$

where $\mathbf{U}$ is introduced to simplify the derivation, and it is given by

$$\mathbf{U} = \begin{bmatrix} 0 & -1 \\ 1 & 0 \end{bmatrix} \tag{3.37}$$

From Eq. (3.34) and (3.37), it can be shown that:

$$\mathbf{R}_j\mathbf{R}_j^T = \mathbf{R}_j^T\mathbf{R}_j = \mathbf{U}\mathbf{U}^T = \mathbf{U}^T\mathbf{U} = \mathbf{I}_2 \tag{3.38}$$

$$\mathbf{U}\mathbf{U}^T = \mathbf{U}^T\mathbf{U} = \mathbf{I}_2 \tag{3.39}$$

where $\mathbf{I}_2$ is a 2×2 identity matrix. Using these formulations, the velocity and acceleration of each point on the rigid body or beam-like structure central line could be derived as:

$$\dot{\mathbf{X}}_R = \dot{\mathbf{X}}_{cR} + \dot{\mathbf{R}}_R\mathbf{x}_R = \dot{\mathbf{X}}cR + \mathbf{R}_R\mathbf{U}\dot{\theta}_R\mathbf{x}_R \tag{3.40}$$

$$\dot{\mathbf{X}}_{fi} = \dot{\mathbf{X}}_{cR} + \dot{\mathbf{R}}_R\mathbf{x}_{ofi} + \dot{\mathbf{R}}_{fi}\boldsymbol{\xi}_i + \mathbf{R}_{fi}\dot{\boldsymbol{\xi}}_i = \dot{\mathbf{X}}_{cR} + \mathbf{R}_R\mathbf{U}\dot{\theta}_R\mathbf{x}_{ofi} + \mathbf{R}_{fi}\mathbf{U}\dot{\theta}_{fi}\boldsymbol{\xi}_i + \mathbf{R}_{fi}\dot{\boldsymbol{\xi}}_i \tag{3.41}$$

$$\ddot{\mathbf{X}}_R = \ddot{\mathbf{X}}_{cR} + \ddot{\mathbf{R}}_R\mathbf{x}_R = \ddot{\mathbf{X}}_{cR} + (\mathbf{R}_R\mathbf{U}\ddot{\theta}_R - \mathbf{R}_R\dot{\theta}_R^2)\mathbf{x}_R \tag{3.42}$$

$$\begin{aligned}\ddot{\mathbf{X}}_{fi} =& \ddot{\mathbf{X}}_{cR} + \ddot{\mathbf{R}}_R\mathbf{x}_{ofi} + \ddot{\mathbf{R}}_{fi}\boldsymbol{\xi}_i + 2\dot{\mathbf{R}}_{fi}\dot{\boldsymbol{\xi}}_i + \mathbf{R}_{fi}\ddot{\boldsymbol{\xi}}_i \\ =& \ddot{\mathbf{X}}_{cR} + (\mathbf{R}_R\mathbf{U}\ddot{\theta}_R - \mathbf{R}_R\dot{\theta}_R^2)\mathbf{x}_{ofi} + (\mathbf{R}_{fi}\mathbf{U}\ddot{\theta}_{fi} - \mathbf{R}_{fi}\dot{\theta}_{fi}^2)\boldsymbol{\xi}_i + \\ & 2\mathbf{R}_{fi}\mathbf{U}\dot{\theta}_{fi}\dot{\boldsymbol{\xi}}_i + \mathbf{R}_{fi}\ddot{\boldsymbol{\xi}}_i\end{aligned} \tag{3.43}$$

In the computation, the perimeter of the whole structure is represented by a set of discrete points. Each point on the rigid-body part could be defined by Eq. (3.27), after the corresponding variables are obtained. For the beam-like structure part, Eq. (3.33) only gives the position of the points on its central line. The points on its perimeter are determined in the following way: The coordinates of each point is updated by linearly combining the rigid and flexible parts. For the rigid part, the position is simply determined as a normal rigid-body. The flexible deformation is updated based on the assumption that the beam is made up by multiple layers of materials and each layer will undergo the same deformation around its own central line. More specifically, for the points that are not on the beam central line, the flexible deformation is obtained by shifting the corresponding value from the layer that is on the beam central line.

3.2.2 Modal superposition approach

By using the modal superposition method mentioned in Section 3.1, the small elastic deflection part $\eta(s,t)$ for each beam could be represented as:

$$\eta(s,t) = \mathbf{\Phi}^T\mathbf{q} \tag{3.44}$$

where $\mathbf{\Phi}$ and $\mathbf{q}$ are the vectors of mode shape functions and the corresponding generalized coordinates. They are defined as follows:

$$\mathbf{\Phi} = [\phi_1(s), \phi_2(s), \cdots, \phi_N(s)]^T \tag{3.45}$$

$$\mathbf{q} = [q_1(t), q_2(t), \cdots, q_N(t)]^T \tag{3.46}$$

where N is the number of modes that has been taken into account. Separating the spatial and time variables in Eq. (3.44), the time derivatives of $\eta(s,t)$ could be further expressed as:

$$\dot{\eta} = \mathbf{\Phi}^T \dot{\mathbf{q}} \tag{3.47}$$

$$\ddot{\eta} = \mathbf{\Phi}^T \ddot{\mathbf{q}} \tag{3.48}$$

The mode shape functions are obtained based on the Euler beam equation with different boundary conditions by either analytical or numerical methods. Furthermore, the orthogonal relationships should also be satisfied, which is,

$$\int_f \mathbf{\Phi}\mathbf{\Phi}^T \rho_l ds = \mathbf{I}_N \tag{3.49}$$

$$\int (\frac{d^2\mathbf{\Phi}}{ds^2}) EJ (\frac{d^2\mathbf{\Phi}}{ds^2})^T ds = \mathbf{\Lambda}, \mathbf{\Lambda} = diag(\omega_k^2), \quad k = 1, 2, \cdots, N \tag{3.50}$$

where ω_k represents the k^{th} natural circular frequency of the beam, and E, ρ_l and J are Young's module, the line density and the 2^{nd} moment of the beam's cross section, respectively. $\mathbf{I}_N$ is the $N \times N$ identity matrix, where N is the number of modes that is used. The line integration is conducted along the neutral line of the beam. Unlike the general orthogonal relations in Eq. (3.9) and (3.10), in order to simplify the derivation in the following section, the mode function is normalized so that the integration in Eq. (3.49) is 1 for each frequency.

As mentioned in Section 3.1.3, introducing the modal superposition model makes it possible to use the generalized coordinates $\mathbf{q}$ to represent the flexible deformation of the beam. This would enable us to use the desirable orthogonal properties of Eq. (3.49) and (3.50) to further simplify the form of these equations in the following content.

Moreover, in order to simplify the equations derived in Section 3.2.3, the following definitions are introduced:

$$\mathbf{\Psi}_0 = [\psi_{01}, \psi_{02}, \psi_{03}, \cdots, \psi_{0N}] = \int \mathbf{\Phi} \rho_l ds \tag{3.51}$$

$$\mathbf{\Psi}_1 = [\psi_{11}, \psi_{12}, \psi_{13}, \cdots, \psi_{1N}] = \int s\mathbf{\Phi}\rho_l ds \tag{3.52}$$

In this work, two types of methods are used to obtain the mode shape function and the corresponding natural frequencies. For the uniform beam cases i.e. free floating beam on free surface and wedge with flexible bottoms (which will be shown in Chapter 6) the analytical solution could be solved based on the Euler beam equation and its corresponding boundary conditions, as shown in Eq. (3.20) and (3.16). The scaling factor C_d in these two equations is chosen as $C_d \equiv \frac{1}{\sqrt{M_f}}$ (where M_f is the mass of the beam) to be consistent with the orthogonality condition in Eq. (3.49) and (3.50). For the non-uniform beam case, i.e. the 46000*tones* oil ship in Section 6.3, the numerical approach called Myklestad's method is used instead. The details of the implementation of Myklestad's method is given in Appendix C and the result of the mode shape functions is given in Section 6.3.

3.2.3 General governing equations

Based on the discussion in Sections 3.2.1 and 3.2.2, the motion of the structure could be fully described by the generalised position variables $\mathbf{D}$ and the corresponding generalised force variables $\mathbf{Q}$ as follows:

$$\mathbf{D} = [\mathbf{X}_{cR}^T, \theta, \mathbf{q}_A^T, \mathbf{q}_B^T, \cdots]^T \tag{3.53}$$

$$\mathbf{Q} = [\mathbf{Q}_{X_{cR}}^T, Q_\theta, \mathbf{Q}_{qA}^T, \mathbf{Q}_{qB}^T, \cdots]^T \tag{3.54}$$

As shown in Eq. (3.24), θ_R and θ_{fi} are not independent to each other. Therefore for simplicity, the angle variable θ in $\mathbf{D}$ is selected to be the rigid rotational angle θ_R without affecting the structure of the formulations. Moreover, although the time derivatives of θ_R and θ_{fi} are the same (i.e., Eq. (3.25) and (3.26)), they are still annotated differently in the following derivations in order to show clearly the origin of each term. The variables $\mathbf{q}_i$ are the generalised coordinates for Beam A or Beam B, respectively, which are defined by Eq. (3.46).

The force variables $\mathbf{Q}_{X_{cR}}$,Q_θ and $\mathbf{Q}_{q_i}$ are non-conservative forces corresponding to the rigid-body motion part (i.e. $\mathbf{X}_{cR}$ and θ) and the elastic parts (i.e. $\mathbf{q}_i$), respectively. The vector type forces are defined as:

$$\mathbf{Q}_{X_{cR}} = [Q_{X_{cR}}, Q_{Y_{cR}}]^T \tag{3.55}$$

$$\mathbf{Q}_{qi} = [Q_{qi1}, Q_{qi2}, \cdots, Q_{qiN}]^T \tag{3.56}$$

According to the extended Hamilton's principle, the motion of the structure could be described by the following Lagrange's Equation:

$$\mathbf{Q}_{X_{cR}} = \frac{d}{dt}(\frac{\partial T}{\partial \dot{\mathbf{X}}_{cR}}) + \frac{\partial V}{\partial \mathbf{X}_{cR}} - \frac{\partial T}{\partial \mathbf{X}_{cR}} \tag{3.57}$$

$$Q_\theta = \frac{d}{dt}(\frac{\partial T}{\partial \dot{\theta}}) + \frac{\partial V}{\partial \theta} - \frac{\partial T}{\partial \theta} \tag{3.58}$$

$$\mathbf{Q}_{qi} = \frac{d}{dt}(\frac{\partial T}{\partial \dot{\mathbf{q}}_i}) + \frac{\partial V}{\partial \mathbf{q}_i} - \frac{\partial T}{\partial \mathbf{q}_i} \tag{3.59}$$

where T and V are kinetic and potential energies of the whole structure, respectively. The kinetic energies for the rigid body (T_R), flexible (T_{fi}) beams and the whole structure are given by:

$$T_{fi} = \frac{1}{2}\int_{fi} \dot{\mathbf{X}}_{fi}^T \rho_l \dot{\mathbf{X}}_{fi} ds \tag{3.60}$$

$$T_R = \frac{1}{2}\int_R \dot{\mathbf{X}}_R^T \rho \dot{\mathbf{X}}_R dx dy \tag{3.61}$$

$$T = T_R + \sum_i T_{fi} \tag{3.62}$$

For the potential energies, they are given by:

$$V_R = M_R g Y_{cR} \tag{3.63}$$

$$\begin{aligned} V_{fi} &= \frac{1}{2}\int_{fi} \frac{d^2\eta_{fi}}{ds^2} E_i J_i \frac{d^2\eta_{fi}}{ds^2} ds + M_{fi} g Y_{cfi} \\ &= \frac{1}{2}\mathbf{q}_i^T (\int_{fi} (\frac{d^2\mathbf{\Phi}_i}{ds^2}) E_i J_i (\frac{d^2\mathbf{\Phi}_i}{ds^2})^T ds)\mathbf{q}_i + M_{fi} g Y_{cfi} \\ &= \frac{1}{2}\mathbf{q}_i^T \mathbf{\Lambda}_i \mathbf{q}_i + M_{fi} g (Y_{cR} + \sin\theta_R x_{ofi} + \cos\theta_R y_{ofi}) \end{aligned} \tag{3.64}$$

$$V = V_R + \sum_i V_{fi} \tag{3.65}$$

where V_R and V_{fi} are the rigid body and flexible beams potential energies, respectively, and M_R and M_{fi} are the masses for the corresponding parts.

The generalised forces corresponding to the rigid-body motion (i.e. $\mathbf{X}_{cR}$ and θ) and the elastic ones (i.e., $\mathbf{q}_i$) could be determined using the virtual work principle. This is achieved by establishing an equation that the virtual work done by the generalised forces should be equal to the one done by active external

non-conservative forces through generalised virtual displacements. In this work, we assume that the whole structure is subject to distributed pressure p only (e.g. water pressure). As no concentrated force or moment is applied on it, the following equations are obtained:

$$\delta \mathbf{X}_{cR}^T \mathbf{Q}_{X_{cR}} = \delta \mathbf{X}_{cR}^T \oint_{all} (p\mathbf{n}) dl \tag{3.66}$$

$$\delta\theta Q_\theta = \delta\theta \oint_{all} p(X_p n_y - Y_p n_x) dl \tag{3.67}$$

$$\delta \mathbf{q}_i^T \mathbf{Q}_{q_i} = \oint_{fi} [(p\mathbf{n}) \cdot \mathbf{e}_{iw}] \delta\eta_{fi} dl = \delta \mathbf{q}_i^T \oint_{fi} [(p\mathbf{n}) \cdot \mathbf{e}_{iw}] \mathbf{\Phi}_i dl \tag{3.68}$$

where $\mathbf{n} = [n_x, n_y]^T$ is the unit normal vector of points on the perimeter of the whole surface, which points towards the interior structural domain (i.e., outside the fluid domain if fluid is in the vicinity). $\mathbf{X}_p = [X_p, Y_p]^T$ are the vectors pointing from O_R to the points on the perimeter of the whole structure, and $\mathbf{e}_{iw} = [e_{iw1}, e_{iw2}]^T$ is the unit vector of the w_i direction. All these vectors are represented in the global $X - Y$ system. The integrations with subscripts *all* or fi mean that the calculations are conducted on the perimeter of the whole structure or just on the corresponding beams.

Thus, the generalised forces are:

$$\mathbf{Q}_{X_{cR}} = \oint_{all} p\mathbf{n} dl \tag{3.69}$$

$$Q_\theta = \oint_{all} p(X_p n_y - Y_p n_x) dl \tag{3.70}$$

$$Q_{q_i} = \oint_{fi} [(p\mathbf{n}) \cdot \mathbf{e}_{iw}] \mathbf{\Phi}_i dl \tag{3.71}$$

Substituting T, V, $\mathbf{Q}_{X_{cR}}$, Q_θ and $\mathbf{Q}_{q_i}$ into the Lagrange equation, the governing equations for the coupled rigid-body and flexible beams system become (after some tedious derivations using the chain rule):

$$\begin{aligned}
&\sum_i \int_{fi} (\ddot{\mathbf{X}}_{CR} - \mathbf{R}_R \dot{\theta}_R^2 \mathbf{x}_{ofi} + \mathbf{R}_R \mathbf{U} \ddot{\theta}_R \mathbf{x}_{ofi} - \mathbf{R}_{fi} \dot{\theta}_{fi}^2 \boldsymbol{\xi}_i + \mathbf{R}_{fi} \mathbf{U} \ddot{\theta}_{fi} \boldsymbol{\xi}_i + 2\mathbf{R}_{fi} \mathbf{U} \dot{\theta}_{fi} \dot{\boldsymbol{\xi}}_i + \mathbf{R}_{fi} \ddot{\boldsymbol{\xi}}_i) \rho_l ds \\
&+ \iint_R (\ddot{X}_{cR} - \mathbf{R}_R \dot{\theta}_R^2 \mathbf{x}_R + \mathbf{R}_R \mathbf{U} \ddot{\theta}_R \mathbf{x}_R) \rho dx dy + (M_R + \sum_i M_{fi}) g \begin{bmatrix} 0 \\ 1 \end{bmatrix} = \mathbf{Q}_{X_{cR}}
\end{aligned} \tag{3.72}$$

$$\sum_i \int_{fi} (\ddot{\mathbf{X}}_{cR}^T + \ddot{\theta}_R \mathbf{x}_{ofi}^T \mathbf{U}^T \mathbf{R}_R^T - \dot{\theta}_R^2 \mathbf{x}_{ofi}^T \mathbf{R}_R^T + \ddot{\theta}_{fi} \boldsymbol{\xi}_i^T \mathbf{U}^T \mathbf{R}_{fi}^T + 2\dot{\theta}_{fi} \dot{\boldsymbol{\xi}}_i^T \mathbf{U}^T \mathbf{R}_{fi}^T - \dot{\theta}_{fi}^2 \boldsymbol{\xi}_i^T \mathbf{R}_{fi}^T + \ddot{\boldsymbol{\xi}}_i^T \mathbf{R}_{fi}^T)$$
$$(\mathbf{R}_R \mathbf{U} \mathbf{x}_{ofi} + \mathbf{R}_{fi} \mathbf{U} \boldsymbol{\xi}_i) \rho_l ds + \iint_R (\ddot{X}_{cR}^T - \dot{\theta}_R^2 \mathbf{x}_R^T \mathbf{R}_R^T + \ddot{\theta}_R \mathbf{x}_R^T \mathbf{U}^T \mathbf{R}_R^T)(\mathbf{R}_R \mathbf{U} \mathbf{x}_R) \rho dx dy +$$
$$\sum_i M_{fi} (\cos\theta_R x_{ofi} - \sin\theta_R y_{ofi}) = Q_\theta \tag{3.73}$$

$$\int_{fi} (\ddot{\mathbf{X}}_{cR}^T + \ddot{\theta}_R \mathbf{x}_{ofi}^T \mathbf{U}^T \mathbf{R}_R^T - \dot{\theta}_R^2 \mathbf{x}_{ofi}^T \mathbf{R}_R^T + \ddot{\theta}_{fi} \boldsymbol{\xi}_i^T \mathbf{U}^T \mathbf{R}_{fi}^T + 2\dot{\theta}_{fi} \boldsymbol{\xi}_i^T \mathbf{U}^T \mathbf{R}_{fi}^T - \dot{\theta}_{fi}^2 \boldsymbol{\xi}^T \mathbf{R}_{fi}^T + \ddot{\boldsymbol{\xi}}_i^T \mathbf{R}_{fi}^T)$$
$$(\mathbf{R}_{fi} \begin{bmatrix} 0 \\ 1 \end{bmatrix} \boldsymbol{\Phi}_i) \rho_l ds + \boldsymbol{\Lambda}_i \mathbf{q}_i = \mathbf{Q}_{qi} \tag{3.74}$$

For the rigid body part, the following integrations hold:

$$\iint_R \rho dx dy = M_R \tag{3.75}$$

$$\iint_R \rho \mathbf{R}_R \mathbf{x}_R dx dy = 0 \tag{3.76}$$

$$\iint_R \mathbf{x}_R^T \mathbf{x}_R \rho dx dy = I_R \tag{3.77}$$

which also means:

$$\iint_R \rho \mathbf{R}_R \mathbf{U} \mathbf{x}_R dx dy = 0 \tag{3.78}$$

where I_R is the rotational inertia of the rigid body. The integration for the rigid-body part could be simplified as:

$$\iint_R (\ddot{\mathbf{X}}_{cR} - \mathbf{R}_R \dot{\theta}_R^2 \mathbf{x}_R + \mathbf{R}_R \mathbf{U} \ddot{\theta}_R \mathbf{x}_R \rho) dx dy$$
$$= \ddot{\mathbf{X}}_{cR} \iint_R \rho dx dy - \dot{\theta}_R^2 \iint_R \rho \mathbf{R}_R \mathbf{x}_R dx dy + \ddot{\theta}_R \iint_R \rho \mathbf{R}_R \mathbf{U} \mathbf{x}_R dx dy = M_R \ddot{\mathbf{X}}_{cR} \tag{3.79}$$

$$\iint_R (\ddot{\mathbf{X}}_{cR}^T - \dot{\theta}_R^2 \mathbf{x}_R^T \mathbf{R}_R^T + \ddot{\theta}_R \mathbf{x}_R^T \mathbf{U}^T \mathbf{R}_R^T)(\mathbf{R}_R \mathbf{U} \mathbf{x}_R) \rho dx dy = \ddot{\mathbf{X}}_{cR}^T \iint_R \rho \mathbf{R}_R \mathbf{U} \mathbf{x}_R dx dy$$
$$+ \ddot{\theta}_R \iint_R \mathbf{x}_R^T \mathbf{U}^T \mathbf{R}_R^T \mathbf{R}_R \mathbf{U} \mathbf{x}_R \rho dx dy - \dot{\theta}_R^2 \iint_R \mathbf{x}_R^T \mathbf{R}_R^T \mathbf{R}_R \mathbf{U} \mathbf{x}_R \rho dx dy = I_R \ddot{\theta}_R \tag{3.80}$$

Finally, by substituting Eq. (3.79) and (3.80) into Eq. (3.72) to (3.74), the governing equations for the whole structure become:

$$\sum_i \int_{fi} (\ddot{\mathbf{X}}_{CR} - \mathbf{R}_R \dot{\theta}_R^2 \mathbf{x}_{ofi} + \mathbf{R}_R \mathbf{U} \ddot{\theta}_R \mathbf{x}_{ofi} - \mathbf{R}_{fi} \dot{\theta}_{fi}^2 \boldsymbol{\xi}_i + \mathbf{R}_{fi} \mathbf{U} \ddot{\theta}_{fi} \boldsymbol{\xi}_i + 2\mathbf{R}_{fi} \mathbf{U} \dot{\theta}_{fi} \dot{\boldsymbol{\xi}}_i + \mathbf{R}_{fi} \ddot{\boldsymbol{\xi}}_i) \rho_l ds + M_R \ddot{\mathbf{X}}_{cR} + (M_R + \sum_i M_{fi}) g \begin{bmatrix} 0 \\ 1 \end{bmatrix} = \mathbf{Q}_{X_{cR}} \tag{3.81}$$

$$\sum_i \int_{fi} (\ddot{\mathbf{X}}_{cR}^T + \ddot{\theta}_R \mathbf{x}_{ofi}^T \mathbf{U}^T \mathbf{R}_R^T - \dot{\theta}_R^2 \mathbf{x}_{ofi}^T \mathbf{R}_R^T + \ddot{\theta}_{fi} \boldsymbol{\xi}_i^T \mathbf{U}^T \mathbf{R}_{fi}^T + 2\dot{\theta}_{fi} \dot{\boldsymbol{\xi}}_i^T \mathbf{U}^T \mathbf{R}_{fi}^T - \dot{\theta}_{fi}^2 \boldsymbol{\xi}_i^T \mathbf{R}_{fi}^T + \ddot{\boldsymbol{\xi}}_i^T \mathbf{R}_{fi}^T)(\mathbf{R}_R \mathbf{U} \mathbf{x}_{ofi} \mathbf{R}_{fi} \mathbf{U} \boldsymbol{\xi}_i) \rho_l ds + I_R \ddot{\theta}_R + \sum_i M_{fi} (\cos\theta_R x_{ofi1} - \sin\theta_R x_{ofi2}) = Q_\theta \tag{3.82}$$

$$\int_{fi} (\ddot{\mathbf{X}}_{cR}^T + \ddot{\theta}_R \mathbf{x}_{ofi}^T \mathbf{U}^T \mathbf{R}_R^T - \dot{\theta}_R^2 \mathbf{x}_{ofi}^T \mathbf{R}_R^T + \ddot{\theta}_{fi} \boldsymbol{\xi}_i^T \mathbf{U}^T \mathbf{R}_{fi}^T + 2\dot{\theta}_{fi} \dot{\boldsymbol{\xi}}_i^T \mathbf{U}^T \mathbf{R}_{fi}^T - \dot{\theta}_{fi}^2 \boldsymbol{\xi}^T \mathbf{R}_{fi}^T + \ddot{\boldsymbol{\xi}}_i^T \mathbf{R}_{fi}^T)(\mathbf{R}_{fi} \begin{bmatrix} 0 \\ 1 \end{bmatrix} \boldsymbol{\Phi}_i) \rho_l ds + \boldsymbol{\Lambda}_i \mathbf{q}_i = \mathbf{Q}_{qi} \tag{3.83}$$

3.2.3.1 Rigid-body

If the object under consideration is just a rigid body, all the integrations corresponding to flexible beams in the above general governing equations would vanish. This means the final equations would simply reduce to the following form:

$$M_R \ddot{\mathbf{X}}_{cR} + M_R g \begin{bmatrix} 0 \\ 1 \end{bmatrix} = \mathbf{Q}_{X_{cR}} \tag{3.84}$$

$$I_R \ddot{\theta}_R = Q_\theta \tag{3.85}$$

These equations are obviously identical to the classical rigid-body dynamics results, as expected.

3.2.3.2 Floating flexible beam

The case of a floating flexible beam is studied in this section. The beam assumption is a common practice in marine engineering when describing the overall Hydroelasticity property of a ship structure. However, as mentioned

before, the traditional Hydroelasticity theory actually performs the calculation in the way that rigid-body motion and flexible deformation are calculated separately without considering the mutual interaction effect, i.e. first computing the overall motion with rigid-body assumption and then calculating the flexible deformation with modal superposition technique based on the fluid force from rigid-body computation. The model proposed here provides the possibility to compute the coupled effect of rigid-body and flexible motions. As shown in

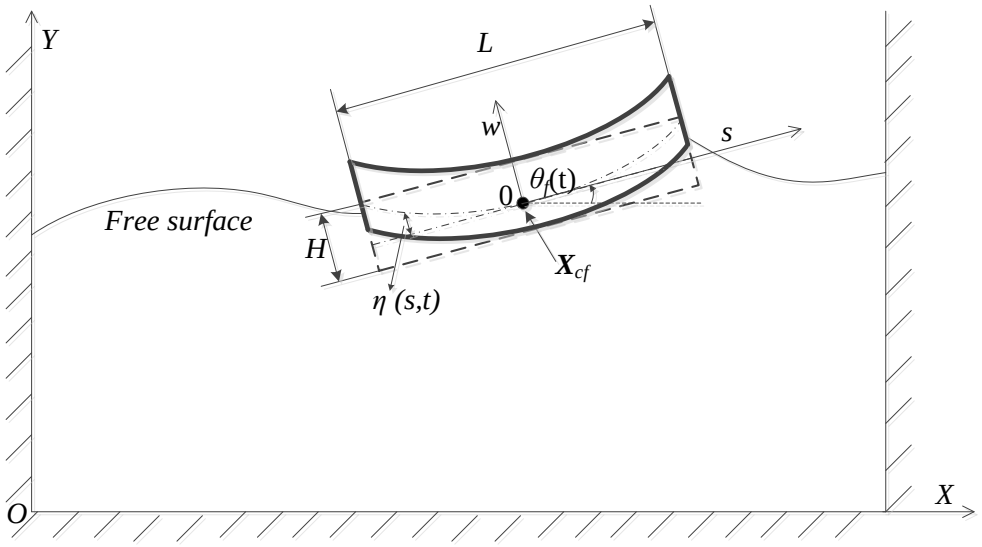

Figure 3.3: Sketch of the flexible floating beam system

Figure 3.3, there is only one flexible beam in this case. The subscript $i(i = A, B)$, which indicates different beams, could be omitted in the above equations. Furthermore, since the purely rigid body part does not exist in this case, the rigid-body system $x_R - y_R$ and flexible beam system $x_f - y_f$ coincide with each other, which lead to the following relations:

$$\begin{cases} \mathbf{x}_{of} \equiv \mathbf{0} \\ \theta_R \equiv \theta_f \\ \mathbf{R}_R \equiv \mathbf{R}_f \\ \mathbf{X}_{cR} \equiv \mathbf{X}_{cf} \end{cases} \tag{3.86}$$

Substituting the above relations into the general governing equations Eq. (3.81) to (3.83), lead to the following simplified expression for this case:

$$\int_f (\ddot{\mathbf{X}}_{cf} - \mathbf{R}_f\dot{\theta}_f^2\boldsymbol{\xi} + \mathbf{R}_f\mathbf{U}\ddot{\theta}_f\boldsymbol{\xi} + 2\mathbf{R}_f\mathbf{U}\dot{\theta}_f\dot{\boldsymbol{x}}\boldsymbol{i} + \mathbf{R}_f\ddot{\boldsymbol{\xi}})\rho_l ds + M_f g \begin{bmatrix} 0 \\ 1 \end{bmatrix} = \mathbf{Q}_{X_{cf}} \tag{3.87}$$

$$\int_f (\ddot{\mathbf{X}}_{cf}^T + \ddot{\theta}_f\boldsymbol{\xi}^T\mathbf{U}^T\mathbf{R}_f^T + 2\dot{\theta}_f\dot{\boldsymbol{\xi}}_f\dot{\boldsymbol{\xi}}^T\mathbf{U}^T\mathbf{R}_f^T - \dot{\theta}_f^2\boldsymbol{\xi}^T\mathbf{R}_f^T + \ddot{\boldsymbol{\xi}}^T\mathbf{R}_f^T)(\mathbf{R}_f\mathbf{U}\boldsymbol{\xi})\rho_l ds = Q_\theta \tag{3.88}$$

$$\int_f (\ddot{\mathbf{X}}_{cf}^T + \ddot{\theta}_f\boldsymbol{\xi}^T\mathbf{U}^T\mathbf{R}_f^T + 2\dot{\theta}_f\dot{\boldsymbol{\xi}}_f\mathbf{U}^T\mathbf{R}_f^T - \dot{\theta}_f^2\boldsymbol{\xi}^T\mathbf{R}_f^T + \ddot{\boldsymbol{\xi}}^T\mathbf{R}_f^T)(\mathbf{R}_f \begin{bmatrix} 0 \\ 1 \end{bmatrix} \boldsymbol{\Phi})\rho_l ds + \boldsymbol{\Lambda}\mathbf{q} = \mathbf{Q}_q \tag{3.89}$$

Considering that the local coordinate centre is also the mass centre and its symmetry property about w and s axis, the following relationships hold:

$$\int \rho_l ds = M_f \tag{3.90}$$

$$\int s\rho_l ds = 0 \tag{3.91}$$

$$\int s^2\rho_l ds = I_f \tag{3.92}$$

$$\int \eta^2\rho_l ds = \iint (\boldsymbol{\Phi}^T\mathbf{q})(\boldsymbol{\Phi}^T\mathbf{q})\rho_l ds = \mathbf{q}^T[\int \boldsymbol{\Phi}\rho_l\boldsymbol{\Phi}^T ds]\mathbf{q} = \mathbf{q}^T\mathbf{I}\mathbf{q} = \mathbf{q}^T\mathbf{q} \tag{3.93}$$

$$\int \eta\dot{\eta}\rho_l ds = \int (\boldsymbol{\Phi}^T\mathbf{q})(\boldsymbol{\Phi}^T\dot{\mathbf{q}})\rho_l ds = \mathbf{q}^T\dot{\mathbf{q}} \tag{3.94}$$

where $I_f = M_f(L^2 + H^2)/12$ is the rotation inertia of the beam about mass centre.

If the mode function is chosen up to third-order, and by substituting the above relationships into Eq. (3.87) to (3.89), the governing equations finally become:

$$\begin{aligned} &M_f\ddot{X}_{cR} + \dot{\theta}_f^2\sin\theta_f(\psi_{01}q_1 + \psi_{02}q_2 + \psi_{03}q_3) - 2\dot{\theta}_f\cos\theta_f(\psi_{01}\dot{q}_1 + \psi_{02}\dot{q}_2\psi_{03}\dot{q}_3) \\ &- \ddot{\theta}_f\cos\theta_f(\psi_{01}q_1 + \psi_{02}q_2 + \psi_{03}q_3) - \sin\theta_f(\psi_{01}\ddot{q}_1 + \psi_{02}\ddot{q}_2 + \psi_{03}\ddot{q}_3) = Q_{X_{cR}} \end{aligned} \tag{3.95}$$

$$\begin{aligned} &M_f\ddot{Y}_{cR} - \dot{\theta}_f^2\cos\theta_f(\psi_{01}q_1 + \psi_{02}q_2 + \psi_{03}q_3) - 2\dot{\theta}_f\sin\theta_f(\psi_{01}\dot{q}_1 + \psi_{02}\dot{q}_2\psi_{03}\dot{q}_3) \\ &- \ddot{\theta}_f\sin\theta_f(\psi_{01}q_1 + \psi_{02}q_2 + \psi_{03}q_3) + \cos\theta_f(\psi_{01}\ddot{q}_1 + \psi_{02}\ddot{q}_2 + \psi_{03}\ddot{q}_3) + M_f g = Q_{Y_{cR}} \end{aligned} \tag{3.96}$$

$$-(\ddot{X}_{cR}\cos\theta_f+\ddot{Y}_{cR}\sin\theta_f)(\psi_{01}q_1+\psi_{02}q_2+\psi_{03}q_3)+I_f\ddot{\theta}_f+\ddot{\theta}_f(q_1^2+q_2^2+q_3^2)$$
$$+2\dot{\theta}_f(\dot{q}_1q_1+\dot{q}_2q_2+\dot{q}_3q_3)+(\psi_{11}\ddot{q}_1+\psi_{12}\ddot{q}_2+\psi_{13}\ddot{q}_3)=Q_\theta \tag{3.97}$$

$$[-\ddot{X}_{cR}\sin\theta_f+\ddot{Y}_{cR}\cos\theta_f]\psi_{01}+\psi_{11}\ddot{\theta}_f-\dot{\theta}_f^2q_1+\ddot{q}_1+\omega_1^2q_1=Q_{q_1} \tag{3.98}$$

$$[-\ddot{X}_{cR}\sin\theta_f+\ddot{Y}_{cR}\cos\theta_f]\psi_{02}+\psi_{12}\ddot{\theta}_f-\dot{\theta}_f^2q_2+\ddot{q}_2+\omega_2^2q_2=Q_{q_2} \tag{3.99}$$

$$[-\ddot{X}_{cR}\sin\theta_f+\ddot{Y}_{cR}\cos\theta_f]\psi_{03}+\psi_{13}\ddot{\theta}_f-\dot{\theta}_f^2q_3+\ddot{q}_3+\omega_3^2q_3=Q_{q_3} \tag{3.100}$$

where Q_{q_1}, $Q_{q_2}$and Q_{q_3} are the three components in Eq. (3.71), corresponding to the three modes. As can be seen, there are several non-linear terms in each of these equations, which represent the interaction effect between rigid-body motion and flexible deformation. This set of equations is then solved at each FSI iterations using Newmark method [110] and Newton-Raphson methods. The detailed procedure of the solution process is given in the Appendix A.

3.2.3.3 Symmetric flexible wedge

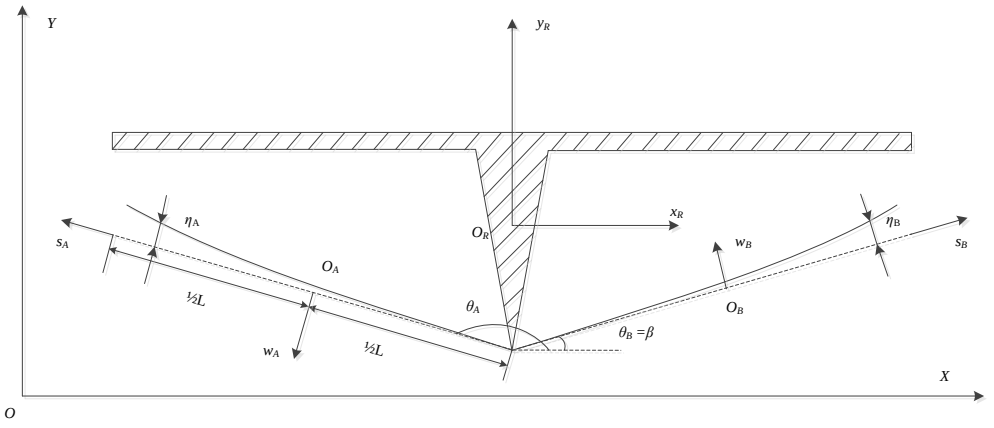

Figure 3.4: Sketch of the wedge with flexible bottom

In this part, the case of a 2D wedge with flexible bottom vertically and freely dropping into water is investigated. The wedge model is shown in Figure 3.4. Both of the bottoms are fixed at the junction point on the wedge top and free at the other ends. The bottoms are flexible whereas the other parts are treated as rigid body. Both of the two bottom beams have the same mass, which is defined as M_f, i.e.:

$$M_{fA}=M_{fB}=M_f \tag{3.101}$$

The symmetric property will make the dropping motion only occurs in the vertical direction and always perpendicular to the calm water surface, which means there would be no rotational motion during the dropping. Therefore, all the time derivatives of the angular variables are all zeros, i.e.:

$$\dot{\theta}_R = \ddot{\theta}_R = \dot{\theta}_{fA} = \ddot{\theta}_{fA} = \dot{\theta}_{fB} = \ddot{\theta}_{fB} = 0 \tag{3.102}$$

These angular conditions make all the angle-related terms in the general governing equations to be zeros. Moreover, the equation corresponding to angular motion (Eq. (3.82)) is not included since the angular variables are constants. As a result, the simplified governing equations for this case become:

$$\sum_i \int_{fi} (\ddot{\mathbf{X}}_{cR} + \mathbf{R}_{fi}\ddot{\boldsymbol{\xi}}_i)\rho_l ds + M_R\ddot{\mathbf{X}}_{cR} + (M_R + \sum_i M_{fi})g \begin{bmatrix} 0 \\ 1 \end{bmatrix} = \mathbf{Q}_{X_{cR}} \tag{3.103}$$

$$\sum_i \int_{fi} (\ddot{\mathbf{X}}_{cR} + \ddot{\boldsymbol{\xi}}_i^T \mathbf{R}_{fi}^T)(\mathbf{R}_{fi} \begin{bmatrix} 0 \\ 1 \end{bmatrix} \boldsymbol{\Phi}_i)\rho_l ds + \boldsymbol{\Lambda}_i \mathbf{q}_i = \mathbf{Q}_{q_i} \tag{3.104}$$

To simplify further the forms of these equations, the following relations between θ_{fA} and θ_{fB}, which are derived from the symmetric configuration of the wedge, are used to expand the vectors and matrices in the above equations, i.e.

$$\sin(\theta_{fA}) = \sin(\pi - \theta_{fB}) = \sin(\theta_{fB}) \tag{3.105}$$

$$\cos(\theta_{fA}) = \cos(\pi - \theta_{fB}) = -\cos(\theta_{fB}) \tag{3.106}$$

Moreover, the vertical motion constraint also means the wedge should be motionless in the horizontal direction, i.e.:

$$X_{cR} = \dot{X}_{cR} = \ddot{X}_{cR} = 0 \tag{3.107}$$

As the wedge is symmetric about the y_R axis and the entry speed is perpendicular to the free surface, the flexible deformation of the two bottom beams will have the same absolute amount but opposite direction when measured in their corresponding local $x_f i - y_f i$ coordinate system. Therefore, if the mode functions for the left beam $\boldsymbol{\Phi}_A$ are chosen to be the opposite ones of the right beam $\boldsymbol{\Phi}_B$, i.e.:

$$\boldsymbol{\Phi}_B = -\boldsymbol{\Phi}_A = \boldsymbol{\Phi} \tag{3.108}$$

where $\mathbf{\Phi}$ is the is the vector of the mode function defined by Eq. (3.20), then the generalised coordinates $\mathbf{q}_i$ would be identical for both sides, that is,

$$\mathbf{q}_A = \mathbf{q}_B \tag{3.109}$$

Substituting Eq. (3.108) and (3.109) into Eq. (3.71) (for the calculation of $\mathbf{Q}_{q_i}$), and considering the water pressure $(-p\mathbf{n})$ pointing in the same and opposite direction of w_i for Beam A ($\mathbf{e}_{Aw}$) and Beam B ($\mathbf{e}_{Bw}$), respectively (i.e. $(p\mathbf{n}) \cdot \mathbf{e}_{Aw}$ and $(p\mathbf{n}) \cdot \mathbf{e}_{Bw}$ would be of the opposite sign), then the value of the generalized force $\mathbf{Q}_{q_i}$ for both of the two beams would be the same, i.e.:

$$\mathbf{Q}_{q_A} = \mathbf{Q}_{q_B} \tag{3.110}$$

After substituting the above relations, the final governing equations for the flexible wedge dropping problem are:

$$(2M_f + M_R)\ddot{Y}_{cR} + 2\cos\theta(\psi_{01}\ddot{q}_1 + \psi_{02}\ddot{q}_2 + \psi_{03}\ddot{q}_3) + (2M_f + M_R)g = Q_{Y_{cR}} \tag{3.111}$$

$$\ddot{Y}_{cR}\cos\theta\psi_{01} + \ddot{q}_1 + \omega_1^2 q_1 = Q_{q_1} \tag{3.112}$$

$$\ddot{Y}_{cR}\cos\theta\psi_{02} + \ddot{q}_2 + \omega_2^2 q_2 = Q_{q_2} \tag{3.113}$$

$$\ddot{Y}_{cR}\cos\theta\psi_{03} + \ddot{q}_3 + \omega_3^2 q_3 = Q_{q_3} \tag{3.114}$$

where the subscript $i (i = A, B)$ (which is used for indicating different beams in $\mathbf{q}_i$, ψ_{i0}, ψ_{i1} and $\mathbf{Q}_{q_i}$) is omitted based on the equivalent conditions aforementioned. What is worth mentioning is that the angle θ and mode function vector $\mathbf{\Phi}$ are chosen to be the value of beam B, although the structure of these equations would be the same if they are chosen from beam A. As before, this set of equations is also solved by coupled Newmark and Newton-Raphson methods. The detailed formulation is given in AppendixA.

3.3 FSI coupling scheme

The interaction between the structure and fluid is computed in an iterative way. The Gauss-Seidel method with Aitken relaxation approach is adopted in this study.

More specifically, we suppose that all the fluid and structure variables are known at $t = t_{(k-1)}$. Then, the detailed process of interaction for next time step at $t = t_k$ is illustrated as follows:

1) Based on the assumption that the acceleration of the structure motion at $t = t_k$ is the same as in the previous time step, i.e. $\ddot{\mathbf{D}}^k = \ddot{\mathbf{D}}^{(k-1)}$, the position $\mathbf{D}^k$ and velocity $\dot{\mathbf{D}}^k$ at $t = t_k$ can be calculated accordingly by the normal finite difference approach.

Then by using Eq. (3.27), (3.28) and Eq. (3.40) to (3.43), the corresponding position, velocity and acceleration values of each points on the fluid structure interface, i.e. $\mathbf{\Gamma}^k_{fsi,0}$, $\dot{\mathbf{\Gamma}}^k_{fsi,0}$ and $\ddot{\mathbf{\Gamma}}^k_{fsi,0}$ could be calculated from these newly predicted kinetic values. The index number in the subscript represent the sequence number of iteration.

2) Using the updated kinetic information of interface as a new boundary condition, calculate the fluid motion at $t = t_k$, by the modified MPS method. Then, obtain the new pressure $p^k_{fsi,i+1}$ applied on the interface for i^{th} iteration at $t = t_k$.

3) Use the new fluid pressure $p^k_{fsi,i+1}$ to update the structure position, velocity and acceleration by the structural model for $t = t_k$, i.e.,$\tilde{\mathbf{D}}^k_{i+1}$, $\dot{\tilde{\mathbf{D}}}^k_{i+1}$ and $\ddot{\tilde{\mathbf{D}}}^k_{i+1}$. Then, find the corresponding kinetic values $\tilde{\mathbf{\Gamma}}^k_{fsi,i+1}$, $\dot{\tilde{\mathbf{\Gamma}}}^k_{fsi,i+1}$ and $\ddot{\tilde{\mathbf{\Gamma}}}^k_{fsi,i+1}$ of the points on the interface (by Eq. (3.27), (3.28) and (3.40) to (3.43) in Section 3.2.1).

4) Check the difference between $\tilde{\mathbf{\Gamma}}^k_{fsi,i+1}$ and $\mathbf{\Gamma}^k_{fsi,i}$. If the convergence condition

$$|\tilde{\mathbf{\Gamma}}^k_{fsi,i+1} - \mathbf{\Gamma}^k_{fsi,i}| \leq \epsilon \tag{3.115}$$

is satisfied, then go to step (1) to continue the computation for the next time step ($t = t_{(k+1)}$). Otherwise, correct the structure position $\mathbf{D}^k_{i+1}$ for $(i+1)^{th}$ iteration using Eq. (3.116):

$$\mathbf{D}^k_{i+1} = \chi_i \tilde{\mathbf{D}}^k_{i+1} + (1 - \chi_i)\mathbf{D}^k_i \tag{3.116}$$

and update the velocity $\dot{\mathbf{D}}^k_{i+1}$ and acceleration $\ddot{\mathbf{D}}^k_{i+1}$ by Newmark method (see Appendix A). The corresponding interface variables $\mathbf{\Gamma}^k_{fsi,i+1}$, $\dot{\mathbf{\Gamma}}^k_{fsi,i+1}$ and $\ddot{\mathbf{\Gamma}}^k_{fsi,i+1}$ are then calculated according to $\mathbf{D}^k_{i+1}$, $\dot{\mathbf{D}}^k_{i+1}$ and $\ddot{\mathbf{D}}^k_{i+1}$.

Using these corrected interface information, conduct $(i+1)^{th}$ iteration by going back to step (2). The total number of iteration is limited to 20 times in this study.

In Eq. (3.116), χ_i is the Aitken relaxation factor [76]. The central idea is to improve the accuracy of predication by using two previous iterations. Its value

is calculated by the following equation:

$$\chi_i = -\chi_{i-1} \frac{(\Delta \mathbf{\Gamma}^k_{fsi,i})^T (\Delta \mathbf{\Gamma}^k_{fsi,i+1} - \Delta \mathbf{\Gamma}^k_{fsi,i})}{(\Delta \mathbf{\Gamma}^k_{fsi,i+1} - \Delta \mathbf{\Gamma}^k_{fsi,i})^T (\Delta \mathbf{\Gamma}^k_{fsi,i+1} - \Delta \mathbf{\Gamma}^k_{fsi,i})} \tag{3.117}$$

in which $\Delta \mathbf{\Gamma}^k_{fsi,j} = \tilde{\mathbf{\Gamma}}^k_{fsi,j} - \mathbf{\Gamma}^k_{fsi,j-1}$. The initial value for first iteration of each time is chosen to be 0.2.

The whole procedure is illustrated in Figure 3.5.

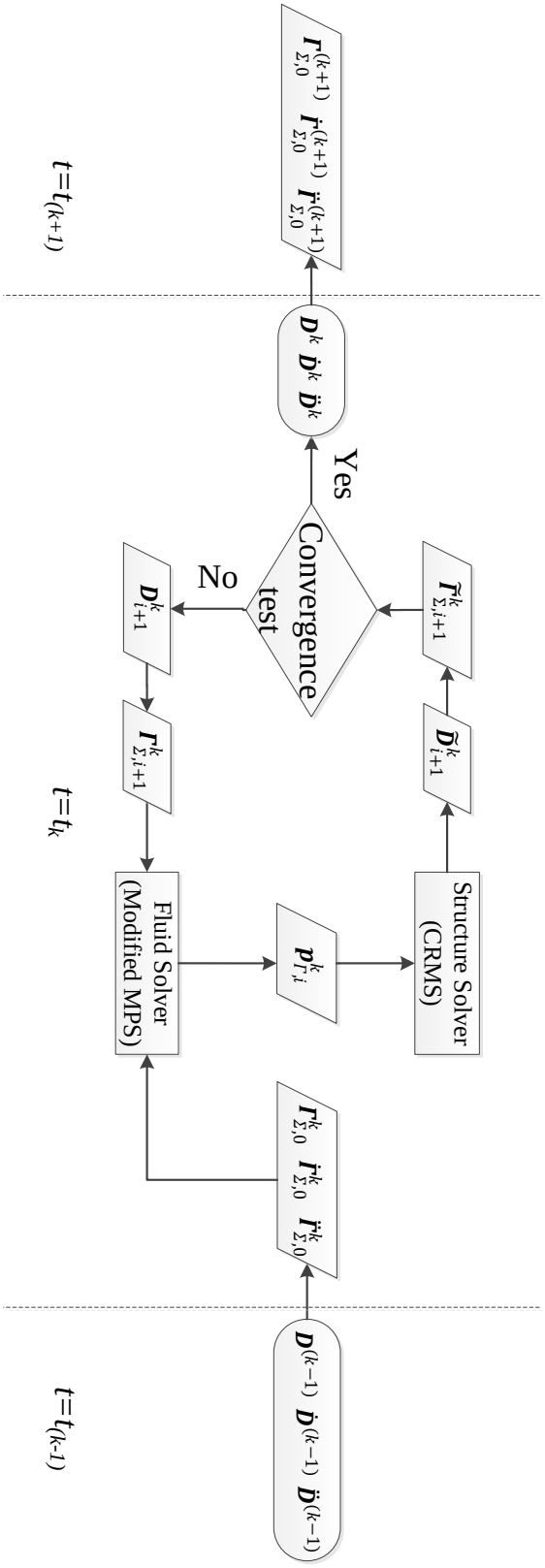

Figure 3.5: Flow chart of the iterative process of fluid structure interaction

Chapter 4

Validation of modified MPS

In this Chapter, the modifications of the MPS method proposed in Chapter 2 will be validated using 2D Dam-break problem with various boundary conditions. The aspects that will be checked include efficiency improvement of the new neighbor particle searching strategy, pressure computation and the impact load on the structures, and the mass conservation convergence properties. The flow evaluation and pressure results will be validated against the experimental results published in the literuture.

4.1 Efficiency test of the new neighbor particle searching

The efficiency of the new proposed and traditional neighbour particle searching strategies are tested and compared, using the 2D dam-break problem with different particle numbers.

Basically, the neighbour search requires two times neighbour searching in each time step for the particle method, as the particle distribution will change twice, i.e. advancing particle positions to the intermediate stage (Eq. (2.3)) without considering pressure, and then update the particle position using the corrected pressure from solving Poisson equation (Eq. (2.4), (2.36) and (2.38)). The following approaches are tested for this two times neighbour searching in each single time step:

a) Pure traditional cell-linked

This approach is about conducting the two times neighbour searching within the area contained by the yellow and green line as shown in Figure 2.4

b) New strategy

As illustrated in Section 2.3.4, by using the new strategy, the two times neighbour searching is only needed within the area covered by blue color in Figure 2.4

c) Verlet list combined with traditional cell-linked

This approach means we first generate a Verlet list using traditional cell-linked approach, and then conduct the refined searching within the Verlet list twice. As discussed in Section 2.3.4, the refined searching within the Verlet list with $6r_0$ radius will not be more efficient than directly searching within the nine $4r_0$ length cells in 2D (as shown in Figure 2.4). Moreover, if we add the time consumed on establishing the Verlet list using the $6r_0$ length cells, the total time would be absolutely larger than the traditional cell-linked approach with $4r_0$ length cell (this will require twice the time used in comparison to strategy a)).

If we repeat the above analysis for the case of $5r_0$ radius, the comparison of overall time cost with a) is not so obvious. Hence, this situation will be tested here.

d) Verlet list enhanced by new strategy

The radius is taken to be the same as c), i.e. $5r_0$. The difference of the approach used in d) as compared to the one in c) is that the establishing of Verlet list is accelerated by the new strategy; since as mentioned in Section 2.3.4, the new strategy is applicable for the acceleration of cells with any length.

Figure 4.1 shows the comparison of the computational time used in a single time step by these four neighbour searching strategies. Figure 4.2 shows the proportion of the time cost used by each part of the four searching strategies. It is worth mentioning here that the cell generation time is the same for different size cells, as explained in Section 2.3.4. Moreover, as shown in Figure 4.2, the time spent on cell generation is indeed almost negligible compared with other parts (as mentioned in Section 2.3.4). All the simulations in this work were run on computer with Intel(R) Core(TM) i5-2400 (duo 3.1GHz) CPU, RAM 4.0 GB. The compiler used is Microsoft Visual Studio.

From Figure 4.1, it can be seen that by using the new searching strategy, the computation time in one single time step has been reduced at least by half

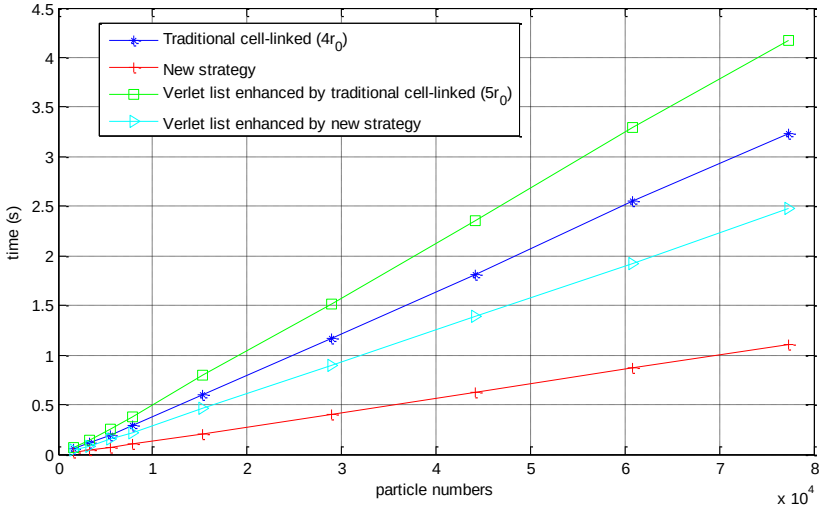

Figure 4.1: Computation time per time step comparison of new and traditional neighbour search strategies

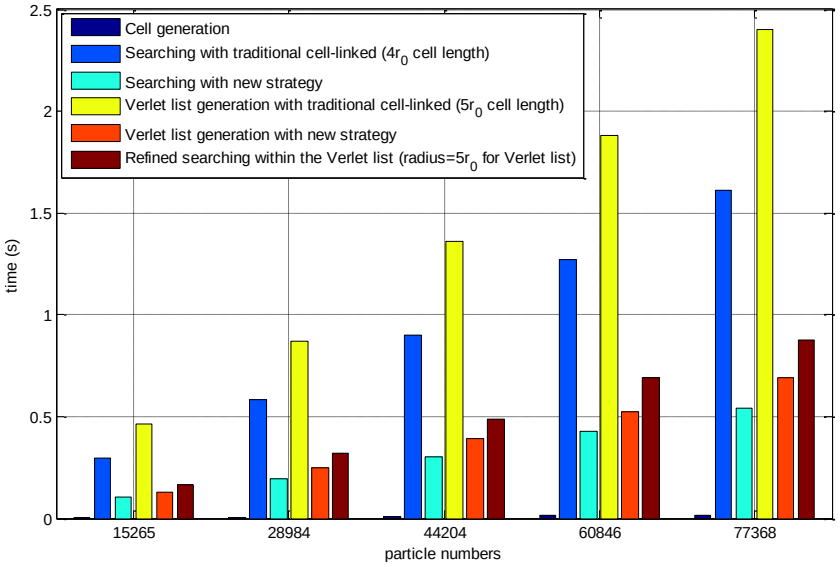

Figure 4.2: Proportion of time consumed in each part of the new and traditional neighbour search strategies

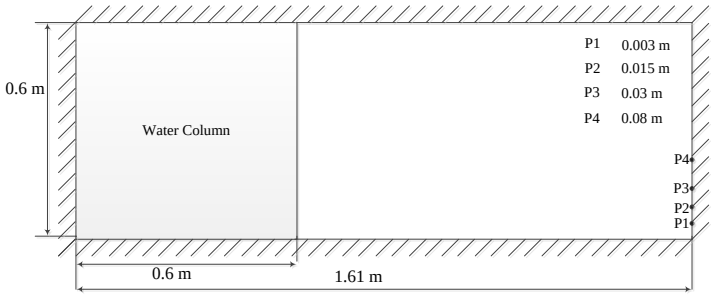

Figure 4.3: Sketch of the 2D Dam-break calculation model

compared with all the other three approaches. The new searching time (red line) is only about one third of the traditional cell linked model (blue line), which is consistent with the prediction in Section 2.3.4. The efficiency of the neighbour particle searching has been improved remarkably.

The Verlet list combined with the traditional cell-linked (i.e. c)) is more time-consuming than the pure traditional cell-linked approach (i.e. d)). From Figure 4.2, it can be seen that the average time of the two parts in c) i.e. Verlet generation (yellow bar) and refined searching (brown bar) with this list are basically equal to that of traditional cell-linked model (blue bar). However, strategy c) requires two times of refined searching within the Verlet list, which makes it slower.

Moreover, in Figure 4.2, the comparison of time in traditional cell-linked (blue and yellow bar) and that after being accelerated by the new strategy (light blue and orange bar) proves that the new strategy will reduce the searching time to about 2.5/9, as illustrated in Section 2.3.4.

4.2 Pressure computation performance

Table 4.1: The conditions of different test cases

	Source term	Boundary condition	Particle shifting
Original MPS	Density invariant type (DI)	Traditional MPS type	No
Model A	Density invariant type (DI)	New proposed type (including all modifications in section 2.3.2)	No
Model B	Divergence free type (DF)	New proposed type (including all modifications in section 2.3.2)	No
Model C	Density error compensation (Eq. (2.38))	New proposed type (including all modifications in section 2.3.2)	No
Modified MPS	Density error compensation (Eq. (2.38))	New proposed type (including all modifications in section 2.3.2)	Yes

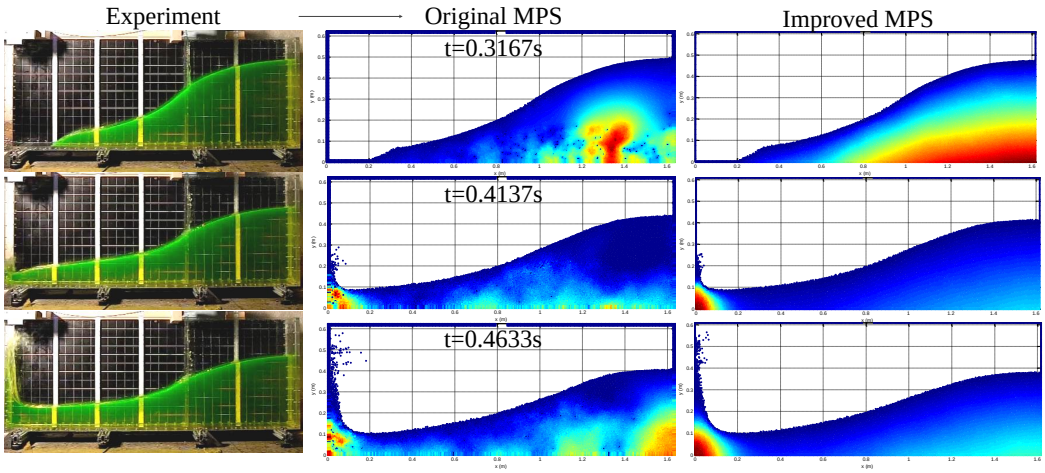

Figure 4.4: Free surface profile and pressure contour comparison between experiment [93], original MPS and improved MPS

In order to test the effect of the modifications, A 2D dam-break problem is calculated with different combinations of the aforementioned modifications, as shown in Table 4.1. The geometry set-up is shown in Figure 4.3. The initial particle distance is $0.005m$, which corresponds to 14400 fluid particles (16164 particles in total). For the time step, the CFL condition is applied with a maximum value of $0.001s$. Four points on the impacting wall are selected to monitor the pressure time history, as shown in Figure 4.3.

Figure 4.4 shows the comparison of free surface profiles and pressure contours from experiment results by Lobovsky et al. [93], the original MPS and the MPS with all the proposed modifications. Although both the original MPS and the Modified MPS can give consistent flow configuration at various typical time instants compared with experiment results, the smoothness of the pressure field produced by the modified MPS is much better than the one generated by the original MPS.

The pressure time history results at P2 are depicted in Figure 4.5. The pressure fluctuation of the original MPS is quite large and finally triggers the termination of the simulation, as shown in Figure 4.5 (a). Figure 4.5 (b) shows the result of Model A in Table 4.1 (which illustrates the effect of the new boundary conditions). The use of Neumann type solid boundary condition and the simplified version of the free surface recognition method adopted by [71] could reduce the fluctuation after the initial impact period. But the pressure is still too noisy because of the DI type source. Actually, comparison between Figure 4.5 (b) and Figure 4.5 (c) shows clearly that the DI type tend to generate larger

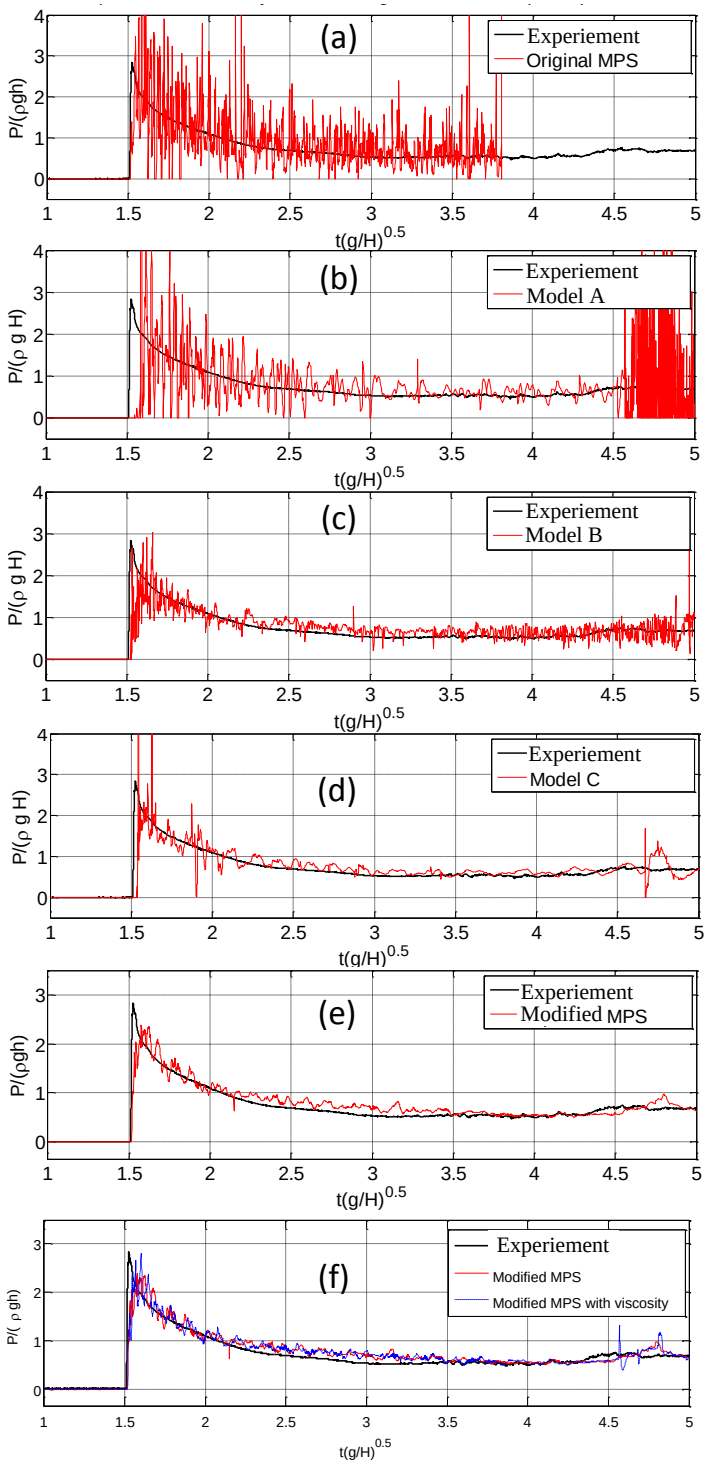

Figure 4.5: Pressure history of different models monitored at P2 ((a) Original MPS; (b) DI source term, no particle shifting, proposed boundary condition; (c) DF source term, no particle shifting, proposed boundary condition; (d) Density error compensation source term, no particle shifting, proposed boundary condition; (e) MPS with all the proposed modifications (f) Viscous and inviscid MPS with all the proposed modifications

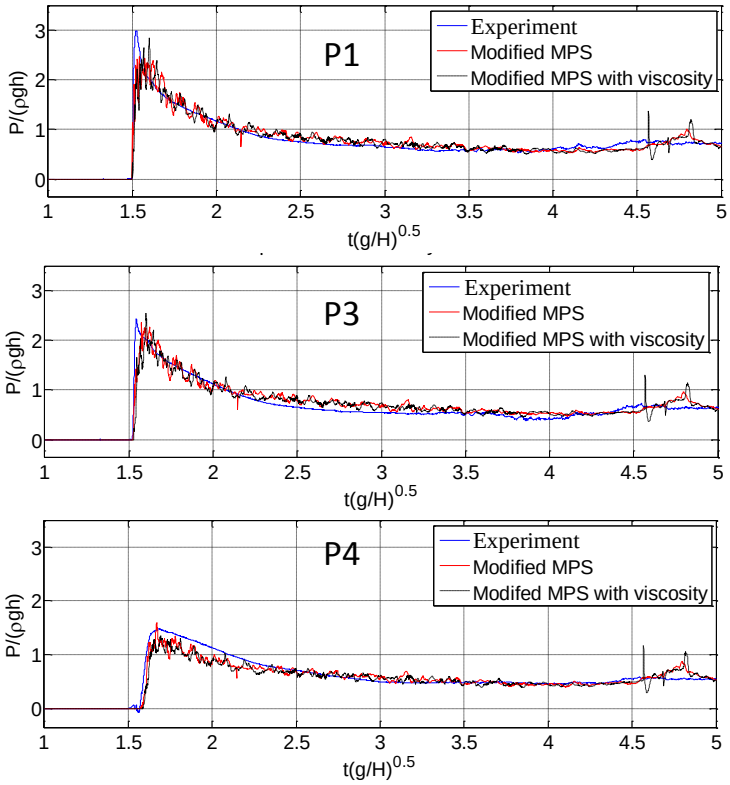

Figure 4.6: Pressure history monitored at P1, P3 and P4

fluctuation compared with DF type, as discussed in Section 2.3.1. The density error compensation scheme could further smooth out the high frequency part in the pressure time history, as shown in Figure 4.5 (d). Finally, in Model C, the use of particle position shifting successfully eliminates the singular pressure impulse by improving the regularity of the particle distribution, as shown in Figure 4.5(e). All the modifications proposed here make the numerical pressure history to be consistent with the experiment results in a very high level. Finally, the viscous effect is tested by performing the simulation using Eq. (2.2). The pressure time history of viscous and inviscous situations are compared in Figure 4.5 (f), together with the experimental results. From this figure, it is clearly that the viscosity does not make any difference that exceeds the numerical noise. This result is consistent with expectation since the Reynolds number for this problem is as high as the order of 10^6. This confirms that for the low speed impact flow problems investigated in this study, the inertia force is the dominant one compared with viscosity. Furthermore, for the case where turbulence modeling is the major concern like flow around cylinder, special turbulence models should be adopted to handle the viscous term instead of the directly discretization of the velocity Laplacian operator in Eq. (2.2) as in this case.

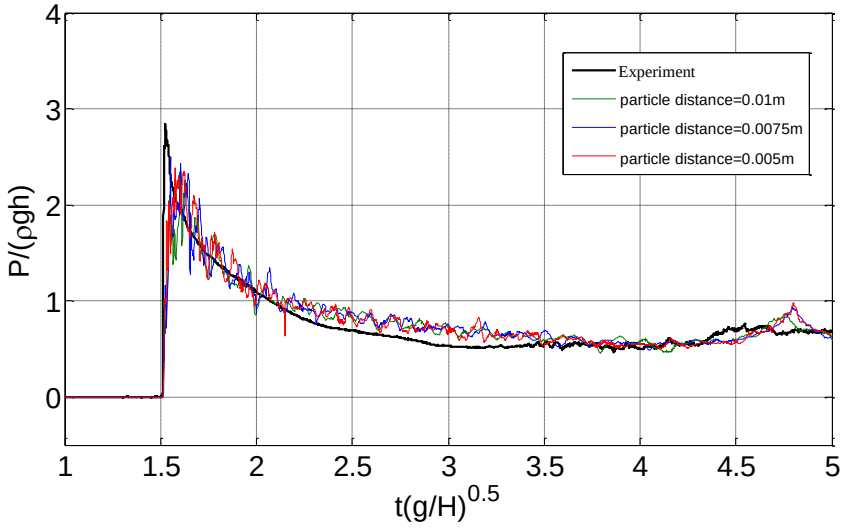

Figure 4.7: Comparison of pressure time history for different particle distances

Figure 4.6 shows the pressure time histories monitored at the other three points, i.e. P1, P3 and P4 by modified MPS with and without viscosity. Again, the difference between viscous and inviscid case is very small. All the numerical curves at the four monitor points match well with the experimental data.

4.3 Mass conservation and convergence

In order to test the convergence property of the modified MPS method, three different initial particle distances, which are $0.01m$, $0.0075m$ and $0.005m$, are used to compute the same dam-break problem described in Figure 4.3.

The pressure time history at the P2 monitor point and the pressure contour of the three cases are shown in Figures 4.7 and 4.9. The consistency of the pressure time history for different particle distances is well maintained, and they all agree well with the experiment results. The characteristic features of the free surface profile and the pressure contour at the same instant ($t = 1.25s$) for the three cases are also very consistent, as shown in Figure 4.9.

The mass conservation performance of the MPS with proposed modifications is checked using the same dam-break problem with different initial particle distances i.e. $0.01m$ and $0.0075m$. The mass conservation is measured by the total volume (area in 2D) of the fluid domain [121]. More specially, the Delaunay

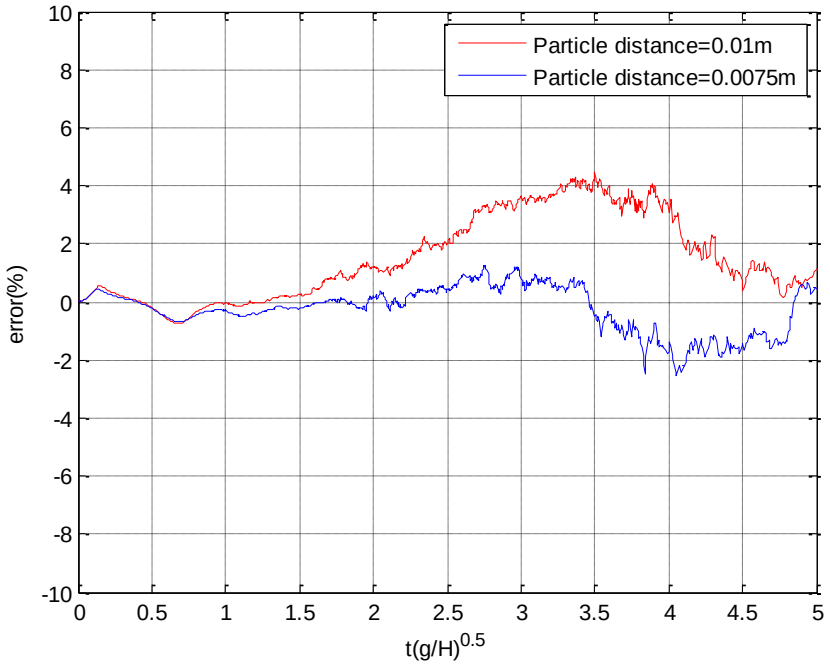

Figure 4.8: Mass conservation comparison between different particle resolutions

triangulation is first established for the particle configuration at each time step, and then the area of the fluid domain is calculated by the summation of these triangles. The mass loss percentage is shown in Figure 4.8. As is shown in this figure, the mass loss is within 5% and the refinement of particle distribution improves the mass conservation performance. The relatively large fluctuation after $t(g/h)^{0.5} = 1.5$ is caused by the splashing and re-entering of the water into the main body. The density error drops back after $t(g/h)^{0.5} = 4.7$ is due to the fact that the splashed water, which will be ignored by the Delaunay triangulation process, have re-entered the fluid domain.

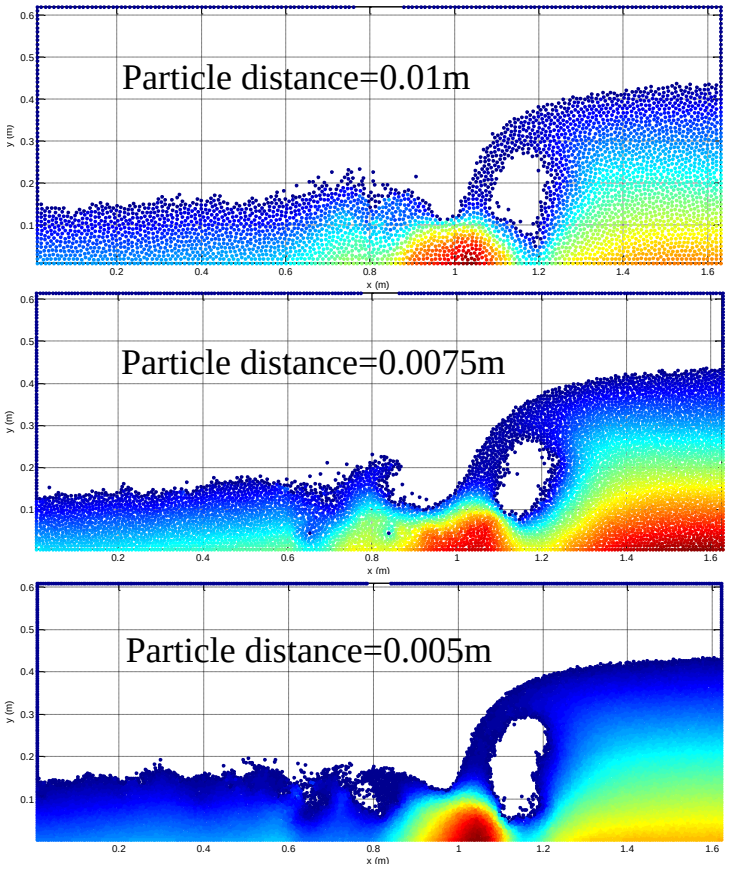

Figure 4.9: Comparison of pressure contour at t=1.25s for different particle distances

Chapter 5

Impact flow simulation results

One of the advantages of particle method is that it is capable to efficiently handle the violent and rapid flow motion with complex free surface deformation. The situations such as impact wave (generated by collapsing of dam) hitting the structure, sloshing and slamming are very representative cases in the area of marine engineering. In this Chapter, this kind of extreme scenarios are simulated to show the capablity of the modified MPS for marine industry applications.

5.1 Dam-break with various boundary conditions

5.1.1 2D cases

5.1.1.1 With obstacle in the middle

The model of breaking-dam impacting with a beam in the middle of tank is simulated, as shown in Figure 5.1. The initial particle distance is also $0.005m$. The fluid particle number is 1682 (2440 particles in total). Figure 5.2 compares the improved MPS results (third and last column from left) with experiment (first and fourth column from left) by Koshizuka et al. [75] and Particle Finite Element Method (middle column) by Larese et al. [79]. The results of the improved MPS are matching well with the experimental results and the Particle Finite Element Method, except at the time instant around $0.5s$. During about $0.4s$ $0.5s$, the experiment results show the process of the air bubble (which is

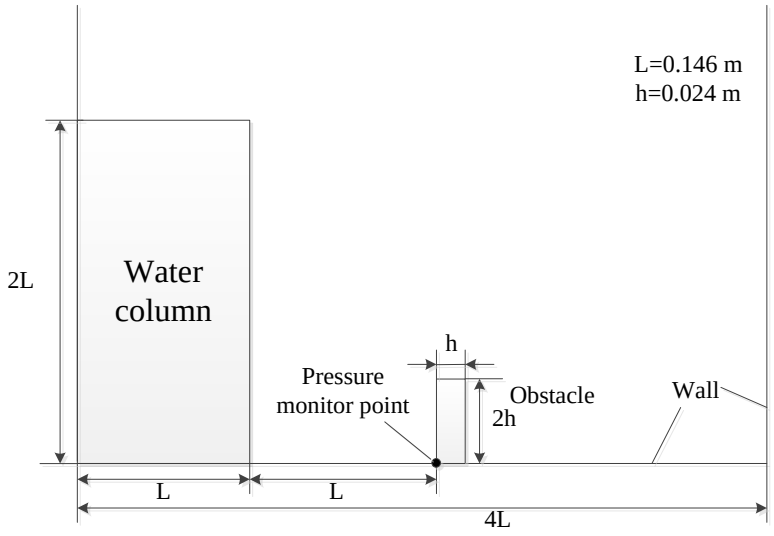

Figure 5.1: Sketch of the 2D Dam-break with obstacle model

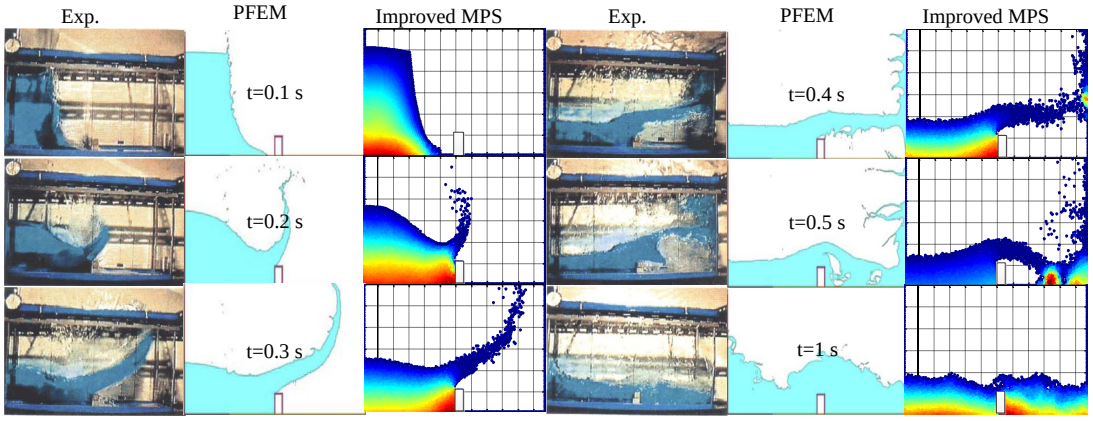

Figure 5.2: Dam break with obstacle: free surface profiles (comparison between experiment [75],PFEM [79] and Improved MPS

trapped by the jet) breaking out from the water. In the experiment this causes the water jet to be higher than that in both of the numerical results (PFEM and Improved MPS). This disagreement is reasonable since the air phase is not considered in both of the numerical computations. When the air is compressed out from the water, e.g. in the time instant of 1.0s, the Improved MPS results agree better with experiment than the PFEM results.

5.1.1.2 With spring supported rigid wall

The computational model of the rigid wall with spring hinged joint at the impacting side of the tank is illustrated in Figure 5.3. The initial particle distance is chosen as $0.01m$, i.e., 7200 fluid particles are involved (8652 particles in total). The motion of the rotating beam is governed by the following equation:

$$I_b\ddot{\theta}_b - \frac{1}{2}M_bL_bg\sin\theta_b + K_b\theta_b = T_b \tag{5.1}$$

where θ_b is the rotation angle of the beam, I_b is the moment of inertia with respect to rotating axis, and T_b is the torque generated by the fluid pressure. The other related parameters are chosen as: mass of the beam $M_b = 1kg$, stiffness coefficient $K_b = 1500N/m$, and length of the beam $L_b = 2m$. In order to compare the effect of rigid and this rotational beam, the two cases are both computed in this study.

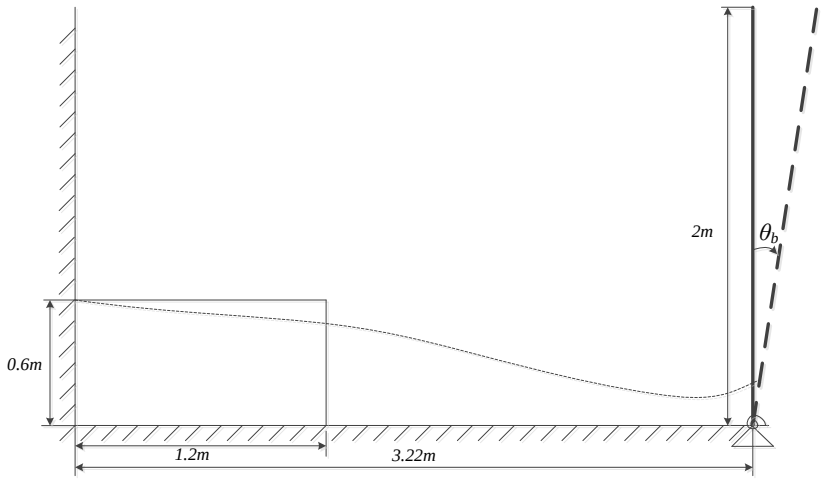

Figure 5.3: Sketch of the 2D Dam-break with spring supported wall

Figure 5.4 shows the pressure contour at several typical time instants. From Figure 5.4, it can be seen that the distribution of the pressure is quite smooth in space domain. Two major impacts are found to occur in two durations, i.e. from 0.75 to 2s and from 5.1 to 5.9s. During these two periods, the large fluid pressure which is generated from the falling of the water column pushes the beam to relatively large angles. Figure 5.5(a) shows the time history of the rotational angle of the beam. The two significant angle impulses are consistent with the time of the two major impacts. Except from these violent interactions, the water

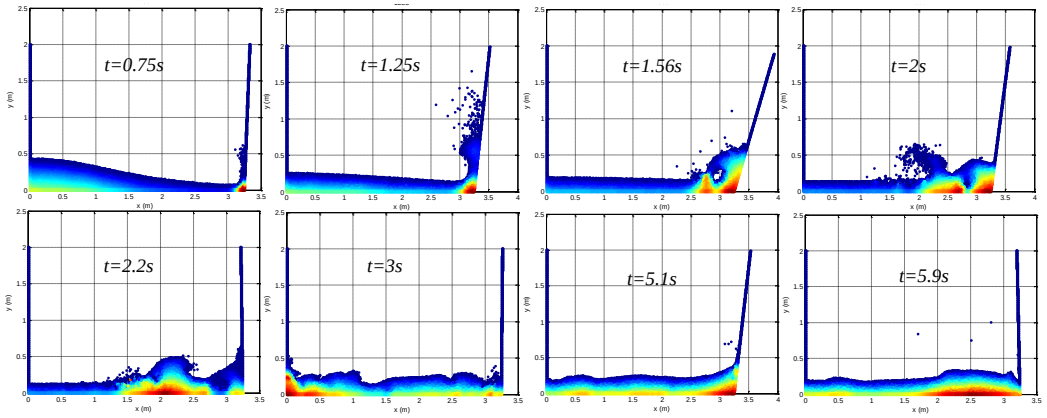

Figure 5.4: Pressure contour and free surface profiles at several typical instants

pressure applied on the beam is relatively much smaller. As a consequence, the beam oscillates with a period ($\approx$ 0.2s) which is very close to the natural frequency $w = 33.4312 rad/s$ ($T = 0.1879s$), as expected. In order to investigate

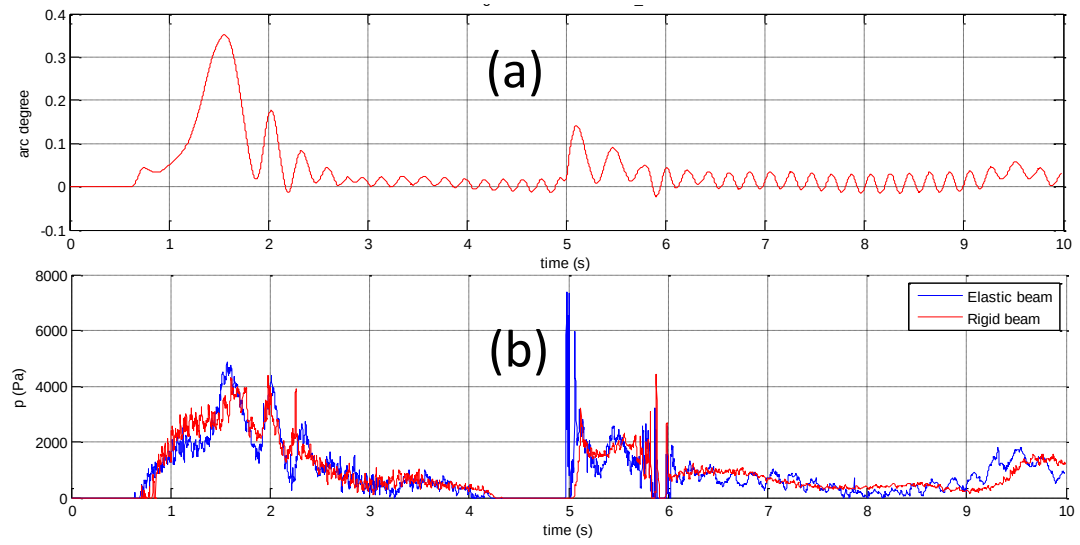

Figure 5.5: Time history of rotation angle and the pressure monitor point

the effect of the beam rotation to pressure field, the time history of the pressure monitored at the point, which is 0.16m above the right corner of the beam, is compared in Figure 5.5(b).

As can be seen in Figure 5.5(b), the time history during the first major impact of rotational beam case is basically the same as the one in rigid supported beam case. However, the peak pressure value during the second major impact is larger than the one in first major impact for the rotational case. This is probably because

that at the beginning of the second impact, the beam is bouncing back (which can be seen in Figure 5.4 at about $t = 5s$) which means that the water front and the beam are moving towards each other. And this consequently makes this impact more violent than the first one. The second difference is that there is a regular oscillation after $t = 6s$ for the rotational case, this is the reflection of the beam oscillation with its near-natural frequency. The pressure fluctuations which occur at about $t = 2.4s$ and $t = 6s$ for both the rigid supported and rotational cases are caused by the isolated water particles re-entering the main fluid field near right corner, which shows that this is not due to the stability issue of the MPS solver.

5.1.1.3 With fixed end elastic wall

Figure 5.6 shows the sketch of the elastic cantilever wall impacted by a breaking-dam. The related parameters are chosen as: Young's modulus $E = 0.2GPa$, thickness $\delta = 0.006m$, line density $m = 47.16kg/m$, and the moment of inertia of the beam cross section $I = 1.8 \times 10^{-8}m^3$. The other geometric parameters are shown on the sketch picture in Figure 5.6. The initial particle distance is $0.004m$. This corresponds to 1250 fluid particles used in the simulation (1736 particles in total).

The beam is fixed on the bottom, and its motion is solved by the standard linear Finite Element (FE) method, as in Ref [139]. Similar to the spring supported beam case, both rigid and elastic beam cases are computed and then compared.

The pressure contours and the beam deformation at some typical time instants are shown in Figure 5.7. Smooth pressure fields are successfully generated, as seen in Figure 5.7.

The trajectory of the top end of the beam, which is represented by the global X coordinate of this point, is shown in Figure 5.8 (a). The frequency of the oscillation (which corresponds to roughly a period of $0.6s$) is very close to its first order natural frequency $w = 10.5235$ ($T = 0.5971s$). This is also consistent with the fact that the first modal shape is the dominant one as is shown in Figure 5.7. The pressure history monitored at $Y = 0.02m$ at the right corner for both rigid and elastic wall cases are shown in Figure 5.8 (b). For both cases, the fluctuation of pressure at the time domain is very small. And the difference between them is also negligible, which means the small elastic deformation will not greatly change the fluid motion and consequently the pressure field.

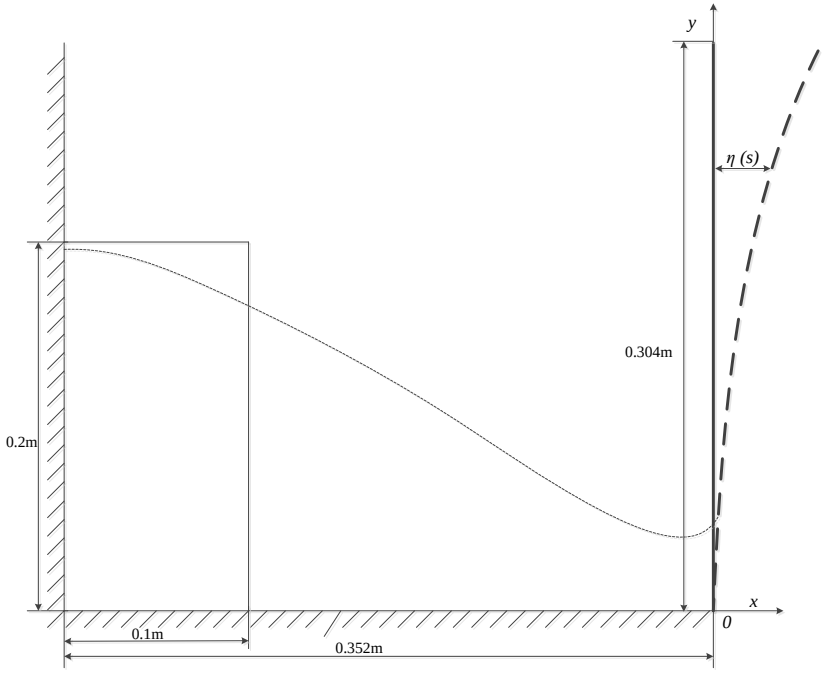

Figure 5.6: Sketch of the 2D Dam-break with elastic wall

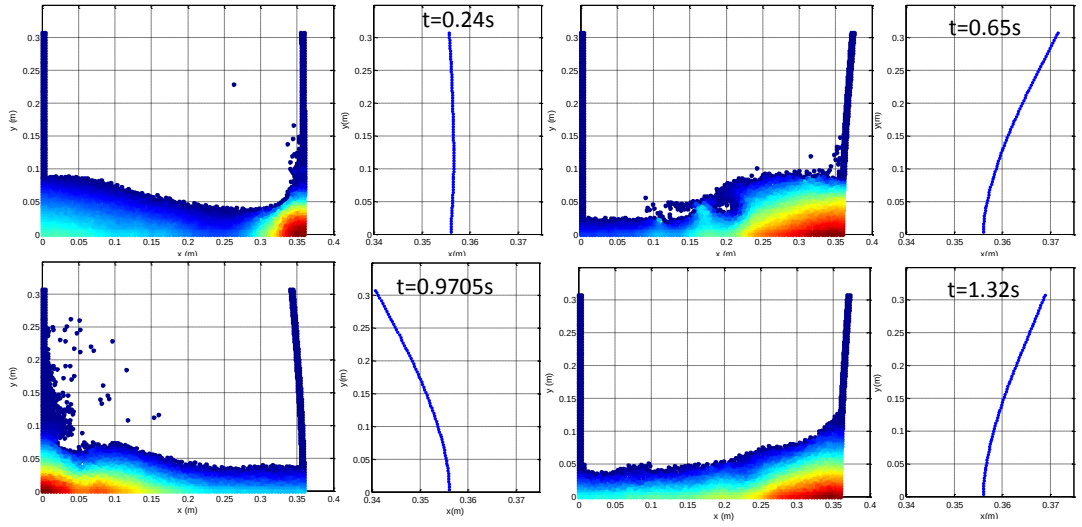

Figure 5.7: Pressure contour, free surface profiles and beam deformations at several typical instants

5.1.2 3D cases

The 3D Dam-break problem investigated in [69] is computed here to test the 3D extension of the proposed modifications to MPS method. The sketch of the problem setup is shown in Figure 5.9. This problem can be regarded as a

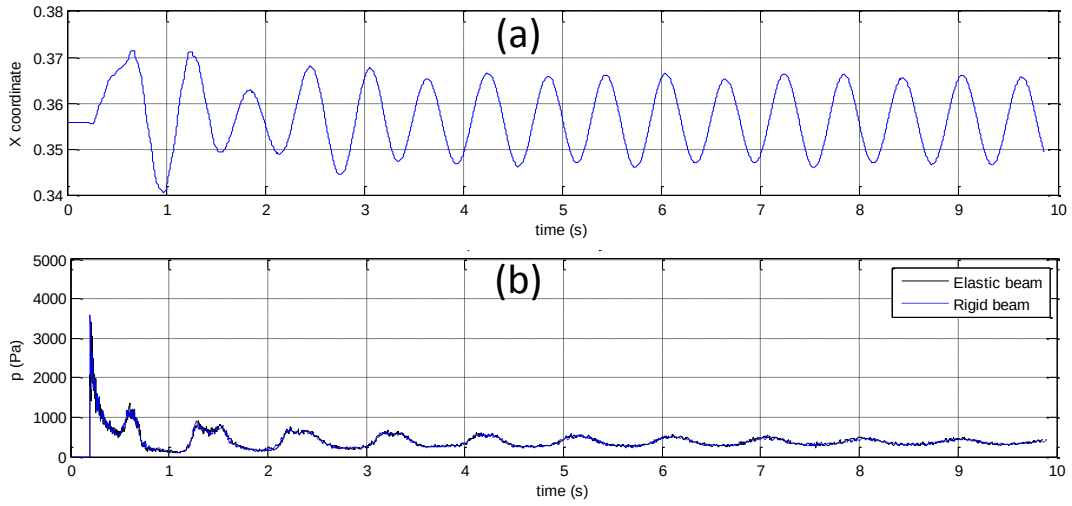

Figure 5.8: Trajectory at the beam top and pressure time history at the impacting corner

simplification of the green water flow problem [69]. A box is placed in the tank to represent a scale model of a container. The top and side views are shown in Figure 5.9(a) and (b), and Figure 5.9(c) shows the layout of the pressure sensors on the box. There are also four vertical height probes that have been used in the tank to monitor the water height history.

The initial particle distance is chosen to be $0.015m$, which results in 200244 fluid particles and 308460 particles in total. The time step is controlled by CFL condition with $0.002s$ as initial value. The numerical results of the proposed modified MPS method are compared to the experimental results and another numerical scheme (ComFLOW) [69].

The free surface profiles comparison are shown in Figure 5.10. Two typical time instants of the early flow stages, i.e. right before the impact to the box $t = 0.4s$ (upper row) and after the impact $t = 0.56s$ (lower row), are shown in this figure. The small pictures at the right-up corners of each figure are the flow situations of the volume where the water column occupies originally, i.e. the so-called reservoir as referred in [69]. The red color particles in the modified MPS results represent the free surface particles, whereas the blue color particles are the inner fluid particles. In order to highlight the free surface deformation, only the position of the free surface particles (i.e. the red particles) are shown in the two main figures of the modified MPS result. As shown in Figure 5.10, there is a good agreement with the experiment. In comparison with the VOF based approach in ComFLOW results, the splash of small water droplets after

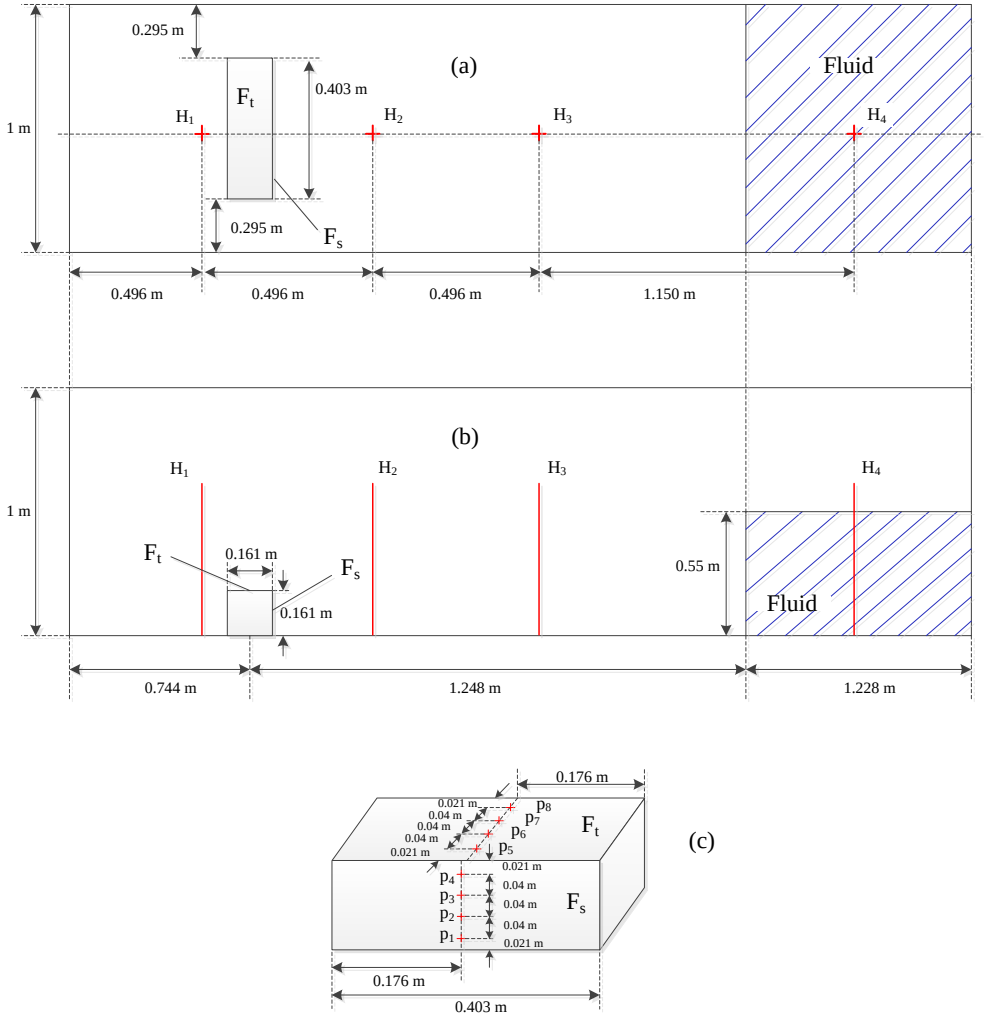

Figure 5.9: Sketch of 3D Dam-break problem

the impact is well captured by the modified MPS method due to the inherently advantage of particle method. The fact that no red particles exist under the free surface in the modified MPS result means the inner flow field is free of misidentified free surface particle. This proves that the 3D free surface particle identification scheme works well even for this kind of violent flow scenario.

The water height time history at the position of H2 and H4 are compared with results from experiment and ComFLOW [69] in Figure 5.11 (a) and (b), respectively. The position of H2 is close to the impact side of the box, whereas H4 is located inside the reservoir, as shown in Figure 5.9.

The trend of modified MPS results matches well with both the experimental and ComFLOW curves. The major events of the flow are well captured. More

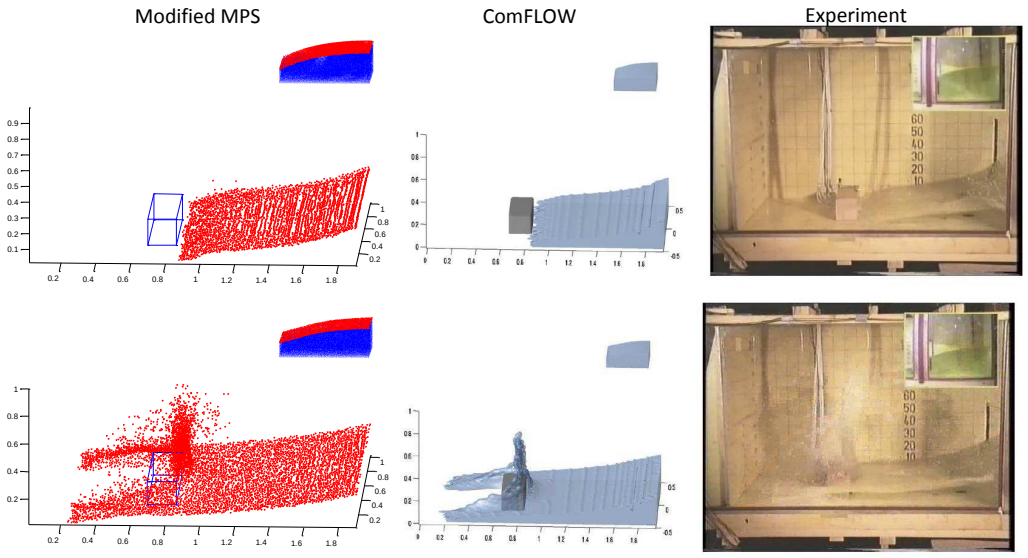

Figure 5.10: Free surface profile comparison at $t = 0.4s$ (upper row) and $t = 0.56s$ (lower row) between modified MPS, experiment [69] and another numerical method (ComFLOW) [69]

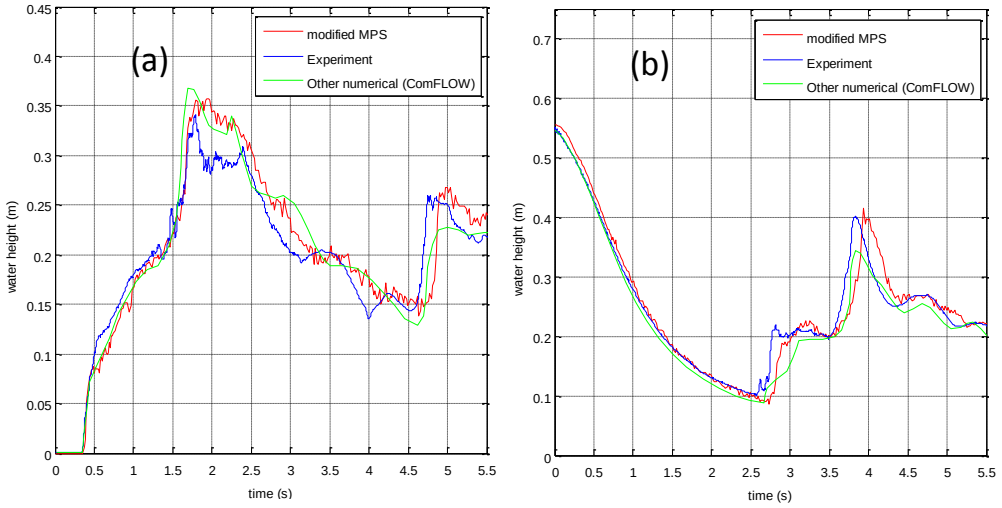

Figure 5.11: Water height comparison at H2 (a) and H4 (b) between modified MPS, experiment [69] and another numerical method (ComFLOW) [69]

specially, for the position of H2, the first water height peak occurs when the water that bounce back from the wall arrives (around $t = 1.8s$). The water then flows back to the reservoir and turns again due to the reflection of the wall (at about $t = 4s$). The returned second wave generates the second peak at about $t = 5s$ in the H2 curve. The same events are also presented in the curve of H4. The water height stops decreasing and starts to climb when the first bouncing

wave reaches the position of H4. The increasing rate gets larger again when the fist bouncing wave hits the wall. Finally a local peak is formed when the second time reflected wave arrives. There are inevitably some discrepancies between numerical and experiment results. One of the notable differences is that, at around $t = 5s$ and $t = 4s$ in Figure 5.11(a) and (b) respectively, there are slight delays of the local peaks in the modified MPS results compared with experiment results. On the other hand, for the amplitude of the local peaks, the modified MPS results are closer to the corresponding experimental ones compared with the ComFLOW results.

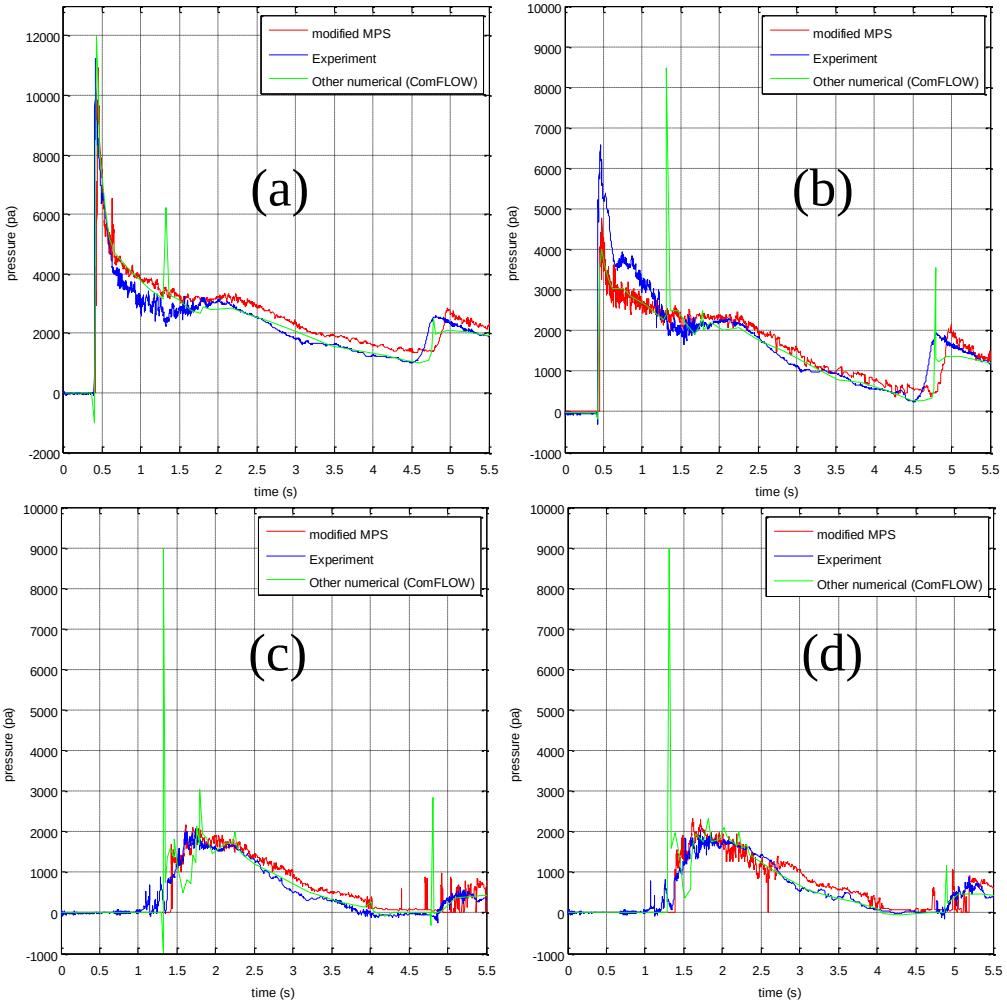

Figure 5.12: Pressure time history comparison at p1, p3, p5 and p7 between modified MPS, experiment [69] and another numerical method (ComFLOW) [69]

The time history of the pressure on the impact side and top of the box are presented in Figure 5.12. The four sub-figures i.e. Figure 5.12(a), (b), (c) and

(d) correspond to the results from sensor p1, p3, p5 and p7, respectively. As shown in Figure 5.9 p1 and p3 are on the impact side, whereas p5 and p7 are on the top of the box.

For the results of impact side,at position of p1, the impact event is captured better by modified MPS than that of ComFLOW in terms of timing and pressure values. However, both of the numerical methods underestimate the impact pressure value at position of p3. The second local pressure peaks at both points p1 and p3 (around $t = 5s$ in Figure 5.12(a) and (b)) are slightly delayed by modified MPS simulation compared to the experimental and ComFLOW results. This is consistent with the corresponding analysis for the water height above.

From Figure 5.12 (c) and (d), the discrepancies of the pressure time history monitored on the top side of the box by ComFLOW are not found to occur in the modified MPS simulation. Also, the "wiggle" [69] in ComFLOW at about $t = 1.3$ is not encountered in this study. The starting of the pressure increase in Figure 5.12 (c) and (d), which corresponds to the impact, in the modified MPS simulation is slower than experimental results at about $t = 1.5s$. This difference might be due to the following reason: in the experiment, when the splashed water starts to drop on the top of box at about $t = 1.0s \sim 1.5s$, the pressure sensor can detect the impact, which is reflected by the impulses of the experiment curves at about $t = 1.0s \sim 1.5s$. However, in the modified MPS, these drops of particles are still too coarse to form a "patch" of fluid, so that they will be recognised as separate free surface particles, and this free surface particles only possess zero pressure due to the dynamic boundary condition, as mentioned in Chapter 2. When the particles are accumulated to some level, the pressure can then be calculated properly, i.e. the pressure starts to increase at about $t = 1.5s$. Similar reasoning could also be applied to explain the frequent zero pressures of the modified MPS results during the period of $t = 4.8s \sim 5.3s$. More specially, the second time reflected wave starts to pass the box, where the fluid over the top is still quite thin. This will lead to the situation that sometimes the fluid around the sensor is too coarse to form fluid "patch". And this means the pressure will be zero.

It is worth to point out that the extreme spikes of pressure from ComFLOW are not encoutered in the modified MPS simulation.

5.2 Sloshing simulation

A 2D sloshing phenomenon in partially filled tank is simulated in this section. The physical dimensions are shown in Figure 5.13. The initial particle distance is $0.005m$, which corresponds to 2880 particles used (3592 particles in total).

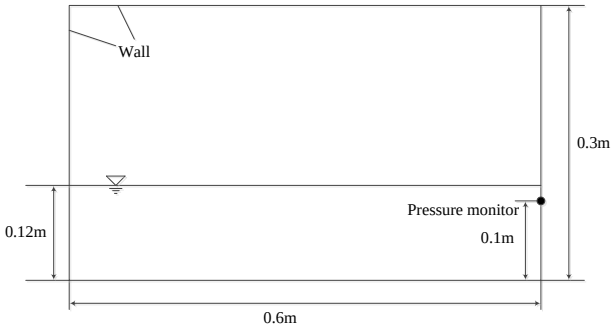

Figure 5.13: Sketch of the sloshing model

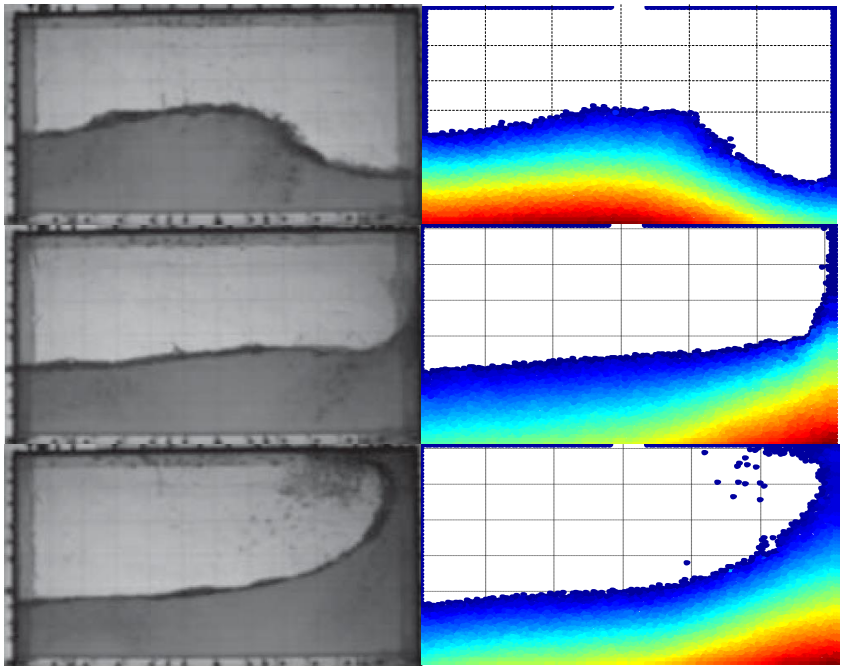

Figure 5.14: Comparison of free surface profiles between experiment and Improved MPS at $t = 0.1T$(top), $0.2T$(middle) and $0.3T$(bottom)

The tank moves sinusoidally in horizontal direction as: $X = A\sin(\omega t)$, where A is the amplitude of motion and ω is the circular frequency of the excitation.

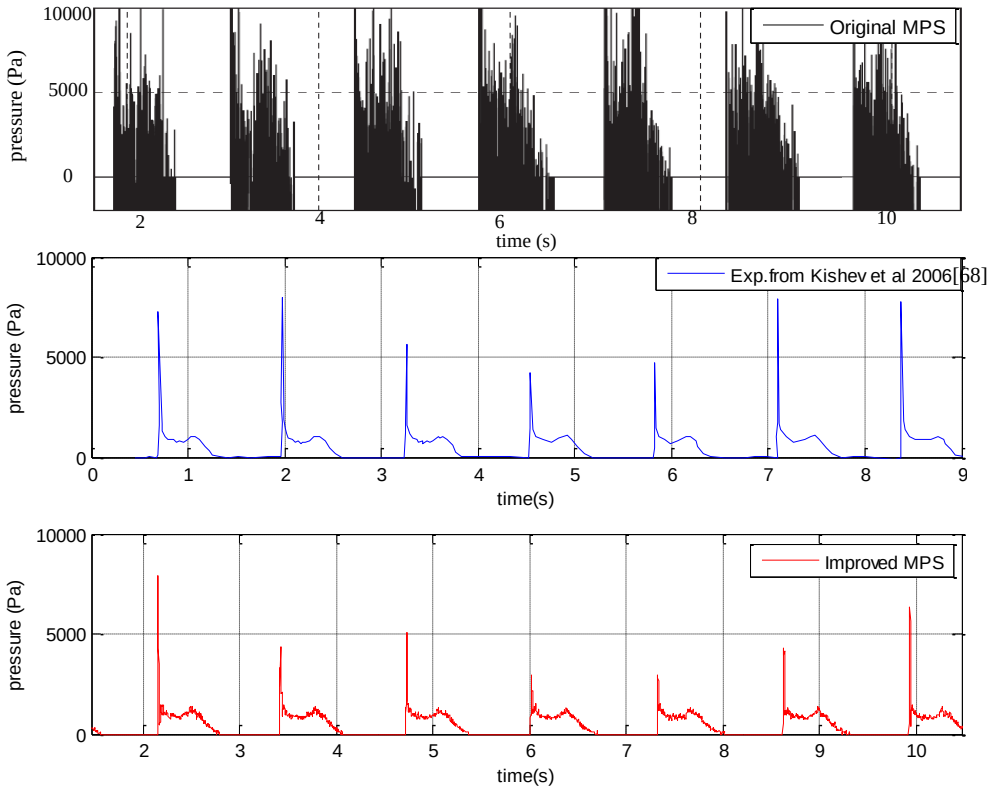

Figure 5.15: Comparison of pressure with experiment of Kishev et al [68] and original MPS from B. H. Lee et al [82]

In this simulation, the frequency ω is $4.8332 rad/s$ (period T is $1.3s$) and the amplitude A is $0.05m$. In order to simplify the coding, the equivalent acceleration, which is equal to the tank acceleration, is added into the right hand side of the governing equation (Eq. (2.1)). And the benefit is that all the boundaries remain stationary.

Figure 5.14 shows the free surface profiles of both the experiment results and the Improved MPS at three representative time instants, i.e. $0.1T$, $0.2T$ and $0.3T$, where T is the period of the sloshing ($1.3s$). Again, since no falsely recognized free surface particles exist in the main fluid body, the pressure contour is very smoothly distributed, as shown in Figure 5.14. The Improved MPS shows a good agreement with experiment for the free surface profiles as well.

Figure 5.15 compares the pressure results of the original MPS, experiment and the Improved MPS results. The original MPS results are scanned from Ref [82], and the experiment data are extracted from the paper of Kishev et al. [68]. From this Figure, it is obvious that the fluctuation of pressure in the original MPS

method is too large to be used for FSI application. In contrast, the Improved MPS could successfully capture the typical pressure characteristics. The period of the results also match well, although a shifting manipulation (also found in Ref [68, 82]) is made to align the first impulse. This may be due to the starting of the measuring time in the experiment, is not exactly the same as the start of the tank motion. The peak values of each impulse are not exactly the same as those in experiment results, but the overall maximum value, which is about $7000Pa$ at around $2s$ and $10s$, is successfully captured.

5.3 Slamming simulation

5.3.1 V shape wedge dropping

The Wedge-dropping problem is frequently employed as a simplified model to investigate slamming phenomenon in marine engineering. In this part, a 2D wedge-dropping model which has been studied through experiment by Aarsnes [1] and numerical computation (Boundary Element Method) by Sun [143] is investigated again by the improved MPS method.

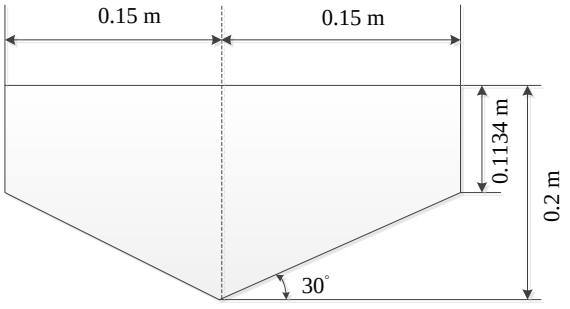

Figure 5.16: Sketch of the V shape section

The geometry information of the V-shape wedge is shown in Figure 5.16. The deadrise angle and width of the wedge are 30 degrees and $0.3m$, respectively. In the experiment, two dummy sections with thickness of $0.45m$ were affiliated on the measuring section whose thickness is $0.1m$. This means that the vertical force shown below is only 10% of the total force experienced by the whole rig. The reason for this is to minimize the $3D$ effect of the flow and makes the comparison

with $2D$ computation results more reasonable. The total weight of the falling rig is $288kg$.

Two scenarios are studied here. The dropping heights (defined from the apex of the wedge to the calm water surface) are $0.195m$ and $0.5m$ respectively, which means the entry speeds are $1.91m/s$ and $3.05m/s$ for these two situations.

The size of the calm water for the computation is $0.9m$ in width and $0.6m$ in depth. As in the previous sections, the CFL condition is applied to determine the time step. The initial distance between particles is $0.01m$, which corresponds to 5400 fluid particles involved in the simulation. At the beginning of the simulation, the wedge is placed just above the water with a distance (from the apex of the wedge to the calm water surface) of $0.01m$ and the initial velocity as aforementioned . Because of the symmetrical shape of the wedge and for programming convenience, the horizontal motion of the wedge is constrained.

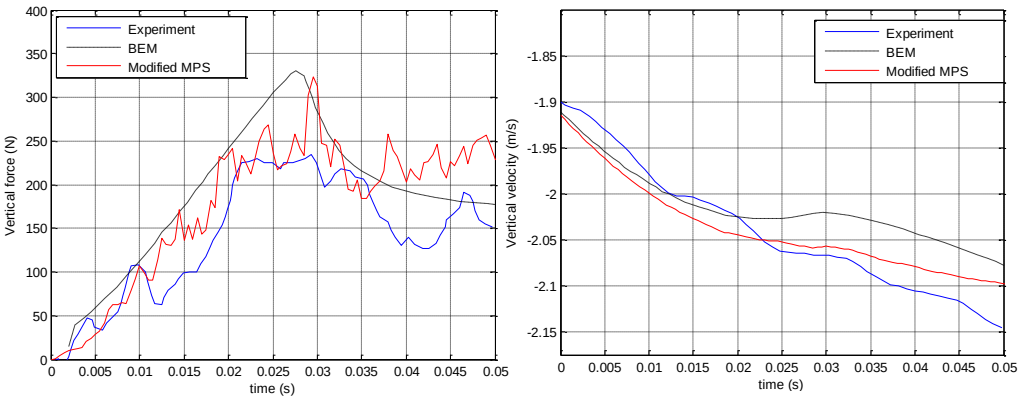

Figure 5.17: Vertical force and velocity comparison between experiment [1], BEM [143] and modified MPS (entry speed $v_0 = 1.91m/s$)

The vertical force and velocity are compared in Figure 5.17 (Scenario1: entry speed $1.91m/s$) and Figure 5.18 (Scenario2: entry speed $3.05m/s$) for the modified MPS, BEM and experiments. Generally, the velocity results of Improved MPS match better with the experiment than the BEM results. For the acceleration results, both of the BEM and Improved MPS methods give overestimate. This could be caused by the 3D effect when the water jet approaches the knuckles [143]. Actually, at about $0.03s$ for scenario 1 (Figure 5.17) and $0.017s$ for scenario 2 (Figure 5.18), the water just approaches the edge of the wedge. And at about the same time, the vertical force begins to deviate from the experiment results. Another possible reason could be the neglecting of the frictional force along the guide trail [143].

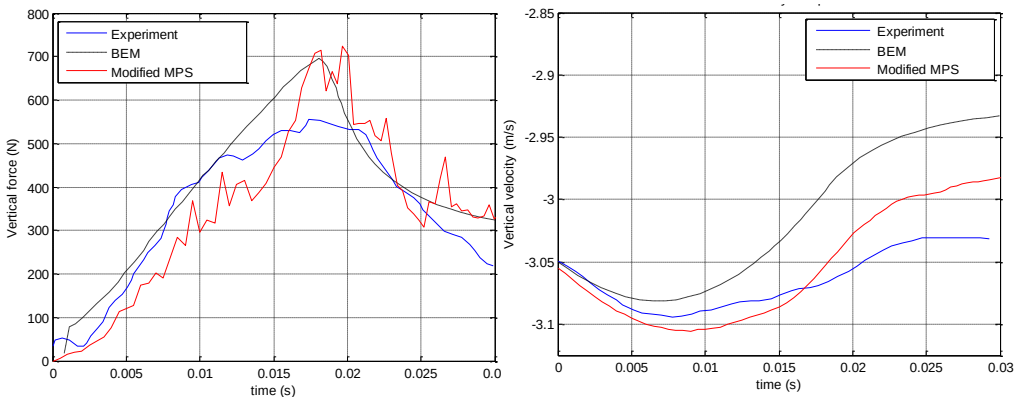

Figure 5.18: Vertical force and velocity comparison between experiment [1], BEM [143] and modified MPS (entry speed $v_0 = 3.05m/s$)

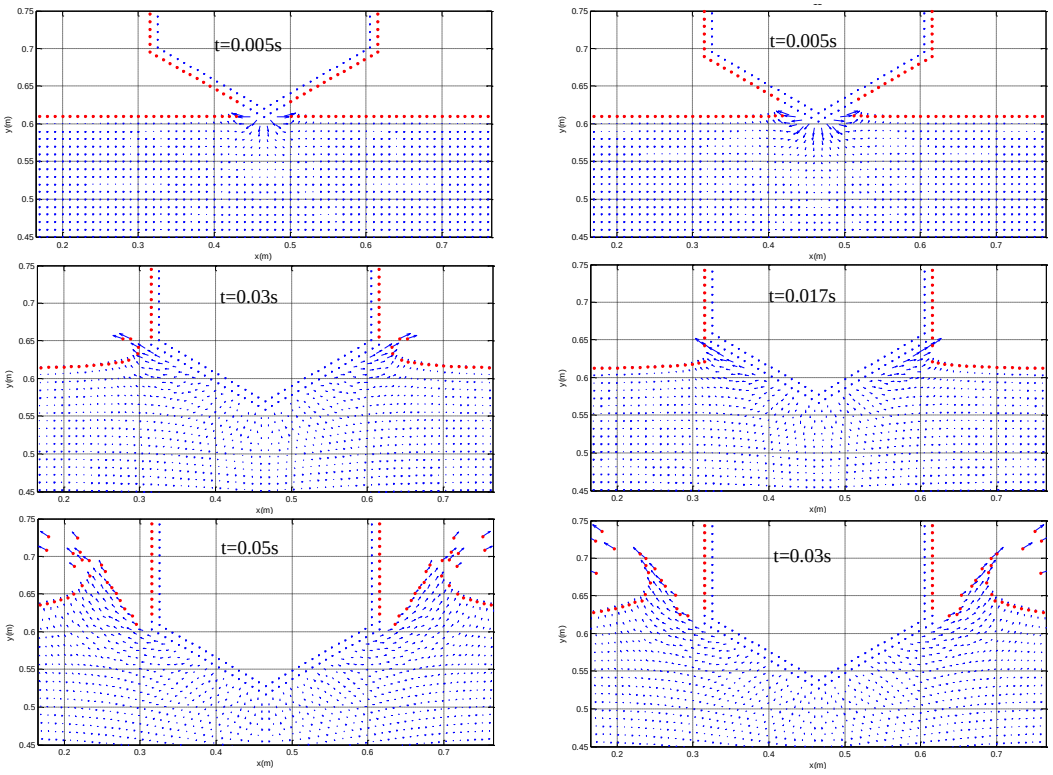

(a) entry speed $v_0 = 1.91m/s$ (b) entry speed $v_0 = 3.05m/s$

Figure 5.19: Free surface profile and velocity distribution at some typical time instants

Figure 5.19 show the free surface profiles for two scenarios at typical time instants. The middle of each figure shows the time when water just approaches the edge of the wedge. The particle distribution is symmetrical and quite uniform. The last image of each figure gives the shape of the water jet. The

red point means detected free surface particles. There are no falsely recognized free surface particles in the main fluid body.

5.3.2 Ship cross-section dropping

The ship bow section dropping has also been studied by Aarsnes [1] experimentally and Sun [143] numerically. The computational model is shown in Figure 5.20. Two scenarios are investigated here: the dropping heights of $0.02m$

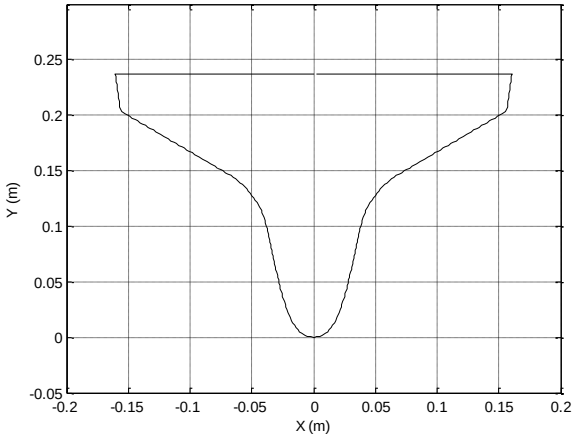

Figure 5.20: Shape of the ship section

and $0.118m$. The corresponding entry velocities are $0.61m/s$ and $1.48m/s$, respectively. Except from the shape of the section, other experimental set-up is the same as the one described in wedge dropping case. The total weight of the falling rig is $261kg$.

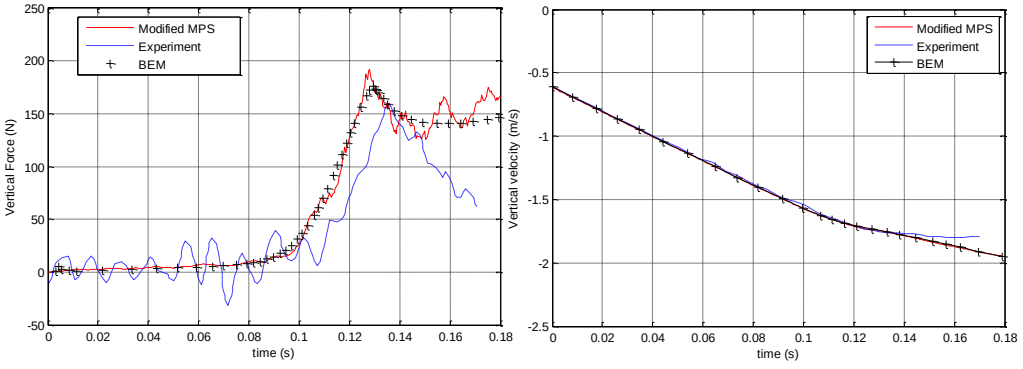

Figure 5.21: Vertical force and velocity comparison with experiment [1] and BEM [143](entry speed =0.61m/s)

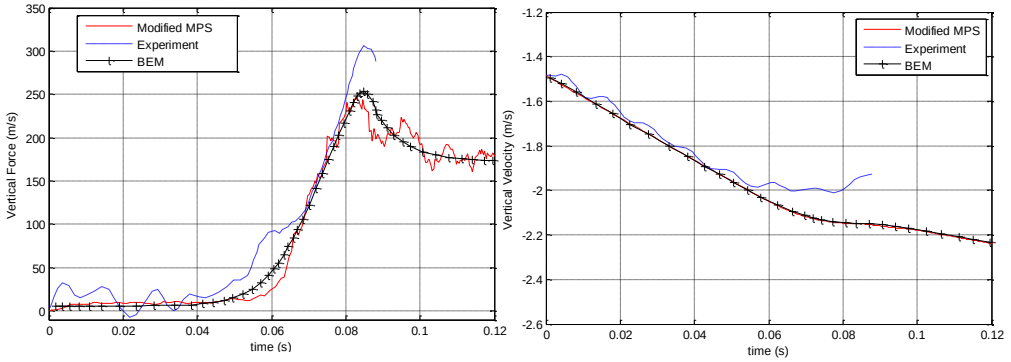

Figure 5.22: Vertical force and velocity comparison with experiment [1] and BEM [143] (entry speed =1.48m/s)

The simulation is conducted in a tank with the length of 2.4m and water depth of 1m. As in the above sections, the CFL condition is applied to determine the time step. The initial distance between particles is 0.005m, which corresponds to 96000 fluid particles involved in the simulation. Here, the same set-up as in the wedge dropping case is used. At the beginning of the simulation, the wedge (ship section) is placed just above the water with a distance (from the apex of the wedge to the calm water surface) of the initial particle distance i.e. 0.005m with the aforementioned initial velocity. Because of the symmetrical shape of the wedge and for programming convenience, the horizontal motion of the wedge is constrained. The physical simulation time is 0.12s to 0.18s, which takes roughly 8 CPU hours. The velocity and vertical forces are compared in Figures 5.21 and 5.22. The results of the Improved MPS are generally in good agreement with experimental results [1]; and very close to the BEM results [143]. However, it can be noticed that after about 0.13s in scenario 1 (entry speed 0.61m/s) or 0.085s in scenario 2 (entry speed 1.48m/s), the Improved MPS and BEM results start to deviate from the experimental one, this may also be explained by the same reason as with the wedge dropping case.

In order to illustrate the space distribution of pressure and velocity, the pressure and velocity contours of the fluid fields for scenario 1 (entry speed 0.61m/s) are shown in Figure 5.23. The three time instants selected here are representative ones when the water reaches the characteristic positions. The pressure and velocity fields obtained are all quite smooth.

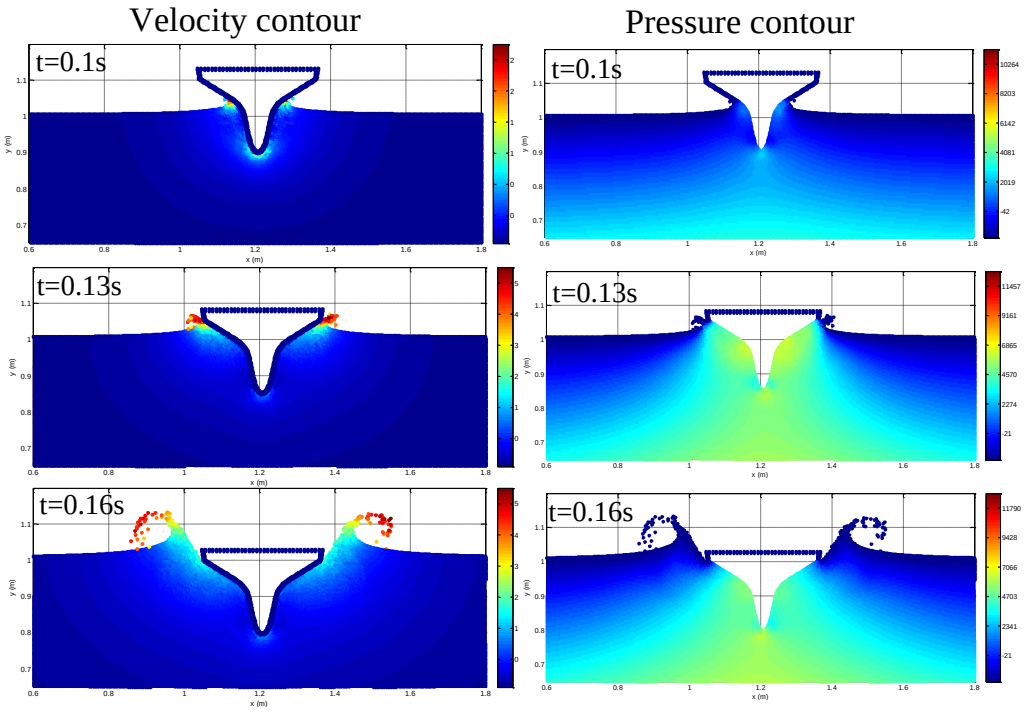

Figure 5.23: Velocity and pressure contour of scenario 1(entry speed $0.61m/s$)

5.4 Breaking wave impacting flexible wall by weak coupling BEM and MPS

For many free surface flow problems in marine engineering, the violent flow phenomena like wave breaking is only restricted within a small area which is close to the ship or other marine structures. For this kind of cases, the majority of the flow could be simply described by potential flow theory, which is more efficient than the direct simulation using Navier-Stokes equations. In this section, the 2D weak coupling between the potential flow based Boundary Element Method (BEM) and the proposed modified MPS method as shown in Figure 5.24 is investigated. A brief description of the BEM methodology and the process of the weak coupling strategy are given in Appendix B.

In order to test the weak coupling scheme, the process of a violent breaking wave interaction with vertical flexible wall was simulated [67, 139]. The problem setup, results and discussions are presented in this section.

As shown in Figure 5.25, a wave tank with piston-type wave-maker is used to generate solitary wave, which then runs up on a gentle slop. A flexible

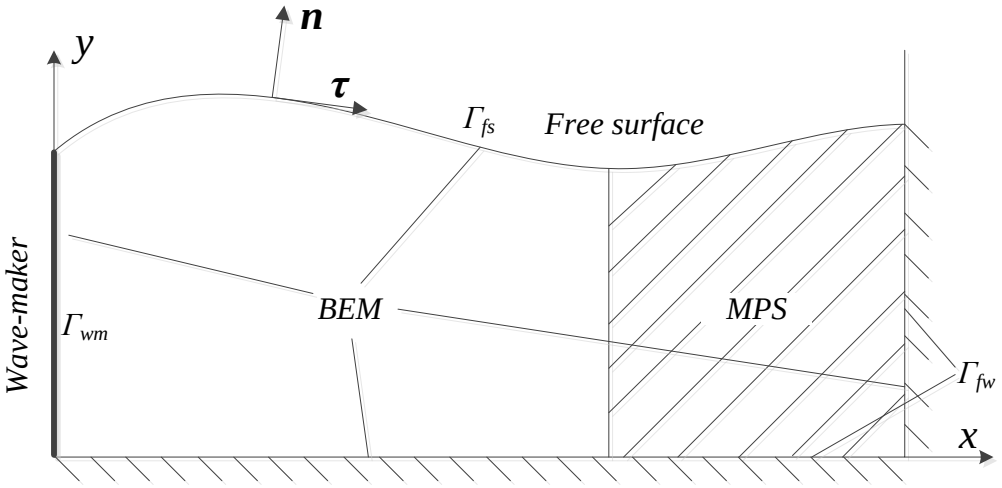

Figure 5.24: Computational domain layout and coordinates system for weak coupling between BEM and MPS

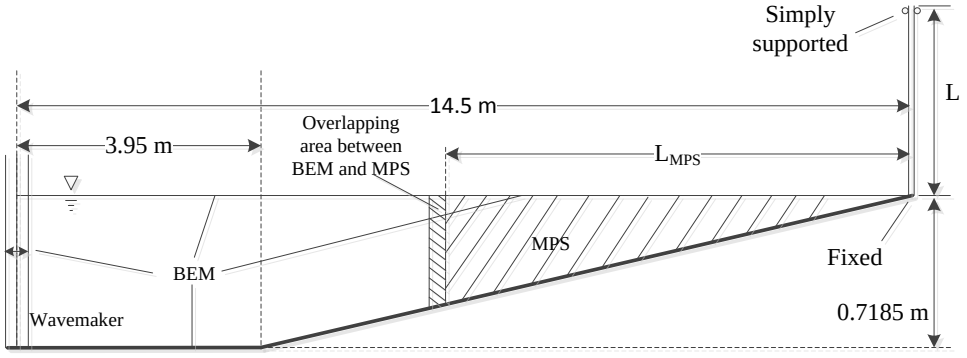

Figure 5.25: Sketch of the solitary wave climbing small slope ramp by coupling BEM and MPS.

vertical plate with length of $1m$ is mounted at the end of the tank and simply supported at $0.88s$ from the plate bottom, with the top free of restriction. The width of the plate is $0.65m$. The density and Young's modulus of the elastic plate are $1190kg/m^3$ and $3250MPa$. The geometric dimensions of the wave tank is depicted in Figure 5.25. The method mentioned in [39] is used to generated the solitary wave with amplitude of $0.08m$. Both experimental [67] and numerical [139] studies of this problem have been conducted. The comparison between those and the current results will be presented later.

For the case reported below, the length of the MPS domain, including the

overlapping area, is chosen to be 7.5m. The first four columns of particle will be treated as interface particles whose pressure and velocity are determined by the BEM solver. The initial particle distance is chosen to be 0.0075m, which leads to a total of 33772 fluid particles. If the whole domain is discritized by MPS method, the fluid particle used for this geometry would be more than double of the current number. The time step is controlled by CFL condition with initial value of 0.0015s.

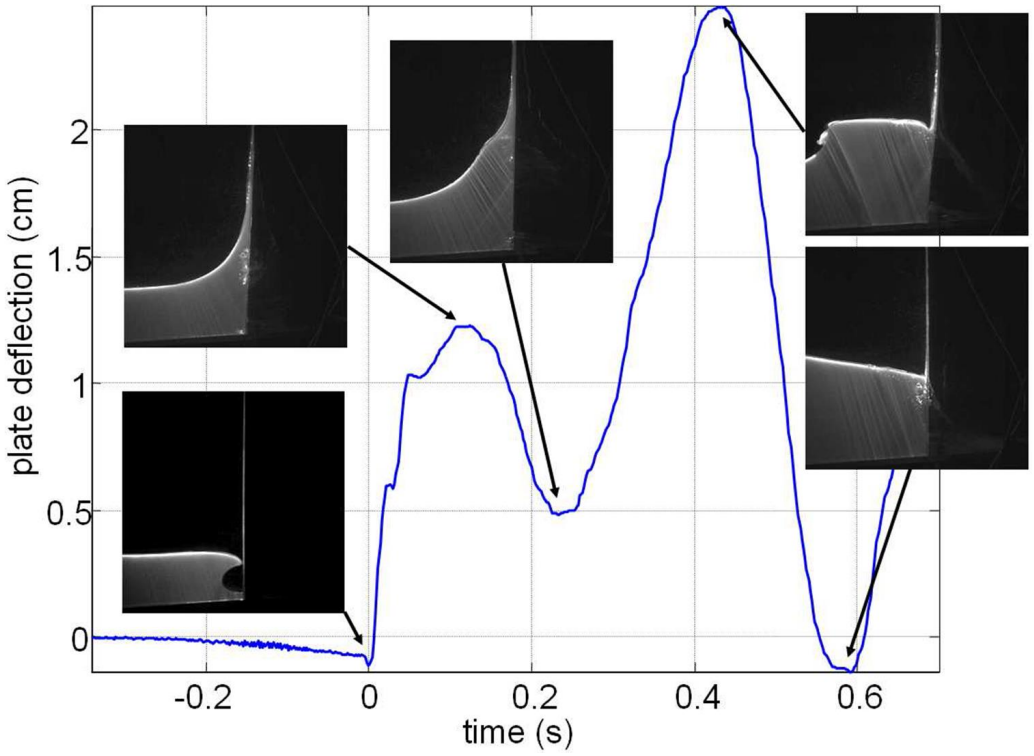

Figure 5.26: Experimental results of the plate deformation and wave profiles at some typical time instants

The flexible deformation of the plate is modeled as a beam and computed by modal superposition approach. And the first 3 principle modes are used in the simulation. The time history of the plate deformation at 0.3623m from the plate bottom and the wave profiles of some typical time instants, from the experiment [67] and the proposed BEM-MPS model are shown in Figure 5.26 and Figure 5.27, respectively. The major trend of these two deflection time history curves match each other very well. The two peaks of the deformation occur at about 0.12s and 0.43s in the experiment, whereas in the numerical result the times for these two peaks are 0.10s and 0.414s. The wave profiles for the corresponding time instants are very similar as well.

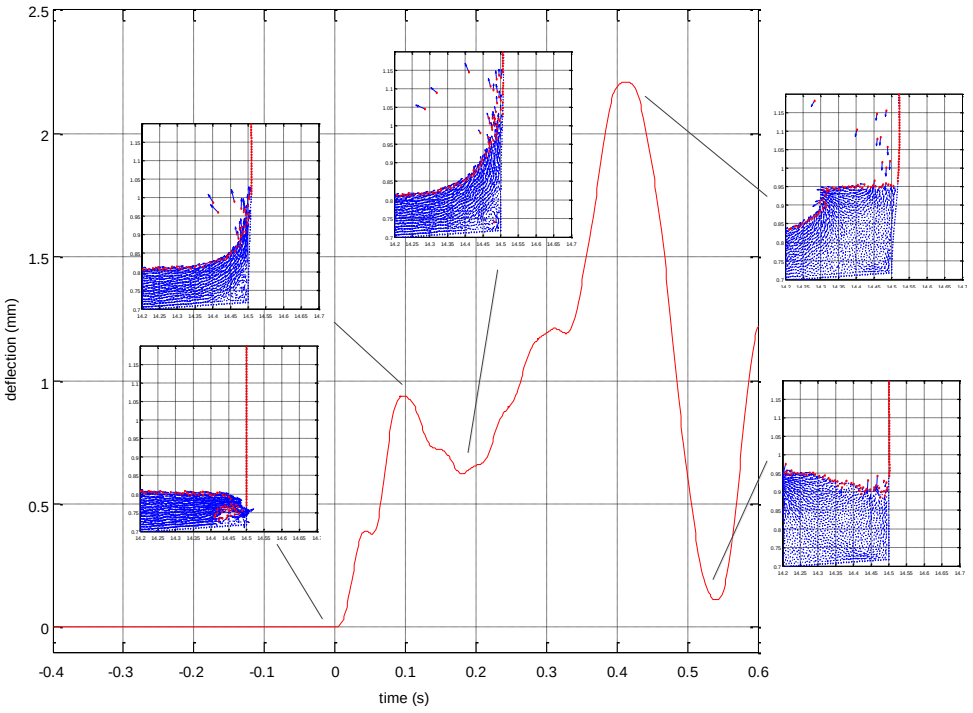

Figure 5.27: Coupled BEM-MPS results of the plate deformation and wave profiles at some typical time instants

The comparison of deflection time history at the same position between experiment, other numerical approach (MLPG_R) [139] and the proposed BEM-MPS coupling model is shown in Figure 5.28. As discussed in [139], the reason of the negative deflection before the impact of the breaking wave in the experimental result is unclear. This may due to the way of mounting the plate at the bottom. Besides that, although the main trend of these three curves are quite similar, there are inevitablly some discrepancies between them. The first peak value of both numerical results are lower than the experimental one. For the second peak, the value from proposed model is slightly lower than the experiment and MLPG_R. Also, the second trough from proposed model is slightly earlier than others. These differences between numerical and experimental results could be due to various reasons such as the leakage of water from the wave-maker and plate in the experiment [139].

In terms of efficiency, compared to another particle method, i.e. MLPG_R [139], where the whole domain is discretised by a similar resolution with 86670 fluid particles (compared with 33772 fluid particles in this simulation), this problem

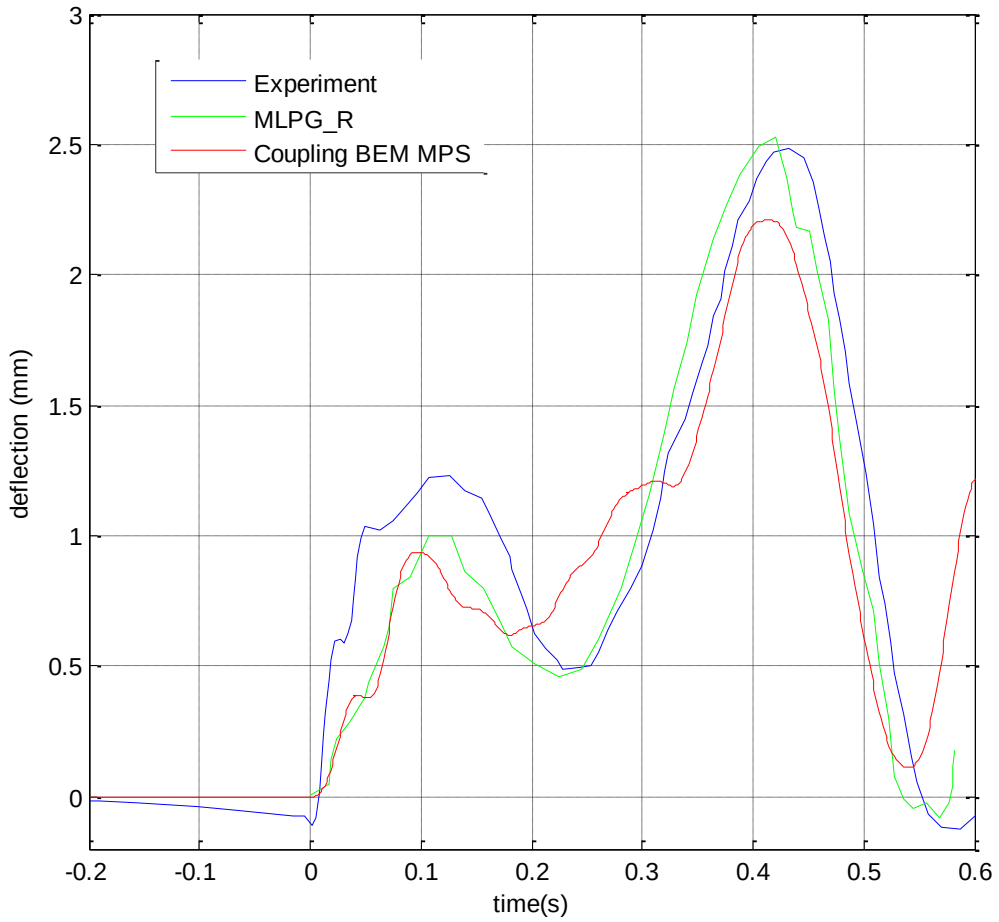

Figure 5.28: Comparison of the plate deflection at $0.3623m$ from the plate bottom between experiment [67], MLPG_R [139] and proposed BEM-MPS coupling

is solved more efficiently by the proposed BEM-MPS coupling approach with similar accuracy achieved.

The BEM wave profiles and MPS pressure contours are shown in Figure 5.29. The BEM simulation stops at $t = 8.821s$ i.e. (c) or (d) in Figure 5.29 as explained before, so the BEM wave profile remains the same from Figure 5.29 (d) to (g). As is shown, the pressure distribution from the MPS simulation is smooth. Figure 5.29 (d_1) highlights the pressure distribution when the wave impacts the plate. It is worth mentioning that a small "jet-like" flow has been developed as highlighted by Figure 5.29 (g_1). This physically unreasonable phenomena could be due to the fact that MPS field gradually starts to flow backward while the interface particles remain the status when BEM simulation stops (i.e. $t = 8.821s$ in (c) or (d) of Figure 5.29), so the fluid particles will be "squeezed out" a bit

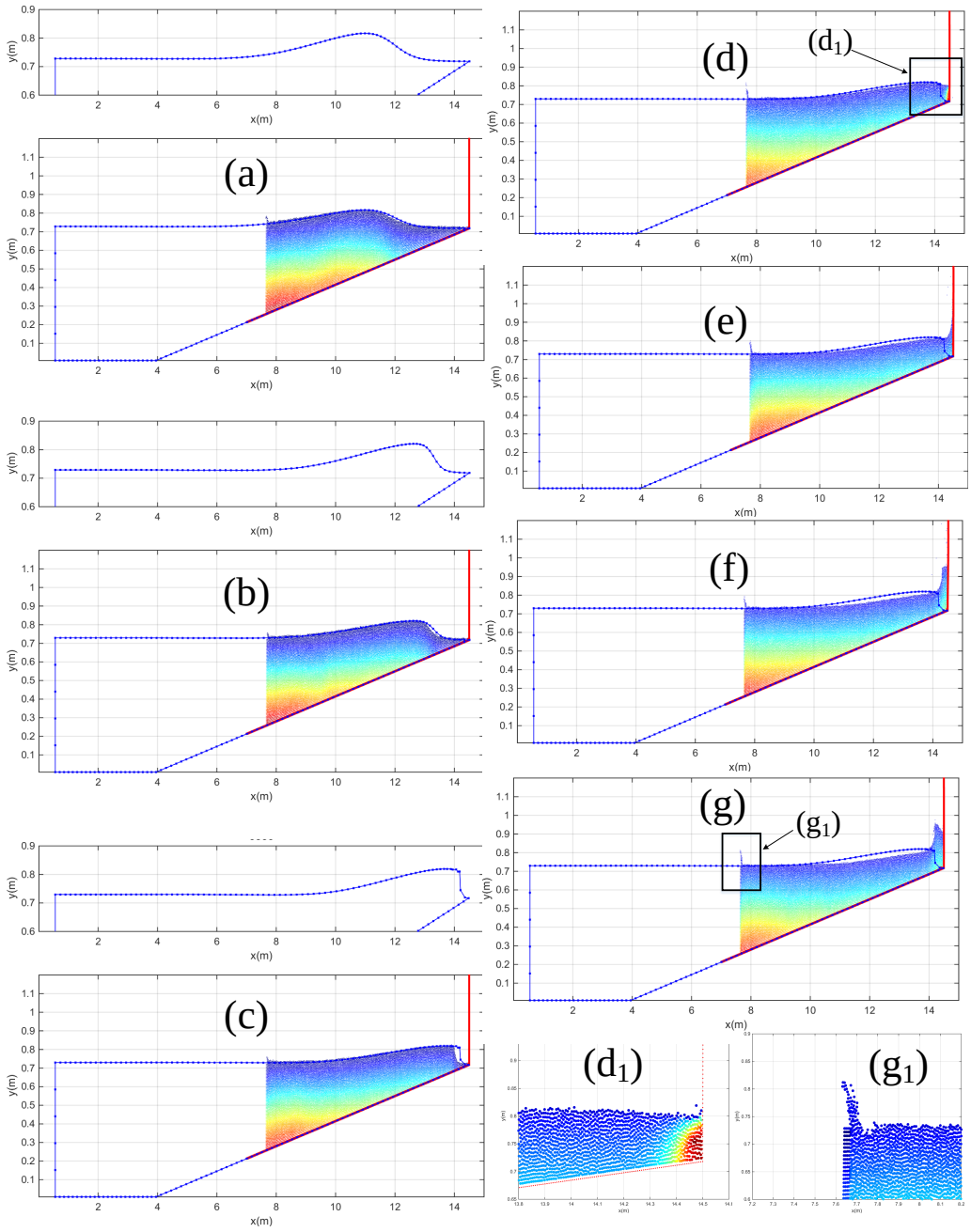

Figure 5.29: Wave profiles and the pressure contour of the BEM and MPS simulation at various typical time instants

more near the interface area. However as shown in the above results, the main flow characteristics near the plate and the flexible plate deformation have both reached an acceptable accuracy compared to the corresponding experimental or other numerical results, which is the major concern of this simulation. This means if we consider the balance between the efficiency improvement and the accuracy level it can get, this weak coupling between BEM and MPS is capable to simulate this kind of locally violent flow problems. But obviously a strong

coupling, i.e. the BEM solver only covers part of the computational domain and depends on the information from MPS solver at interface, would be an advanced and better choice in the future.

Chapter 6

Hydroelasticity computation results

6.1 Symmetric flexible wedge dropping

The case of flexible wedge dropping are simulated and discussed in this section. Figure 6.1 shows the initial configuration of the problem. The numerical results are also compared with the experimental data provided in [118]. Considering that during the period after releasing from height H^* and before touching the free surface, the flexible bottom will also develop a small amount of deformation. Therefore, in order to make the simulation more consistent with the real experimental condition, the simulation is started from the releasing instant, as shown in Figure 6.1.

In this study, three different cases are simulated. The related parameters of the flexible wedge are listed in Table 6.1.

The first three modes are taken into account and the corresponding first three circular frequencies are calculated by the beam Euler beam theory. (e.g. for case 1 and 2 in Table 6.1, the first three circular frequencies are: $\omega_1 = 96.2104$, $\omega_2 = 602.9434$ and $\omega_3 = 1688.2579$).

The fluid field is discretised by particles with the initial space of $0.005m$, which corresponds to 38400 fluid particles (40122 particles in total). The time interval is determined by the CFL condition with a maximum limit of $0.0002s$. With an average iteration number of 6.5 times for each FSI coupling time step, about 22 CPU hours' time are required for the simulation of $0.06s$ physical duration using the same computer hardware, as described in Chapter 4 For the simulation, it is worth mentioning that the majority of the computational time is used for the

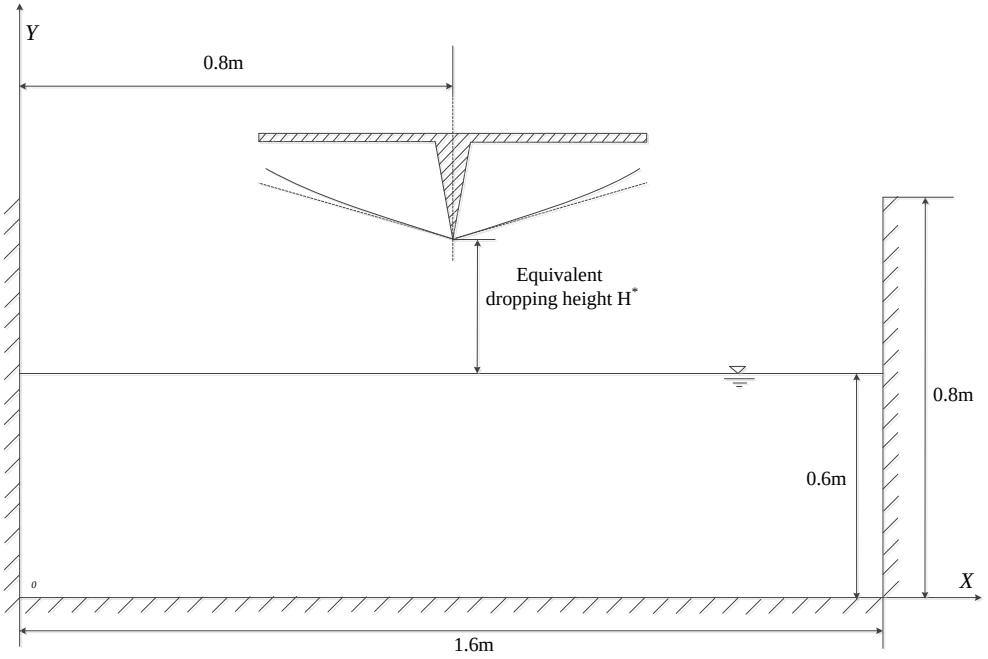

Figure 6.1: Initial configuration of the wedge dropping problem

Table 6.1: The parameters used in the flexible wedge dropping simulation

	Case 1	Case 2	Case 3
Material	E-Glass (woven)/epoxy		Aluminium
Young' modulus E (GPa)	30.3		68
Density ρ (kg/m^3)	2015		2700
Mass of the rig (kg/m)	22		
Length of each bottom L (m)	0.3		
Thickness (mm)	2.2		2
Deadrise angle β ($^\circ$)	30		
Entry speed(m/s)	4.29	5.57	4
Equivalent Height $H^*(m)$	0.938	1.5813	0.8155

fluid solver, i.e. MPS part. The time used for structure solver is neglectable considering the scale of the linear system is only 4×4, and that only one time iteration is required for an order of 10^{-5} computational accuracy.

The accelerations of the flexible wedges that are calculated by the coupled Modified MPS and CRMS model are compared with the results from experiment [118], rigid-body simulation and Wagner's theory in Figure 6.2, respectively.

The rigid-body computation is conducted by the normal routine for 2D situation, as derived in Section 3.2.3.1. Since the motion in X direction is also constrained due to the symmetry property as in flexible cases, only the equation corresponding to Y part in Eq. (3.84) is required to be solved.

As shown in Figure 6.2 (a) and (b), the numerical results agree well with the experimental data in terms of both the main trend and the first impact pressure peak time. In contrast to the rigid case in Figure 6.2 (c) and (d), there is a trough in both the experimental and numerical results for flexible cases in Figure 6.2 (a) and (b) (at about $0.025s$). Another distinguished feature in flexible cases is that after the trough of the curve, the acceleration tends to oscillate around a constant value until the end of the simulation. The numerical model gives an overshot for the second peak acceleration value. And the peak time is also earlier than the experimental data. This is probably caused by the 2D limitation, since the water cannot be pushed aside along the tip direction like in real 3D environment and consequently the improper gathering water could generate a higher pressure. The difference of the dynamic characteristics between 2D beam assumption and the real 3D plate used in the experiment (e.g. different natural frequency) might be another reason of the deviation shown in Figure 6.2 (a) and (b).

The pressure and velocity contours are shown in Figure 6.3 and Figure 6.4, respectively. Due to the flexibility of the wedge bottom, the cavitation starts to develop from roughly $t = 0.02s$ and vanishes at about $t = 0.04s$. Because the current model only involves the water phase, the dynamics which is caused by the entrapped air between the wedge bottom and water could not be captured correctly. This is probably the reason that the numerical accelerations in Figure 6.2 (a) and (b) show a larger fluctuation during the cavitation period.

Figure 6.5 shows the deformation of the flexible bottoms at some typical time instants. During the initial stage of the impact, the bottoms are bended by the coupling effect of the inertia and the concentrated impact force near the wedge tip. After about $t = 0.02s$, the deformation of the beam starts to bounce back towards the symmetry line of the wedge. This process is also reflected in the time history of strain that is monitored at two different locations on upper surface of each bottom, i.e. $30mm$ and $120mm$ away from the wedge tip respectively, as is shown in Figure 6.6. The positive part of the strain in Figure 6.6 (b) (monitored at $120mm$, which is about the middle of the bottom) represents the initial bending stage, as is shown in Figure 6.5. After that, the strain remains negative because of the pressure of the surrounding water. The modified MPS

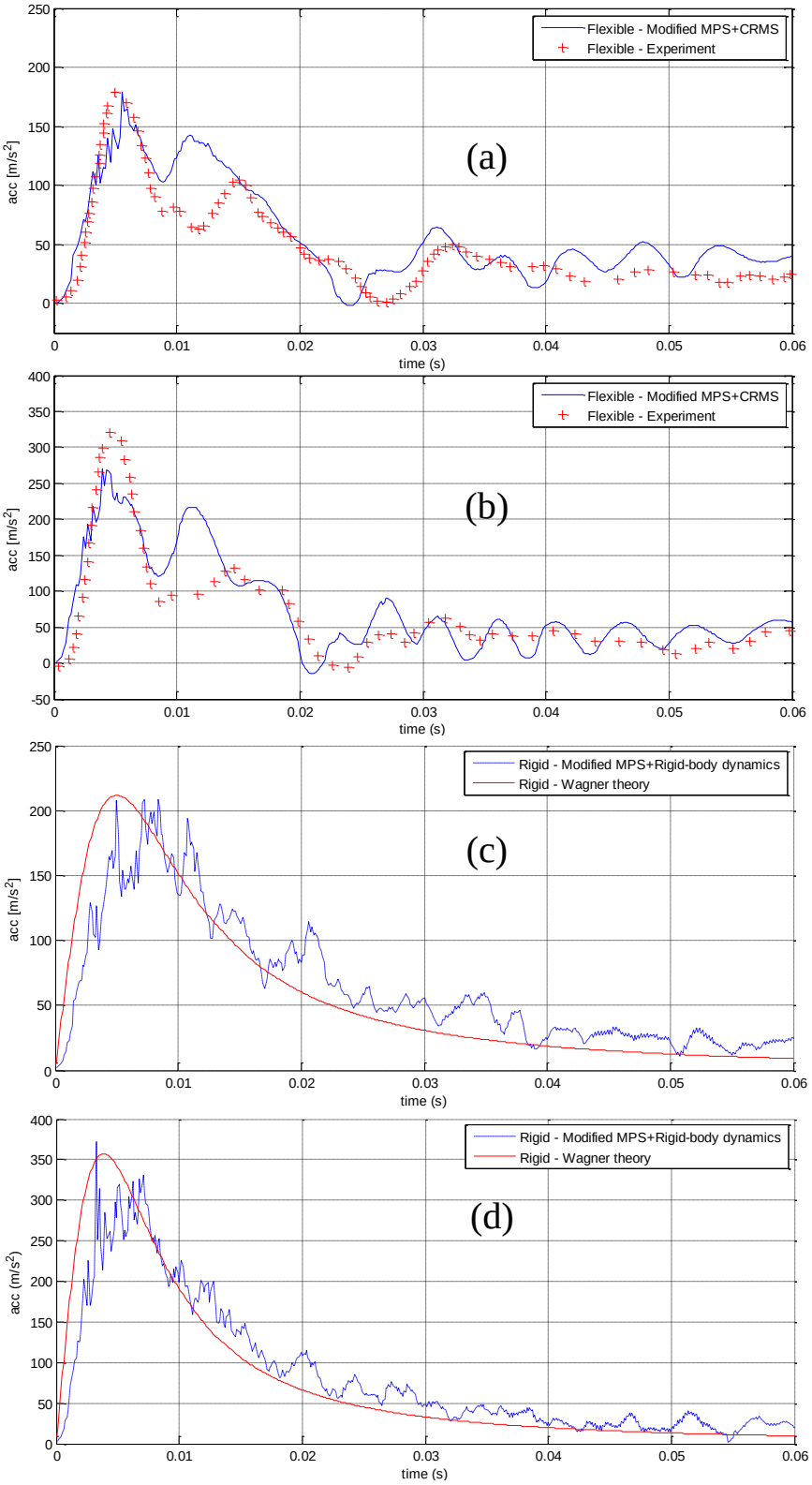

Figure 6.2: The acceleration of the flexible/rigid wedge: (a) comparison for Case 1 between Modified MPS+CRMS and Experiment [117];(b) comparison for Case 2 between Modified MPS+CRMS and Experiment [117]; (c) comparison for rigid wedge between Modified MPS+Rigid-body dynamics and Wagner's theory with the same entry speed as in Case 1 (4.29m/s); (d) comparison for rigid wedge between Modified MPS+Rigid-body dynamics and Wagner's theory with the same entry speed as in Case 2 (5.57m/s)

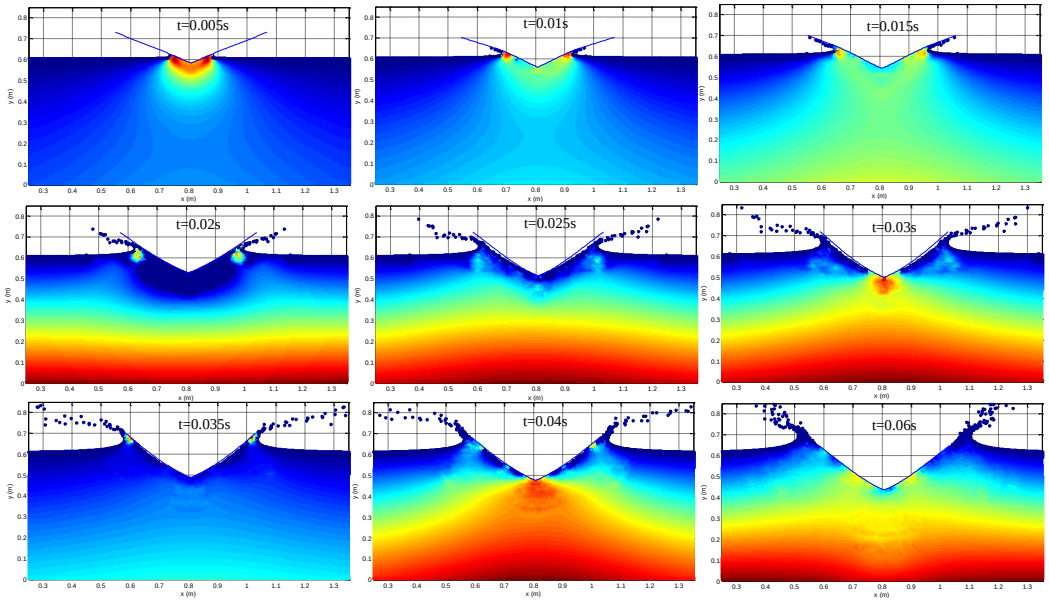

Figure 6.3: The pressure contour at different time instants for Case 2

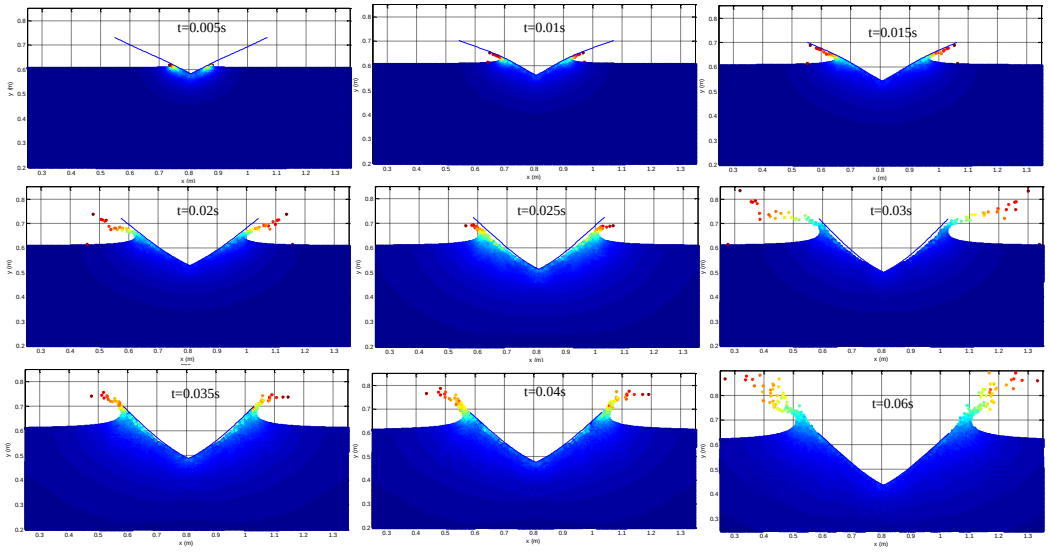

Figure 6.4: The velocity contour at different time instants for Case 2

results match reasonably well with experimental results that the SPH ones [117].

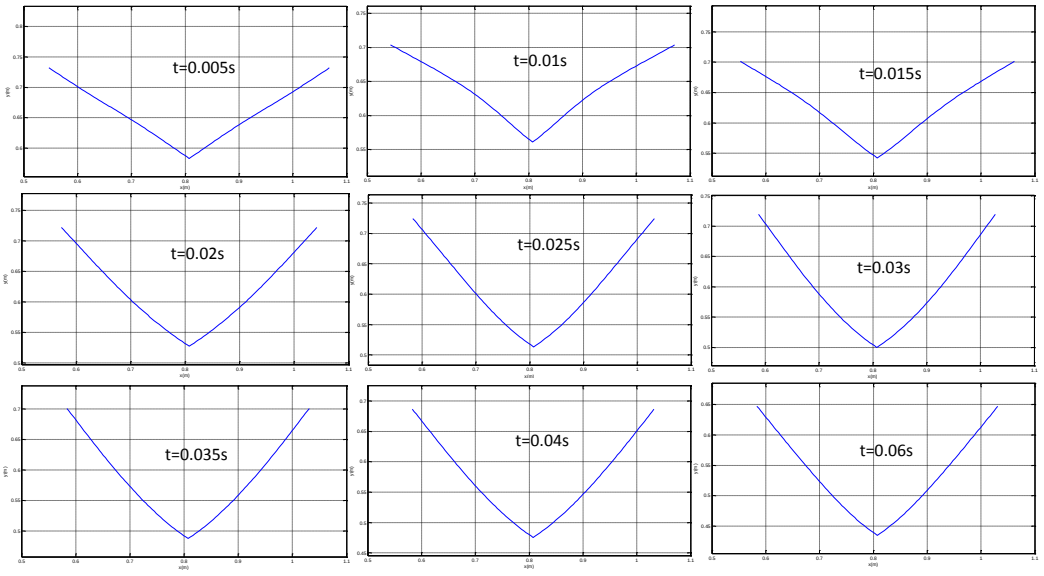

Figure 6.5: Deformation of the flexible bottom at different time instants for Case 2

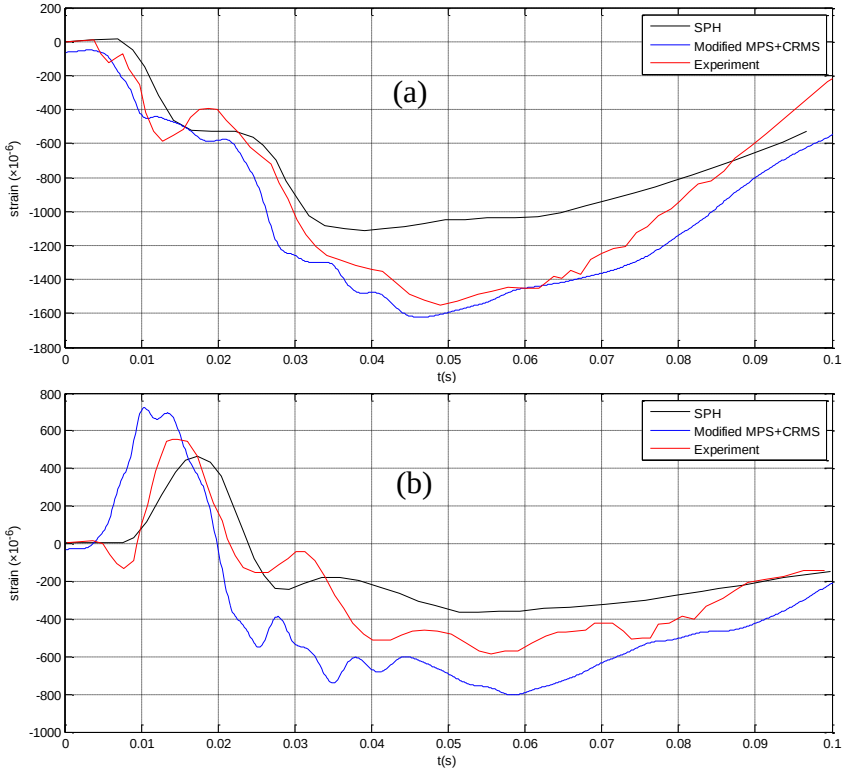

Figure 6.6: The comparison of strain results for case 3 between experiment [117], Modified MPS+CRMS and SPH [117] at different positions ((a) and (b) corresponds to 30mm and 120mm from the wedge tip respectively)

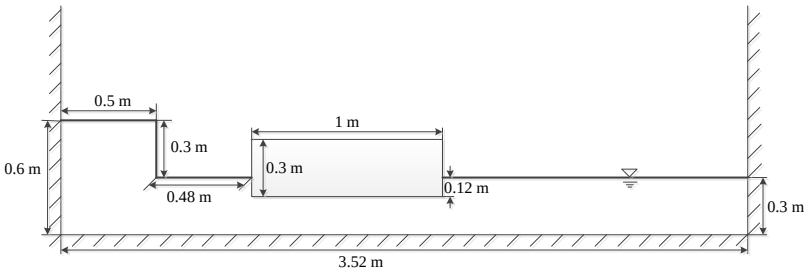

Figure 6.7: Initial configuration of 2D free floating beam slamming problem

6.2 Slamming of floating flexible beam

6.2.1 2D case

The case of a break-dam hitting floating flexible beam is calculated as shown in Figure 6.7. The simulation starts from the equilibrium state in which the beam gravity is balanced out by the water buoyancy.

For the beam structural property, two cases with different flexibility (i.e. bending stiffness) have been simulated by the proposed model. The conditions are as follows:

Case 1 (High flexibility):

Bending stiffness $EJ = 4.5N/m^2$; density $\rho = 400kg/m^3$; and the first three nature circular frequencies are: $\omega_1 = 4.3325$, $\omega_2 = 11.9429$ and $\omega_3 = 23.4128$

Case 2 (Low flexibility):

Bending stiffness $EJ = 4.5 \times 10^2 N/m^2$; density $\rho = 400kg/m^3$; and the first three nature circular frequencies are: $\omega_1 = 43.3249$, $\omega_2 = 119.4288$ and $\omega_3 = 234.1281$

The fluid domain is discretized by particles with an initial distance of $0.02m$. The total fluid particles number is 2643. The time interval is determined by the CFL condition with an upper limit of $0.001s$.

The physical duration is 5 seconds (about 5000 time steps). Each of the two cases requires approximately 2 CPU hours' time using the same computer mentioned before.

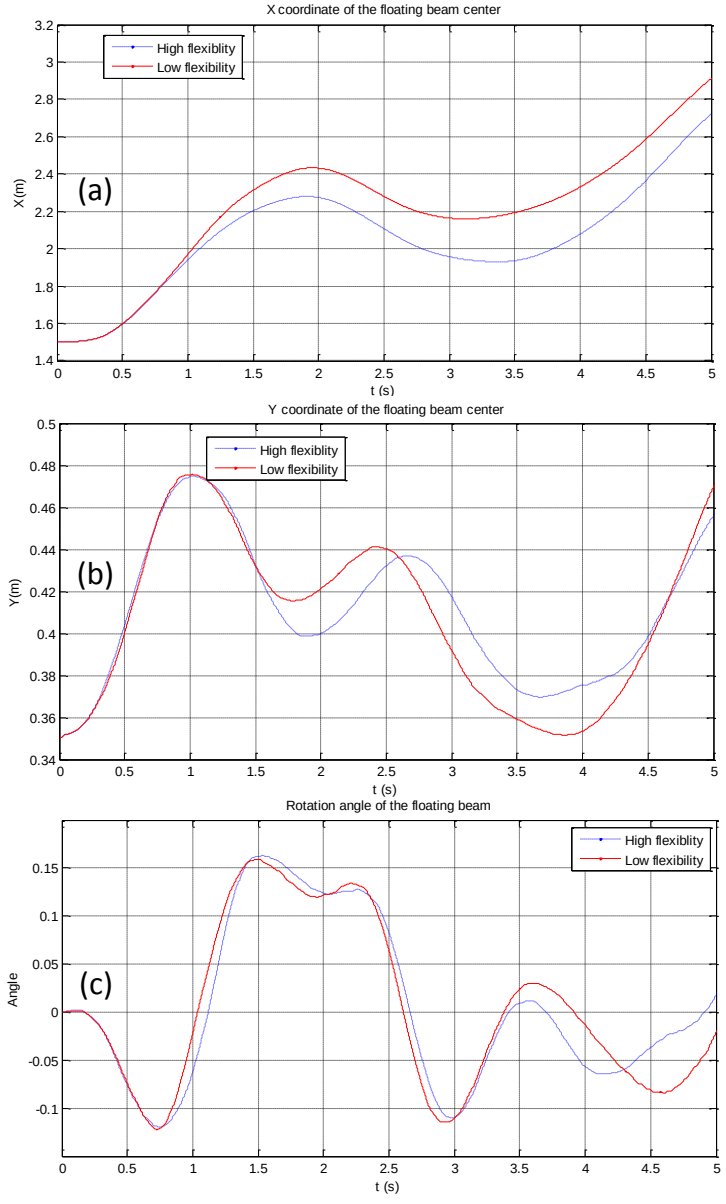

Figure 6.8: Comparison of the rigid-body motion time history for different flexibilities: (a) X coordinate of mass centre; (b) Y coordinate of mass centre; (c) Rotation angle round mass centre

The comparison of high and low flexibility cases are given in Figures 6.8 and 6.9. For the rigid-body motion part, the effect of flexibility is accumulated to a remarkable level during the simulation period, especially for the translational variables (Figure 6.8 (a) and (b)). This shows that for violent water flexible structure interaction problem, the coupling term should be taken into account to get accurate overall trajectory.

For the elastic motion part, as is shown in Figure 6.9, the values for low flexibility are much smaller than that of high flexibility, as expected. The oscillation frequency at the far-end quarter is higher than the ones for middle or far-end of the beam, which means the 2^{nd} or 3^{rd} modes contribute more at that position compared with others. This is consistent with the mode shape distribution at corresponding positions. More specifically, at the far-end quarter, the amplitude of 1^{st} order mode shape is very close to zero, whereas the amplitude of the other two mode shapes roughly take their maximum value at this position. The middle and far-end are the positions where the 1^{st} order mode displacement is the dominating part.

The beam response to the slamming impact can be recognized clearly from the time period between roughly $t = 0.3s$ and $t = 1.2s$, in both the high and low flexibility cases. This shows the capability of this coupling CRF and MPS model to conduct the sea-keeping simulation along with slamming/whipping event in the process at the same time.

The pressure contour of the fluid field and the deformation of the beam for the two cases are depicted in Figure 6.10. As is shown, for both cases there is no singular point in the fluid field and the pressure field is quite smooth. The interaction between beam and fluid motion is physically reasonable as well.

The structure solver turns out to be quite efficient. For most of the time, only one time iteration is required for the Newton-Raphson method to reach the convergence criteria of 10^{-5}, and the computation time for structure is negligible.

The average iteration times required for the FSI coupling is 2.8 for an accuracy of $10^{-5}m$. The accuracy of $10^{-5}m$ means the summation of the distance between new and old iteration position for all the particles on the beam surface has to be smaller than $10^{-5}m$ to be regarded as converged.

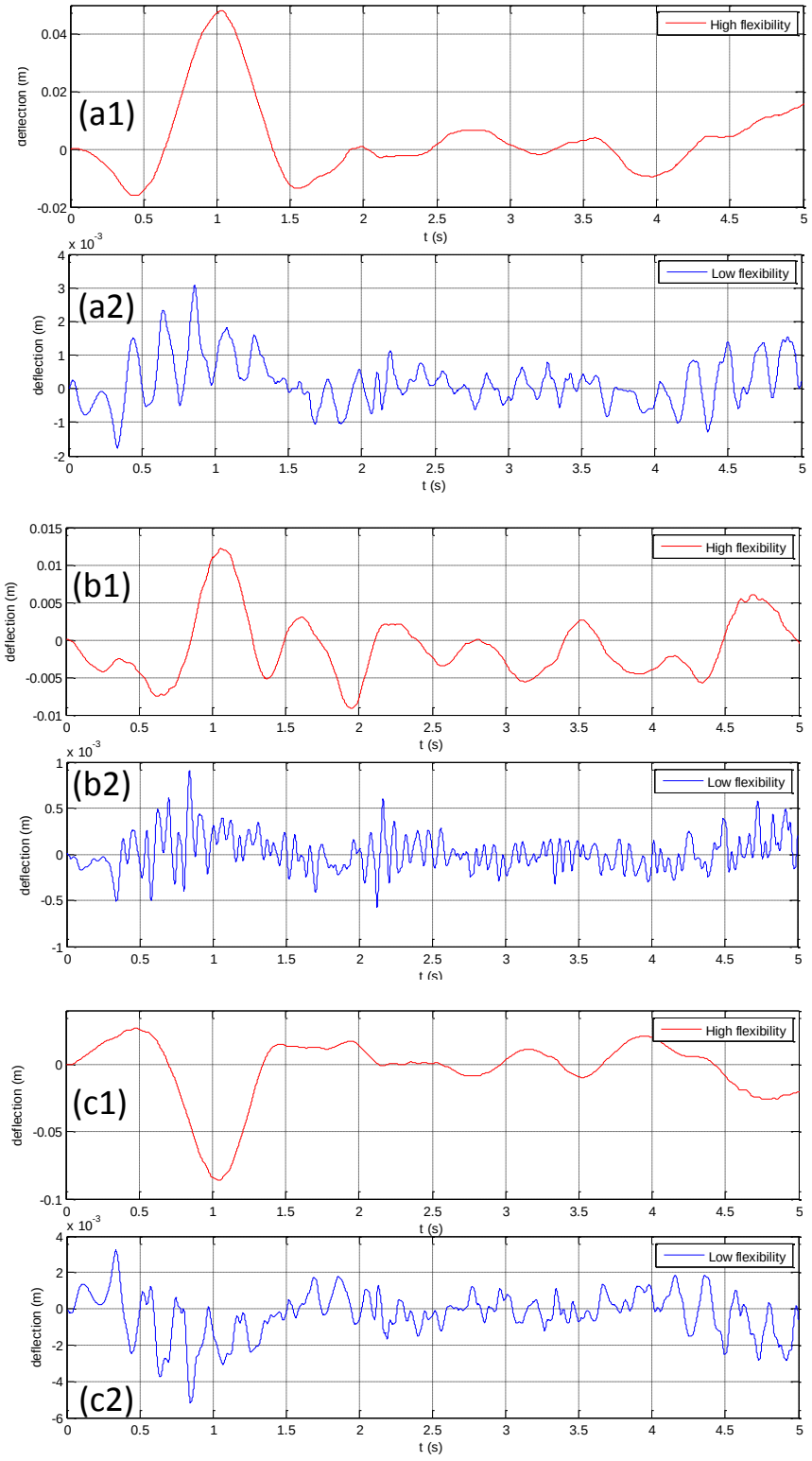

Figure 6.9: The comparison of deflection time history for different flexibilities at different positions: (a1) & (a2) middle of the beam; (b1) & (b2) far-end quarter of the beam; (c1) & (c2) far-end of the beam

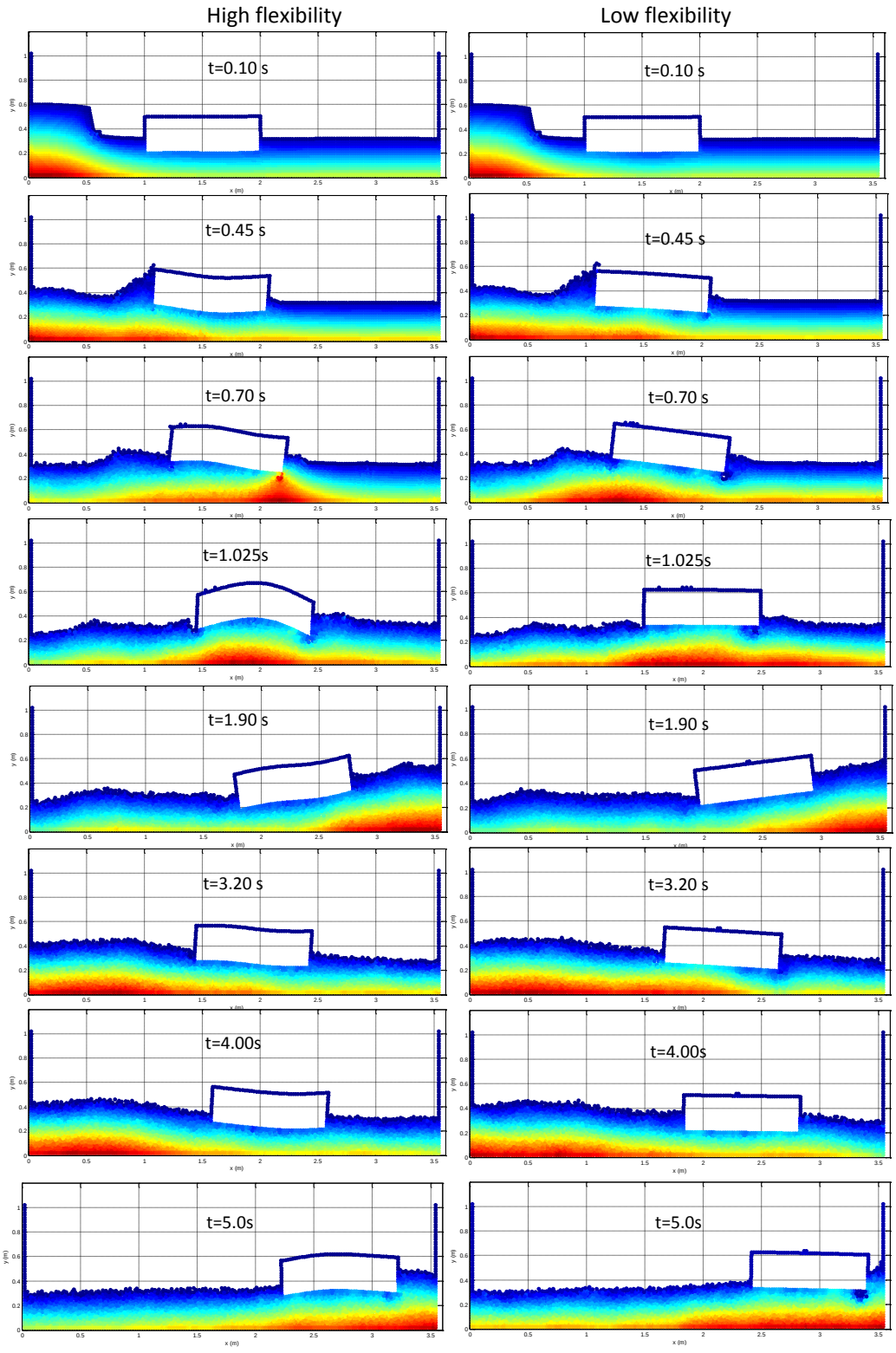

Figure 6.10: Pressure contour comparison of different flexibility

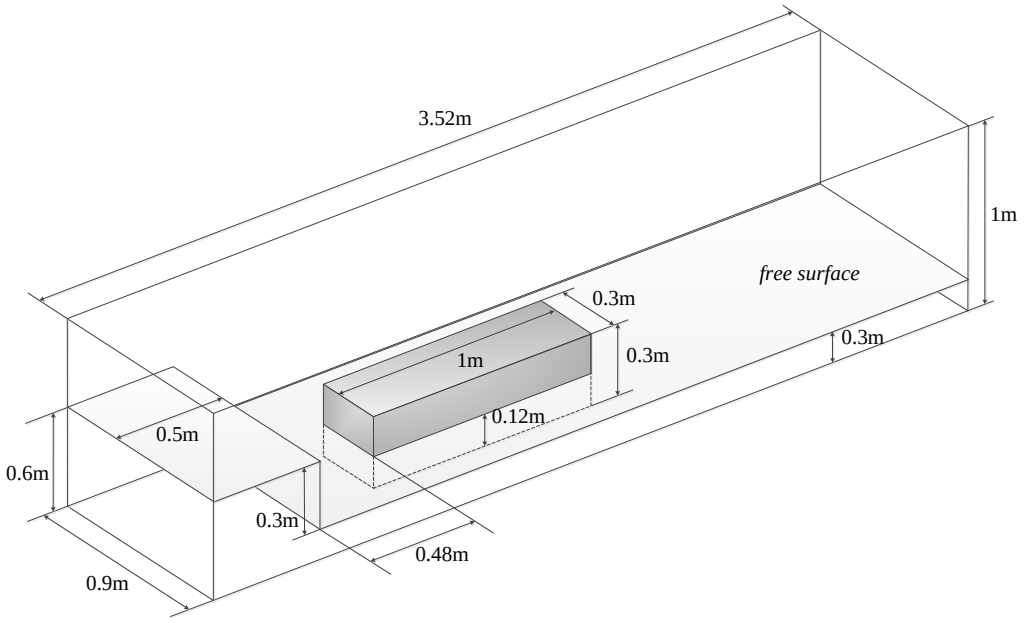

Figure 6.11: Initial configuration of the 3D flexible floating beam slamming problem

6.2.2 3D case

In this section, the 3D version of aforementioned floating flexible beam impacted by breaking dam is simulated. Compared with the corresponding 2D case, this is actually a more reasonable approximation of the slamming phenomena when the ship encounters head sea incident wave, which is one of the most important aspects to access the ship structural safety. Considering that the ship motion only occurs in the plane which is vertical to free surface and perpendicular to wave crest in this case, the 2D structure model proposed in Chapter 3 is capable to handle the structure dynamics for this 3D case.

The initial configuration of the problem is shown in Figure 6.11. All the dimensions in the vertical plane are the same as the $2D$ case. For the layout in transverse dimension, the beam with width of $0.3m$ is placed in the middle of the $0.9m$ width tank. Since the width in $3D$ is not assumed to be $1m$ anymore as in the $2D$ case, the nature frequencies of the beam change accordingly, and they are $\omega_1 = 7.9100$, $\omega_2 = 21.8046$ and $\omega_3 = 42.7457$.

The initial particle distance is chosen to be $0.02m$, which results in 126288 fluid particles and 194360 particles in total. The time step (which is the same as in the previous sections) is controlled by CFL condition. The initial value is set to be $0.002s$.

The beam condition corresponding to the High flexibility case in the $2D$ simulation is used here. For the structural model computation part, similar to the $2D$ case, only one time iteration is required to reach the convergence of 10^{-5} by Newton-Raphson method. And the computational time is also negligible.

The convergence criteria for FSI iteration is chosen to be 10^{-4}. This is chosen to let the criteria in $3D$ case to be in a similar level to the value in $2D$ case. More specifically, the number of points on $3D$ beam surface is roughly 10 times of the number in $2D$ case, so the criteria should be multiplied with a factor of 10 accordingly. The average iteration time for FSI iteration is 3.2, which is also similar to the $2D$ case.

The free surface profiles and the corresponding beam deformations are shown in Figure 6.12. The "bold" blue lines represent the beam edges that are above the free surface, whereas the "light" blue lines are the ones below the free surface. And based on the same reason as in Section 5.1.2, i.e. to highlight the free surface deformation, only the free surface particles are shown in red color.

As is shown in Figure 6.12, the free surface particles of the fluid domain are correctly identified by the 3D scheme proposed in Section 2.3.2.4. For the particles on the beam edge, most of the ones below the free surface are correctly identified as non-free surface particles. For the faces close to splashing area (such as the impacting side in (c) and the trailing side in (f)), the identification indeed generates a stagger distribution of free surface and non-free surface particles. However, this is consistent with the fact that the fluid distribution around those splashing area is indeed in a mixture state of water and air (void in this study since it is a single phase model).

The interaction process between the impacting wave (which is generated by the collapsed dam) and the beam is also shown in Figure 6.12. The deformation process of the beam is consistent with what would be expected in the real physical circumstance.

6.3 Slamming of 3D flexible ship

In the final case, in order to test the performance of the proposed fluid and structure models under practical complex geometry condition, the slamming problem of a scaled oil ship is simulated. The body plan of the 1 : 100 model of

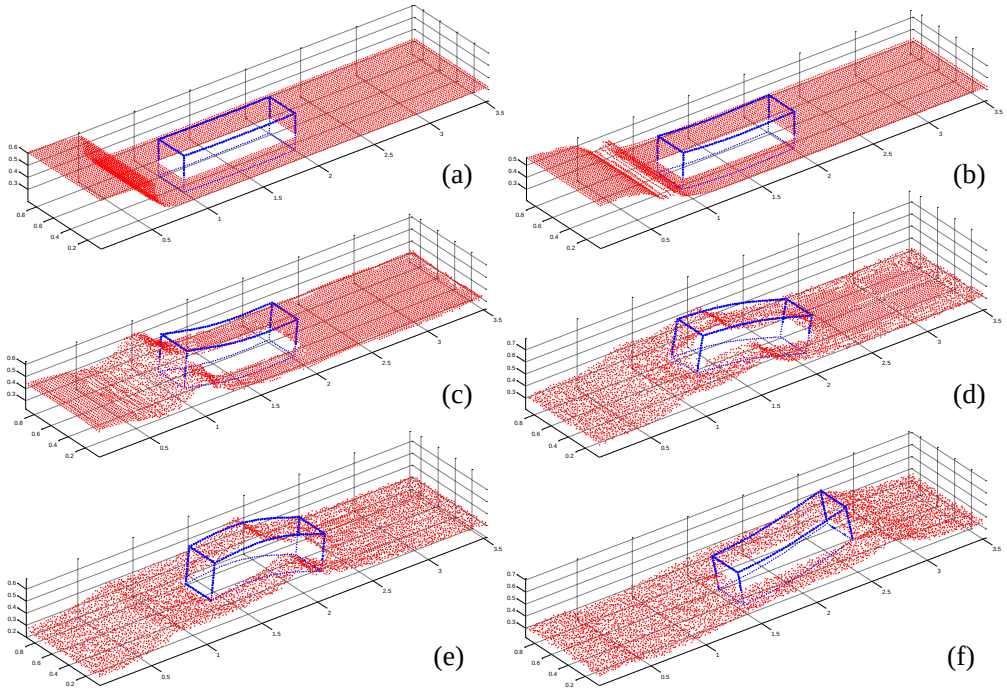

Figure 6.12: Free surface profiles and beam deflection of 3D slamming at some typical time instants: (a) $t = 0.1s$, (b) $t = 0.2s$, (c) $t = 0.418s$, (d) $t = 0.684s$, (e) $t = 0.864s$ and (f) $t = 1.282s$

Table 6.2: Main parameters of the ship model

Length $L_{PP}(m)$	1.8
Width $B(m)$	0.322
Draught $T(m)$	0.12
Mass (kg)	54.99

46000 tones oil ship is shown in Figure 6.13. The main parameters of this model ship is given in Table 6.2.

The original station interval in the above body plan is $0.087m$. In order to make the particle distribution on the ship surface to have roughly the same particle interval as the fluid domain, the station distribution along the ship is first refined with the same particle interval used for fluid discretization (i.e. $0.02m$). Each of the resultant station is then further refined with the same interval (i.e. $0.02m$) by spline interpolation. Finally, the ship surface is discretized with 4289 particles as shown in Figure 6.14.

The mass distribution of the ship is set to be consistent with the buoyancy distribution, which means the "lumped" mass for each refined station is considered to be equal to the mass of the displaced water "strip" between adjacent stations.

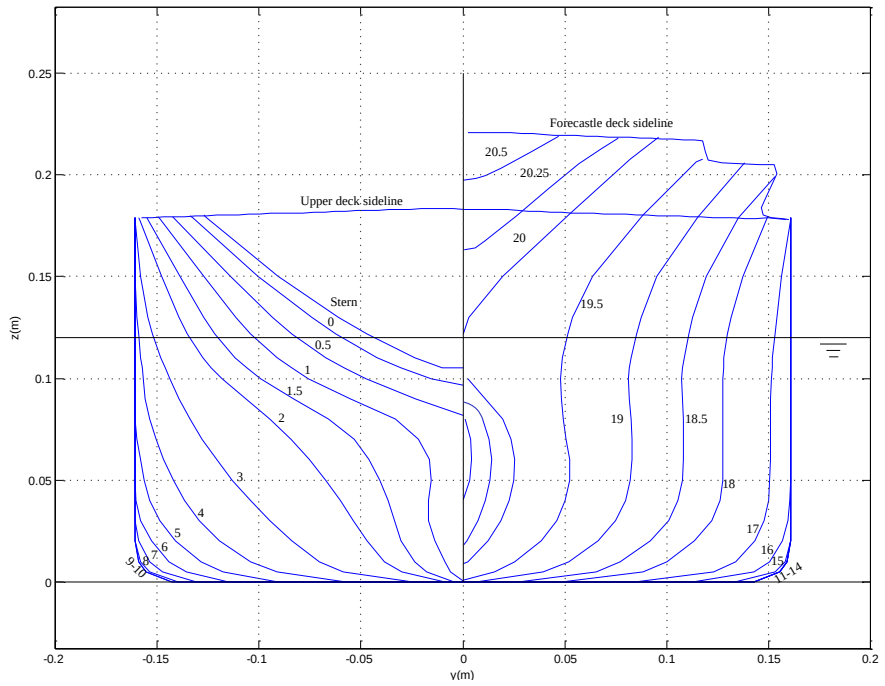

Figure 6.13: The body plan of the 46000t oil ship

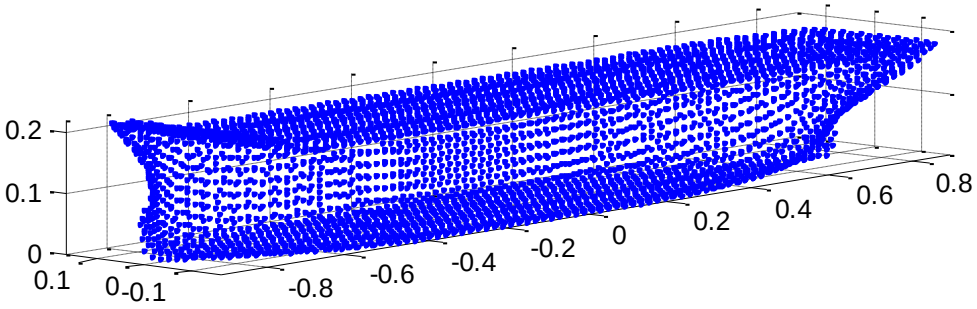

Figure 6.14: The final discretization of the ship surface

The resultant mass center is located at 0.0404m to midship towards bow direction.

The ship hull thickness is chosen to be 0.05m for the 2^{nd} moment calculation of each cross-section. Consequently, the lumped mass and 2^{nd} moment of cross-section distribution of the ship model are shown in Figures 6.15 and 6.16.

After applying the so-called Myklestad's method (see details of implementation in Appendix C), the mode shape functions of the first 3 modes are shown in Figure 6.17. The mode shapes are similar to the ones of uniform beams in

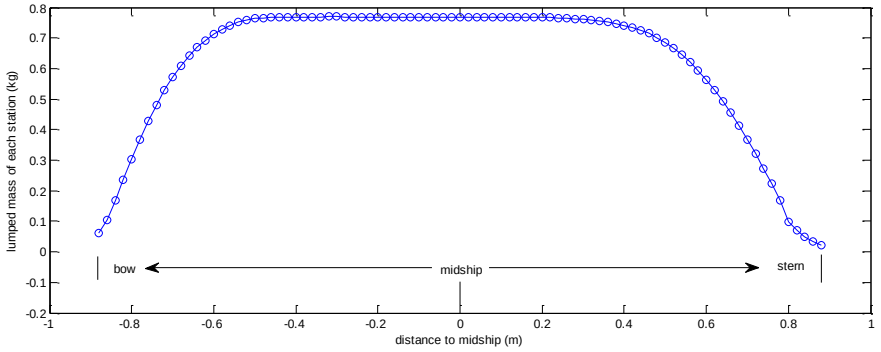

Figure 6.15: The lumped mass distribution along the ship model

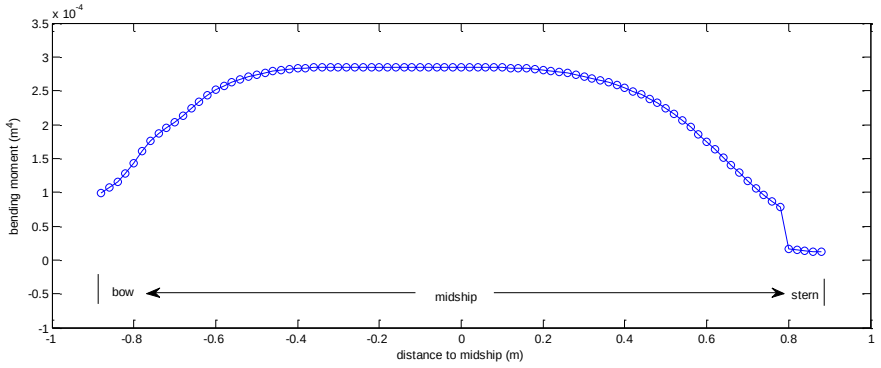

Figure 6.16: The moment of inertia distribution along the ship model

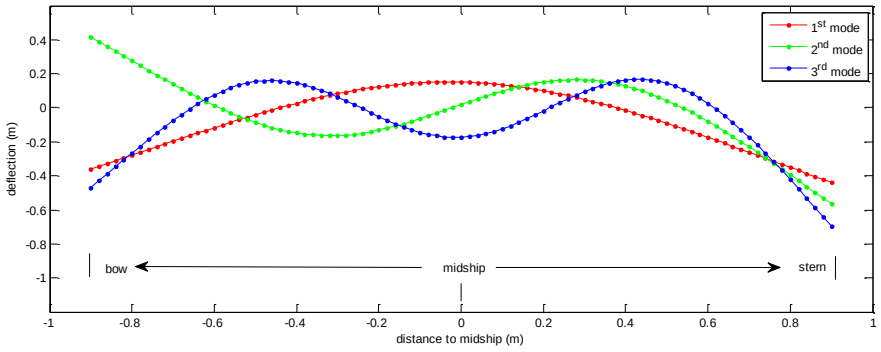

Figure 6.17: The first 3 mode shapes of the ship model

general, but the distribution near both ends have clearly been modified due to the non-uniform mass and inertia moment distribution.

The first three circular frequencies corresponding to $E = 2 \times 10^4 N/m^2$ are:

$\omega_1 = 3.78574, \quad \omega_2 = 9.7777$ and $\quad \omega_3 = 18.2063.$

The parameters of the tank are almost the same as the ones shown in Figure 6.11, the only difference is the length of $5.5m$ instead. The ship is placed in the same position as well, i.e. the distance between bow and tank wall is $0.98m$. The fluid field and tank boundaries are evenly discretized with interval of $0.02m$, which result in 193284 fluid particles and 289417 particles in total.

Similar to the $3D$ beam case mentioned before, the computation time of the structure model take on average one or twice iteration to reach 10^{-5} accuracy by Newton-Raphson method with negligible computational time.

Considering that the length of the ship model is roughly twice of the 3D beam in Section 6.2.2, the convergence criteria of the FSI iteration is chosen to be twice of the beam case, i.e. 2×10^{-4}. The average iteration time for this ship case is 2.49.

The free surface profiles and ship vertical bending motion at some typical time instants are shown in Figure 6.18. The surface marked by blue is the part above the water on the ship, while the black color area represents the "wet" surface of the ship. It is clear that the free surface identification scheme works well for the complex ship surface as well as the rectangular beam one in last section.

For the fluid part, again only the free surface particles, which are marked by red color, are shown to highlight its deformation. As shown in Figure 6.18, non inner fluid particles are falsely identified as free surface, which proves that the $3D$ free surface particle identification scheme can provide accurate results for the wave and complex geometry structure interaction.

From Figure 6.18, it can be seen that the amplitude of the flexible deformation of the ship is larger than what normally could happen in the real world. This specific choice of low stiffness of the ship hull structure is aiming to test the capability of the model under extreme conditions. Figure 6.18 show the full interaction process between the impact wave and ship. More specifically, Figure 6.18 (a), (b) and (c) show the developing process of the impact wave caused by the breaking dam at different times. The fact that the draught of the ship remains the same proves that the buoyancy force calculated by the MPS is accurate and stable to support the ship weight. The impact of the wave on the bow of ship occurs at $t = 0.418s$ in Figure 6.18 (c). Then the wave propagates along the ship as depicted in Figure 6.18 (d), (e) and (f). The ship deforms accordingly as the wave passing by. The crescent of the wave generate the largest bending moment, and correspondingly causes the largest deformations.

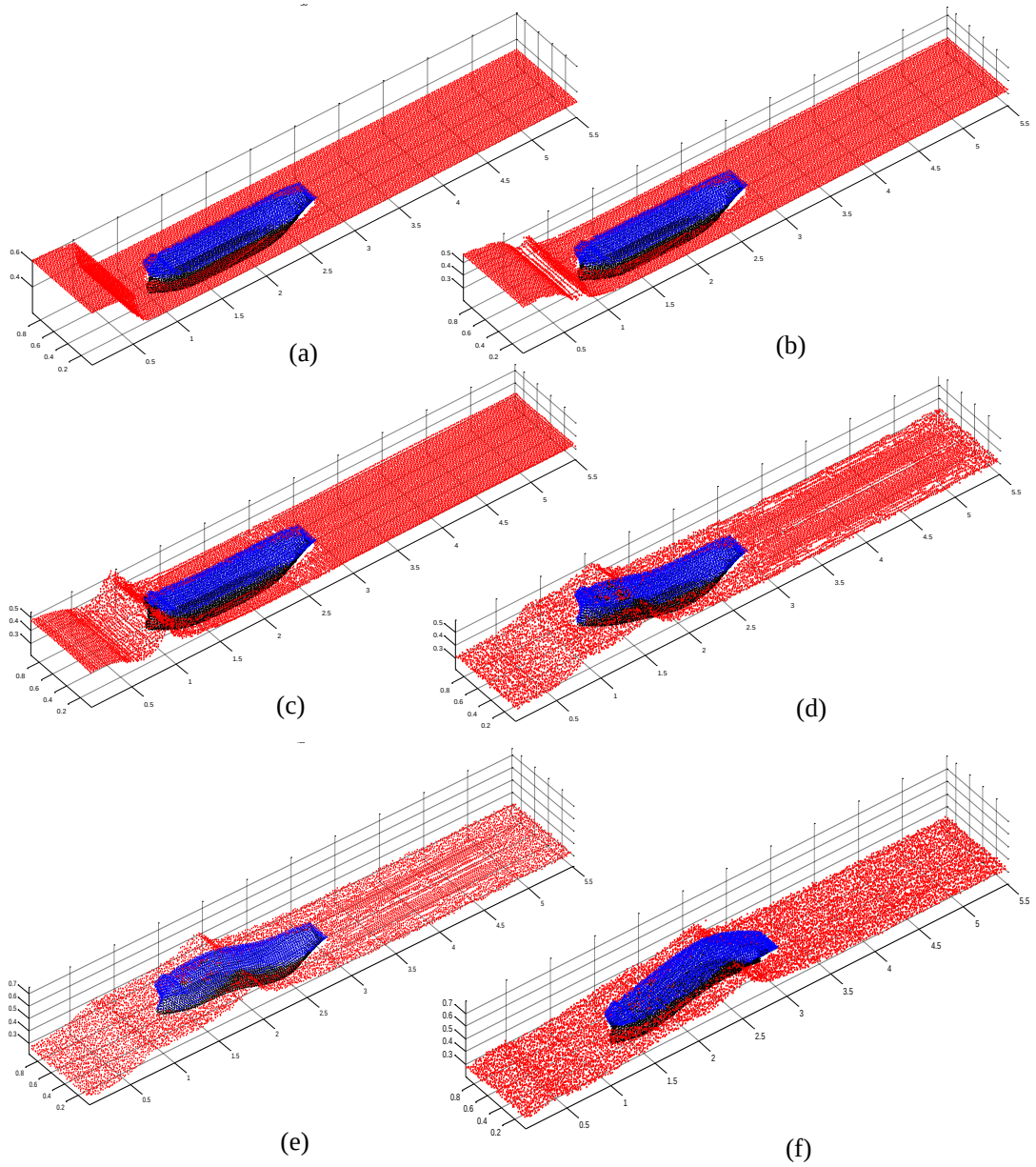

Figure 6.18: Free surface profiles and ship deflection of 3D slamming at some typical time instants: (a) $t = 0.1s$, (b) $t = 0.2s$, (c) $t = 0.418s$, (d) $t = 0.684s$, (e) $t = 0.91s$, (f) $t = 1.05s$

This qualitative analysis shows that the coupling between modified MPS and the proposed structure model is capable of providing reasonable results for the simulation of wave and structure interaction. However, more quantitative analysis by comparing against published experimental or numerical results would be required to further verify the reliability of this model in the future.

Chapter 7

Conclusions and perspectives

7.1 Conclusions

In this work, a computational model that couples particle method and modal superposition method is developed to compute the violent fluid structure interaction problems with free surface. Moreover, based on this model, a computer code was developed using *C*.

For the fluid part, the two distinguished properties of the particle method, which are mesh-less geometry discretization and Lagrangian type motion, makes it very suitable for the fluid structure interaction problems with large interface deformation such as wave-breaking and large amplitude structure motion. As a typical particle method, the MPS method has been successfully applied to many free surface flow problems. But because of the inherent shortcomings of original MPS method such as noisy pressure distribution and instability problem, various modifications have been proposed for different applications. In this study, the following modifications are proposed:

(i). New source term of density error compensation in pressure Poisson equation

Due to the nature of Lagrangian algorithm, it is inevitable that the particles will not necessarily display a perfectly uniform distribution across the whole fluid domain. The clustering and void of particles will lead to the bad pressure distribution and sometimes cause instability. To tackle this problem, a mixed velocity divergence and particle density error term are proposed to be used in the source term of pressure Poisson equation. This density error term could counteract the effect of large uneven particle distribution and consequently

improve the pressure calculation. This model is more robust than some similar compensation terms [66, 72, 82] as the calculation of this term does not involve any artificial coefficient which is often problem dependent.

(ii). New approach to handle the free surface and solid boundaries

The falsely identified free surface particle is one of the issues that contributes to the noisy distribution of pressure field. In this study, different identification schemes for $2D$ and $3D$ are proposed based on the previous work of other researchers [71, 101, 150]. In $2D$ case, a circle is assigned to each particle (with the particle as its center). If this circle is fully covered by the circles of neighbour particles, it will be regarded as a inner particle (inner fluid or solid particles under water), otherwise it will be regarded as a free surface particle. This checking process is enabled by discretizing each cirlce with 360 evenly distributed points, i.e. if all the points are covered, this circle is regarded as covered. The $3D$ case consists of two steps: a preliminary filtering by the neighbour particle number is first applied to eliminate the majority of the inner particles (again inner fluid or solid particles under the water); secondly as in the $2D$ case, a similar geometric checking process is applied to further filter out the inner particles from the result of first step. More specifically, a patch of the sphere centered by particle is checked to see whether it is fully covered by the same spheres of its neighbours. The non-fully covered case is regarded as free surface. Similar to the $2D$ case, the patch is discretized by evenly distributed points and if all the points are covered then the whole patch is regarded as covered. The position of the patch on the sphere is determined by local particle distribution and always pointing towards to the most sparse area.

For the solid boundary particles, the Neumann boundary condition is applied instead of the pressure Poisson equation. This condition means the dummy or ghost particles used in many MPS implementations is not required. For the fluid particle near solid boundaries, the MPS Laplacian operator would cover the area that goes beyond the solid boundary, where no particles are presented to support the operator. A virtual particle approach is proposed to compensate the particle distribution of this area based on the Neumann type pressure boundary condition. These virtual particles only affect the Laplacian operator of the corresponding fluid particles near solid boundary, but would not be actually generated in the geometry configuration. The last part of the solid boundary condition improvement is the intermediate velocity calculation of solid boundary particles. This intermediate velocity will affect the velocity

divergence computation of the source term in the pressure Poisson equation for the fluid particles near solid boundary. The scheme that suggested in Ref [12] is adopted in this study to calculate the intermediate velocity by considering the pressure.

(iii). New approach for particle shifting and collision handling

In order to reduce the disorder of particle distribution, which is the main sources of pressure fluctuation, a simple particle shifting approach is proposed. Only the position of the fluid particles will be shifted slightly according to the local particle distributions. No artificial coefficient will be required in the formulation. Moreover, to prevent the extreme proximity between particles, which could happen between the isolated free surface and neighbour fluid or solid particles due to the lack of pressure gradient between them, a collision handling scheme is proposed to control the relative velocity between the very close particles. The particle distribution is already quite regular due to the aforementioned modifications for pressure Poisson equation and particle shifting, this collision handling would only be applied to very few fluid particles which are isolated from the main fluid body.

(iv). New neighbour particle searching strategy

The neighbour particle searching efficiency is improved by using following two modifications to the "cell-link" approach: reducing the size of cell from supporting radius (i.e. $4r_0$ or $5r_0$) to be initial particle distance (i.e. r_0); using non-repetitive searching strategy. These two modifications reduce the searching area to be roughly 2.5/9 of the one used in traditional "cell-link" method. Because the particle distribution is roughly even over the whole domain, the number of the neighbour particles for each concerned particle is proportional to the searching area, which means the number of neighbour particles required to be searched is roughly 2.5/9 of ones in traditional "cell-link" method. The complexity of the resultant searching strategy is linear, i.e. $O(N)$

(v). To further improve the efficiency, the weak coupling between BEM and MPS are implemented for the problems where the violent free surface deformation only occurs in a constrained area. In the weak coupling scheme, the BEM covers the whole computational domain and runs until the time when free surface is about to break. The MPS solver, which also starts from the beginning but only occupy the rapid fluid structure interaction area, will continue the simulation for the post-breaking phase. The MPS solver are enabled by the information

from BEM solver (i.e. velocity and pressure) and there is no feedback from MPS to BEM. The MPS will continue to use the BEM information of the time before BEM solver stops, since the flow changing in the BEM-MPS interface area is small enough.

For the structure part, an efficient computational model is developed to handle the typical motion of a floating marine structure, which is large rigid-body motion with relatively small flexible deformation. Compared with the general FEM solution, this feature of the structure dynamics makes the modal superposition approach more efficient and hence very suitable for computing the flexible deformation. However, in the traditional Hydroelasiticity model [155] of marine engineering, the rigid-body and flexible modes are actually calculated separately. The fluid field is calculated subjecting to the rigid-body geometry of the structure and then the resultant fluid force is used to compute the flexible deformation.

In this study, by assuming the flexible structure to behave like a beam and then using the Lagrange equation of mechanics, a $2D$ computational model that couples the rigid-body and flexible motion modes (in a same set of formulations) is developed for the simulation of the structure dynamics. Unlike the traditional modal analysis, this model takes the mutual effect between rigid-body motion and flexible deformation into account. The efficiency is higher than the FE (Finite Element) method. For example, if only the first three flexible modes are considered (which is adequate for many situations), the resultant formulation is 6×6, regardless of the size of structure.

The iterative computation is conducted between the fluid and structure solvers until a convergence criteria is satisfied. More specifically, this iteration is realized by the Gauss-Seidel method with Aitken relaxation.

The aforementioned modifications to the original MPS method are first validated by a $2D$ Dam-break problem. More specifically, the efficiency improvement of the proposed neighbour searching strategy is verified, then different combination of the MPS algorithm modifications are tested to show the effectiveness of the corresponding modifications by comparing the pressure results with experimental/original ones. The convergence performance under various resolution and the mass conservation property have also been checked.

After the validation of the fluid solver, various typical violent impact problems are then simulated to demonstrate the capability of the solver for marine engineering applications. First, a series of $2D/3D$ Dam-break problems with different boundary conditions are simulated, including the cases of obstacle in the middle of tank, spring supported rigid wall and flexible cantilever wall. Then, the $2D$ liquid sloshing problem is computed and validated against experimental result in the literature. In addition, the $2D$ slamming problems of wedge-shape and ship-section-shape dropping are also simulated and compared with available experimental/numerical results from other researchers. Next, the weak coupling scheme between BEM and modified MPS is validated by a solitary wave breaking problem. And a flexible wall is also placed at the end of the slope in the tank, where the BEM-MPS coupled fluid solver interacts with the structural solver (based on the modal superposition model). The numerical result are then compared with experimental results published in the literature, and good agreement was obtained.

The Hydroelasticity computation of some typical ship structures are conducted as well. The accuracy of the proposed structural model is first tested on a $2D$ symmetric flexible wedge dropping problem. The dynamics of the wedge motion and deformation are analyzed and validated against experimental results from other researchers. Then the problem of $2D/3D$ floating flexible beam impacted by breaking-dam is simulated to test the performance of slamming between slim ship-like structure and breaking waves. Finally, in order to test the performance for complex geometry of the structure, a $3D$ typical oil tanker geometry is used to simulate the slamming problem with similar configuration as the beam case.

Although the proposed models for both fluid and structural solvers have been successfully applied to various problems as mentioned above, there are some limitations as well. First, no turbulence models are adopted in the MPS solver, because the problems investigated in this thesis are high Reynolds number and short duration cases where the turbulent effect does not play an important role in the flow dynamics. The computational cost is another shortcoming of particle methods or even for CFD in general. Using the hybrid solver between BEM and MPS, the strong coupling will surely be more accurate than the current weak coupling approach, as the pressure results from MPS are still not smooth and accurate enough to provide the feedback for BEM solver. For the structural model, it can only consider the $2D$ deformation such as vertical bending as

shown in Chapter 6 (though it is one of the most important features of ship hull structure).

7.2 Recommendation for future work

For large scale industrial problems, the parallelization of the fluid solver would become necessary. From perspective of high performance computing, the MPI (Message Passing Interface) and OpenMP (Open Multi-Processing) techniques [102] are both popular ones that have been successfully applied to various meshless or mesh-based solvers. The using of GPU (Graphics Processing Unit) [48] on the other hand is an alternative hardware-based parallelization approach.

The multi-resolution simulation is another way of improving the computational efficiency by using more economically domain discretization. Generally there are two types of implementation of multi-resolution computation. The first one is using two different uniform resolutions to cover different parts of computational domain [5, 132]. Alternatively, the resolution could vary continuously from the dense area (where flow dynamics is rapid) to the coarse area (where the flow variables change very gently) [113]. A detailed investigation could be conducted to evaluate which strategy is more suitable to the modified MPS model.

For the structure part, the current $2D$ model could be extended to $3D$ situations. The simple and straightforward way of model extension for beam-like structure is to linearly superpose transverse bending and distortion motion into the $2D$ model. However, it certainly cannot consider the nonlinear coupling effect between bending and distortion motions, which in fact is quite important for bulk cargo ship with large opening in deck. Therefore a fully $3D$ model which employs the $3D$ mode shapes (rather than the linearly superposition of $2D$ mode shapes) should be derived for arbitrary $3D$ geometry.

Appendix A

Formulation of CRF implementation

For a variable ζ (e.g. X_{cR}, θ or q_i in Eq. (3.95) to (3.100) and Eq. (3.111) to (3.114)), its first and second order time derivatives $\dot{\zeta}_{k+1}$, $\ddot{\zeta}_{k+1}$ at next time step $t = t_{k+1}$, can be expressed using Newmark method as:

$$\ddot{\zeta}_{k+1} = \frac{1}{\beta\Delta t^2}\zeta_{k+1} - [\frac{\zeta_k}{\beta\Delta t^2} + \frac{\dot{\zeta}_k}{\beta\Delta t} + (\frac{1}{2\beta} - 1)\ddot{\zeta}_k] \tag{A.1}$$

$$\dot{\zeta}_{k+1} = \frac{\gamma}{\beta\Delta t}\zeta_{k+1} + (1 - \frac{\gamma}{\beta})\dot{\zeta}_k + \Delta t[(1-\gamma) - \gamma(\frac{1}{2\beta} - 1)]\ddot{\zeta}_k - \frac{\gamma}{\beta\Delta t}\zeta_k \tag{A.2}$$

where $\gamma = \frac{1-2\alpha}{2}$, $\beta = \frac{(1-\alpha)^2}{4}$, and α is chosen to be $\alpha = -0.05$ in this study. To simplify the above equations, the following definitions are introduced:

$$C_1 = \frac{1}{\beta\Delta t^2} \tag{A.3}$$

$$C_3 = \frac{\gamma}{\beta\Delta t} \tag{A.4}$$

$$C_{2\zeta} = -[\frac{\zeta_k}{\beta\Delta t^2} + \frac{\dot{\zeta}_k}{\beta\Delta t} + (\frac{1}{2\beta} - 1)\ddot{\zeta}_k], \tag{A.5}$$

$$C_{4\zeta} = (1 - \frac{\gamma}{\beta})\dot{\zeta}_k + \Delta t[(1-\gamma) - \gamma(\frac{1}{2\beta} - 1)]\ddot{\zeta}_k - \frac{\gamma}{\beta\Delta t}\zeta_k \tag{A.6}$$

in which $C_{2\zeta}$ and $C_{4\zeta}$ correspond to the particular variable ζ

Using Newmark method to replace the velocity and acceleration terms with position values, the governing equations of floating beams (i.e. Eq. (3.95) to

(3.100)) then become

$$\begin{aligned} f_1 =& M(C_1 X_{cR} + C_{2X_{cR}}) + (C_{3\theta} + C_{4\theta})^2 \sin\theta(\psi_{01}q_1 + \psi_{02}q_2 + \psi_{03}q_3) \\ & - 2(C_3\theta + C_{4\theta})\cos\theta[\psi_{01}(C_3 q_1 + C_{4q_1}) + \psi_{02}(C_3 q_2 + C_{4q_2}) + \psi_{03}(C_3 q_3 + C_{4q_3})] \\ & - (C_1\theta + C_{2\theta})\cos\theta(\psi_{01}q_1 + \psi_{02}q_2 + \psi_{03}q_3) - \sin\theta[\psi_{01}(C_1 q_1 + C_{2q_1}) \\ & + \psi_{02}(C_1 q_2 + C_{2q_2}) + \psi_{03}(C_1 q_3 + C_{2q_3})] - Q_{X_{cR}} = 0, \end{aligned} \tag{A.7}$$

$$\begin{aligned} f_2 =& M(C_1 Y_{cR} + C_{2Y_{cR}}) - (C_{3\theta} + C_{4\theta})^2 \cos\theta(\psi_{01}q_1 + \psi_{02}q_2 + \psi_{03}q_3) \\ & - 2(C_3\theta + C_{4\theta})\sin\theta[\psi_{01}(C_3 q_1 + C_{4q_1}) + \psi_{02}(C_3 q_2 + C_{4q_2}) + \psi_{03}(C_3 q_3 + C_{4q_3})] \\ & - (C_1\theta + C_{2\theta})\sin\theta(\psi_{01}q_1 + \psi_{02}q_2 + \psi_{03}q_3) + \cos\theta[\psi_{01}(C_1 q_1 + C_{2q_1}) \\ & + \psi_{02}(C_1 q_2 + C_{2q_2}) + \psi_{03}(C_1 q_3 + C_{2q_3})] + Mg - Q_{Y_{cR}} = 0, \end{aligned} \tag{A.8}$$

$$\begin{aligned} f_3 =& -[(C_1 X_{cR} + C_{2X_{cR}})\cos\theta + (C_1 Y_{cR} + C_{2Y_{cR}})\sin\theta](\psi_{01}q_1 + \psi_{02}q_2 + \psi_{03}q_3) \\ & + (C_1\theta + C_{2\theta})(I_f + q_1^2 + q_2^2 + q_3^2) \\ & + 2(C_3\theta + C_{4\theta})[(C_3 q_1 + C_{4q_1})q_1 + (C_3 q_2 + C_{4q_2})q_2 + (C_3 q_3 + C_{4q_3})q_3] \\ & + [\psi_{11}(C_1 q_1 + C_{2q_1}) + \psi_{12}(C_1 q_2 + C_{2q_2}) + \psi_{13}(C_1 q_3 + C_{2q_3})] - Q_\theta = 0, \end{aligned} \tag{A.9}$$

$$\begin{aligned} f_4 =& [-(C_1 X_{cR} + C_{2X_{cR}})\sin\theta + (C_1 Y_{cR} + C_{2Y_{cR}})\cos\theta]\psi_{01} \\ & + (C_1\theta + C_{2\theta})\psi_{11} - (C_3\theta + C_{4\theta})^2 q_1 + C_1 q_1 + C_{2q_1} + \omega_1^2 q_1 - Q_{q_1} = 0, \end{aligned} \tag{A.10}$$

$$\begin{aligned} f_5 =& [-(C_1 X_{cR} + C_{2X_{cR}})\sin\theta + (C_1 Y_{cR} + C_{2Y_{cR}})\cos\theta]\psi_{02} \\ & + (C_1\theta + C_{2\theta})\psi_{12} - (C_3\theta + C_{4\theta})^2 q_2 + C_1 q_2 + C_{2q_2} + \omega_2^2 q_2 - Q_{q_2} = 0, \end{aligned} \tag{A.11}$$

$$\begin{aligned} f_6 =& [-(C_1 X_{cR} + C_{2X_{cR}})\sin\theta + (C_1 Y_{cR} + C_{2Y_{cR}})\cos\theta]\psi_{03} \\ & + (C_1\theta + C_{2\theta})\psi_{13} - (C_3\theta + C_{4\theta})^2 q_3 + C_1 q_3 + C_{2q_3} + \omega_3^2 q_3 - Q_{q_3} = 0, \end{aligned} \tag{A.12}$$

These set of equations are solved by Newton-Raphson method. The elements of the Jacobi matrix are:

$$\frac{\partial f_1)}{\partial X_{cR}} = MC_1, \tag{A.13}$$

$$\frac{\partial f_1}{\partial Y_{cR}} = 0, \tag{A.14}$$

$$\begin{aligned}\frac{\partial f_1}{\partial \theta} =&(\psi_{01}q_1+\psi_{02}q_2+\psi_{03}q_3)[(C_3\theta+C_{4\theta})^2\cos\theta+2C_3(C_3\theta+C_{4\theta})\sin\theta]\\&-2[\psi_{01}(C_3q_1+C_{4q_1})+\psi_{02}(C_3q_2+C_{4q_2})+\psi_{03}(C_3q_3+C_{4q_3})][C_3\cos\theta\\&-(C_3\theta+C_{4\theta})\sin\theta]-(\psi_{01}q_1+\psi_{02}q_2+\psi_{03}q_3)[C_1\cos\theta-(C_1\theta+C_{2\theta})\sin\theta]\\&-\cos\theta[\psi_{01}(C_1q_1+C_{2q_1})+\psi_{02}(C_1q_2+C_{2q_2})+\psi_{03}(C_1q_3+C_{2q_3})],\end{aligned} \tag{A.15}$$

$$\begin{aligned}\frac{\partial f_1}{\partial q_1} =&\psi_{01}(C_3\theta+C_{4\theta})^2\sin\theta-2\psi_{01}C_3(C_3\theta+C_{4\theta})\cos\theta\\&-\psi_{01}(C_1\theta+C_{2\theta})\cos\theta-C_1\psi_{01}\sin\theta,\end{aligned} \tag{A.16}$$

$$\begin{aligned}\frac{\partial f_1}{\partial q_2} =&\psi_{02}(C_3\theta+C_{4\theta})^2\sin\theta-2\psi_{02}C_3(C_3\theta+C_{4\theta})\cos\theta\\&-\psi_{02}(C_1\theta+C_{2\theta})\cos\theta-C_1\psi_{02}\sin\theta,\end{aligned} \tag{A.17}$$

$$\begin{aligned}\frac{\partial f_1}{\partial q_3} =&\psi_{03}(C_3\theta+C_{4\theta})^2\sin\theta-2\psi_{03}C_3(C_3\theta+C_{4\theta})\cos\theta\\&-\psi_{03}(C_1\theta+C_{2\theta})\cos\theta-C_1\psi_{03}\sin\theta,\end{aligned} \tag{A.18}$$

$$\frac{\partial f_2}{\partial X_{cR}} = 0, \tag{A.19}$$

$$\frac{\partial f_2}{\partial Y_{cR}} = MC_1, \tag{A.20}$$

$$\begin{aligned}\frac{\partial f_2}{\partial \theta} =&(\psi_{01}q_1+\psi_{02}q_2+\psi_{03}q_3)[(C_3\theta+C_{4\theta})^2\sin\theta-2C_3(C_3\theta+C_{4\theta})\cos\theta]\\&-2[\psi_{01}(C_3q_1+C_{4q_1})+\psi_{02}(C_3q_2+C_{4q_2})+\psi_{03}(C_3q_3+C_{4q_3})][C_3\sin\theta\\&+(C_3\theta+C_{4\theta})\cos\theta]-(\psi_{01}q_1+\psi_{02}q_2+\psi_{03}q_3)[C_1\sin\theta+(C_1\theta+C_{2\theta})\cos\theta]\\&-\sin\theta[\psi_{01}(C_1q_1+C_{2q_1})+\psi_{02}(C_1q_2+C_{2q_2})+\psi_{03}(C_1q_3+C_{2q_3})],\end{aligned} \tag{A.21}$$

$$\begin{aligned}\frac{\partial f_2}{\partial q_1} =&-\psi_{01}(C_3\theta+C_{4\theta})^2\cos\theta-2\psi_{01}C_3(C_3\theta+C_{4\theta})\sin\theta\\&-\psi_{01}(C_1\theta+C_{2\theta})\sin\theta+C_1\psi_{01}\cos\theta,\end{aligned} \tag{A.22}$$

$$\begin{aligned}\frac{\partial f_2}{\partial q_2} =&-\psi_{02}(C_3\theta+C_{4\theta})^2\cos\theta-2\psi_{02}C_3(C_3\theta+C_{4\theta})\sin\theta\\&-\psi_{02}(C_1\theta+C_{2\theta})\sin\theta+C_1\psi_{02}\cos\theta,\end{aligned} \tag{A.23}$$

$$\begin{aligned}\frac{\partial f_2}{\partial q_3} =&-\psi_{03}(C_3\theta+C_{4\theta})^2\cos\theta-2\psi_{03}C_3(C_3\theta+C_{4\theta})\sin\theta\\&-\psi_{03}(C_1\theta+C_{2\theta})\sin\theta+C_1\psi_{03}\cos\theta,\end{aligned} \tag{A.24}$$

$$\frac{\partial f_3}{\partial X_{cR}} = -C_1\cos\theta(\psi_{01}q_1+\psi_{02}q_2+\psi_{03}q_3), \tag{A.25}$$

$$\frac{\partial f_3}{\partial Y_{cR}} = -C_1 \sin\theta(\psi_{01}q_1 + \psi_{02}q_2 + \psi_{03}q_3), \tag{A.26}$$

$$\begin{aligned}\frac{\partial f_3}{\partial \theta} =& -[-(C_1X_{cR} + C_{2X_{cR}})\sin\theta + (C_1Y_{cR} + C_{2Y_{cR}})\cos\theta](\psi_{01}q_1 + \psi_{02}q_2 + \psi_{03}q_3) \\ &+ C_1(I_f + q_1^2 + q_2^2 + q_3^2) \\ &+ 2C_3[(C_3q_1 + C_{4q_1})q_1 + (C_3q_2 + C_{4q_2})q_2 + (C_3q_3 + C_{4q_3})q_3],\end{aligned} \tag{A.27}$$

$$\begin{aligned}\frac{\partial f_3}{\partial q_1} =& -\psi_{01}[(C_1X_{cR} + C_{2X_{cR}})\cos\theta + (C_1Y_{cR} + C_{2Y_{cR}})\sin\theta] + 2q_1(C_1\theta + C_{2\theta}) \\ &+ 2(C_3\theta + C_{4\theta})(2C_3q_1 + C_{4q_1}) + \psi_{11}C_1,\end{aligned} \tag{A.28}$$

$$\begin{aligned}\frac{\partial f_3}{\partial q_2} =& -\psi_{02}[(C_1X_{cR} + C_{2X_{cR}})\cos\theta + (C_1Y_{cR} + C_{2Y_{cR}})\sin\theta] + 2q_2(C_1\theta + C_{2\theta}) \\ &+ 2(C_3\theta + C_{4\theta})(2C_3q_2 + C_{4q_2}) + \psi_{12}C_1,\end{aligned} \tag{A.29}$$

$$\begin{aligned}\frac{\partial f_3}{\partial q_3} =& -\psi_{03}[(C_1X_{cR} + C_{2X_{cR}})\cos\theta + (C_1Y_{cR} + C_{2Y_{cR}})\sin\theta] + 2q_3(C_1\theta + C_{2\theta}) \\ &+ 2(C_3\theta + C_{4\theta})(2C_3q_3 + C_{4q_3}) + \psi_{13}C_1,\end{aligned} \tag{A.30}$$

$$\frac{\partial f_4}{\partial X_{cR}} = -C_1\psi_{01}\sin\theta, \tag{A.31}$$

$$\frac{\partial f_4}{\partial Y_{cR}} = C_1\psi_{01}\cos\theta, \tag{A.32}$$

$$\frac{\partial f_4}{\partial \theta} = -[(C_1X_{cR} + C_{2X_{cR}})\cos\theta + (C_1Y_{cR} + C_{2Y_{cR}})\sin\theta]\psi_{01} + C_1\psi_{11} - 2C_3q_1(C_3\theta + C_{4\theta}) \tag{A.33}$$

$$\frac{\partial f_4}{\partial q_1} = C_1 + \omega_1^2 - (C_3\theta + C_{4\theta})^2, \tag{A.34}$$

$$\frac{\partial f_4}{\partial q_2} = \frac{\partial f_4}{\partial q_3} = 0, \tag{A.35}$$

$$\frac{\partial f_5}{\partial X_{cR}} = -C_1\psi_{02}\sin\theta, \tag{A.36}$$

$$\frac{\partial f_5}{\partial Y_{cR}} = C_1\psi_{02}\cos\theta, \tag{A.37}$$

$$\frac{\partial f_5}{\partial \theta} = -[(C_1X_{cR} + C_{2X_{cR}})\cos\theta + (C_1Y_{cR} + C_{2Y_{cR}})\sin\theta]\psi_{02} + C_1\psi_{12} - 2C_3q_2(C_3\theta + C_{4\theta}) \tag{A.38}$$

$$\frac{\partial f_5}{\partial q_2} = C_1 + \omega_2^2 - (C_3\theta + C_{4\theta})^2, \tag{A.39}$$

$$\frac{\partial f_5}{\partial q_1} = (\partial f_5)/(\partial q_3) = 0, \tag{A.40}$$

$$\frac{\partial f_6}{\partial X_{cR}} = -C_1\psi_{03}\sin\theta, \tag{A.41}$$

$$\frac{\partial f_6}{\partial Y_{cR}} = C_1\psi_{03}\cos\theta, \tag{A.42}$$

$$\frac{\partial f_6}{\partial \theta} = -[(C_1X_{cR} + C_{2X_{cR}})\cos\theta + (C_1Y_{cR} + C_{2Y_{cR}})\sin\theta]\psi_{03} + C_1\psi_{13} - 2C_3q_3(C_3\theta + C_{4\theta}) \tag{A.43}$$

$$\frac{\partial f_6}{\partial q_3} = C_1 + \omega_3^2 - (C_3\theta + C_{4\theta})^2, \tag{A.44}$$

$$\frac{\partial f_6}{\partial q_1} = \frac{\partial f_6}{\partial q_2} = 0 \tag{A.45}$$

Similarly, the governing equations for the wedge with flexible bottom (Eq. (3.111) to (3.114)) and its Jacobi matrix are:

$$\begin{aligned} f_1 =& (2M_f + M_R)(C_1Y_{cR} + C_{2Y_{cR}}) \\ &+ 2\cos\theta(\psi_{01}(C_1q_1 + C_{2q_1}) + \psi_{02}(C_1q_2 + C_{2q_2}) + \psi_{03}(C_1q_3 + C_{2q_3})) \\ &+ (2M_f + M_R)g - Q_{Y_{cR}} = 0 \end{aligned} \tag{A.46}$$

$$f_2 = 2(C_1Y_{cR} + C_{2Y_{cR}})\cos\theta\psi_{01} + 2(C_1q_1 + C_{2q_1}) + 2\omega_1^2q_1 - Q_{q_1} = 0 \tag{A.47}$$

$$f_3 = 2(C_1Y_{cR} + C_{2Y_{cR}})\cos\theta\psi_{02} + 2(C_1q_2 + C_{2q_2}) + 2\omega_2^2q_2 - Q_{q_2} = 0 \tag{A.48}$$

$$f_4 = 2(C_1Y_{cR} + C_{2Y_{cR}})\cos\theta\psi_{03} + 2(C_1q_3 + C_{2q_3}) + 2\omega_3^2q_3 - Q_{q_3} = 0 \tag{A.49}$$

$$\frac{\partial f_1}{\partial Y_{cR}} = (2M_f + M_R)C_1, \tag{A.50}$$

$$\frac{\partial f_1}{\partial q_1} = 2C_1\psi_{01}\cos\theta, \tag{A.51}$$

$$\frac{\partial f_1}{\partial q_2} = 2C_1\psi_{02}\cos\theta, \tag{A.52}$$

$$\frac{\partial f_1}{\partial q_3} = 2C_1\psi_{03}\cos\theta, \tag{A.53}$$

$$\frac{\partial f_2}{\partial Y_{cR}} = 2C_1\psi_{01}\cos\theta, \tag{A.54}$$

$$\frac{\partial f_2}{\partial q_1} = 2C_1 + 2\omega_1^2, \tag{A.55}$$

$$\frac{\partial f_2}{\partial q_2} = \frac{\partial f_2}{\partial q_3} = 0, \tag{A.56}$$

$$\frac{\partial f_3}{\partial Y_{cR}} = 2C_1\psi_{02}\cos\theta, \tag{A.57}$$

$$\frac{\partial f_3}{\partial q_2} = 2C_1 + 2\omega_2^2, \tag{A.58}$$

$$\frac{\partial f_3}{\partial q_1} = \frac{\partial f_3}{\partial q_3} = 0, \tag{A.59}$$

$$\frac{\partial f_4}{\partial Y_{cR}} = 2C_1\psi_{03}\cos\theta, \tag{A.60}$$

$$\frac{\partial f_4}{\partial q_3} = 2C_1 + 2\omega_3^2, \tag{A.61}$$

$$\frac{\partial f_4}{\partial q_1} = \frac{\partial f_4}{\partial q_2} = 0, \tag{A.62}$$

Appendix B

Implementation of weak couplging between BEM and MPS

B.1 Boundary Element Method (BEM)

B.1.1 Governing equations and boundary conditions

As a well established method, there are several ways of implementing BEM. In this study, the approach described in [39, 147] are adopted.

Under the inviscid and irrotational assumption, the fluid velocity $\mathbf{u}$ could be expressed by the gradient of a so-called potential function $\varphi(\mathbf{r}, t)$ as $\mathbf{u} = \nabla\varphi$. As a consequence, the continuity equation becomes a Laplace equation of velocity potential φ, which is also the governing equation for the potential flow as the form of Eq. (B.1):

$$\Delta\varphi = 0 \tag{B.1}$$

Eq. (B.1) could be transformed into the following boundary integral equation by Green's third identity:

$$\alpha_u(\mathbf{r}_{col}, t)\varphi(\mathbf{r}_{col}, t) = \oint [\frac{\partial \ln(|\mathbf{r}_{int} - \mathbf{r}_{col}|)}{\partial n}\varphi(\mathbf{r}_{int}, t) - \frac{\partial\varphi(\mathbf{r}_{int}, t)}{\partial n}\ln(|\mathbf{r}_{int} - \mathbf{r}_{col}|)]dl, \tag{B.2}$$

where $\mathbf{r}_{int}$ and $\mathbf{r}_{col}$ are the position vectors of integration and collocation points on the boundary, respectively. And the value of $\alpha_u(\mathbf{r}_{col}, t)$ depends on the position of collocation point. If it is inside the computational domain, $\alpha_u(\mathbf{r}_{col}, t) = 2\pi$; if it is on the boundary, the value is the opening angle (subtending towards

the fluid domain) of the boundary at $\mathbf{r}_{col}$. For continuous boundary such as at least 1^{st} smooth curve or straight-line, this angle is $\alpha_u(\mathbf{r}_{col}, t) = \pi$. The direction of the normal vector $\mathbf{n}$ is pointing towards outside of fluid domain as shown in Figure 5.24

This boundary integral equation will be discritized and solved numerically on the whole boundary of the computational domain at each time step. The integration will be singular when the integration point passing the collocation point on the boundary. This is handled in the Cauchy Principal Value (CPV) sense.

The boundary conditions that this equation is subject to are given as follows. First, on the moveable solid boundaries such as wave-maker or other fixed wall boundaries, the following impenetrable condition is applied:

$$\frac{\partial \varphi}{\partial n} = \begin{cases} \mathbf{V}(\mathbf{r}, t) \cdot \mathbf{n} = V_n, & on \quad \Gamma_{wm} \\ 0, & on \quad \Gamma_{fw} \end{cases} \tag{B.3}$$

where $\mathbf{V}(\mathbf{r}, t)$ is the velocity of the point at $\mathbf{r}$ on the boundary. By rearranging the Bernoulli equation, the dynamic condition for potential φ on the free surface takes the following form:

$$\frac{D\varphi}{Dt} = \frac{1}{2}|\nabla\varphi|^2 - gy, \tag{B.4}$$

where $\frac{D}{Dt}$ is the material derivative, defined as: $\frac{D}{Dt} = \frac{\partial}{\partial t} + (\nabla\varphi \cdot \nabla)$. And the dynamic condition of zero pressure on the free surface is applied in the derivation of Eq. (B.4). The kinetic condition on the free surface is given by:

$$\frac{D\mathbf{r}}{Dt} = \nabla\varphi \tag{B.5}$$

The time stepping scheme and other numerical implementation details are given below.

B.1.2 The time integration for free surface

The position and velocity potential φ have to be advanced to next time step to initialize the solving of the boundary integral equation. Instead of the traditional Runge-Kutta or Adams-Bashforth-Moulton methods, a truncated

Taylor expansion formulation [39, 147] is employed in this study:

$$\mathbf{r}(t+\Delta t) = \mathbf{r}(t) + \sum_{k=1}^{m} \frac{\Delta t^k}{k!} \frac{D^k \mathbf{r}(t)}{Dt^k} + O[(\Delta t)^{m+1}] \tag{B.6}$$

$$\varphi(\mathbf{r}(t+\Delta t), t+\Delta t) = \varphi(\mathbf{r}(t), t) + \sum_{k=1}^{m} \frac{\Delta t^k}{k!} \frac{D^k \varphi(\mathbf{r}(t), t)}{Dt^k} + O[(\Delta t)^{m+1}] \tag{B.7}$$

The first and second order material derivatives in Eq. (B.6) and (B.7) are expressed in the local coordinate system $\mathbf{n} - \boldsymbol{\tau}$ as shown in Figure 5.24. After some mathematical operations, the forms of these derivatives can be expressed as:

$$\frac{D\mathbf{r}}{Dt} = [\frac{\partial \varphi}{\partial \tau}\frac{dx}{d\tau} - \frac{\partial \varphi}{\partial n}\frac{dy}{d\tau}, \frac{\partial \varphi}{\partial n}\frac{dx}{d\tau} + \frac{\partial \varphi}{\partial \tau}\frac{dy}{d\tau}] \tag{B.8}$$

$$\begin{aligned}
\frac{D^2\mathbf{r}}{Dt^2} =& [(\frac{\partial^2 \varphi}{\partial t \partial \tau} + \frac{\partial \varphi}{\partial \tau}\frac{\partial^2 \varphi}{\partial s^2} + \frac{\partial \varphi}{\partial n}\frac{\partial^2 \varphi}{\partial n \partial \tau})\frac{dx}{d\tau} \\
&+ (\frac{\partial \varphi}{\partial n}\frac{\partial^2 \varphi}{\partial \tau^2} - \frac{\partial \varphi}{\partial \tau}\frac{\partial^2 \varphi}{\partial \tau^2} - \frac{\partial^2 \varphi}{\partial t \partial n} - (\frac{\partial^2 y}{\partial \tau^2}\frac{\partial x}{\partial \tau} - \frac{\partial^2 x}{\partial \tau^2}\frac{\partial y}{\partial \tau})|\nabla \varphi|^2)\frac{dy}{d\tau} \\
&, (\frac{\partial^2 \varphi}{\partial t \partial \tau} + \frac{\partial \varphi}{\partial \tau}\frac{\partial^2 \varphi}{\partial \tau^2} + \frac{\partial \varphi}{\partial n}\frac{\partial^2 \varphi}{\partial n \partial \tau})\frac{dy}{d\tau} \\
&+ (\frac{\partial^2 \varphi}{\partial t \partial n} - \frac{\partial \varphi}{\partial n}\frac{\partial^2 \varphi}{\partial \tau^2} + \frac{\partial \varphi}{\partial \tau}\frac{\partial^2 \varphi}{\partial n \partial \tau} + (\frac{\partial^2 y}{\partial \tau^2}\frac{\partial x}{\partial \tau} - \frac{\partial^2 x}{\partial \tau^2}\frac{\partial y}{\partial \tau})|\nabla \varphi|^2)\frac{dx}{d\tau}]
\end{aligned} \tag{B.9}$$

$$\begin{aligned}
\frac{D^2\varphi}{Dt^2} =& \frac{\partial \varphi}{\partial \tau}\frac{\partial^2 \varphi}{\partial t \partial \tau} + \frac{\partial \varphi}{\partial n}\frac{\partial^2 \varphi}{\partial t \partial n} + \frac{\partial \varphi}{\partial \tau}(\frac{\partial \varphi}{\partial \tau}\frac{\partial^2 \varphi}{\partial \tau^2} + \frac{\partial \varphi}{\partial n}\frac{\partial^2 \varphi}{\partial n \partial \tau}) - \frac{\partial \varphi}{\partial n}(\frac{\partial \varphi}{\partial n}\frac{\partial^2 \varphi}{\partial \tau^2} - \frac{\partial \varphi}{\partial \tau}\frac{\partial^2 \varphi}{\partial n \partial \tau}) \\
&+ \frac{\partial \varphi}{\partial n}|\nabla \varphi|^2(\frac{d^2 y}{d\tau^2}\frac{dx}{d\tau} - \frac{d^2 x}{d\tau^2}\frac{dy}{d\tau}) - g(\frac{\partial \varphi}{\partial n}\frac{dx}{d\tau} + \frac{\partial \varphi}{\partial \tau}\frac{dy}{d\tau})
\end{aligned} \tag{B.10}$$

In Eq. (B.8) to (B.10), the tangent spatial derivatives of φ and $\frac{\partial \varphi}{\partial n}$, such as $\frac{\partial \varphi}{\partial \tau}$ and $\frac{\partial^2 \varphi}{\partial n \tau}$, can be calculated directly from the φ and $\frac{\partial \varphi}{\partial n}$ distributions provided by boundary condition Eq. (B.3) to (B.5). Whilst the time derivatives such as $\frac{\partial \varphi}{\partial t}$ and $\frac{\partial^2 \varphi}{\partial n \partial t}$ are calculated in the following manner:

After taking the time derivatives on both sides of Eq. (B.2), A new boundary integral equation about $\frac{\partial \varphi}{\partial t}$ and $\frac{\partial \varphi}{\partial n \partial t}$ can be obtained and then be solved in the same way for Eq. (B.2). The boundary conditions for this new boundary integral equation are as follows:

For the free surface, the value of $\frac{\partial \varphi}{\partial t}$ could be obtained by Bernoulli equation.

$$\frac{\partial \varphi}{\partial t} = -\frac{1}{2}|\nabla \varphi|^2 - gy \tag{B.11}$$

On the wave-maker or other fixed wall boundaries, the time derivative of Eq. (B.3) is applied:

$$\frac{\partial^2 \varphi}{\partial n \partial t} = \begin{cases} \frac{\partial(\mathbf{V}(\mathbf{r},t)\cdot\mathbf{n})}{\partial t}, & on \quad \Gamma_{wm} \\ 0, & on \quad \Gamma_{fw} \end{cases} \tag{B.12}$$

For a piston type wave-maker, which will be used later in the simulation, it can be expressed as:

$$\frac{\partial^2 \varphi}{\partial n \partial t} = -\dot{\mathbf{V}}_p - \mathbf{V}_p \frac{\partial^2 \varphi}{\partial \tau^2} \tag{B.13}$$

B.1.3 Numerical implementation

At each time step, Eq. (B.2) is solved by Boundary Element Method (BEM) on the whole boundary of the computational domain. The boundary is first discretized by a set of discrete nodes and then the integration is conducted on the elements between nodes as follows:

$$\begin{aligned} \alpha_u(\mathbf{r}_{col},t)\varphi(\mathbf{r}_{col},t) &= \sum_{k=1}^{M}\left(\int_{\Gamma_k}\left[\frac{\partial \ln(|\mathbf{r}_{int}-\mathbf{r}_{col}|)}{\partial n}\varphi(\mathbf{r}_{int},t) - \frac{\partial \varphi(\mathbf{r}_{int},t)}{\partial n}\ln(|\mathbf{r}_{int}-\mathbf{r}_{col}|)\right]dl\right) \\ &= \sum_{k=1}^{M}(I_d^k - I_s^k) \end{aligned} \tag{B.14}$$

where Γ_k denotes the geometry element between node k and $k+1$, I_d^k and I_s^k represent the integration of dipole (i.e. $\frac{\partial \ln(|\mathbf{r}_{int}-\mathbf{r}_{col}|)}{\partial n}$) and source (i.e. $\ln(|\mathbf{r}_{int}-\mathbf{r}_{col}|)$) distribution on that element, respectively. For the singular part of them, they are calculated in the CPV sense as mentioned above.

The discretization of the geometry and field functions (e.g. φ, $\frac{\partial \varphi}{\partial n}$), and then the calculation of the integration on these discrete elements are discussed in the following sections.

B.1.3.1 Discretization of field functions

The field functions (e.g. φ, $\frac{\partial \varphi}{\partial n}$) on an element Γ_k are represented by the 3^{rd} order polynomial among the 4 adjacent nodes as shown by the curved line in Figure B.1

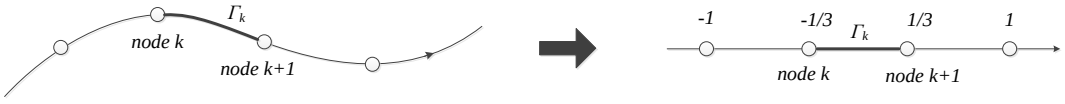

Figure B.1: Intrinsic coordinate for the integration on each element

In order to simplify the form of interpolation, the geometry is mapped into an intrinsic coordinates ξ, which varies from -1 to 1 as shown in Figure B.1. If f is used to represent the field function value (e.g. φ, $\frac{\partial \varphi}{\partial n}$) at an arbitrary position on an element Γ_k(which means ξ varies from $-1/3$ to $1/3$ as shown in Figure B.1), it can be interpolated as follows:

$$f(\xi) = \sum_{j=1}^{4} N_j(\xi) f_j^k, \tag{B.15}$$

where f_j^k is the value on j^{th} node of the adjacent 4 nodes, which corresponds to $\xi = -1, -1/3, 1/3, 1$ in Figure B.1, respectively. The shape function $N_j(\xi)$ is given by:

$$\begin{aligned} N_1 &= \frac{1}{16}(1-\xi)(9\xi^2-1) \quad N_3 = \frac{9}{16}(1-\xi^2)(1+3\xi) \\ N_2 &= \frac{9}{16}(1-\xi^2)(1-3\xi) \quad N_4 = \frac{1}{16}(1+\xi)(9\xi^2-1) \end{aligned} \tag{B.16}$$

B.1.3.2 Discretization of geometry

The geometry discretization of the whole computational domain could be categorized into two types, i.e. the ever-changing curved free surface and the straight-line solid boundaries (which include wave-maker , bottom and side walls). Those straight-lines are simply discretized by beeline segments. While the curved free surface is described by the so-called "Quasi-Spline" model [40, 147]. More specifically, both the x and y coordinates are interpolated against

the node index numbers. Taking x for example (the same formulation for y), after obtaining the first order derivative of x against node indexing number $\frac{dx}{d\zeta}$ by performing the normal spline interpolation procedure, the coordinates of points on the element between node k and $k+1$ (i.e. Γ_k) are approximated by the following interpolation:

$$x(\zeta) = \alpha_1(\zeta)x(k) + \beta_1(\zeta)\frac{dx}{d\zeta}|_{\zeta=k} + \alpha_2(\zeta)x(k) + \beta_2(\zeta)\frac{dx}{d\zeta}|_{\zeta=k+1} \tag{B.17}$$

where ζ varies continuously from k to $k+1$, indicating the position between node k and $k+1$. The shape function α_1,α_2,β_1 and β_2 are defined as:

$$\begin{aligned} \alpha_1(\zeta) &= (\zeta-k-1)^2[1+2(\zeta-k)]\beta_1(\zeta) = (\zeta-k-1)^2(\zeta-k) \\ \alpha_2(\zeta) &= (\zeta-k)^2[1+2(k+1-\zeta)]\beta_2(\zeta) = (\zeta-k)^2(\zeta-k-1) \end{aligned} \tag{B.18}$$

The relation between the arc length of the curved line s and ζ has to be established for conducting the integration (which will be explained in Section B.1.3.3) The Jacobian between s and the intrinsic coordinate ζ mentioned in Section B.1.3.1 are given by:

$$\begin{aligned} \frac{ds}{d\xi} =& \frac{3}{2}[(\frac{d\alpha_1(\zeta)}{d\zeta}x(k) + \frac{d\beta_1(\zeta)}{d\zeta}\frac{dx}{d\zeta}|_{\zeta=k} + \frac{d\alpha_2(\zeta)}{d\zeta}x(k+1) + \frac{d\beta_1(\zeta)}{d\zeta}\frac{dx}{d\zeta}|_{\zeta=k+1})^2 + \\ & (\frac{d\alpha_1(\zeta)}{d\zeta}y(k) + \frac{d\beta_1(\zeta)}{d\zeta}\frac{dy}{d\zeta}|_{\zeta=k} + \frac{d\alpha_2(\zeta)}{d\zeta}y(k+1) + \frac{d\beta_2(\zeta)}{d\zeta}\frac{dy}{d\zeta}|_{\zeta=k+1})^2]^{\frac{1}{2}} \end{aligned} \tag{B.19}$$

$$\begin{aligned} \frac{d^2s}{d\xi^2} =& \frac{9}{4}[\frac{dx}{ds}(\frac{d^2\alpha_1(\zeta)}{d\zeta^2}x(k) + \frac{d^2\beta_1(\zeta)}{d\zeta^2}\frac{dx}{d\zeta}|_{\zeta=k} + \frac{d^2\alpha_2(\zeta)}{d\zeta^2}x(k+1) + \frac{d^2\beta_2(\zeta)}{d\zeta^2}\frac{dx}{d\zeta}|_{\zeta=k+1}) + \\ & \frac{dy}{ds}(\frac{d^2\alpha_1(\zeta)}{d\zeta^2}y(k) + \frac{d^2\beta_1(\zeta)}{d\zeta^2}\frac{dy}{d\zeta}|_{\zeta=k} + \frac{d^2\alpha_2(\zeta)}{d\zeta^2}y(k+1) + \frac{d^2\beta_2(\zeta)}{d\zeta^2}\frac{dy}{d\zeta}|_{\zeta=k+1})]/\frac{ds}{d\zeta} \end{aligned} \tag{B.20}$$

where $\frac{dx}{ds}$ and $\frac{dy}{ds}$ are calculated by

$$\frac{dx}{ds} = \frac{3}{2}\frac{dx}{d\zeta}/\frac{ds}{d\xi} \tag{B.21}$$

$$\frac{dy}{ds} = \frac{3}{2}\frac{dy}{d\zeta}/\frac{ds}{d\xi} \tag{B.22}$$

In the process of deriving Eq. (B.21) and (B.22), the following relation between intrinsic coordinate ξ and the continuous index ζ are used:

$$\zeta = \frac{3}{2}\xi - \frac{3}{2}\xi_1 + k \tag{B.23}$$

where ξ_1 indicates the intrinsic coordinate corresponding to node k. More specifically, as shown in Figure B.1, when node k is the first or last node of a particular segment of the boundary, $\xi_1 = -1$ or $\xi_1 = 1/3$ since the integration element is between the first or last two nodes among the adjacent four nodes, whilst when node k is somewhere in the middle of a segment, $\xi_1 = -1/3$.

B.1.3.3 Integration on the elements

Based on the aforementioned preparation of the geometry and field function discretizations, the integration on each element could now be conducted.

For the straight-line boundary such as the wave-maker and other fixed walls, the polynomial field function integration could be calculated analytically as illustrated in Ref [44], which will not be repeated here.

For the integration on the curved-line free surface, the case for distributed dipole I_d^k and source I_s^k on element Γ_k are discussed separately.

a) Calculation of I_d^k on "Quasi-spline" element

A transformation of the integrand, which is similar to the one used in Ref [94], is used here to avoid the singularity issue when integration point passing the collocation point. The angle θ_d, which is the angle of the vector $\mathbf{r}_{int} - \mathbf{r}_{col}$ rotating from node $k+1$ to an arbitrary point on the element Γ_k as shown inFigure B.2, is introduced. It is defined to be positive when the vector turn anti-clockwise.

As a consequence, the following transformation can be derived:

$$\begin{aligned} I_d^k &= \int_{\Gamma_k} \varphi(\mathbf{r},t) \frac{\partial \ln(|\mathbf{r}_{int} - \mathbf{r}_{col}|)}{\partial n} dl \\ &= \sum_{j=1}^{4} \varphi|_j^k \int_{\xi_1}^{\xi_1+2/3} N_j(\xi) \frac{\partial \ln(|\mathbf{r}_{int}(\xi) - \mathbf{r}_{col}(\xi)|)}{\partial n} \frac{ds}{d\xi} d\xi \\ &= -\sum_{j=1}^{4} \varphi|_j^k \int_{\xi_1}^{\xi_1+2/3} N_j(\xi) \frac{\partial \theta(\xi)}{\partial \xi} d\xi = -\sum_{j=1}^{4} \varphi|_j^k I_{dj}^k \end{aligned} \tag{B.24}$$

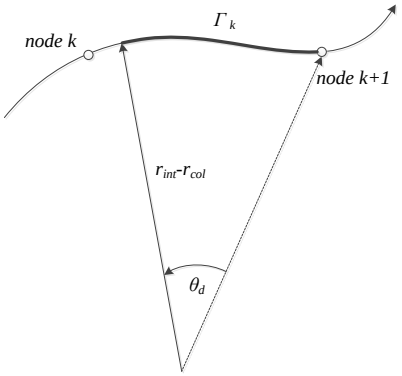

Figure B.2: Definition the transformation used in the integration of distributed dipole

where the parameter ξ_1 is the same as defined in Section B.1.3.2, $\varphi|_j^k$ means the value on j^{th} node among the four adjacent nodes. For the situation that when collocation point lies on node k or $k+1$, the angle for node k or $k+1$ itself is defined to be the tangent angle at that point.

The integration I_{dj}^k is defined as:

$$I_{dj}^k = \int_{\xi}^{\xi+2/3} N_j(\xi)\frac{\partial\theta(\xi)}{\partial\xi}d\xi = N_j(\xi)\theta(\xi)|_{\xi}^{\xi+2/3} - \int_{\xi}^{\xi+2/3}\frac{dN_j(\xi)}{d\xi}\theta(\xi)d\xi \quad \text{(B.25)}$$

This integration is calculated by the Gauss-Legendre quadrature.

b) Calculation of I_s^k on "Quasi-spline" element

For the case of distributed source, similar to the case of I_d^k, the geometry and field function discretization are first substituted into I_s^k as:

$$\begin{aligned} I_s^k &= \int_{\Gamma_k}(\mathbf{r},t)\frac{\partial\varphi(\mathbf{r},t)}{\partial n}\ln(|\mathbf{r}_{int}-\mathbf{r}_{col}|)dl \\ &= \sum_{j=1}^{4}\frac{\partial\varphi}{\partial n}|_j^k\int_{\xi_1}^{\xi_1+2/3}N_j(\xi)\ln(|\mathbf{r}_{int}(\xi)-\mathbf{r}_{col}(\xi)|)\frac{ds}{d\xi}d\xi \\ &= \sum_{j=1}^{4}\frac{\partial\varphi}{\partial n}|_j^k I_{sj}^k \end{aligned} \quad \text{(B.26)}$$

where I_{sj}^k is the integration corresponding to each node of the adjacent four. For the non-singular case, it will be calculated by the Gauss-Legendre quadrature, whilst for the singular one (i.e. the collocation point is either node k or $k+1$), it is calculated by a quadrature that is able to handle the logarithmic singularity [22].

B.2 Weak coupling process

The main feature of weak coupling strategy, compared with the strong coupling case, is that the information will only be feed from one solver to another, there is no mutual exchange. In this particular case, this means the BEM solver, which covers the whole computational domain as shown in Figure 5.24, will provide all the necessary boundary information (e.g. velocity, pressure) to the MPS area. And the MPS solver do not provide feedback to BEM solver. This way of coupling is easier to implement than the strong coupling case, and it will also avoid the stability issue that is introduced by the exchanging of information in strong coupling. Apparently, it will not be as capable as the strong coupling for the situation where significant interaction of flow occurs between potential flow and Navier-Stokes domains. However, as mentioned in the beginning of this chapter, for many cases where the violent free surface deformation only occurs in a restricted area, this simple way of coupling is a more efficient choice. The details of the coupling is described as follows:

As shown in Figure 5.24, the area covered by shadow is modeled by MPS method. The whole computational domain is discretised by BEM nodes. The weak coupling procedure is adopted here. More specifically, as aforementioned, the whole domain will be initially modeled by BEM method up to the time when the wave is about to break (but not breaking yet). The MPS area will also be running from the beginning by taking the pressure and velocity results of BEM as boundary condition at the interface area (i.e. overlapping area shown in Figure 5.24). When the wave modeled by BEM is about to break, the BEM simulation will stop and all the boundary values remain the same. The MPS simulation will continue for the wave structure impact calculation. Considering that the interface area is chosen to be far away from the impacting area, the pressure and velocity of this area will not vary a lot for the whole "post-breaking" duration and close to the state of the calm water. As a result, using the "pre-breaking" BEM value to impose the MPS boundary condition on interface area for post-breaking duration will not affect the results significantly.

At the interface between MPS and BEM domain, the pressure and velocity for MPS particles are calculated based on the BEM solution. These interface particles also move based on the calculated velocity from BEM. The particle arrangement at the interface area is shown in Figure B.3. The first four columns of MPS particles are treated as the interface particles. Their velocity are calculated based on the values of φ and $\frac{\partial \varphi}{\partial n}$ on the BEM boundaries. More specifically, the velocity

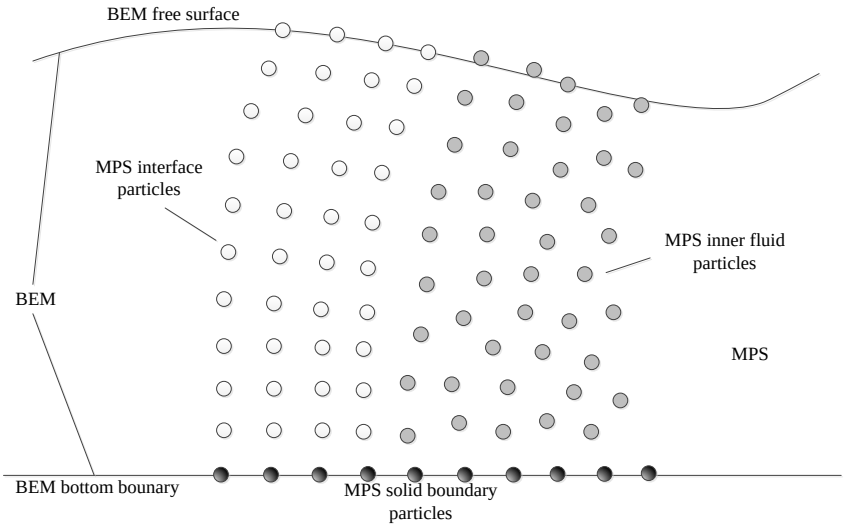

Figure B.3: Sketch of the BEM-MPS interface

is calculated by taking gradient operation on both side of Eq. (B.2) as follows:

$$\alpha_u(\mathbf{r}_{col},t)\nabla_{col}\varphi(\mathbf{r}_{col},t) = \oint[\nabla_{col}(\frac{\partial \ln(|\mathbf{r}_{int}-\mathbf{r}_{col}|)}{\partial n})\varphi(\mathbf{r}_{int},t) - \frac{\partial\varphi(\mathbf{r}_{int},t)}{\partial n}\nabla_{col}(\ln(|\mathbf{r}_{int}-\mathbf{r}_{col}|))]dl, \tag{B.27}$$

where ∇_{col} indicates that the gradient operation is with respect to the coordinates of the collocation point $\mathbf{r}_{col}$. On the straight-line boundaries such as wavemaker or fixed solid walls, the integration on the right hand side could be calculated analytically by the formulation provided in Ref [44]. For the curved free surface, the "Quasi-spline" element (between two adjacent nodes) is further divided into several "sub-elements", which are simply represented by straight-lines. And then the integrations are calculated on these "sub-elements" by the same analytical approach used for straight-line boundaries.

The pressure of the interface MPS particles are calculated based on Bernoulli equation as:

$$p = -(\frac{\partial\varphi}{\partial t} + \frac{1}{2}|\nabla\varphi|^2 + gy)\rho \tag{B.28}$$

The value of $\frac{\partial\varphi}{\partial t}$ is calculated directly from the solution of the additional integral equation for $\frac{\partial\varphi}{\partial t}$ and $\frac{\partial\varphi^2}{\partial n\partial t}$ as mentioned in Appendix B.1.2.

Appendix C

Calculation of mode shape and natural frequency of ship hull structure

The structure model proposed in Section 3 requires the mode shape and natural frequency information of a structure. It is easy to obtain them for regular shape structures (such as beam), since the analytical solution is available. For an arbitrary structure like the ship model, it has to be calculated numerically. As a general approach, the FEM method is of course capable to the job, however in the field of ship hydroelasticity, the so-called Myklestad's method [26, 107] is more commonly used. The detailed procedure of this method used for the calculation of Section 6.3 are presented in this section.

The core idea of Myklestad's method is to discretize the non-uniform beam, which is considered as a representation of ship hull , into a set of lumped mass connected with massless flexible beams. This method could be used to calculate the mode shape and natural frequency of a non-uniform beam with any boundary condition. In this study, corresponding to the case of floating ship, the free-free case is used and shown in Figure C.1. The force and moment applied on n^{th} element is shown in Figure C.2. y, θ, S, m and M represent deflection, slope, shear force, mass of lumped element and bending moment respectively. It has to be mentioned that the shear force is taken from the cross-section right after the lumped mass (as marked by the bold line at corresponding positions in Figure C.2). The beam is assumed to be undergoing an harmonic vibration, therefore the acceleration of the lumped mass should be pointing to

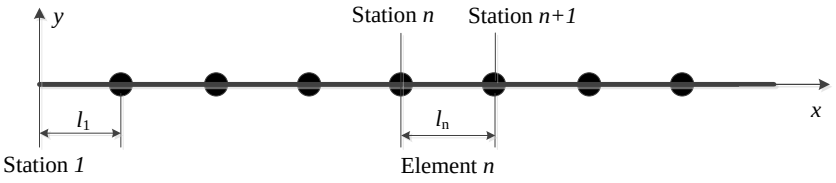

Figure C.1: Sketch of lumped-mass free free beam model

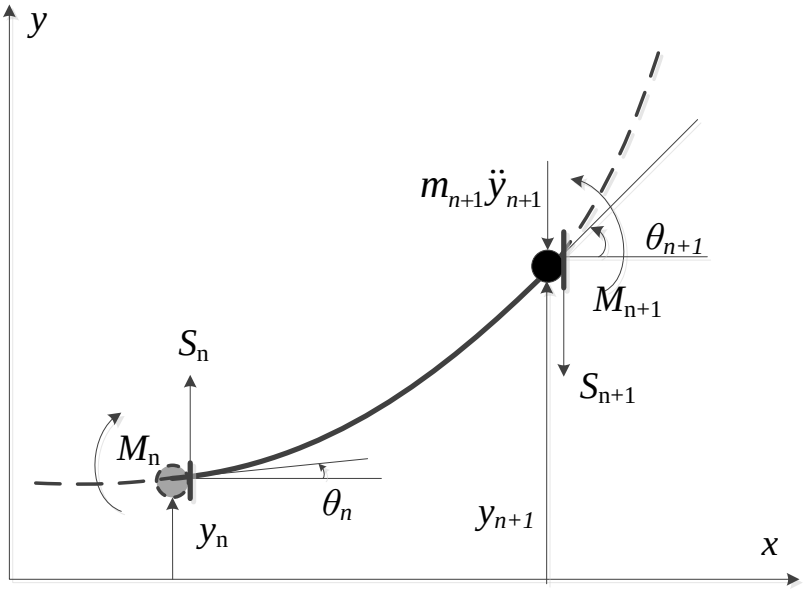

Figure C.2: Force and moment on n^{th} element

the opposite direction of beam deflection y (which is the reason $\ddot{y}$ is pointing downward since the positive direction of y is set to be up). The relation between them is given by Eq. (C.1):

$$y = -\omega^2 \ddot{y} \tag{C.1}$$

where ω is the circular frequency of the vibration. Finally, the dynamic equilibrium of this element could be derived as follows:

$$\begin{aligned} y_{n+1} &= y_n + l_n\theta_n + S_n\frac{l_n^3}{3(EI)_n} + M_n\frac{l_n^2}{2(EI)_n} \\ \theta_{n+1} &= \theta_n + S_n\frac{l_n^2}{2(EI)_n} + M_n\frac{l_n}{(EI)_n} \\ S_{n+1} &= S_n + \omega^2 m_{n+1} y_{n+1} \\ M_{n+1} &= S_n l_n + M_n \end{aligned} \tag{C.2}$$

As shown in Figure C.1, the last station is slightly different from others, there is no lumped mass attached to it (the last lumped mass is attached to the element before last). The dynamic equilibrium is slightly modified accordingly, which means the term "ω^2, m_{n+1} and y_{n+1}" vanishes in the shear force equation in Eq. (C.2) for the last element.

Consequently, if a set of boundary value, which is compatible with the required boundary condition, is imposed on station 1 and an initial guess is given to ω, Eq. (C.2) could determine the boundary values at the terminal station. If ω is one of the natural frequencies, the boundary values will then satisfy the corresponding boundary conditions at the end station.

In order to locate the right value of ω that satisfies the boundary condition, the following procedure is employed. Generally speaking, for any boundary condition, there will be only two of the four values (i.e. y, θ, S and M) are known as initial boundary values such as $M_1 = 0$ and $S_1 = 0$ for free-free case, therefore the values at end station can not be fully determined since y_1 and θ_1 are unknown. However, considering the system defined by Eq. (C.2) is linear, the general solution could be obtained by the linear combination of independent element solutions. Each of the two element solutions of the free-free case are calculated in the way that only deflection y or slope θ is given with unit initial value at first station and all other boundary values are set to be zero. Therefore, the general solution could be written as:

$$\begin{pmatrix} y_n \\ \theta_n \\ M_n \\ S_n \end{pmatrix} = a_1 \begin{pmatrix} y_{n,y} \\ \theta_{n,y} \\ M_{n,y} \\ S_{n,y} \end{pmatrix} + a_2 \begin{pmatrix} y_{n,\theta} \\ \theta_{n,\theta} \\ M_{n,\theta} \\ S_{n,\theta} \end{pmatrix} \tag{C.3}$$

where the subscript of $\{n, y\}$ and $\{n, \theta\}$ mean the element solution at n^{th} station corresponding to unit y and θ input. a_1 and a_2 are arbitrary coefficients.

For free-free beam, the boundary condition for end terminal is $M_{end} = 0$ and $S_{end} = 0$ at natural frequency. As a consequence, the non-trivial solution of coefficients a_1 and a_2 requires the following condition to be satisfied:

$$\Delta(\omega) = \begin{vmatrix} M_{end,y} & M_{end,\theta} \\ S_{end,y} & S_{end,\theta} \end{vmatrix} = 0 \tag{C.4}$$

The value of Δ changes accordingly to different value of frequency ω. Therefore, different root finding approaches could be used to find the natural frequency based on this relation between Δ and ω. Although the Newton-Raphson [26] method is popular one for rooting finding, the convergence rate is found to be very slow for the case investigated in this study, hence the bisection method is used instead with the initial guess from a similar size uniform beam.

After finding the natural frequency ω, the coefficient a_1, a_2 could be obtained by substituting M (or S) value at the end station back into Eq. (C.3). Then the mode shape i.e. the deflection y at each station could be obtained by Eq. (C.2) and (C.3).

Bibliography

[1] Aarsnes, J. V. (1996). Drop test with ship sections – effect of roll angle. Technical report, Norwegian Marine Technology Research Institute.

[2] Akimoto, H. (2013). Numerical simulation of the flow around a planing body by MPS method. *Ocean Engineering*, 64:72–79.

[3] Ataie-Ashtiani, B. and Farhadi, L. (2006). A stable moving-particle semi-implicit method for free surface flows. *Fluid Dynamics Research*, 38(4):241–256.

[4] Atluri, S. N. and Shen, S. (2002). The meshless local petrov-galerkin (MLPG) method: A simple & less-costly alternative to the finite element and boundary element methods. *CMES*, 3(1):11–51.

[5] Barcarolo, D. A., Le Touzé, D., Oger, G., and de Vuyst, F. (2014). Adaptive particle refinement and derefinement applied to the smoothed particle hydrodynamics method. *Journal of Computational Physics*, 273:640–657.

[6] Bathe, K.-J. (1996). *Finite Element Procedures*. Prentice-Hall.

[7] Belytschko, T., Lu, Y., and Gu, L. (1994). Element-free galerkin method. *International Journal for Numerical Methods in Engineering*, 37:229–256.

[8] Belytschko, T. and O.Neal, M. (1991). Contact-impact by the pinball method with penalty and lagrangian methods. *International Journal for Numerical Methods in Engineering*, 31:547–572.

[9] Benra, F.-K., Dohmen, H. J., Pei, J., Schuster, S., and Wan, B. (2011). A comparison of one-way and two-way coupling methods for numerical analysis of fluid-structure interactions. *Journal of Applied Mathematics*, 2011:1–16.

[10] Bishop, R. and Price, W. (1979). *Hydroelasticity of Ships*. Cambridge University Press.

[11] Bishop, R. E. D., Price, W. G., and Wu, Y. (1986). A general linear hydroelasticity theory of floating structures moving in a seaway. *Philosophical Transactions of the Royal Society A: Mathematical, Physical and Engineering Sciences*, 316(1538):375–426.

[12] Brown, D. L., Cortez, R., and Minion, M. L. (2001). Accurate projection methods for the incompressible navier–stokes equations. *Journal of Computational Physics*, 168(2):464–499.

[13] Chaniotis, A. K., Poulikakos, D., and Koumoutsakos, P. (2002). Remeshed smoothed particle hydrodynamics for the simulation of viscous and heat conducting flows. *Journal of Computational Physics*, 182(1):67–90.

[14] Chen, R. H., Tian, W. X., Su, G. H., Qiu, S. Z., Ishiwatari, Y., and Oka, Y. (2011). Numerical investigation on coalescence of bubble pairs rising in a stagnant liquid. *Chemical Engineering Science*, 66(21):5055–5063.

[15] Chen, X.-j., Wu, Y.-s., Cui, W.-c., and Jensen, J. J. (2006). Review of hydroelasticity theories for global response of marine structures. *Ocean Engineering*, 33(3-4):439–457.

[16] Chorin, A. (1967). A numerical method for solving incompressible viscous flow problems. *Journal of Computational Physics*, 2:12–26.

[17] Chowdhury, S. d. (2014). *SPH Simulation of nonlinear water waves*. Phd thesis, Inidan Institute of Technology Madras.

[18] Colagrossi, A., Antuono, M., and Le Touzé, D. (2009). Theoretical considerations on the free-surface role in the smoothed-particle-hydrodynamics model. *Physical Review E*, 79(5).

[19] Colagrossi, A. and Landrini, M. (2003). Numerical simulation of interfacial flows by smoothed particle hydrodynamics. *Journal of Computational Physics*, 191(2):448–475.

[20] Colicchio, G., Greco, M., and Faltinsen, O. M. (2006). A BEM-level set domain-decomposition strategy for non-linear and fragmented interfacial flows. *International Journal for Numerical Methods in Engineering*, 67(10):1385–1419.

[21] Crespo, A. J. C. (2008). *Application of the Smoothed Particle Hydrodynamics model SPHysics to free-surface hydrodynamics*. Phd thesis, Universidade De Vigo.

[22] Crow, J. (1993). Quadrature of integrands with a logarithmic singularity. *Mathematics of Computation*, 60(201):297–301.

[23] Cummins, S. J. and Rudmany, M. (1999). ISPH-an SPH projection method. *Journal of Computational Physics*, 152:584–607.

[24] Dai, Y. S. and Duan, W. Y. (2008). *Potential Flow Theory of Ship Motions in Waves (in Chinese)*. National Defend Industry Press.

[25] Dalrymple, R. A. and Rogers, B. D. (2006). Numerical modeling of water waves with the SPH method. *Coastal Engineering*, 53(2-3):141–147.

[26] Dawson, B. and Davies, M. (1975). An addition to myklestad's method giving convergence to a natural frequency. *Journal of Ship Research*, 19(2):130–132.

[27] De Vuyst, T., Vignjevic, R., and Campbell, J. C. (2005). Coupling between meshless and finite element methods. *International Journal of Impact Engineering*, 31(8):1054–1064.

[28] Degroote, J., Souto-Iglesias, A., Van Paepegem, W., Annerel, S., Bruggeman, P., and Vierendeels, J. (2010). Partitioned simulation of the interaction between an elastic structure and free surface flow. *Computer Methods in Applied Mechanics and Engineering*, 199(33-36):2085–2098.

[29] Delorme, L., Colagrossi, A., Souto-Iglesias, A., Zamora-Rodríguez, R., and Botía-Vera, E. (2009). A set of canonical problems in sloshing, part i: Pressure field in forced roll—comparison between experimental results and SPH. *Ocean Engineering*, 36(2):168–178.

[30] Eça, L., Oñate, E., García, J., Kvamsdal, T., and Bergan, P. (2011). In *MARINE 2011–Computational Methods in Marine Engineering IV*. International Center for Numerical Methods in Engineering (CIMNE).

[31] Feng, A. c. (2014). *Numerical Simulation of Nonlinear Wave-body Problem Based on Desingularized Rankine Source and Mixed Euler-Lagrange Method*. Phd thesis, University of Southampton.

[32] Fernández, M. A., Gerbeau, J.-F., and Grandmont, C. (2007). A projection semi-implicit scheme for the coupling of an elastic structure with an incompressible fluid. *International Journal for Numerical Methods in Engineering*, 69(4):794–821.

[33] Ferrari, A., Dumbser, M., Toro, E. F., and Armanini, A. (2009). A new 3d parallel SPH scheme for free surface flows. *Computers & Fluids*, 38(6):1203–1217.

[34] Fourey, G., Touzé, D. L., Alessandrini, B., and Oger, G. (2010). SPH-FEM coupling to simulate fluid-structure interactions with complex free-surface flows.

[35] Gingold, R. and Monaghan, J. (1977). Smoothed particle hydrodynamics theory and application to non-spherical stars. *Monthly Notices of the Royal Astronomical Society*, 181:375–389.

[36] Gomez-Gesteira, M., Rogers;, B. D., Dalrymple, R. A., and Crespo, A. J. (2010). State-of-the-art of classical SPH for free-surface flows. *Journal of Hydraulic Research*.

[37] Gotoh, H. and Sakai, T. (2006). Key issues in the particle method for computation of wave breaking. *Coastal Engineering*, 53(2-3):171–179. review of improvement.

[38] Grilli, S. (2008). On the development and application of hybrid numerical models in nonlinear free surface hydrodynamics. In *8th International Conference on Hydrodynamics*, Nantes, France.

[39] Grilli, S. and Subramanya, R. (1996). Numerical modeling of wave breaking induced by fixed or moving boundaries. *Computational Mechanics*, 17(6):374–391.

[40] Grilli, S. and Svendsen, I. (1990). Corner problems and global accuracy in the boundary element solution of nonlinear wave. *Engineering Analysis with Boundary Elements*, 7(4):178–195.

[41] Grilli, S. T., Guyenne, P., and Dias, F. (2001). A fully non-linear model for three dimensional overturning waves over an arbitrary bottom. *International Journal for Numerical Methods in Fluids*, 35(7):829–867.

[42] Guruswamy, G. P. (2002). A review of numerical fluids/structures interface methods for computations using high-fidelity equations. *Computers and Structures*, 80:31–41.

[43] Hübner, B., Walhorn, E., and Dinkler, D. (2004). A monolithic approach to fluid–structure interaction using space–time finite elements. *Computer Methods in Applied Mechanics and Engineering*, 193(23-26):2087–2104.

[44] He, W. and Dai, Y. (1991). On the calculation of induced potentials and velocities by some most used singularity line segments (in chinese). *Journal of Harbin Shipbuilding Engineering Institute*, 12(2):139–147.

[45] Heil, M. (2004). An efficient solver for the fully-coupled solution of large-displacement fluid-structure interaction problems. *Computer Methods in Applied Mechanics and Engineering*, 193:1–23. monolithic.

[46] Heil, M., Hazel, A. L., and Boyle, J. (2008). Solvers for large-displacement fluid–structure interaction problems: segregated versus monolithic approaches. *Computational Mechanics*, 43(1):91–101.

[47] Hirt, C. W. and Nichols, B. D. (1981). Volume of fluid (vof) method for the dynamics of free boundaries. *Journal of Computational Physics*, 39(1):201–225.

[48] Hori, C., Gotoh, H., Ikari, H., and Khayyer, A. (2011). GPU-acceleration for moving particle semi-implicit method. *Computers & Fluids*, 51(1):174–183.

[49] Hsiao, K.-M. and Jang, J.-Y. (1991). Dynamic analysis of planar flexible mechanisms by co-rotational formulation. *Computer Methods in Applied Mechanics and Engineering*, 87(1):1–14.

[50] Hu, C. H., Faltinsen, O. M., and Kasawagi, M. (2005). 3-d numerical simulation of freely moving floating body by cip method.

[51] Hu, C. H. and Kashiwagi, M. (2004). A cip-based method for numerical simulation of violent free-surface flows. *Journal of Marine Science and Technology*, 9(4):143–157.

[52] Hu, C. H., Kashiwagi, M., and Kishev, Z. (2004). Numerical simulation of violent sloshing by cip method.

[53] Hu, X. Y. and Adams, N. A. (2007). An incompressible multi-phase SPH method. *Journal of Computational Physics*, 227(1):264–278.

[54] Idelsohn, S. R., Del Pin, F., Rossi, R., and Onate, E. (2009). Fluid-structure interaction problems with strong added-mass effect. *International Journal for Numerical Methods in Engineering*, 80(10):1261–1294.

[55] Janssen, C., Grilli, S., and Krafczyk, M. (2010). Modeling of wave breaking and wave–structure interactions by coupling of fully nonlinear potential flow and lattice–boltzmann models. In *20th International Offshore Polar Engineering Conference*, Beijing,China.

[56] Jin, J. Z. (2007). *A Mixed Mode Function – Boundary Element Method for Very Large Floating Structure – Water Interaction Systems Excited by Airplane Landing Impacts*. PhD thesis, University of Southampton.

[57] Jin, J. Z. and Xing, J. T. (2007). Transient dynamic analysis of a floating beam–water interaction system excited by the impact of a landing beam. *Journal of Sound and Vibration*, 303(1-2):371–390.

[58] Kashiwagi, M. (2000). A time-domain mode-expansion method for calculating transient elastic responses of a pontoon-type vlfs. *Journal of Marine Science and Technology*, 5:89–100.

[59] Kassiotis, C. (2009). *Nonlinear fluid-structure interaction: a partitioned approach and its application through component technology*. PhD thesis, University of Paris-Est.

[60] Kassiotis, C., Ferrand, M., Violeau, D., and Rogers, B. (2011). Coupling SPH with a 1-D boussinesq-type wave model. In *The 6th International SPHERIC Workshop*, Hamburg,Germany.

[61] Khayyer, A. (2008). *Improved Particle Methods by Refined Differential Operator Models for Free-Surface Fluid Flows*. PhD thesis, Kyoto University.

[62] Khayyer, A. and Gotoh, H. (2008). Development of CMPS method for accurate water-surface tracking in breaking waves. *Coastal Engineering Journal*, 50(2).

[63] Khayyer, A. and Gotoh, H. (2009). Modified moving particle semi-implicit methods for the prediction of 2d wave impact pressure. *Coastal Engineering*, 56(4):419–440.

[64] Khayyer, A. and Gotoh, H. (2010). A higher order laplacian model for enhancement and stabilization of pressure calculation by the MPS method. *Applied Ocean Research*, 32(1):124–131.

[65] Khayyer, A. and Gotoh, H. (2011). Enhancement of stability and accuracy of the moving particle semi-implicit method. *Journal of Computational Physics*, 230(8):3093–3118. tensile stability.

[66] Khayyer, A. and Gotoh, H. (2013). Enhancement of performance and stability of MPS mesh-free particle method for multiphase flows characterized by high density ratios. *Journal of Computational Physics*, 242:211–233.

[67] Kimmoun, O., Malenica, ., and Scolan, Y.-M. (2009). Fluid structure interactions occuring at a flexible vertical wall impacted by a breaking wave.

[68] Kishev, Z. R., Hu, C., and Kashiwagi, M. (2006). Numerical simulation of violent sloshing by a cip-based method. *Journal of Marine Science and Technology*, 11(2):111–122.

[69] Kleefsman, K. M. T., Fekken, G., Veldman, A. E. P., Iwanowski, B., and Buchner, B. (2005). A volume-of-fluid based simulation method for wave impact problems. *Journal of Computational Physics*, 206(1):363–393.

[70] Knoll, D. A. and Keyes, D. E. (2004). Jacobian-free newton–krylov methods: a survey of approaches and applications. *Journal of Computational Physics*, 193(2):357–397.

[71] Koh, C. G., Gao, M., and Luo, C. (2012). A new particle method for simulation of incompressible free surface flow problems. *International Journal for Numerical Methods in Engineering*, 89(12):1582–1604.

[72] Kondo, M. and Koshizuka, S. (2011). Improvement of stability in moving particle semi-implicit method. *International Journal for Numerical Methods in Fluids*, 65(6):638–654.

[73] Koshizuka, S. and Oka, Y. (1996). Moving-particle semi-implicit method for fragmentation of incompressible fluid. *Nuclear Science and Engineering*, 123:421–434.

[74] Koshizuka, S. and Oka, Y. (2001). Application of moving particle semi-implicit method to nuclear reactor safety. *Computational Fluid Dynamics*.

[75] Koshizuka, S., Tamako, H., and Oka, Y. (1995). A particle method for incompressible viscous flow with fluid fragmentation. *Computational Fluid Dynamic Journal*, 4(1):29–46.

[76] Küttler, U. and Wall, W. A. (2008). Fixed-point fluid–structure interaction solvers with dynamic relaxation. *Computational Mechanics*, 43(1):61–72.

[77] Lachaume, C., Biausser, B., Grilli, S., Fraunie, P., and Guignard, S. (2003). Modeling of breaking and post-breaking waves on slopes by coupling of BEM and VOF methods. In *13th International Offshore Polar Engineering Conference*, Honolulu,HI, USA.

[78] Lancaster, P. and Salkauskas, K. (1981). Surface generated by moving least square methods. *Mathematics of Computation*, 37(155).

[79] Larese, A., Rossi, R., Oñate, E., and Idelsohn, S. R. (2008). Validation of the particle finite element method (pfem) for simulation of free surface flows. *Engineering Computations*, 25(4):385–425.

[80] Le Touzé, D., Colagrossi, A., Colicchio, G., and Greco, M. (2013). A critical investigation of smoothed particle hydrodynamics applied to problems with free-surfaces. *International Journal for Numerical Methods in Fluids*, pages 660–691.

[81] Le Touzé, D., Marsh, A., Oger, G., Guilcher, P. M., Khaddaj-Mallat, C., Alessandrini, B., and Ferrant, P. (2010). SPH simulation of green water and ship flooding scenarios. *Journal of Hydrodynamics, Ser. B*, 22(5):231–236.

[82] Lee, B. H., Park, J. C., Kim, M. H., and Hwang, S. C. (2011). Step-by-step improvement of MPS method in simulating violent free-surface motions and impact-loads. *Computer Methods in Applied Mechanics and Engineering*, 200(9-12):1113–1125.

[83] Lee, B. H., Park, J. C., Kim, M. H., Jung, S. J., Ryu, M. C., and Kim, Y. S. (2010). Numerical simulation of impact loads using a particle method. *Ocean Engineering*, 37(2-3):164–173.

[84] Lee, C.-H. and Newman, J. N. (2004). Computation of wave effects using the panel method. In *Numerical models in fluid-structure interaction–WIT Transactions on State-of-the-art in Science and Engineering*, Southampton,UK.

[85] Lee, C. J. K., Noguchi, H., and Koshizuka, S. (2007). Fluid–shell structure interaction analysis by coupled particle and finite element method. *Computers & Structures*, 85(11-14):688–697.

[86] Li, S. and Liu, W. K. (2002). Meshfree and particle methods and their applications. *Applied Mechanics Reviews*, 55(1):1.

[87] Liao, K., Hu, C., and Duan, W. (2013). Two-dimensional numerical simulation of an elastic wedge water entry by a coupled fdm-fem method. *Journal of Marine Science and Application*, 12(2):163–169.

[88] Lin, H. and Atluri, S. (2001). The meshless local petrov-galerkin (MLPG) method for solving incompressible navier-stokes equations. *CMES*, 2(2):117–142.

[89] Liszka, T., Duarte, C., and Tworzydlo, W. (1996). Hp-meshless cloud method. *Computer Methods in Applied Mechanics and Engineering*, 139:263–288.

[90] Liu, G. and Gu, Y. (2005). *An Introduction to Meshfree Methods and Their Programming*. Springer.

[91] Liu, G. and Liu, M. B. (2003). *Smoothed Paricle Hydrodynamics—A meshfree particle method*. World scientific.

[92] Liu, W. K., Jun, S., and Zhang, Y. F. (1995). Reproducing kernel particle methods. *International Journal for Numerical Methods in Fluids*, 20:1081–1106.

[93] Lobovsky, L., Botia-Vera, E., Castellana, F., Mas-Soler, J., and Souto-Iglesias, A. (2014). Experimental investigation of dynamic pressure loads during dam break. *Journal of Fluids and Structures*, 48:407–434.

[94] Longuet-Higgins, M. and Cokelet, E. (1976). The deformation of steep surface waves on water. i. a numerical method of computation. *Proceeding s of the Royal Society of London, Series A, Mathematical and Physical Sciences*, 350:1–26.

[95] Loon, R. v., Anderson, P., Vosse, F. v. d., and Sherwin, S. (2007). Comparison of various fluid-structure interaction methods for deformable bodies. *Computers and Structures*, 85:833–843.

[96] Lu, H., Yang, C., and Löhner, R. (2010). Numerical studies of green water impact on fixed and moving bodies.

[97] Lucy, L. (1977). A numerical approach to the testing of the fission hypothesis. *The Astronomical Journal*, 82(12):1013–1024.

[98] Ma, Q.W.and Zhou, J. (2009). MLPG_R method for numerical simulation of 2d breaking waves. *CMES*, 43(3):277–303.

[99] Ma, Q. (2005). MLPG method based on rankine source solution for simulating nonlinear water waves. *CMES*, 9(2):193–209.

[100] Ma, Q. and Yan, S. (2009). Qale-fem for numerical modelling of non-linear interaction between 3d moored floating bodies and steep waves. *International Journal for Numerical Methods in Engineering*, 78(6):713–756.

[101] Marrone, S. (2011). *Enhanced SPH modeling of free-surface flows with large deformation*. PhD thesis, University of Rome.

[102] Marrone, S., Colagrossi, A., Antuono, M., Lugni, C., and Tulin, M. P. (2011). A 2d+t SPH model to study the breaking wave pattern generated by fast ships. *Journal of Fluids and Structures*, 27(8):1199–1215.

[103] Maurel, B., Potapov, S., Fabis, J., and Combescure, A. (2009). Full SPH fluid-shell interaction for leakage simulation in explicit dynamics. *International Journal for Numerical Methods in Engineering*, 80(2):210–234.

[104] McKee, S., Tomé, M. F., Ferreira, V. G., Cuminato, J. A., Castelo, A., Sousa, F. S., and Mangiavacchi, N. (2008). The MAC method. *Computers & Fluids*, 37(8):907–930.

[105] Mittal, R. and Iaccarino, G. (2005). Immersed boundary methods. *Annual Review of Fluid Mechanics*, 37(1):239–261.

[106] Monaghan (1994). Simulating free surface flows with SPH. *Journal of Computational Physics*, 110:399–406.

[107] Myklestad, N. (1944). New method of calculating natural modes of uncoupled bending vibrations. *Journal of Aeronautical Sciences*, 11:153–162.

[108] Nayroles, B., Touzot, G., and Villon, P. (1992). Generalizing the finite element method diffuse approximation and diffuse elements. *Computational Mechanics*, 10:307–318.

[109] Newman, J. N. (1994). Wave effect on deformable bodies. *Applied Ocean Research*, 16:47–59.

[110] Newmark, N. M. (1959). A method of computation for structural dynamics. *Journal of the Engineering Mechanics Division*, 85(3):67–94.

[111] Oñate, E., Idelsohn, S., Zienkiewicz, C., and Taylor, R. (1996). A finite point method in computational mechanics. applications to convective transport and fluid flow. *International Journal for Numerical Methods in Engineering*, 39:3839–3866.

[112] Oñate, E., Sacco, C., and Idelsohn, S. (2001). Advances in the finite point method for meshless analysis of incompressible flow problems.

[113] Oger, G., Doring, M., Alessandrini, B., and Ferrant, P. (2006). Two-dimensional SPH simulations of wedge water entries. *Journal of Computational Physics*, 213(2):803–822.

[114] Oger, G., Doring, M., Alessandrini, B., and Ferrant, P. (2007). An improved SPH method: Towards higher order convergence. *Journal of Computational Physics*, 225(2):1472–1492.

[115] Osher, S. and Fedkiw, R. (2001). Level set methods: An overview and some recent results. *Journal of Computational Physics*, 169:463–502.

[116] Paik, K.-J., Carrica, P. M., Lee, D., and Maki, K. (2009). Strongly coupled fluid–structure interaction method for structural loads on surface ships. *Ocean Engineering*, 36(17-18):1346–1357.

[117] Panciroli, R. (2013). Hydroelastic impacts of deformable wedges. *Solid Mechanics and Its Applications*, 192:1–45.

[118] Panciroli, R., Abrate, S., and Minak, G. (2013). Dynamic response of flexible wedges entering the water. *Composite Structures*, 99:163–171.

[119] Park, S. and Jeun, G. (2011). Coupling of rigid body dynamics and Moving Particle Semi-implicit method for simulating isothermal multi-phase fluid interactions. *Computer Methods in Applied Mechanics and Engineering*, 200(1-4):130–140.

[120] Patel, M., Vignjevic, R., and Campbell, J. (2009). An SPH technique for evaluating the behaviour of ships in extreme ocean waves. *International Journal of Maritime Engineering*, 151:39–47.

[121] Ryzhakov, P., Oñate, E., Rossi, R., and Idelsohn, S. (2012). Improving mass conservation in simulation of incompressible flows. *International Journal for Numerical Methods in Engineering*, 90(12):1435–1451.

[122] Ryzhakov, P. B., Rossi, R., Idelsohn, S. R., and Oñate, E. (2010). A monolithic lagrangian approach for fluid–structure interaction problems. *Computational Mechanics*, 46(6):883–899.

[123] Shadloo, M. S., Zainali, A., Yildiz, M., and Suleman, A. (2012). A robust weakly compressible SPH method and its comparison with an incompressible SPH. *International Journal for Numerical Methods in Engineering*, 89(8):939–956.

[124] Shakibaeinia, A. and Jin, Y. C. (2009). A weakly compressible MPS method for modeling of open-boundary free-surface flow. *International Journal for Numerical Methods in Fluids*, pages 1208–1232.

[125] Shakibaeinia, A. and Jin, Y.-C. (2012). MPS mesh-free particle method for multiphase flows. *Computer Methods in Applied Mechanics and Engineering*, 229-232:13–26.

[126] Shao, J. R., Li, H. Q., Liu, G. R., and Liu, M. B. (2012). An improved SPH method for modeling liquid sloshing dynamics. *Computers & Structures*, 100-101:18–26.

[127] Shao, S. (2009). Incompressible SPH simulation of water entry of a free-falling object. *International Journal for Numerical Methods in Fluids*, 59(1):91–115.

[128] Shao, S. and Lo, E. Y. M. (2003). Incompressible SPH method for simulating newtonian and non-newtonian flows with a free surface. *Advances in Water Resources*, 26(7):787–800.

[129] Shao, Y.-L. and Faltinsen, O. M. (2014). A harmonic polynomial cell (HPC) method for 3d laplace equation with application in marine hydrodynamics. *Journal of Computational Physics*, 274(1):312–332.

[130] Shao fan, L. and Wing kam, L. (2007). *Meshfree Particle Methods*. Springer.

[131] Sheu, T. W. H., Chiao, C., and Huang, C. (2011). Development of a particle interaction kernel function in MPS method for simulating incompressible free surface flow. *Journal of Applied Mathematics*, 2011:1–16.

[132] Shibata, K., Koshizuka, S., Tamai, T., and Murozono, K. (2012). Overlapping particle techniques and application on green water on deck. In *International Conference on Violent Flows*, Nantes, France.

[133] Shibata, K., Koshizuka, S., and Tanizawa, K. (2009). Three-dimensional numerical analysis of shipping water onto a moving ship using a particle method. *Journal of Marine Science and Technology*, 14(2):214–227.

[134] Shibata, K., Tanizawa, K., and Koshizuka, S. (2007). Numerical analysis of coupling between ship motion and green water on deck using MPS method. In *International Conference on Violent Flows (VF-2007)*, Fukuoka, Japan.

[135] Shu, C., Ding, H., and Yeo, K. (2002). Local radial basis function-based differential quadrature method and its application to solve two-dimensional incompressible navier–stokes equations. *Comput. Methods in Applied Mechanics Engineering*, 192:941–954.

[136] Souto-Iglesias, A., Macià, F., González, L. M., and Cercos-Pita, J. L. (2013). On the consistency of MPS. *Computer Physics Communications*, 184(3):732–745.

[137] Springel, V., Yoshida, N., and White, S. D. (2001). Gadget: a code for collisionless and gasdynamical cosmological simulations. *New Astronomy*, 6:79–117.

[138] Sriram, V., Ma, Q. W., and Schlurmann, T. (2014). A hybrid method for modelling two dimensional non-breaking and breaking waves. *Journal of Computational Physics*, 272:429–454.

[139] Sriram, V. and Ma.Q.W. (2012). Improved MLPG_R method for simulating 2d interaction between violent waves and elastic structures. *Journal of Computational Physics*, 231(22):7650–7670.

[140] Starke, A., Van der Ploeg, A., and Raven, H. (2010). Viscous free surface flow computations for self-propulsion conditions using parnassos.

[141] Sueyoshi, M., Kihara, H., and Kashiwagi, M. (2007). A hybrid technique using particle and boundary-element methods for wave-body interaction problems.

[142] Sun, F. (2013). *Investigation of Smoothed Particle Hydrodynamics Method for Fluid-Rigid Body Interactions*. Phd thesis, University of Southampton.

[143] Sun, H. (2007). *A Boundary Element Method Applied to Strongly Nonlinear Wave-Body Interaction Problems*. Phd thesis, Norwegian University of Science and Technology.

[144] Sun, Z., Djidjeli, K., Xing, J. T., and Cheng, F. (2015a). Modified MPS method for the 2d fluid structure interaction problems with free surface. *Computers and Fluids*, 122:47–65.

[145] Sun, Z., Djidjeli, K., Xing, J. T., and Cheng, F. (2016). Coupled MPS-modal superposition method for 2d nonlinear fluidstructure interaction problems with free surface. *Journal of Fluids and Structures*.

[146] Sun, Z., Djidjeli, K., Xing, J. T., Cheng, F., and Javed, A. (2014). Some modifications of MPS method for incompressible free surface flow. In *11th World Congress on Computational Mechanics (WCCM XI)*, Barcelona, Spain.

[147] Sun, Z., Pang, Y., and Li, H. (2012). Two dimensional fully nonlinear numerical wave tank based on the BEM. *Journal of Marine Science and Application*, 11(4):437–446.

[148] Sun, Z., Xing, J. T., Djidjeli, K., and Cheng, F. (2015b). Coupling MPS and modal superposition method for flexible wedge dropping simulation. In *25th International Offshore and Polar Engineering Conference (ISOPE)*, Kona, Hawaii, US.

[149] Suzuki, Y. (2007). *Study on Multi-physics Simulator and Accuracy of Particle Method (in Japanese)*. Phd thesis, University of Tokyo.

[150] Tamai, T. and Koshizuka, S. (2014). Least squares moving particle semi-implicit method. *Computational Particle Mechanics*, 1(3):277–305.

[151] Tan, M., Nair, P. B., Djidjeli, K., and Chinchapatnam, P. P. (2009). A compact rbf-fd based meshless method for the incompressible navier–stokes equations. *Proceedings of the Institution of Mechanical Engineers, Part M: Journal of Engineering for the Maritime Environment*, 223(3):275–290.

[152] Tanaka, M. and Masunaga, T. (2010). Stabilization and smoothing of pressure in MPS method by quasi-compressibility. *Journal of Computational Physics*, 229(11):4279–4290.

[153] Taylor, R., Wu, G., Bai, W., and Hu, Z. (2008). Numerical wave tanks based on finite element and boundary element modeling. *Journal of Offshore Mechanics and Arctic Engineering-Transactions of the ASME*, 130(3).

[154] Teixeira, P. R. F. and Awruch, A. M. (2005). Numerical simulation of fluid–structure interaction using the finite element method. *Computers & Fluids*, 34(2):249–273.

[155] Temarel, P. and Hirdaris, S. E. (2009). Hydroelasticity of ships: recent advances and future trends. *Proceedings of the Institution of Mechanical Engineers, Part M: Journal of Engineering for the Maritime Environment*, 223(3):305–330.

[156] The Seakeeping Committee of 26th ITTC (2011). Seakeeping committee report. Technical report, International Towing Tank Conference.

[157] The Specialist Committee on Computational Fluid Dynamics of 26th ITTC (2011). Computional fluid dynamics committee report. Technical report, International Towing Tank Conference.

[158] Tolstykh, A. I. and Shirobokov, D. A. (2003). On using radial basis functions in a "finite difference mode" with applications to elasticity problems. *Computational Mechanics*, 33(1):68–79.

[159] Tsuruta, N., Khayyer, A., and Gotoh, H. (2013). A short note on dynamic stabilization of moving particle semi-implicit method. *Computers & Fluids*, 82:158–164.

[160] Udofe, P. T. F. (2010). *Simulation and Analysis of Wave-Structure Interaction*. Phd thesis, Newcastle University.

[161] Veen, D. J. and Gourlay, T. P. (2009). An investigation of slamming events in two dimensions using smooth particle hydrodynamics. In *10th International Conference on Fast Sea Transportation, FAST 2009*, Athens, Greece.

[162] Wang, C. and Wu, G. (2006a). An unstructured mesh based finite element simulation of wave interactions with non-wall-sided bodies. *Journal of Fluids and Structures*, 22(4).

[163] Wang, C. and Wu, G. X. (2006b). An unstructured mesh based finite element simulation of wave interactions with non-wall-sided bodies. *Journal of Fluids and Structures*, 22(4):441–461.

[164] Wright, G. B. and Fornberg, B. (2006). Scattered node compact finite difference-type formulas generated from radial basis functions. *Journal of Computational Physics*, 212(1):99–123.

[165] Wu, G. and Taylor, R. E. (2001). The coupled finite element and boundary element analysis of nonlinear interactions between waves and bodies.

[166] Wu, G. X., Hu, Z., Wang, C., and Drake, K. (2005). A numerical tank through linear and quadratic finite element methods.

[167] Xing, J. T. (2016). Developments of numerical methods for linear and nonlinear fuid-solid interaction dynamics with applications. *Advances in Mechanics*, 46(2):95–138.

[168] Xing, J. T. and Price, W. G. (1991). A mixed finite element method for the dynamic analysis of coupled fluid-solid interaction problems. *Proceedings of the Royal Society: Mathematical and Physical Science*, pages 235–255.

[169] Xing, J. T., Price, W. G., and Chen, Y. (2002). A mixed finite-element finite-difference method for nonlinear fluid-structure interaction dynamics. i. fluid-rigid structure interaction. *The Royal Society*, pages 2399–2430.

[170] Xing, J. T., Zhou, S., and E.J., C. (1997). Overview of fluid structure interaction mechanics (in chinese). *Advances in Mechanics*, 27(1):19–38.

[171] Xu, R. (2010). *An Improved Incompressible Smoothed Particle Hydrodynamics Method and Its Application in Free-Surface Simulations*. PhD thesis, University of Manchester.

[172] Xu, R., Stansby, P., and Laurence, D. (2009). Accuracy and stability in incompressible SPH (ISPH) based on the projection method and a new approach. *Journal of Computational Physics*, 228(18):6703–6725.

[173] Yang, Q., Jones, V., and McCue, L. (2012). Free-surface flow interactions with deformable structures using an SPH–FEM model. *Ocean Engineering*, 55:136–147.

[174] Zhang, Q. and Hisada, T. (2004). Studies of the strong coupling and weak coupling methods in fsi analysis. *International Journal for Numerical Methods in Engineering*, 60(12):2013–2029.

[175] Zhang, X., Song, Z. K., and Lu, M. W. (2003). Research progress and application of meshless method. *Chinese Journal of Computational Mechanics*, 20(6).

[176] Zhou, J. and Ma, Q. (2010). MLPG method based on rankine source solution formodelling 3d breaking waves. *CMES*, 56(2):179–210.

[177] Zhu, X. Y. (2006). *Application of the CIP Method to Strongly Nonlinear Wave-Body Interaction Problems*. Phd thesis, Norwegian University of Science and Technology.